School of Science and Engineering
Department of Physics and Astronomy

Spectral Analysis of Estuarine Water for Characterisation of Inherent Optical Properties and Phytoplankton Concentration

Daniel Stephen Marrable

This thesis is presented for the Degree of
Doctor of Philosophy
of
Curtin University

August 2018

Declaration

To the best of my knowledge and belief this thesis contains no material previously published by any other person except where due acknowledgement has been made.

This thesis contains no material which has been accepted for the award of any other degree or diploma in any university.

Signature:

Date: 6/6/2019

Statement of contribution by others

The work - sampling, analysis, writing and software development - in this thesis is entirely my own work. There has been no data, analysis, coding or writing contributed by another author.

Access to laboratories, boats and open source code are acknowledged in Acknowledgments.

Signature of candidate
18/07/2019

Signature of supervisor
18/07/2019

Abstract

The Swan River, Western Australia, is a valuable asset to the city of Perth. It is used for transport, recreational fishing, water sports and is home to the symbolic black swan. In 2004, it was awarded the status of Western Australia's first heritage icon. Its catchment area includes farms and other nutrient inputs; however, warm weather, mixed with nutrient run-off has, at times, caused toxic algal blooms, which require regular detection and monitoring. Current monitoring methods are labour-intensive, point-based, and slow to process in a laboratory before useful results are available to decision-makers.

Remote sensing of water quality has been successfully demonstrated in marine systems where the water is relatively clear and the colour tends to be dominated by the phytoplankton. In comparison, the Swan River is a dark water colour which is dominated by coloured dissolved organic matter (CDOM). Commonwealth Scientific and Industrial Research Organisation (CSIRO) studies using remote sensing techniques to monitor algae in the Swan River have reported that radiometric instruments, such as the Compact Airborne Spectrographic Imager (CASI) are sensitive to radiometric spectral features but are too expensive to use as regular monitoring tools. These studies have also suggested that development of a hyperspectral boat-mounted radiometer and further classification of water IOPs would be required to monitor the river water quality and conditions. This study investigates whether such an instrument, along with existing established remote sensing models and monitoring techniques can be used to measure the abundance of phytoplankton in the Swan River. In particular, it examines whether these techniques can be used to improve and support the Swan-Canning Cleanup Program (SCCP) by making continuous underway measurements between the ten discrete SCCP sample locations.

In this study, a hyperspectral radiometer was used to measure the remote sensing reflectance continuously along the SCCP water sampling sites. Water samples were measured in the laboratory for absorption by phytoplankton and gelbstoff, and in situ measurements of particle scattering and other environmental ancillary data were collected. A remote sensing optical model was used to investigate whether it was possible to derive the concentration of phytoplankton in the Swan River from radiometric measurements of remote sensing reflectance. It was found that it was possible to derive phytoplankton concentration where gelbstoff absorption coefficients of $a_g(440)$ were between 0.00 m^{-1} and 3.402 m^{-1} and phytoplankton absorption coefficients of $a_\phi(440)$ ranged between 0.00

m^{-1} and 0.739 m^{-1} with an error up to ∼23% when compared to in situ measurements. The model inversion uncertainty was ∼34% for the corresponding absorption coefficients. For larger gelbstoff absorption coefficients of $a_g(440)$ between 3.402 m^{-1} and 5.573 m^{-1}, it was found that gelbstoff absorption was too high for the model to accurately determine the phytoplankton levels. At these high concentrations of gelbstoff, the model often underestimated the phytoplankton concentrations.

Unique mathematical techniques were developed to accomplish the outcomes of this work; firstly, an approach to modeling the scattering of individual phytoplankton species was developed, capable of modeling the spectral scattering of spheres, non-spherical particles and modelling the scattering of multilayered volumes. This has future applications to modeling site-specific SIOPs. Secondly, a mathematical inversion procedure was developed for improving IOP retrieval reliability in low light environments as well as estimating derived IOP uncertainties from remote sensing reflectance. This approach has wider applications and can also be applied to other disciplines of science.

The outcomes of this research demonstrate that the model and methods used in this study are capable of accurately estimating the phytoplankton concentrations in the Swan River for a continuous transect encompassing and connecting half of the SCCP sample locations. This corresponds to approximately half (∼15 km) of the river monitoring program assuming that the gelbstoff concentrations do not significantly increase over time at these sites. For sites further up river, the gelbstoff absorption is too high to use the method described, to accurately monitor the phytoplankton concentrations with confidence.

Acknowledgements

Firstly, I would like to express my sincere gratitude to my supervisor Dr Peter Fearns for the generous amount of time and support he gave me over the years and towards my Ph.D. study.

I would also like to thank my collogues and mentors. Firstly, J.D Hedley for access to FDTD code, RTcode, and for the radiative transfer code, PlanarRad. Dr Alec Duncan for his advice on all things signal processing and data analysis. Lastly, Ms Lesley Clementson for her time, patience and advice on all the laboratory work covered in this thesis.

This work was supported by resources provided by the Pawsey Supercomputing Centre with funding from the Australian Government and the Government of Western Australia.

I would like to acknowledge the Swan River Trust for their support, access to their boat and funding towards equipment. Furthermore, thank you to Murdoch University Algae R&D Centre for access to their laboratories and cultures, as well as the time donated in training in laboratory techniques.

Mr Glen Lawson and Mr Mark Whinstanley, for access to laboratories and workshops, as well as help and expertise on these matters.

To all my family and friends that supported me during my studies. Without their support and patience, it would not be possible to conduct this research.

Last but not least, to whom dedicate all of this work. I would like to thank my late grandfather, Mr Harry Kneafsey, who I love and miss every day. Without Pop, I wouldn't be the man I am today nor would I have been able to conducted this research.

Contents

1 Introduction **24**
1.1 Background . . . 24
1.2 Significance . . . 27
1.3 Research Aim . . . 27
1.4 Objectives . . . 28
1.5 Structure of Thesis . . . 29

2 Literature Review **32**
2.1 Introduction . . . 32
2.2 Phytoplankton and Harmful Algal Blooms in Inland Waters . . . 32
2.3 Multispectral and Hyperspectral Monitoring of Algal Blooms . . . 34
2.3.1 Satellite Remote Sensing . . . 35
2.3.2 Airborne Hyperspectral Remote Sensing . . . 39
2.3.3 Field-deployed Remote Sensing Instruments . . . 40
2.4 Optical Models for Measuring Phytoplankton . . . 41
2.4.1 Bio-optical Models . . . 41
2.4.2 In-water Constituents . . . 42
2.4.3 Semi-analytical and Quasi-analytical Models . . . 44
2.4.4 Uncertainty in Bio-optical Models . . . 46
2.5 Phytoplankton in the Swan River . . . 46
2.5.1 Ecological Issues in the Swan River . . . 46
2.5.2 Seasonal and Site Variation in Phytoplankton . . . 48
2.5.3 Swan River Monitoring Programmes . . . 49
2.5.4 Optical Studies and Modelling in the Swan River . . . 50
2.6 Summary . . . 51

3 Comparative Assessment: Mie Theory and FDTD Scattering Methods **52**
3.1 Introduction . . . 52

3.1.1 Particle Scattering . . . 54
3.1.2 General Scattering Problem . . . 57
3.1.3 Mie Theory . . . 62
3.1.4 Finite-Difference Time-Domain (FDTD) . . . 68
3.1.5 FDTD Scattering Modelling of Hydrosols . . . 72
3.2 Method . . . 76
3.2.1 Particle Shape . . . 76
3.2.2 Phytoplankton Internal Structure . . . 76
3.2.3 Model Run . . . 77
3.3 Results . . . 79
3.4 Discussion . . . 90
3.5 Summary . . . 92

4 Phytoplankton Culturing and Absorption 93
4.1 Introduction . . . 93
4.1.1 Phytoplankton Classification . . . 94
4.1.2 Photosynthetic Pigments . . . 96
4.1.3 Harvesting Light Energy . . . 98
4.2 Algal-Culturing Techniques . . . 98
4.3 Algal Spectral Absorption in Optical Model . . . 100
4.4 Summary . . . 102

5 Development of Numerical Techniques for Solving the Optical Model 103
5.1 Introduction . . . 103
5.1.1 Light . . . 103
5.1.2 Coordinate System . . . 103
5.1.3 Radiometry . . . 104
5.1.4 Radiative Transfer Equation . . . 107
5.1.5 Inherent Optical Properties . . . 108
5.1.6 Characterising Volume Scattering Functions . . . 124
5.1.7 Radiative Transfer Equation . . . 126
5.1.8 Solution to the Radiative Transfer Equation . . . 137
5.2 Modelling the Radiative Transfer Equation . . . 137
5.3 Remote Sensing Optical Models . . . 140
5.3.1 HOPE . . . 140
5.3.2 BRDF Corrected Optical Model . . . 143
5.3.3 BRUCE-LUT Optical Model . . . 144

5.3.4 SAMBUCA . . . 146
5.4 Inverting the Model Through Optimisation . . . 148
5.4.1 Optimisation . . . 149
5.4.2 Confidence Intervals . . . 152
5.5 Coherent Noise Modelling for Uncertainty Estimates of Remote Sensing Data . . . 154
5.5.1 Uncertainty calculation methodology . . . 155
5.5.2 Training Stage . . . 160
5.5.3 Generation Stage . . . 165
5.5.4 Solution Stage . . . 173
5.6 Sensitivity Analysis . . . 176
5.7 Summary . . . 180

6 Application to the Swan River 182
6.1 Introduction . . . 182
6.2 Measuring the Above-Water R_{rs} . . . 184
6.3 Calibrating the DALEC . . . 184
6.4 Fieldwork . . . 188
6.4.1 Radiometric Measurements . . . 188
6.4.2 Backscattering Coefficients . . . 190
6.4.3 Water Sample Acquisition . . . 190
6.5 Laboratory Work . . . 193
6.5.1 Optical Density of $(a_\phi + a_{nap})$ . . . 194
6.5.2 Depigmented Absorption (a_{nap}) . . . 195
6.5.3 Gelbstoff Absorption . . . 195
6.6 Sample Data Processing . . . 196
6.7 Results . . . 199
6.7.1 Modelling Comparisons . . . 199
6.7.2 Spot Measurements . . . 206
6.7.3 Continuous Underway Measurements . . . 213
6.7.4 IOP Retrievals for the BLA Location . . . 220
6.7.5 IOP Retrievals for the ARM Location . . . 224
6.7.6 IOP Retrievals for the HEA Location . . . 228
6.7.7 IOP Retrievals for the NAR Location . . . 231
6.7.8 IOP Retrievals for the NIL Location . . . 236
6.7.9 IOP Retrievals for the STJ Location . . . 240

6.7.10 IOP Retrievals for the RON Location . . . 244
6.7.11 IOP Retrievals for the KIN Location . . . 248
6.7.12 IOP Retrievals for the SUC Location . . . 252
6.7.13 In situ Measurements at the 10 SCCP Locations . . . 256
6.7.14 Swan River Profiling . . . 259
6.8 Summary . . . 269

7 Discussion 273
7.1 Introduction . . . 273
7.2 Swan River Results and Validation . . . 274
7.2.1 DALEC and Field Measurements . . . 274
7.2.2 Measurement Uncertainties . . . 276
7.2.3 Model Sensitivity . . . 279
7.2.4 Optical Model Assessment . . . 281
7.3 Optical Scattering Comparison and Assessment . . . 283
7.4 Phytoplankton Culturing and Absorption . . . 286
7.5 Software and Open Source Community Tools . . . 287
7.6 Project Challenges and Limitations - Lessons Learned . . . 290
7.6.1 Fieldwork . . . 290
7.6.2 Laboratory work . . . 291

8 Conclusions 294
8.1 Recommendations and Future Work . . . 300

Appendices 303

A Dominant Phytoplankton Species by Cell Count 304

B Software and Data Processing Scripts 307
B.1 DalecOnTransect . . . 307
B.2 DalecPPT . . . 308
B.3 Planarradpy . . . 310
B.4 Bootstrappy . . . 311
B.5 DALEC and Boat Mount . . . 312

C Coherent Noise Model 313
C.1 Training Stage . . . 313
C.2 Generation Stage . . . 320

C.3 Solution Stage 329

References **331**

List of Figures

1.1 Map of the Swan River, Perth, Western Australia. SCCP sampling locations noted by stars and abbreviated names. 26

2.1 From Mouw et al. (2015): Length- and timescales of coastal and inland processes in relation to heritage, current and planned aquatic color sensors (SeaWiFS, MODIS, MERIS, VIIRS, HICO, GOCI, OLCI) and missions (PACE/ACE, GEO-CAPE, HyspIRI). Planned sensors and missions were italicized in the original publication but OLCI is now operational. . . . 35

3.1 A grid made of Yee cells. The electric and magnetic field components, shown as arrows, are defined on the surface of the Yee cells. The complex index of refraction is defined at the location of the field components to define a particle of any shape (Hedley, 2012). 53

3.2 Yee cell with the orthogonal electric and magnetic field vectors mapped to its surface. 70

3.3 (Left) Representation of a spherical particle with uniform refractive index. (Right) Scattering phase functions derived using the FDTD method compared with Mie theory for an equivalent volume sphere for the S_{11} Mueller matrix scattering element. The figure shows that both methods closely agree. The small differences that can be seen in the backscattering are due to the discretisation of the grid to approximate a perfect sphere. . . . 74

3.4 (Left) Representation of a tetrahedron shaped particle with uniform refractive index. (Right) Scattering phase functions derived using the FDTD method compared with Mie theory for an equivalent volume sphere for the S_{11} Mueller matrix scattering element for a single scattering angle. The figure shows that both methods do not agree and that Mie theory does not accurately model the scattering of the highly aspherical particle. . . 74

3.5 (Left) Representation of a cube shaped particle with uniform refractive index. (Right) Scattering phase functions derived using the FDTD method compared with Mie theory for an equivalent volume sphere for the S_{11} Mueller matrix scattering element for a single scattering angle. The figure shows that both methods do not agree and that Mie theory does not accurately model the scattering of the highly aspherical particles. 75

3.6 (Left) Representation of a multi-layered virtual phytoplankton cell with a cell wall, cytoplasm and nucleus all modelled with different refractive indices. (Right) Scattering phase functions derived the FDTD method with Mie theory for the S_{11} Mueller matrix scattering element for a single scattering angle. 75

3.7 (Left) S_{11} and; (right) $\frac{S_{11}}{S_{12}}$ scattering of *Microcystis-aeruginosa*. Grey curves show the scattering for individual runs of FDTD. The red curve is the average of those runs. The green curve shows the Mie scattering for a sphere of equivalent volume to the algal cell. The blue dots show the results presented in Volten et al. (1998). 79

3.8 (Left) S_{11} and; (right) $\frac{S_{11}}{S_{12}}$ scattering of *Microcystis-sp*. Grey curves show the scattering for individual runs of FDTD. The red curve is the average of those runs. The green curve shows the Mie scattering for a sphere of equivalent volume to the algal cell. The blue dots show the results presented in Volten et al. (1998). 79

3.9 (Left) S_{11} and; (right) $\frac{S_{11}}{S_{12}}$ scattering of *Prochlorothrix-hollandica*. Grey curves show the scattering for individual runs of FDTD. The red curve is the average of those runs. The green curve shows the Mie scattering for a sphere of equivalent volume to the algal cell. The blue dots show the results presented in Volten et al. (1998). 80

3.10 (Left) S_{11} and; (right) $\frac{S_{11}}{S_{12}}$ scattering of *Oscillatoria-amoena*. Grey curves show the scattering for individual runs of FDTD. The red curve is the average of those runs. The green curve shows the Mie scattering for a sphere of equivalent volume to the algal cell. The blue dots show the results presented in Volten et al. (1998). 80

3.11 (Left) S_{11} and; (right) $\frac{S_{11}}{S_{12}}$ scattering of *Oscillatoria-agarhii*. Grey curves show the scattering for individual runs of FDTD. The red curve is the average of those runs. The green curve shows the Mie scattering for a sphere of equivalent volume to the algal cell. The blue dots show the results presented in Volten et al. (1998). 81

3.12 (Left) S_{11} and; (right) $\frac{S_{11}}{S_{12}}$ scattering of *Melosira-granulata*. Grey curves show the scattering for individual runs of FDTD. The red curve is the average of those runs. The green curve shows the Mie scattering for a sphere of equivalent volume to the algal cell. The blue dots show the results presented in Volten et al. (1998). 81
3.13 (Left) S_{11} and; (right) $\frac{S_{11}}{S_{12}}$ scattering of *Asterionella-formosa*. Grey curves show the scattering for individual runs of FDTD. The red curve is the average of those runs. The green curve shows the Mie scattering for a sphere of equivalent volume to the algal cell. The blue dots show the results presented in Volten et al. (1998). 82
3.14 (Left) S_{11} and; (right) $\frac{S_{11}}{S_{12}}$ scattering of *Selenastrum-capricornutum*. Grey curves show the scattering for individual runs of FDTD. The red curve is the average of those runs. The green curve shows the Mie scattering for a sphere of equivalent volume to the algal cell. The blue dots show the results presented in Volten et al. (1998). 82
3.15 (Left) S_{11} and; (right) $\frac{S_{11}}{S_{12}}$ scattering of *Emiliana-huxleyi* without coccospheres. Grey curves show the scattering for individual runs of FDTD. The red curve is the average of those runs. The green curve shows the Mie scattering for a sphere of equivalent volume to the algal cell. The blue dots show the results presented in Volten et al. (1998). 83
3.16 (Left) S_{11} and; (right) $\frac{S_{11}}{S_{12}}$ scattering of *Emiliana-huxleyi* with coccospheres. Grey curves show the scattering for individual runs of FDTD. The red curve is the average of those runs. The green curve shows the Mie scattering for a sphere of equivalent volume to the algal cell. The blue dots show the results presented in Volten et al. (1998). 83
3.17 The blue line shows the scattering fraction, predicted by Mie, over the range 0.02×10^{-6} m and 6.0×10^{-6} m. The green and magenta marks show the scattering fraction averaged over the cell radius variance for *Microcystis-aeruginosa* calculated using FDTD and Mie respectively. . . 84
3.18 The blue line shows the scattering fraction, predicted by Mie, over the range 0.02×10^{-6} m and 6.0×10^{-6} m. The green and magenta marks show the scattering fraction averaged over the cell radius variance for *Microcystis-sp.* calculated using FDTD and Mie respectively. 85

3.19 The blue line shows the scattering fraction, predicted by Mie, over the range 0.02×10^{-6} m and 6.0×10^{-6} m. The green and magenta marks show the scattering fraction averaged over the cell radius variance for *Prochlorothrix-hollandica* calculated using FDTD and Mie respectively. . 85
3.20 The blue line shows the scattering fraction, predicted by Mie, over the range 0.02×10^{-6} m and 6.0×10^{-6} m. The green and magenta marks show the scattering fraction averaged over the cell radius variance for *Oscillatoria-amoena* calculated using FDTD and Mie respectively. 86
3.21 The blue line shows the scattering fraction, predicted by Mie, over the range 0.02×10^{-6} m and 6.0×10^{-6} m. The green and magenta marks show the scattering fraction averaged over the cell radius variance for *Oscillatoria-agardhii* calculated using FDTD and Mie respectively. 86
3.22 The blue line shows the scattering fraction, predicted by Mie, over the range 0.02×10^{-6} m and 6.0×10^{-6} m. The green and magenta marks show the scattering fraction averaged over the cell radius variance for *Melosira-granulata* calculated using FDTD and Mie respectively. 87
3.23 The blue line shows the scattering fraction, predicted by Mie, over the range 0.02×10^{-6} m and 6.0×10^{-6} m. The green and magenta marks show the scattering fraction averaged over the cell radius variance for *Asterionella-formosa* calculated using FDTD and Mie respectively. . . . 87
3.24 The blue line shows the scattering fraction, predicted by Mie, over the range 0.02×10^{-6} m and 6.0×10^{-6} m. The green and magenta marks show the scattering fraction averaged over the cell radius variance for *Selenastrum-capricornutum* calculated using FDTD and Mie respectively. 88
3.25 The blue line shows the scattering fraction, predicted by Mie, over the range 0.02×10^{-6} m and 6.0×10^{-6} m. The green and magenta marks show the scattering fraction averaged over the cell radius variance for *Emiliania-huxleyi* with calcite, calculated using FDTD and Mie respectively. 88
3.26 The blue line shows the scattering fraction, predicted by Mie, over the range 0.02×10^{-6} m and 6.0×10^{-6} m. The green and magenta marks show the scattering fraction averaged over the cell radius variance for *Emiliania-huxleyi* without calcite, calculated using FDTD and Mie respectively. . . 89
3.27 The scattering fractions of all the hydrosols in Table 3.2, predicted by FDTD and Mie theories, compared with each other. 89

4.1 The relative absorption of the cultures grown in the lab. The absorption has been normalised at 440 nm 102

5.1 Definition of the polar coordinates (θ, ϕ) and of the upward (Ξ_u) and downward (Ξ_d) hemispheres of directions. $\Delta\Omega(\hat{\xi})$ is an element of solid angle centred on $\hat{\xi}$. 104
5.2 The transmitance, scatterance and absorptance of a collimated beam of light through a small volume of water (Mobley, 1994). 107
5.3 Historical data of the pure water absorption coefficient. Open circles (∘) represent Smith and Baker (1981), closed circles (•) represent Pope and Fry (1997). Figure taken from Pope and Fry (1997). 114
5.4 Scattering of pure water and sea water. Pure sea water consists of salts, which average about 35‰ by weight. These salts increase scattering above that of pure water by about 30% (Mobley, 1994). 115
5.5 Spectral absorption of five different phytoplankton classes. Different accessory pigments result in unique absorption characteristics. 117
5.6 Spectral scattering of five different phytoplankton classes. Differences in both shape and chemical composition are responsible for unique scattering characteristics. 118
5.7 The absorption coefficient of CDOM modelled using Equations 5.19. In this model instance, A = 0.1, S = 0.015 and the reference wavelength was set to 440 nm. 119
5.8 The scattering coeffecient of b_{bp} modelled using Equations (5.22). In this model instance, X = 0.1, Y = 1.5 and the reference wavelength was set to 400 nm. 121
5.9 Change in spectral absorption values with variable cell size (Morel and Bricaud, 1981). 122
5.10 The spectral relationship between attenuation and chlorophyll-*a* concentration (Bricaud et al., 1988). 123
5.11 The spectral relationship between scattering and chlorophyll-*a* concentration Bricaud et al. (1988). 123
5.12 Measured volume scattering functions from the three different natural waters (Petzold, 1972), and the computed volume scattering function for pure sea water (Mobley, 1994). The dotted line is the particle phase function in Table 3.10 (Mobley, 1994). 124
5.13 Fournier-Forand phase functions for selected backscatter fractions. 127

5.14 Representation of a plane–parallel water body (Mobley, 1994). 127
5.15 Model of the sea surface as a hexagonal grid of triangular wave facets (Mobley, 1994). 131
5.16 Schematic diagrams of common water-surface scattering events (Mobley, 1994). n_s and n_b show the total number of rays involved in the scattering event. 132
5.17 Reflectances for random capillary waves and water-incident light rays from distant point sources. For each group of θ'_s curves, the solid lines are for $\phi'_s = 0°$ (nadir), and the dashed curves are for $\phi_s = 90°$ (source at right angles to the wind direction). For each pair of solid curves or pair of dashed curves, the top curve is for the total scattering and the bottom curve is for single scattering only (Mobley, 1999). 134
5.18 Spectral values of the albedo for various colour substratum (Fearns et al., 2011). 136
5.19 Data flow diagram for the coherent noise method. 159
5.20 Repeat spectral measurements, at at stationary location, taken at the ARM sample location. 160
5.21 The R_{rs} after detrending by subtracting the mean reflectance of the ensemble average. 161
5.22 The standard deviation of the detrended ensemble average. 162
5.23 The 'stationary' reflectance normalised by dividing each spectra by the standard deviation. 163
5.24 The power spectrum of the ensemble. 164
5.25 The correlation function of the ensemble. 165
5.26 Random data points generated for each spectra at each wavelength. . . . 166
5.27 The random point transformed to the Fourier domain by taking the FFT of the random points. 167
5.28 The Fourier transform of the randomly generated points multiplied by the power spectrum. 168
5.29 The correlated noise transformed back to the real domain by taking the inverse Fourier transform. 169
5.30 Normalised correlated noise calculated by dividing $y(\lambda)$ by the standard deviation of itself. 170
5.31 The standard deviation of the normalised correlated noise. All wavelengths should be 1. This step is taken to ensure that the process has been followed correctly so far. 170

5.32 The detrended simulated reflectance data created by multiplying the normalised correlated noise by the standard deviation of the simulated R_{rs}. . 171
5.33 Simulated remote sensing reflectance generated by multiplying the detrended simulated reflectance by the reflectance spectra. Compare with 'real' R_{rs} spectra shown in Figure 5.34 172
5.34 The original training R_{rs} data. Compare with synthetic $\hat{R}_{rs}$ shown in Figure 5.33 172
5.35 (Left) Hex-bin plot of a_ϕ vs a_g derived from the inverted simulated $\hat{R}_{rs}$. (Right) Hex-bin plot of a_ϕ vs a_g derived from the DALEC measured R_{rs} at ARM. 173
5.36 (Left) Scatter plot of a_ϕ vs a_g derived from the inverted simulated $\hat{R}_{rs}$. (Right) Scatter plot of a_ϕ vs a_g derived from the DALEC measured R_{rs} at ARM. Both plots show the errors ellipse which defines the 95% confidence boundary. The red point is the average IOP values. 174
5.37 (Left) Hex-bin plot of a_g vs b_{bp} derived from the inverted simulated $\hat{R}_{rs}$. (Right) Hex-bin plot of a_g vs b_{bp} derived from the DALEC measured R_{rs} at ARM. 174
5.38 (Left) Scatter plot of a_g vs b_{bp} derived from the inverted simulated $\hat{R}_{rs}$. (Right) Scatter plot of a_g vs b_{bp} derived from the DALEC measured R_{rs} at ARM. Both plots show the errors ellipse which defines the 95% confidence boundary. The red point is the average IOP values 175
5.39 (Left) Hex-bin plot of a_ϕ vs b_{bp} derived from the inverted simulated $\hat{R}_{rs}$. (Right) Hex-bin plot of a_ϕ vs b_{bp} derived from the DALEC measured R_{rs} at ARM. 175
5.40 (Left) Scatter plot of a_ϕ vs b_{bp} derived from the inverted simulated $\hat{R}_{rs}$. (Right) Scatter plot of a_ϕ vs b_{bp} of the DALEC measured R_{rs} at ARM. Both plots show the errors ellipse which defines the 95% confidence boundary. The red point is the average IOP values 176
5.41 A subset of the remote sensing reflectance pairs generated from PlanarRad by altering the phytoplankton concentration by ± 15% for a $a_g(400)$ value of 3.402 m^{-1}. 178
5.42 Percent change in reflectance that is produced by changing $a_\phi(440)$ by ± 15% over a range of $a_g(400)$ concentrations. The values of $a_\phi(440)$ vs $a_g(400)$ of the in situ measurement at each of the SCCP sample locations on 29/11/2011 are shown for comparison. 178

5.43 Change in $a_\phi(440)$ that can be expected for a percentage change in reflectance. 179

6.1 SCCP sampling locations where water samples were collected for laboratory analysis. 192
6.2 Comparison between the model predicted reflectance and the measured reflectance for HOPE at BLA. 201
6.3 Comparison between the model predicted reflectance and the measured reflectance for HOPE at RON. 201
6.4 Comparison between the model predicted reflectance and the measured reflectance for HOPE at SUC. 201
6.5 Comparison between the model predicted reflectance and the measured reflectance for BRUCE-LUT at BLA. 202
6.6 Comparison between the model predicted reflectance and the measured reflectance for BRUCE-LUT at RON. 202
6.7 Comparison between the model predicted reflectance and the measured reflectance for BRUCE-LUT at SUC. 202
6.8 Comparison between the model predicted reflectance and the measured reflectance for the BRDF corrected reflectance model at BLA. 203
6.9 Comparison between the model predicted reflectance and the measured reflectance for the BRDF corrected reflectance model at RON. 203
6.10 Comparison between the model predicted reflectance and the measured reflectance for the BRDF corrected reflectance model at SUC. 203
6.11 A comparison between the Python implementation of HOPE used for this project and the more complex PlanarRad radiative transfer model. The figure shows an acceptable tolerance between the two outputs for the same input parameters. 205
6.12 DALEC measured, HOPE-derived phytoplankton estimates compared with laboratory processed in situ water measurements 208
6.13 DALEC measured HOPE-derived phytoplankton estimates compared with laboratory processed in situ water measurements. 209
6.14 DALEC measured, HOPE-derived phytoplankton estimates compared with laboratory processed in situ water measurements. 210
6.15 DALEC measured phytoplankton estimates compared with laboratory processed in situ water measurements. 211

6.16 The green line represents the transect path along the river that DALEC reflectance measurements were made together with the in situ water sample locations marked in blue. 214
6.17 The model derived $a_\phi(440)$ measurements over the length of the transect. The phytoplankton in situ measurements are plotted as points on the figure, as well as the relative difference of those points when compared to the inverted parameters at those points. 216
6.18 The model derived $a_g(440)$ measurements over the length of the transect. The CDOM in situ measurements are plotted as points on the figure, as well as the relative difference of those points when compared to the inverted parameters at those points. 216
6.19 The model derived $b_{bp}(550)$ measurements over the length of the transect. The particle scattering in situ measurements are plotted as points on the figure, as well as the relative difference of those points when compared to the inverted parameters at those points. 217
6.20 The model derived $a_\phi(440)$ measurements over the length of the transect when restricing to a single parameter retrieval. The phytoplankton in situ measurements are plotted as points on the figure, as well as the relative difference of those points when compared to the inverted parameters at those points. 218
6.21 R_{rs} measurements taken at BLA with a stationary boat on 29/11/2011. The shaded area shows the maximum and minimum R_{rs} values. The full range of R_{rs} values were used to train the coherent noise model. 220
6.22 Inverted IOP parameters $a_\phi(440)$ versus $a_g(440)$ for the 2400 synthetic R_{rs} data produced using the coherent noise model, trained with measured R_{rs} taken at BLA with a stationary boat on 29/11/2011 221
6.23 Inverted IOP parameters $a_\phi(440)$ versus $a_g(440)$ for the 2400 synthetic R_{rs} data produced using the coherent noise model, trained with measured R_{rs} taken at BLA with a stationary boat on 29/11/2011. The error ellipse represents the 95% confidence interval. The red point represents the average IOP value. 221
6.24 Inverted IOP parameters $a_g(440)$ versus $b_{bp}(550)$ for the 2400 synthetic R_{rs} data produced using the coherent noise model, trained with measured R_{rs} taken at BLA with a stationary boat on 29/11/2011 222

6.25 Inverted IOP parameters $a_g(440)$ versus $b_{bp}(550)$ for the 2400 synthetic R_{rs} data produced using the coherent noise model, trained with measured R_{rs} taken at BLA with a stationary boat on 29/11/2011. The error ellipse represents the 95% confidence interval. The red point represents the average IOP value. 222
6.26 Inverted IOP parameters $a_\phi(440)$ versus $b_{bp}(550)$ for the 2400 synthetic R_{rs} data produced using the coherent noise model, trained with measured R_{rs} taken at BLA with a stationary boat on 29/11/2011 223
6.27 Inverted IOP parameters $a_\phi(440)$ versus $b_{bp}(550)$ for the 2400 synthetic R_{rs} data produced using the coherent noise model, trained with measured R_{rs} taken at BLA with a stationary boat on 29/11/2011. The error ellipse represents the 95% confidence interval. The red point represents the average IOP value. 223
6.28 R_{rs} measurements taken at ARM with a stationary boat on 29/11/2011. The shaded area shows the maximum and minimum R_{rs} values. The full range of R_{rs} values were used to train the coherent noise model. 224
6.29 Inverted IOP parameters $a_\phi(440)$ versus $a_g(440)$ for the 2400 synthetic R_{rs} data produced using the coherent noise model, trained with measured R_{rs} taken at ARM with a stationary boat on 29/11/2011 225
6.30 Inverted IOP parameters $a_\phi(440)$ versus $a_g(440)$ for the 2400 synthetic R_{rs} data produced using the coherent noise model, trained with measured R_{rs} taken at ARM with a stationary boat on 29/11/2011. The error ellipse represents the 95% confidence interval. The red point represents the average IOP value. 225
6.31 Inverted IOP parameters $a_g(440)$ versus $b_{bp}(550)$ for the 2400 synthetic R_{rs} data produced using the coherent noise model, trained with measured R_{rs} taken at ARM with a stationary boat on 29/11/2011 226
6.32 Inverted IOP parameters $a_g(440)$ versus $b_{bp}(550)$ for the 2400 synthetic R_{rs} data produced using the coherent noise model, trained with measured R_{rs} taken at ARM with a stationary boat on 29/11/2011. The error ellipse represents the 95% confidence interval. The red point represents the average IOP value. 226
6.33 Inverted IOP parameters $a_\phi(440)$ versus $b_{bp}(550)$ for the 2400 synthetic R_{rs} data produced using the coherent noise model, trained with measured R_{rs} taken at ARM with a stationary boat on 29/11/2011 227

6.34 Inverted IOP parameters $a_\phi(440)$ versus $b_{bp}(550)$ for the 2400 synthetic R_{rs} data produced using the coherent noise model, trained with measured R_{rs} taken at ARM with a stationary boat on 29/11/2011. The error ellipse represents the 95% confidence interval. The red point represents the average IOP value. 227
6.35 R_{rs} measurements taken at HEA with a stationary boat on 29/11/2011. The shaded area shows the maximum and minimum R_{rs} values. The full range of R_{rs} values were used to train the coherent noise model. 228
6.36 Inverted IOP parameters $a_\phi(440)$ versus $a_g(440)$ for the 2400 synthetic R_{rs} data produced using the coherent noise model, trained with measured R_{rs} taken at HEA with a stationary boat on 29/11/2011 229
6.37 Inverted IOP parameters $a_\phi(440)$ versus $a_g(440)$ for the 2400 synthetic R_{rs} data produced using the coherent noise model, trained with measured R_{rs} taken at HEA with a stationary boat on 29/11/2011. The error ellipse represents the 95% confidence interval. The red point represents the average IOP value. 229
6.38 Inverted IOP parameters $a_g(440)$ versus $b_{bp}(550)$ for the 2400 synthetic R_{rs} data produced using the coherent noise model, trained with measured R_{rs} taken at HEA with a stationary boat on 29/11/2011 230
6.39 Inverted IOP parameters $a_g(440)$ versus $b_{bp}(550)$ for the 2400 synthetic R_{rs} data produced using the coherent noise model, trained with measured R_{rs} taken at HEA with a stationary boat on 29/11/2011. The error ellipse represents the 95% confidence interval. The red point represents the average IOP value. 230
6.40 Inverted IOP parameters $a_\phi(440)$ versus $b_{bp}(550)$ for the 2400 synthetic R_{rs} data produced using the coherent noise model, trained with measured R_{rs} taken at HEA with a stationary boat on 29/11/2011 231
6.41 Inverted IOP parameters $a_\phi(440)$ versus $b_{bp}(550)$ for the 2400 synthetic R_{rs} data produced using the coherent noise model, trained with measured R_{rs} taken at HEA with a stationary boat on 29/11/2011. The error ellipse represents the 95% confidence interval. The red point represents the average IOP value. 232
6.42 R_{rs} measurements taken at NAR with a stationary boat on 29/11/2011. The shaded area shows the maximum and minimum R_{rs} values. The full range of R_{rs} values were used to train the coherent noise model. 232

6.43 Inverted IOP parameters $a_\phi(440)$ versus $a_g(440)$ for the 2400 synthetic R_{rs} data produced using the coherent noise model, trained with measured R_{rs} taken at NAR with a stationary boat on 29/11/2011 233
6.44 Inverted IOP parameters $a_\phi(440)$ versus $a_g(440)$ for the 2400 synthetic R_{rs} data produced using the coherent noise model, trained with measured R_{rs} taken at NAR with a stationary boat on 29/11/2011. The error ellipse represents the 95% confidence interval. The red point represents the average IOP value. 233
6.45 Inverted IOP parameters $a_g(440)$ versus $b_{bp}(550)$ for the 2400 synthetic R_{rs} data produced using the coherent noise model, trained with measured R_{rs} taken at NAR with a stationary boat on 29/11/2011 234
6.46 Inverted IOP parameters $a_g(440)$ versus $b_{bp}(550)$ for the 2400 synthetic R_{rs} data produced using the coherent noise model, trained with measured R_{rs} taken at NAR with a stationary boat on 29/11/2011. The error ellipse represents the 95% confidence interval. The red point represents the average IOP value. 234
6.47 Inverted IOP parameters $a_\phi(440)$ versus $b_{bp}(550)$ for the 2400 synthetic R_{rs} data produced using the coherent noise model, trained with measured R_{rs} taken at NAR with a stationary boat on 29/11/2011 235
6.48 Inverted IOP parameters $a_\phi(440)$ versus $b_{bp}(550)$ for the 2400 synthetic R_{rs} data produced using the coherent noise model, trained with measured R_{rs} taken at NAR with a stationary boat on 29/11/2011. The error ellipse represents the 95% confidence interval. The red point represents the average IOP value. 235
6.49 R_{rs} measurements taken at NIL with a stationary boat on 29/11/2011. The shaded area shows the maximum and minimum R_{rs} values. The full range of R_{rs} values were used to train the coherent noise model. 236
6.50 Inverted IOP parameters $a_\phi(440)$ versus $a_g(440)$ for the 2400 synthetic R_{rs} data produced using the coherent noise model, trained with measured R_{rs} taken at NIL with a stationary boat on 29/11/2011 237
6.51 Inverted IOP parameters $a_\phi(440)$ versus $a_g(440)$ for the 2400 synthetic R_{rs} data produced using the coherent noise model, trained with measured R_{rs} taken at NIL with a stationary boat on 29/11/2011. The error ellipse represents the 95% confidence interval. The red point represents the average IOP value. 237

6.52 Inverted IOP parameters $a_g(440)$ versus $b_{bp}(550)$ for the 2400 synthetic R_{rs} data produced using the coherent noise model, trained with measured R_{rs} taken at NIL with a stationary boat on 29/11/2011 238
6.53 Inverted IOP parameters $a_g(440)$ versus $b_{bp}(550)$ for the 2400 synthetic R_{rs} data produced using the coherent noise model, trained with measured R_{rs} taken at NIL with a stationary boat on 29/11/2011. The error ellipse represents the 95% confidence interval. The red point represents the average IOP value. 238
6.54 Inverted IOP parameters $a_\phi(440)$ versus $b_{bp}(550)$ for the 2400 synthetic R_{rs} data produced using the coherent noise model, trained with measured R_{rs} taken at NIL with a stationary boat on 29/11/2011 239
6.55 Inverted IOP parameters $a_\phi(440)$ versus $b_{bp}(550)$ for the 2400 synthetic R_{rs} data produced using the coherent noise model, trained with measured R_{rs} taken at NIL with a stationary boat on 29/11/2011. The error ellipse represents the 95% confidence interval. The red point represents the average IOP value. 239
6.56 R_{rs} measurements taken at STJ with a stationary boat on 29/11/2011. The shaded area shows the maximum and minimum R_{rs} values. The full range of R_{rs} values were used to train the coherent noise model. 240
6.57 Inverted IOP parameters $a_\phi(440)$ versus $a_g(440)$ for the 2400 synthetic R_{rs} data produced using the coherent noise model, trained with measured R_{rs} taken at STJ with a stationary boat on 29/11/2011 241
6.58 Inverted IOP parameters $a_\phi(440)$ versus $a_g(440)$ for the 2400 synthetic R_{rs} data produced using the coherent noise model, trained with measured R_{rs} taken at STJ with a stationary boat on 29/11/2011. The error ellipse represents the 95% confidence interval. The red point represents the average IOP value. 241
6.59 Inverted IOP parameters $a_g(440)$ versus $b_{bp}(550)$ for the 2400 synthetic R_{rs} data produced using the coherent noise model, trained with measured R_{rs} taken at STJ with a stationary boat on 29/11/2011 242
6.60 Inverted IOP parameters $a_g(440)$ versus $b_{bp}(550)$ for the 2400 synthetic R_{rs} data produced using the coherent noise model, trained with measured R_{rs} taken at STJ with a stationary boat on 29/11/2011. The error ellipse represents the 95% confidence interval. The red point represents the average IOP value. 242

6.61 Inverted IOP parameters $a_\phi(440)$ versus $b_{bp}(550)$ for the 2400 synthetic R_{rs} data produced using the coherent noise model, trained with measured R_{rs} taken at STJ with a stationary boat on 29/11/2011 243
6.62 Inverted IOP parameters $a_\phi(440)$ versus $b_{bp}(550)$ for the 2400 synthetic R_{rs} data produced using the coherent noise model, trained with measured R_{rs} taken at STJ with a stationary boat on 29/11/2011. The error ellipse represents the 95% confidence interval. The red point represents the average IOP value. 243
6.63 R_{rs} measurements taken at RON with a stationary boat on 29/11/2011. The shaded area shows the maximum and minimum R_{rs} values. The full range of R_{rs} values were used to train the coherent noise model. 244
6.64 Inverted IOP parameters $a_\phi(440)$ versus $a_g(440)$ for the 2400 synthetic R_{rs} data produced using the coherent noise model, trained with measured R_{rs} taken at RON with a stationary boat on 29/11/2011 245
6.65 Inverted IOP parameters $a_\phi(440)$ versus $a_g(440)$ for the 2400 synthetic R_{rs} data produced using the coherent noise model, trained with measured R_{rs} taken at RON with a stationary boat on 29/11/2011. The error ellipse represents the 95% confidence interval. The red point represents the average IOP value. 245
6.66 Inverted IOP parameters $a_g(440)$ versus $b_{bp}(550)$ for the 2400 synthetic R_{rs} data produced using the coherent noise model, trained with measured R_{rs} taken at RON with a stationary boat on 29/11/2011 246
6.67 Inverted IOP parameters $a_g(440)$ versus $b_{bp}(550)$ for the 2400 synthetic R_{rs} data produced using the coherent noise model, trained with measured R_{rs} taken at RON with a stationary boat on 29/11/2011. The error ellipse represents the 95% confidence interval. The red point represents the average IOP value. 246
6.68 Inverted IOP parameters $a_\phi(440)$ versus $b_{bp}(550)$ for the 2400 synthetic R_{rs} data produced using the coherent noise model, trained with measured R_{rs} taken at RON with a stationary boat on 29/11/2011 247
6.69 Inverted IOP parameters $a_\phi(440)$ versus $b_{bp}(550)$ for the 2400 synthetic R_{rs} data produced using the coherent noise model, trained with measured R_{rs} taken at RON with a stationary boat on 29/11/2011. The error ellipse represents the 95% confidence interval. The red point represents the average IOP value. 247

6.70 R_{rs} measurements taken at KIN with a stationary boat on 29/11/2011. The shaded area shows the maximum and minimum R_{rs} values. The full range of R_{rs} values were used to train the coherent noise model. 248
6.71 Inverted IOP parameters $a_\phi(440)$ versus $a_g(440)$ for the 2400 synthetic R_{rs} data produced using the coherent noise model, trained with measured R_{rs} taken at KIN with a stationary boat on 29/11/2011 249
6.72 Inverted IOP parameters $a_\phi(440)$ versus $a_g(440)$ for the 2400 synthetic R_{rs} data produced using the coherent noise model, trained with measured R_{rs} taken at KIN with a stationary boat on 29/11/2011. The error ellipse represents the 95% confidence interval. The red point represents the average IOP value. 249
6.73 Inverted IOP parameters $a_g(440)$ versus $b_{bp}(550)$ for the 2400 synthetic R_{rs} data produced using the coherent noise model, trained with measured R_{rs} taken at KIN with a stationary boat on 29/11/2011 250
6.74 Inverted IOP parameters $a_g(440)$ versus $b_{bp}(550)$ for the 2400 synthetic R_{rs} data produced using the coherent noise model, trained with measured R_{rs} taken at KIN with a stationary boat on 29/11/2011. The error ellipse represents the 95% confidence interval. The red point represents the average IOP value. 250
6.75 Inverted IOP parameters $a_\phi(440)$ versus $b_{bp}(550)$ for the 2400 synthetic R_{rs} data produced using the coherent noise model, trained with measured R_{rs} taken at KIN with a stationary boat on 29/11/2011 251
6.76 Inverted IOP parameters $a_\phi(440)$ versus $b_{bp}(550)$ for the 2400 synthetic R_{rs} data produced using the coherent noise model, trained with measured R_{rs} taken at KIN with a stationary boat on 29/11/2011. The error ellipse represents the 95% confidence interval. The red point represents the average IOP value. 251
6.77 R_{rs} measurements taken at SUC with a stationary boat on 29/11/2011. The shaded area shows the maximum and minimum R_{rs} values. The full range of R_{rs} values were used to train the coherent noise model. 252
6.78 Inverted IOP parameters $a_\phi(440)$ versus $a_g(440)$ for the 2400 synthetic R_{rs} data produced using the coherent noise model, trained with measured R_{rs} taken at SUC with a stationary boat on 29/11/2011 253

6.79 Inverted IOP parameters $a_\phi(440)$ versus $a_g(440)$ for the 2400 synthetic R_{rs} data produced using the coherent noise model, trained with measured R_{rs} taken at SUC with a stationary boat on 29/11/2011. The error ellipse represents the 95% confidence interval. The red point represents the average IOP value. 253
6.80 Inverted IOP parameters $a_g(440)$ versus $b_{bp}(550)$ for the 2400 synthetic R_{rs} data produced using the coherent noise model, trained with measured R_{rs} taken at SUC with a stationary boat on 29/11/2011 254
6.81 Inverted IOP parameters $a_g(440)$ versus $b_{bp}(550)$ for the 2400 synthetic R_{rs} data produced using the coherent noise model, trained with measured R_{rs} taken at SUC with a stationary boat on 29/11/2011. The error ellipse represents the 95% confidence interval. The red point represents the average IOP value. 254
6.82 Inverted IOP parameters $a_\phi(440)$ versus $b_{bp}(550)$ for the 2400 synthetic R_{rs} data produced using the coherent noise model, trained with measured R_{rs} taken at SUC with a stationary boat on 29/11/2011 255
6.83 Inverted IOP parameters $a_\phi(440)$ versus $b_{bp}(550)$ for the 2400 synthetic R_{rs} data produced using the coherent noise model, trained with measured R_{rs} taken at SUC with a stationary boat on 29/11/2011. The error ellipse represents the 95% confidence interval. The red point represents the average IOP value. 255
6.84 The total phytoplankton pigment absorption spectra measured at each of the sample locations on 29/11/2011. 256
6.85 The total non-algal particulate absorption spectra measured at each of the sample locations on 29/11/2011. 257
6.86 The CDOM absorption spectra measured at each of the sample locations on 29/11/2011. 257
6.87 The total gelbstoff absorption spectra measured at each of the sample locations on 29/11/2011. 258
6.88 The total particulate backscatter of b_{bp} measured by HOBI Labs HydroScat-6 for each of the sample locations on 29/11/2011. 258
6.89 The cumulative distance for each DALEC R_{rs} measurement along the transect for each sample number. The flat points on the transect show the locations where the boat was stationary to collect water samples and repeat DALEC measurements of R_{rs} were made for the training stage of the coherent noise model and uncertainty estimates. 259

6.90 The model-derived $a_\phi(440)$ measurements over the length of the transect. The outer envelope shows the uncertainty estimates from the coherent noise modelling. The phytoplankton in situ measurements are plotted as points on the figure, as well as the relative difference of those points when compared to the model-derived parameters at those points. 260
6.91 The model-derived $a_g(440)$ measurements over the length of the transect. The outer envelope shows the uncertainty estimates from the coherent noise modelling. The phytoplankton in situ measurements are plotted as points on the figure, as well as the relative difference of those points when compared to the model-derived parameters at those points. 261
6.92 The model-derived $b_{bp}(550)$ measurements over the length of the transect. The outer envelope shows the uncertainty estimates from the coherent noise modelling. The phytoplankton in situ measurements are plotted as points on the figure, as well as the relative difference of those points when compared to the model-derived parameters at those points. 262
6.93 The DALEC retrieved $a_\phi(440)$ compared to in situ measured values for the transect on 29/11/2011. 263
6.94 The DALEC retrieved $a_g(440)$ compared to in situ measured values for the transect on 29/11/2011. 263
6.95 The DALEC retrieved $b_{bp}(550)$ compared to in situ measured values for the transect on 29/11/2011. 264
6.96 DALEC-derived $a_\phi(440)$ compared to the in situ measured values for all of the sample sites. The model was restricted to retrieve the $a_\phi(440)$ parameter only. 265
6.97 DALEC-derived $a_\phi(440)$ compared to in situ measured values collected along the transect for 29/11/2011 when restricted to a single $a_\phi(440)$ retrieval parameter. 266
6.98 DALEC-derived $a_\phi(440)$ and in situ measured values for all of the sample sites for all five field trips. The green markers represent the data points where CDOM is relatively low, which corresponds to the sites before NIL. The red markers represent the points further up river from NIL, where the CDOM is high and the model produces less accurate results. 267
6.99 DALEC-derived $a_\phi(440)$ compared to the in situ measured values for all of the sample sites for all five field trips. Here, only the first five sampling sites (up to NIL) are shown, where CDOM values are considered relatively low. 268

6.100In situ measured absorption due to glebstoff at 440 nm for the transect, and relative differences between measured and modelled $a_\phi(440)$. The figure shows that there is a high correlation between the level of CDOM and the uncertainty of the DALEC retrieved $a_\phi(440)$ values. 268
6.101The transect path undertaken on the 29/11/11. The green section of the transect represents the section of the river where the $a_\phi(440)$ measurements, predicted with the single parameter restricted model, agree with the in situ measurements. The red section represents the section of the river where the model is unable to agree with in situ measurements of $a_\phi(440)$ within the uncertainty boundaries. 272

7.1 The transect 29/11/2011 reprocessed using the Murdoch University phytoplankton culture absorption as inputs into HOPE. The mixed culture transect was processed using the normalised absorption profile measured at the in situ sampling locations. The in situ points on the plot show the $a_\phi(440)$ measurement results at the sampling sites. 286

A.1 From Hipsey et al. (2016b) Summary of the dominant phytoplankton species by cell count, identified and quantified for each season and sampling site. 305
A.2 From Hipsey et al. (2016b) Summary of the dominant phytoplankton species by cell count, identified and quantified for each season and sampling site. 306

B.1 The user interface for the software written to operate the DALEC. All of the plots and telemetry are updated in real time. 307
B.2 The community web page with instructions on how to download and use the software. 308
B.3 The user interface for the software written to parse the inputs and outputs to FDTD. The tool is most often driven by scripting. The GUI is useful for visualising outputs and debugging. 309
B.4 Community web for Planarradpy. The page includes instructions for use as well as links to the source code hosted on github. 310
B.5 Jupyter notebook with examples of how to use the coherent noise model of uncertainty estimates. 311
B.6 DALEC mount. 312

C.1 Spectra generated by running PlanarRad many times and changing the $a_\phi(440)$ and $a_g(400)$ concentrations. 314
C.2 The R_{rs} after detrending by subtracting the mean reflectance of the ensemble average. 315
C.3 The standard deviation of the detrended ensemble average. 316
C.4 The stationary reflectance normalised by dividing each spectra by the standard deviation. 317
C.5 The power spectrum of the ensemble. 318
C.6 The correlation function of the ensemble. 319
C.7 Random data points generated for each spectra at each wavelength. . . . 320
C.8 The random point transformed to the Fourier domain by taking the FFT of the random points. 321
C.9 The Fourier transform of the randomly generated points multiplied by the power spectrum. 322
C.10 The correlated noise transformed back to the real domain by taking the inverse Fourier transform. 323
C.11 Normalised correlated noise calculated by dividing by the standard deviation. 324
C.12 The standard deviation of the normalised correlated noise. All wavelengths should be 1. This step is taken to ensure that the process has been followed correctly so far. 325
C.13 The detrended simulated reflectance data created by multiplying the normalised correlated noise by the standard deviation of the simulated R_{rs}. . 326
C.14 Simulated remote sensing reflectance generated by multiplying the detrended simulated reflectance by the reflectance spectra. 327
C.15 Optionally, the simulated reflectance data is filtered to further reduce the simulated data to fall within expected field measurements of reflectance data. 328
C.16 The mean inverted IOP values calculated from the ensemble synthetic data used to forward model the remote sensing reflectance, shown in blue dots. The mean reflectance plotted over the top of the ensemble synthetic data. 329
C.17 Scatter 'Hex' plot of $a_\phi(440)$ versus $a_g(400)$ on the x and y axis. The distribution of each IOP is shown top and right. 330

List of Tables

1 Symbols and units 22

1.1 Swan River sampling site locations 26

3.1 Maxwell's Equations 55
3.2 Summary of the phytoplankton properties modelled. Reproduced in part from Volten et al. (1998) 77
3.3 Ratio of gas vacuoles to volume of plankton cell. Reproduced from Smith and Pete (1967) 77
3.4 FDTD and Mie Calculated Scattering Fractions of Hydrosols 84

4.1 Different Classes of Phytoplankton. Reproduced from Barsanti and Guarltieri (2006) 95
4.2 Photosynthetic pigments found in different classes of algae. The markers; $\otimes$ indicates an important pigment; + indicates the pigment is present and $\pm$ indicates the pigment occurs rarely. (reproduced from Hoek et al., 1995) 97
4.3 Phytoplankton Culture Medium Recipe f/2 99
4.4 Phytoplankton culture details 101

5.1 Physical quantities and their units 107
5.2 Sample Values of $G_0^w(\Omega), G_1^w(\Omega), G_0^p(\Omega), G_1^p(\Omega)$ for Angular R_{rs}. Reproduced from Lee et al. (2011) 144

6.1 SCCP Swan River Sampling dates 192
6.2 The pathlength amplification factors for various particle types. Reproduced from Mueller et al. (2003) 197
6.3 Swan River sampling site locations 207
6.4 In situ measurements of $a_\phi(440)$, $a_g(440)$ and HOPE-derived values of $a_\phi(440)$ for 9 of the SCCP sampling locations on 08/02/2010. 207

6.5 In situ measurements of $a_\phi(440)$, $a_g(440)$ and HOPE-derived values of $a_\phi(440)$ for 9 of the SCCP sampling locations on 22/02/2010 209
6.6 In situ measurements of $a_\phi(440)$, $a_g(440)$ and HOPE-derived values of $a_\phi(440)$ for 9 of the SCCP sampling locations on 18/07/2011 210
6.7 In situ measurements of $a_\phi(440)$, $a_g(440)$ and HOPE inverted values of $a_\phi(440)$ for 9 of the SCCP sampling locations on 14/11/2011 211
6.8 In situ measurements of $a_\phi(440)$, $a_g(440)$ and $b_{bp}(550)$; HOPE inverted values of $a_\phi(440)$, $a_g(440)$ and $b_{bp}(550)$ as well as supplimentary environmental data for all 10 of the SCCP sampling locations on 29/11/2011 . . 214

List of Symbols

Table 1: Symbols and units

Symbols	Description	Units
A	Surface area	m^2
a	Absorption coefficients of total IOPs	m^{-1}
a_w	Absorption coefficient of pure water	m^{-1}
a_ϕ	Absorption coefficient of phytoplankton pigments	m^{-1}
a_{nap}	Absorption coefficient of non-algal particles	m^{-1}
a_{cdom}	Absorption coefficient of CDOM	m^{-1}
a_g	Absorption coefficient of gelbstoff; $a_{nap} + a_{cdom}$	m^{-1}
$\mathbf{B}$	Magnetic flux density	T
b	Backscattering coefficients of total IOPs	m^{-1}
b_b	Backscattering coefficients	m^{-1}
b_f	Forward scattering coefficients	m^{-1}
b_{bp}	Backscattering coefficient of suspended particles	m^{-1}
b_w	Backscattering coefficient of pure water	m^{-1}
β	Volume scattering function	m^{-1}
$\tilde{\beta}$	Phase function	sr^{-1}
c	Attenuation coefficients	m^{-1}
$\mathbf{D}$	Electric flux density	Cm^{-2}
$\mathbf{E}$	Electric field intensity	Vm^{-1}
$\mathbf{E_i}$	Incident electric field intensity	Vm^{-1}
$\mathbf{E_s}$	Scattered electric field intensity	Vm^{-1}
$\mathbf{E_{ext}}$	Extinction electric field intensity	Vm^{-1}
E_d	Downwelling irradiance	$Wnm^{-1}m^{-1}$
E_u	Upward irradiance	$Wnm^{-1}m^{-1}$
$\mathbf{H}$	Magnetic field intensity	$A\,m^{-1}$
$\mathbf{H_i}$	Incident magnetic field intensity	$A\,m^{-1}$

$\mathbf{H_s}$	Scattered magnetic field intensity	$A\,m^{-1}$
$\mathbf{H_{ext}}$	Extinction magnetic field intensity	$A\,m^{-1}$
H	Bottom depth	m
K_d	Diffuse attenuation coefficient	m^{-1}
L	Radiance	$Wm^{-2}nm^{-1}sr^{-1}$
L_u	Above-surface upwelling radiance	$Wm^{-2}nm^{-1}sr^{-1}$
L_w	Water-leaving radiance	$Wm^{-2}nm^{-1}sr^{-1}$
r_{rs}	Subsurface remote sensing reflectance	sr^{-1}
R	Spectral irradiance reflectance	
R_{rs}	Above-surface remote sensing reflectance	sr^{-1}
$\hat{R}_{rs}$	Simulated 'synthetic' above-surface remote sensing reflectance	sr^{-1}
ϕ	Solar azimuth angle	rad
Ξ_u	Upward hemisphere of direction	
Ξ_d	Downward hemisphere of direction	
Ω	Solid angle	sr
$\overrightarrow{x}$	Position vector = $(x_1\hat{\mathbf{i}} + x_2\hat{\mathbf{j}} + x_3\hat{\mathbf{k}})$	
Q	Spectral energy	J
$\hat{\xi}$	Direction of travel of a light wave	
λ	Wavelength of light	nm
t	Time	s
Φ_i	Incident beam of light	
Φ_a	Absorptance	
Φ_s	Scatterance	
Φ_t	Transmitance	
V	Volume of water	m^3
ρ	Single scattering albedo	
μ	Permeability	Hm^{-1}
ϵ	Permittivity	Fm^{-1}

Chapter 1

Introduction

1.1 Background

In February 2000, the Department of Health issued a health warning and closed the Swan River Estuary for 12 days due to toxic levels of cyanobacteria; namely, blue-green algae, (Swan River Trust, 2007). Between April and June 2003, a bloom of blue-green algae killed thousands of fish in both the Swan and Canning rivers (Swan River Trust, 2007). When blue-green algae die, they release dangerous toxins into the water that can accumulate in the gills of fish. These toxins include neurotoxins and hepatotoxins that affect the brain, nervous system and liver of fish, as well as birds, animals and humans that eat the affected fish. This can cause serious health problems in humans (Rao et al., 2002; Zanchett and Oliveira-Filho, 2013) as well as the death of fish and other animals. In 1999, a Swan-Canning Cleanup Program (SCCP) Action Plan was released which outlined the programs long-term objectives and the actions required to achieve them (Swan River Trust 1999). Reducing the level of nutrient inflows to the estuary was one of the key strategies to decreasing the frequency of phytoplankton blooms in the Swan-Canning Estuary.

The Department of Parks and Wildlife (DPAW) and The Swan River Trust (later incorporated into DPAW) identify a range of factors which have the potential to impact on the water quality and ecological health of the Swan River system (e.g. State of Western Australia, 2017; Swan River Trust Riverview, 2015; Department of Parks and Wildlife, 2015; Swan River Trust, 2008; Swan River Trust, 2005).

The Swan Canning Riverpark, under the management of DPAW, was established in 2006. The current program guiding river monitoring is the Swan Canning River Protec-

tion Strategy (SCRPS) through the Swan River Trust, started in 2015 and arising from the Swan and Canning Rivers Management Act 2006 (Department of Parks and Wildlife, 2015). The DPAW was incorporated into the Department of Biodiversity, Conservation and Attractions (DBCA) in July 2017 and it is acknowledged that the work conducted and presented in this thesis was prior to this time. The relevance of the work presented is contiguous throughout the changing department structures and therefore, for consistency, the author refers to the program that existed, and under which this work was funded and conducted, for the remainder of the thesis.

Monitoring programs such as the SCCP, require water samples to be taken from 16 (20 in summer) different sites along the river. These samples are taken back to a laboratory where they are filtered, weighed, cell counts are conducted and the different phytoplankton species are identified (Adeney, 2001). The measured cell counts are used to estimate the biomass of different species of algae. This process takes up to three days to complete before a report on the health of the river can be made public.

Making radiometric measurements of the Swan River is much faster than taking water samples and can be done with much greater spatial and temporal resolution. Therefore, radiometric monitoring of the Swan River has the potential to improve current programs, such as the SCCP, by increasing the sample coverage of the project area and expediting the release of health reports to the public.

Satellite remote sensing has been used to monitor the inherent optical properties (IOPs) of ocean and coastal waters for many years. However, at the time of this study, freely available satellite data did not have the spatial or spectral resolution to precisely map IOPs for inland waterways such as the Swan River (Craig et al., 2006). Recent advances in electronics have allowed ground and airborne sensors to be developed that have much greater spectral and spatial resolution than that of satellites. This enables these sensors to de-convolve much finer details in measured spectra and with more precise detail.

The purpose of this study is to investigate the optical properties of the Swan River and identify if remote sensing techniques could be use to improve or support monitoring programs such as the SCCP. In particular, whether radiometric measurements can be used to estimate algae concentration in the Swan River. A map of the Swan River and sampling locations are shown in Figure 1.1 and the coordinates shown in Table 1.1.

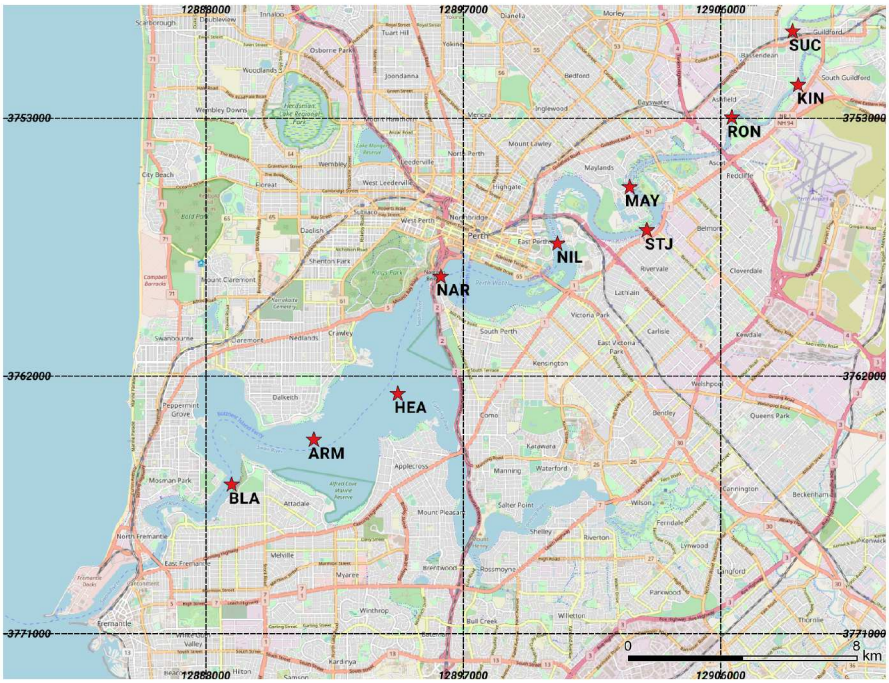

Figure 1.1: Map of the Swan River, Perth, Western Australia. SCCP sampling locations noted by stars and abbreviated names.

Table 1.1: Swan River sampling site locations

Site Name	Station Code	Latitude (°S)	Longitude (°E)
Blackwall Reach	BLA	-32.0190380	115.7831398
Armstrong Spit	ARM	-320070686	115.8089498
Heathcote	HEA	-31.9948919	115.8353485
Narrows Bridge	NAR	-31.9636573	115.8487799
Nile Street	NIL	-31.9548452	115.8853411
Saint John's	STJ	-31.9513718	115.9134004
Maylands Pool	MAY	-31.9398069	115.9081728
Ron Courtney Is	RON	-31.9214037	115.9401324
Kingsley Street	KIN	-31.9125821	115.9610263
Success Hill	SUC	-31.8984402	115.9592501

1.2 Significance

A report released by the Swan River Trust in 2007 entitled *Potential Impacts of Climate Change on the Swan and Canning Rivers* suggests, due to rising sea-surface temperatures and an increase in population density, an increase in eutrophication will result in dangerous blue-green algal blooms occurring more frequently. For this reason, it would be advantageous to develop a faster and more reliable monitoring method, so that hazards can be better managed.

A report released by CSIRO (Jernakoff et al., 1996) on previous studies using remote sensing to monitor algal blooms in the Swan River, found that airborne instruments such as the CASI radiometer are sensitive to spectral features in the presence of moderate concentrations of algal blooms but are logistically too difficult and too expensive to use as regular monitoring tools. The report suggests developing a hyperspectral radiometer very similar to the Curtin University developed, boat-mounted radiometer, DALEC and further classification of water IOPs in low-to-moderate concentration levels is required. This investigation was undertaken in response to the recommendations made by this report.

1.3 Research Aim

The principle research aim of the study presented in this thesis was to establish whether continuous underway measurements of remote sensing reflectance using the DALEC could be used to improve and support river monitoring programs such as the SCCP by making accurate measurements of phytoplankton at locations in between the discrete SCCP sample locations along the Swan River.

This includes researching what new methodological techniques and localised inputs are required to adapt current remote sensing optical models for use with inland waterbodies, such as the Swan River, where the optical environment is dark and primarily dominated by the absorption of light due to gelbstoff. Due to the wide diversity of phytoplankton species found in the Swan River, resulting in a large variability in size and shape of the phytoplankton. A new methodology that includes a complex scattering model using the Finite Difference Time Domain algorithm was developed to accommodate this diversity.

1.4 Objectives

To address the research aim, the research objectives included:

- Performing a review of the literature to determine the scope, limitations and sources of uncertainty in regard to the current body of knowledge of using remote sensing methodologies to measure phytoplankton.
- Conducting a comparative research assessment of Mie Theory and the Finite Difference Time Domain algorithms. Assessing whether modelling light scattering, with a high degree of variability in shape and size of different phytoplankton species, benefits from using the more advanced FDTD algorithm in order to improve results with optical inversion of remote sensing models.
- Assessing existing remote sensing optical models, and determine their applicability and limitations for use with the optically complex Swan River. Further, to develop the inputs and computational tools needed to accurately model the Swan River's water colour, as required. Note that these optical models include radiative transfer models, as well as bio-optical models, required for modelling the spectral inputs to the radiative transfer equation.
- Developing new mathematical inversion methods that improve the inherent optical properties (IOPs) retrieval reliability in low light environments where the relationship between remote sensing reflectance and IOPs have a highly non-linear relationship.
- Develop a new methodology of estimating measurement uncertainties of IOPs calculated from remote sensing reflectance.
- Applying the developed models and tools to investigate the sensitivity of remote sensing reflectance with regard to a range of IOPs using synthetic data sets.
- Developing a method for calculating uncertainties of IOPs derived from remote sensing reflectance.
- Developing an inversion algorithm and workflow capable of retrieving algal absorption concentration using the chosen optical model with inputs specific to the Swan River. Moreover, develop a confidence interval and uncertainty range within which estimates are deemed valid.

- Assessing the accuracy of measuring phytoplankton abundance in the Swan River using the research methods developed in this thesis.
- Developing an approach for using the DALEC, a boat-mounted radiometer, in the field while using concurrent water samples to truth the results.
- Develop quality control algorithms to filter out erroneous data, such as sunglint effects, measurements taken with the incorrect viewing geometry, and inversion results that could not converge to a solution.
- Validating the accuracy of the phytoplankton-retrieval scheme by comparing remote sensing reflectance derived measurements of phytoplankton with in situ water-sampled laboratory measurements.

1.5 Structure of Thesis

Chapter 1, defines the scope and research objectives of this study, and outlines the structure of this thesis.

Chapter 2 is the literature review and survey of the field. This chapter begins by reviewing both the importance of phytoplankton to the ecology of a waterbody as well as how unsafe it can become when the growth and abundance of phytoplankton can increase rapidly to form harmful algal blooms.

This chapter also reviews the different sensors that have been historically used to monitor phytoplankton. Ranging from; Earth observation from space in the form of satellites, airborne sensors used to monitor coastlines and large waterbodies, boat-mounted and hand-held instruments used to monitor local waterbodies such as small rivers and lakes.

Various optical models used for monitoring phytoplankton are reviewed as well as the important optically active constituents and the bio-optical models used to describe them.

The chapter concludes with a detailed assessment of the ecology of the Swan River. The assessment discusses some of the ecological issues surrounding harmful algal blooms and the river monitoring programs used to measure and monitor the water quality and health of the river. Furthermore, optical studies and modelling of Swan River's water quality are discussed as well as attempts to characterise phytoplankton dynamics of the river.

Chapter 3 is the comparative research assessment of Mie theory and the Finite Difference Time Domain technique. We begin this chapter by discussing the limitations of Mie theory and how recent advances in computer hardware make more advanced modelling techniques such FDTD possible.

This chapter derives the analytical solution to the spherical scattering equations first described by Mie (1908), from the canonical Maxwell's equations. The chapter continues deriving the discretized form of the generalized scattering equations described by Yee (1966). A comparison of the results are shown for spherical, cube and 'phytoplankton-like' shapes modelled in a computer simulation using both these methodologies.

The majority of this chapter is dedicated to using the FDTD method to simulate the light scattering of various phytoplankton species and to compare the results to both laboratory measurements made by Volten et al. (1998) and those approximated using Mie theory.

Chapter 4 discusses the spectral absorption of phytoplankton cultured and grown at Murdoch University's Algae R & D Centre. The chapter describes the role of photosynthetic pigments of phytoplankton and the relationship between those pigments and the absorption of light. This chapter also describes, in detail, the methodology and results of culturing phytoplankton in the laboratory as well as the phytoplankton specific absorption of the cultures.

Chapter 5 reviews the optical physics (radiative transfer) required to understand the nature of the underwater light field, as well as the transition of light through the air/water interface and the bio-optical models used in this thesis. Optical models that describe IOPs as a function of remote sensing reflectance are discussed in detail and a comparison and review of their limitations are shown. The justification for a chosen model is discussed as well as the inverse solution to the model. Furthermore, a novel technique for solving the model in difficult and highly non-linear light environments is presented and the method for using this technique to estimate the uncertainty of IOPs derived from the model.

The chapter concludes by presenting a sensitivity analysis of the effect a small change in phytoplankton has on the remote sensing reflectance in high CDOM environments. The outcome of which, is used in the following chapter to help validate the uncertainty

estimates of phytoplankton retrievals.

Chapter 6 is the detailed field survey conducted of the Swan River. This chapter details the field work methodology including: calibration of equipment; making radiometric measurements; taking in situ water samples; and laboratory techniques for processing the water samples. Following sections present the field results, beginning with 'spot' measurements of radiometrically derived phytoplankton concentrations at each of the SCCP Swan River sampling sites. This is followed by a full transect of the Swan River where, radiometrically derived phytoplankton estimates were continuously made along the length of the SCCP, and intersecting the water sample sites.

Chapter 7 is the main discussion of the results, uncertainties and validation. The efficacy of using a boat-mounted radiometer to measure algae, and the validity of the results, are presented in this chapter.

Chapter 8 presents conclusions; recommendations for future work; lessons learned; and any remaining gaps in knowledge.

Chapter 2

Literature Review

2.1 Introduction

The purpose of this chapter is to examine the current body of knowledge around measuring the dominant phytoplankton pigment, chlorophyll-a, with optical models and remote sensing instruments. In this chapter a broad view of the literature is taken, as it relates to this thesis. In subsequent chapters, where relevant to that chapter, the literature is reviewed in further depth.

2.2 Phytoplankton and Harmful Algal Blooms in Inland Waters

Microscopic plants (phytoplankton) have a crucial effect on the ecology of a waterbody because they oxygenate the water and contribute to the production of organic matter through photosynthesis. There are tens of thousands of phytoplankton species around the world (Jeffrey et al., 1997), almost all of which convert the sun's energy to chemical energy via photosynthesis (Chester, 2003). Only the visible part of the solar spectrum can be captured by the ecosystem for photosynthesis, and the interface that couples it to the sun is provided by the pigment molecules (principally chlorophyll, and associated carotenoid pigments, Jeffrey et al., 1997) contained in phytoplankton. When anthropogenic activity alters the balance of the natural system, phytoplankton often respond by growing rapidly in vast numbers (i.e. blooms) and becoming a nuisance. Such nuisance blooms are sometime referred to as harmful algal blooms (HAB), in particular when the dominant bloom species is toxic to humans and animals, or they use up too much oxy-

gen in a water body when they die, subsequently killing fish and lowering water quality (e.g. Anderson et al., 2002). Cyanobacterial harmful algal blooms have been a major cause for concern in aquatic ecosystems around the globe, with increasing pressure from anthropogenic influence (e.g. Ogashawara et al., 2017a; IOCCG, 2014). Such blooms are becoming increasingly common in lakes and rivers, and can be both economically and environmentally devastating (e.g. Page et al., 2018; Clark et al., 2017; IOCCG, 2014; IOCCG, 2008).

The term "inland waters" refer to lakes, reservoirs, rivers, ponds, swamps, wetlands, and even coastal areas, and are usually extremely diverse environments with a wide range of physical, chemical, and optical properties, and can be fresh, saline or brackish. Inland waters only comprise a small percentage of Earth's total land surface; however, they play an essential role in the biogeochemical cycle (Bastviken et al., 2011) and are extremely sensitive to environmental change, development pressure and land use cover change (Ogashawara et al., 2017a) such as those described earlier in this section. Traditional field-based methods to monitor water quality, are usually costly and labour intensive, and satellite remote sensing offers a low-cost, high frequency and broad coverage for accurate monitoring inland water resources and isolating the natural and anthropogenic stressors (e.g. Duan et al., 2010). Application of remote sensing techniques to inland waters can be different from open ocean waters because of the variable composition of water constituents. Concomitant use of bio-optical models to monitor optically active water constituents, such as chlorophyll a, sediments, coloured dissolved organic matter (explained and discussed in more detail later in this section and the thesis) has allowed for increasing application of oceanographic and remote sensing theories and concepts in inland waters. However, there is often a significant challenge to measuring IOPs due to the spatial-temporal variability of water constituents at the same site. Yacobi et al. (1995) and Huang et al. (2015), for example, show that the dominant constituent in the water column at a study site may not only change spatially across short distances but also across seasons and even daily. Australia, like many areas in the world, is experiencing a growing concern over the increasing frequency and spatial extent of algal blooms in inland and estuarine waterways caused by nutrient run-off from water treatment plants, plant fertilisers and detergents (Jernakoff et al., 1996). These issues are examined further later in this section, which a focus on a case study site, the Swan River Estuary in Western Australia, which is particularly affected by cyanobacteria and dinoflagellate species blooms.

Natural resource managers and public health officials need cost effective and reliable tools to detect and monitor HAB events so that mitigation actions can be effectively taken. Traditionally, phytoplankton measurements and monitoring has been conducted in the field, and continues to form an integral part of monitoring programs. Water samples are taken for chlorophyll content assessment, and for algal cell counts of species present. Measurement of the optical properties of water, as a descriptor for algal biomass are also regularly conducted – as they absorb and scatter sunlight, phytoplankton exert a profound influence on the in-water light field, including the flux upwards across the water surface. Variations in phytoplankton communities change the optical properties (e.g. IOCCG, 2014; Ruiz-Verdu et al., 2008; Richardson, 1996), for example the maximum cyanobacteria absorption peak in the red region is shifted into longer wavelengths, probably caused by phycocyanin fluorescence at approximately 650 nm (IOCCG, 2014; Ruiz-Verdu et al., 2008).

2.3 Multispectral and Hyperspectral Monitoring of Algal Blooms

Radiometric remote sensing of coastal and inland water bodies is of interest to a wide variety of research, management, and commercial users as well as the general public. The past and current suite of satellite sensors are multispectral to optimize the detection of phytoplankton pigments such as chlorophyll, chlorophyll fluorescence, and CDOM and NAP absorption (Aurin and Dierssen, 2012; Gitelson et al., 2007; Lee et al., 2007a; Lee et al., 2007b). However, they are mainly designed for observing the global ocean and not necessarily for observing coastal and inland waters (Mouw et al., 2015).

Tyler et al. (2016), Mouw et al. (2015), and the IOCCG reports (e.g. IOCCG, 2008) review in considerable detail the current application of satellite spectral radiometers to coastal and inland waters. All highlight that while there is considerable potential for large scale assessment, and synergistic multiscale observation, coastal and inland process are not adequately captured by any existing or planned missions (Figure 2.1), and there is a need for further algorithm development and validation for optically complex waters (Bracher et al., 2017).

Mouw et al. (2015) point out, however, that use of existing systems and data for inland applications other than the primary requirement target, has expanded the relevance and benefits to environmental and management agencies, driving advances in support of in-situ observations. Here the options for radiometric measurement of inland waterways are examined; in particular, multispectral and hyperspectral applications to algal bloom measurement are highlighted, as the focus of this study is on measuring phytoplankton in a riverine environment with optical techniques.

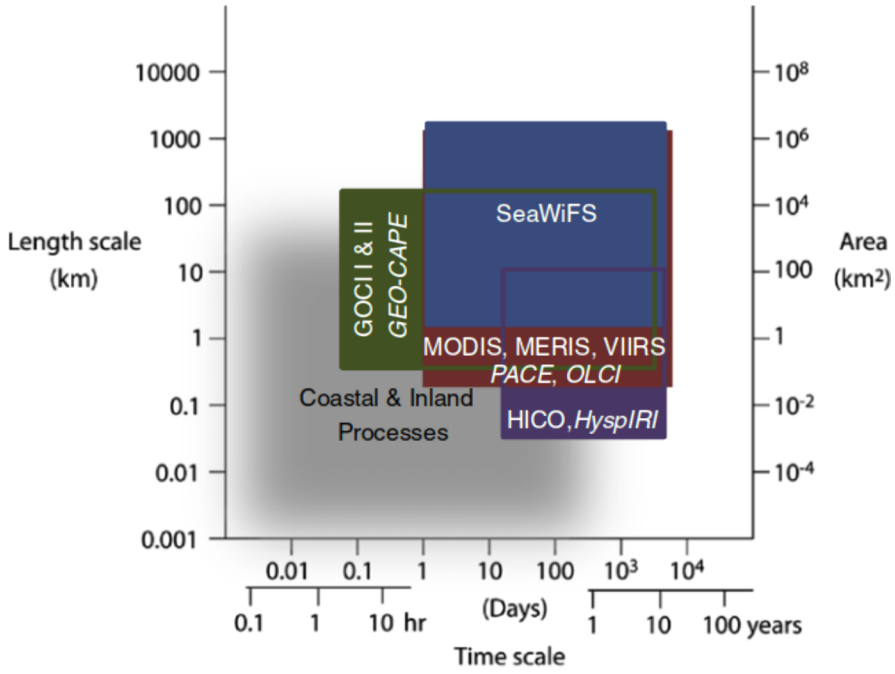

Figure 2.1: From Mouw et al. (2015): Length- and timescales of coastal and inland processes in relation to heritage, current and planned aquatic color sensors (SeaWiFS, MODIS, MERIS, VIIRS, HICO, GOCI, OLCI) and missions (PACE/ACE, GEO-CAPE, HyspIRI). Planned sensors and missions were italicized in the original publication but OLCI is now operational.

2.3.1 Satellite Remote Sensing

In the last few decades there has been increasing attention to the application of remote sensing technologies for algal bloom monitoring, namely data from satellite or airborne systems. The intensity and wavelength of the upward light flux can be measured by radiometers carried on spacecraft, aircraft and in- and above-water instruments, providing the basis for visible spectral radiometry (or ocean colour radiometry, OCR), and con-

verted to chlorophyll-a concentration as a proxy for biomass (e.g. IOCCG, 2000; Jeffrey et al., 1997; Billy, 1986). Ocean colour radiometry by earth-orbiting spacecraft has already been conducted for some thirty years, and offers cost-effective, frequently acquired, synoptic data pertaining to phytoplankton biomass in surface waters; it is thus of considerable value to monitor and better understand primary production, phytoplankton biomass, harmful algal blooms (e.g. IOCCG, 2008) and other environmental parameters. The ability to fully and regularly monitor the Earth's vast oceans is beyond the ability of any ship-based campaign; being global in scope, the technology provides a large-scale view of the marine ecosystem and offers a means to address outstanding issues such as climate change on this scale. Ocean colour products are becoming more widely and more easily accessible, and are central to the more effective use of ocean colour for HAB applications, especially in coastal areas. Algorithm development is of considerable importance and a number of programmes now exist globally aimed at making HAB information more available through web-based dissemination systems (IOCCG, 2008). Examples include the ChloroGIN programme (Chlorophyll Globally Integrated Network)[1], the S-3 Eurohabs project[2], utilising data from the Copernicus program, and the GEOHAB programme[3], a comparative approach across coastal ecosystems aiming to improve global understanding of the ecology of potentially harmful phytoplankton blooms.

There are a number of missions providing freely accessible, research and climate quality data, of which the main ones are reviewed here. The launch of one of the first Earth Observing Satellites, the Earth Resources Technology Satellites 1 (ERTS-1) in 1972 lead to the first bio-optical models (Gordon et al., 1975) which described the ocean colour as a function of its biological constituents. Chlorophyll-a concentration was mapped in lakes as early as 1974 from aircraft and satellite (Strong, 1974), and it was the first parameter derived quantitatively from ocean color satellite sensors, and remains a focus today (Morel and Antoine, 2000). The Coastal Zone Color Scanner (CZCS, launched 1978) was the first satellite scanner optimised for biological oceanography, in particular chlorophyll-a (e.g. Gordon et al., 1983; Aiken et al., 1992). The sensor had four, 20 nm visible spectral bands and one near-infrared (NIR) band used for atmospheric correction. The CZCS was only a proof-of-concept mission, but was the first satellite to provide oceanographers with a large temporal and spatial spread of global data. As such CZCS data were unprecedented and unparalleled at the time and as a result have been used in

[1] http://www.chlorogin.org/
[2] https://www.s3eurohab.eu
[3] http://geohab.org/

numerous studies on the dynamics of phytoplankton blooms, turbidity, and water quality in marine waters including many focused on complex sea-shelf systems (e.g. Yoder et al., 1987; Aarup et al., 1989). CZCS was primarily designed for ocean colour monitoring and thus the coarse spatial resolution (825 m) of the data was suited only to the observation of very large lake systems.

In 1997, the successor to CZCS, SeaWiFS (Sea-viewing Wide Field-of-view Sensor) was launched providing oceanographers with two extra bands in the NIR for more accurate atmospheric correction and a greater number of bands in the visible spectrum for better chlorophyll-a estimates in optically complex water (Bricaud et al., 2001). While SeaWiFS offered improved spectral and radiometric resolutions it captured data at a coarse spatial resolution (1.1 km) that limited its use over inland systems or close to the coast where high spatial complexity exists in near-surface waters. Since SeaWiFS there have been a number of generations of different satellites capable of monitoring chlorophyll concentrations, and at a higher spatial resolution; for example MODIS-Terra (launched 1999) and MODIS-Aqua and MERIS (both launched in 2002) improved the spatial resolution of ocean colour data products down to 250-300m, every 1-3 days globally. The Landsat program spans several decades at spatial resolutions down to 15m, and enables continental, multi-temporal analysis and insights into surface water behaviour through time (e.g. the Water Observation from Space product as described by Mueller et al., 2016). At this resolution, the ability to observe spatial and temporal trends in water quality in large lakes, lagoons and coastal waters was greatly enhanced and the potential for chlorophyll-a retrieval demonstrated (e.g. Palmer et al., 2015a in Lake Balaton, Hungary, Feng et al., 2012 in Poyang Lake, Gitelson et al., 2007 in Chesapeake Bay). Campbell et al. (2011) (for MERIS) and Odermatt et al. (2012) conclude that substantial progress has been made in understanding and improving retrieval of constituents in optically deep and complex waters, but that further validation and intercomparison of spectral inversion procedures is needed. However, for smaller water bodies, these resolutions remain too coarse (e.g. Tyler et al., 2016).

Different species of phytoplankton have varied chlorophyll-a concentration per cell mass and can also have many different accessory pigments. Multispectral sensors, such as OLI, Landsat 8 (albeit at a higher spatial resolution) or MODIS-Aqua are not capable of spectrally separating waters dominated by cyanobacteria from waters dominated by other algae species (Kutser et al., 2006) as they do not have the spectral band configuration capable of detecting absorption features caused by phycocyanin, a unique pigment present

in all blue-green algae species (Olmanson et al., 2008; Jeffrey et al., 1997). Landsat 8 does however show potential for detection of Coloured Dissolved Organic Matter (CDOM) retrieval (Olmanson et al., 2016) and Total Suspended Matter (TSM) retrieval Lymburner et al. (2016) .

Of the newest generation of sensors (launched 2016-2018), the Copernicus Sentinel-2a and 2b, and Sentinel-3a and 3b satellites offer the greatest potential yet for coastal and inland applications (Pahlevan and Scott, 2013). Sentinel-3a and 3b (operating in tandem as a constellation) carry the Ocean Land Colour Instrument (OLCI), building on the heritage of MERIS with daily observations on inland and ocean water quality, and with complete global coverage at 300 m spatial resolution. These missions will be supported by higher spatial resolution data from the Multispectral Instrument (MSI) on-board the Sentinel-2a and 2b satellites, with sufficient spectral and radiometric resolutions for application over turbid waters and with spatial resolution of 10-60 m. The planned operational lifetime of the Sentinel series of satellites sets it apart from previous missions, with continuity planned to 2030 and studies are emerging now examining the potential of Sentinel-2 (Johansen et al., 2018) and Sentinel-3 OLCI (Watanabe et al., 2018) chlorophyll-a algorithms for near HAB detection and potential for near real-time monitoring in lakes and rivers.

Ocean colour sensors with discrete spectral bands risk missing important spectral features, especially in coastal and inland areas (Lee and Carder, 2002), and sensors with higher spectral resolution, or spectrally placed bands, along with high spatial resolution would be beneficial for such special and challenging cases (Lee et al., 2007a). The benefit of increased spectral resolution is increasing attention toward the launch and use of hyperspectral sensors for phytoplankton detection; in particular, hyperspectral algorithm development to address the limited (multi-spectral) applicability of satellite algorithms determining phytoplankton composition for regional, especially coastal or inland, waters (Bracher et al., 2017; Chase et al., 2017). Hyperspectral sensors measure the electromagnetic spectrum in numerous narrow bands. The high spectral resolution of systems such as Hyperion (Pearlman et al., 2003) and HICO (Lucke et al., 2011) allow analysis of narrow spectral features such as chlorophyll-a absorption. For example, Brando and Dekker (2003) demonstrate that Hyperion has sufficient sensitivity to detect concentrations of coloured dissolved organic matter, chlorophyll, and suspended matter in the complex waters of Moreton Bay in Western Australia. Giardino et al. (2015) also apply a bio-optical inversion procedure to Multispectral Infrared Visible Imaging Spectrometer

(MIVIS) data to retrieve suspended particulate matter (SPM), chlorophyll-a and CDOM in optically deep turbid lake water. However, these systems lack the spatial resolution for narrow waterways such as the Swan River.

Aside from the open access satellite campaigns, a number of commercial systems are available, the potential of which has not been widely explored due to the financial cost of acquiring the data, particularly if tasking is required (Tyler et al., 2016). Examples include WorldView-2 and -3, Ikonos and Quickbird. These platforms offer very high spatial resolution data (< 2 m) but lack the spectral range, sensitivity and regularity of acquisition of the multi- and hyperspectral, and are too costly for use in algae monitoring programmes.

2.3.2 Airborne Hyperspectral Remote Sensing

There have been many advances in application of hyperspectral systems over lakes and other inland waters, in particular using airborne and in situ systems, again highlighting the potential for remote sensing for inland water monitoring if, as noted previously, recent achievements are progressed. Palmer et al. (2015b) and Dornhofer and Oppelt (2016) provide some comprehensive overviews of these developments.

Hyperspectral sensors, mounted in small aircraft can also collect landscape images with high spatial and spectral resolution. Some examples include the HyMap, Eagle, CASI-2, AISA, EnMAP, HyspIRI and PRISMA and they offer the ability to collect several hundred spectral bands of data in the infrared, visible and ultraviolet at a high-spatial resolution, suitable for lake and other inland applications. Hestir et al. (2015) show that high fidelity spectral and spatial resolutions are needed for freshwater ecosystem measurements and that HyspIRI has unique capabilities for this. CASI provided 1.23 meter ground resolution per 1 km of aircraft altitude. Hyperspectral sensors, such as this, can be important sources of diagnostic information about a specific target's absorption and reflection characteristics. For example, Klonowski et al. (2003) conducted one of the most extensive, fine scale (3.5m) bathymetric mapping studies, deriving light parameters over a reef in Western Australia using the airborne HyMap imaging system (HyVista Corp.), which records light into 126 spectral channels covering the 450nm to 2500nm spectral range at a typical bandwidth of 15nm. Garcia et al. (2014) show that the precision of bathymetric retrieval from HICO data is dependant on the shallow water inversion algo-

rithm applied, but note that the atmospheric correction steps can add uncertainty that can cumulatively render the geophysical parameter imprecise and potentially unusable. HICO geolocation can also be inconsistent, posing issues for time-series analyses.

The expense of flying such an instrument is high and often negates the potential for regular use in monitoring programs (e.g. Jernakoff et al., 1996). Hick (1997) presents a thorough overview of airborne remote sensing applications in Western Australia, over Geographe Bay and Peel Inlet, and using a CASI in the Swan River; this later site study was published as a CSIRO technical report (Jernakoff et al., 1996) and is reviewed in more detail later in this chapter.

2.3.3 Field-deployed Remote Sensing Instruments

Another option available for determining optical water properties is with hand-held or field-deployed hyperspectral radiometers. A number of different types exist (described in considerable detail in protocols documents such as the NASA protocols (Mueller et al., 2003) and MERIS validation protocols (Barker, 2013a; Barker, 2013b). There are a wide range of radiometers and deployment practices, see Barker (2013a) for all, from whose data are widely used for satellite validation. They include subsurface fixed station instruments (e.g. those on BOUSSOLE and MOBY), above surface such as the TriOS RAMSES fixed on "ships of opportunity" (ferries) in the Scandinavian countries, and profiling radiometers such as the Satlantic, typically deployed in open ocean, clear water environments.

Above water radiometers record the upward, water leaving reflectance and are more suited to shallower water, more optically complex, environments. The DALEC is one such example of these; developed in Australia it simultaneously measures sea and sky radiance together with downwelling hemispherical irradiance during autonomous ship-based deployments being a hand-held instrument held over the edge of a boat. The DALEC (Keen et al., 2012) is used by IMOS (Integrated Marine Observing System)[4] for MODIS and VIIRS validation activities (Brando et al., 2016). An early prototype of the DALEC was used in this thesis for reflectance measurements.

[4]http://imos.org.au/

2.4 Optical Models for Measuring Phytoplankton

In this section, the concept of bio-opticals is introduced; the mathematical details are examined further in Chapter 5, which is dedicated to describing all of the optical concepts required for this study.

2.4.1 Bio-optical Models

The expression "bio-optical" was first used to describe the "state of ocean waters" (Smith and Baker, 1977). Bio-optical models are based on radiometric quantities, inherent optical properties (IOPs) and apparent optical properties (AOPs), such as downwelling spectral solar and sky radiation and the absorption and scattering properties of constituents in the water column. Studies by Cox and Munk (1954), Petzold (1972), Jerlov (1968), Jerlov (1976), and Preisendorfer (1976), were some of the first attempts to use mathematical, bio-optical models, to describe the colour of the oceans as a function of their inherent optical properties.

The Inherent Optical Properties (IOPs) of a water column are defined as the spectral absorption and spectral scattering coefficients of the water. The Apparent Optical Properties (AOPs) are a function of both the IOPs and the light field in which they are measured. Detailed mathematical descriptions of these are covered in Chapter 5. The function of bio-optical models is to quantify the Inherent Optical Properties (IOPs) (Preisendorfer, 1976) as a function of their absorption and specific absorption as well as their backscattering and specific backscattering (Mobley, 2001). Concentration normalized IOPs are called specific inherent optical properties (SIOPs), and are used to describe the optical absorption and scattering coefficients in terms of the specific concentration.

Remote sensing optical models are able to produce accurate predictions of IOPs in oceanic and shallow water environments. However, IOPs vary not only across geographic regions but also within the same site (Ogashawara et al., 2017a). Therefore, the optical complexity of inland waterways require a much greater site-specific knowledge in order produce similar results (Odermatt et al., 2012; Palmer et al., 2015b), and adequate databases for inland waters like LIMNADES (Globolakes, 2014) are still in the evolving phase. Spectral ambiguities and the diversity of composition and SIOPs introduces a fundamental numerical problem to inversion; different combinations of water constituents can lead to indistinguishable reflectance spectra (Defoin-Platel and Chami, 2007), making it difficult

to create an inland optical model that generalises well for all water bodies (Cherukuru et al., 2017).

2.4.2 In-water Constituents

Phytoplankton

The primary pigment in phytoplankton is chlorophyll-a and is the most suitable proxy for phytoplankton abundance (Huot et al., 2007). Chlorophyll-a absorbs in the red and the blue part of the electromagnetic spectrum and reflects in the green. This is what gives phytoplankton its green colour. Phytoplankton contains accessory pigments that in different combinations can alter the colour slightly. Different species of phytoplankton are known to contain different combinations of these accessory pigments and have been used to classify phytoplankton into different ecological functional groups (Nair et al., 2008; Brewin et al., 2011; IOCCG, 2014).

There are numerous bio-optical models describing phytoplankton. One of the first phytoplankton bio-optical models was described by Bricaud et al. (1995) which was an analytical model derived by inverting a model of remote sensing reflectance. Since then a number of other quasi-analytical (Li et al., 2013), semi-analytical (Vos et al., 2003; Mishra and Mishra, 2012), and empirical (Allan et al., 2015) bio-optical models of phytoplankton have been developed. These models have been developed for ocean waters and bio-optical models describing inland waters and lakes are still remain lacking due to the complexity of the optical environments indicative of these waters. Aurin and Dierssen (2012) highlight, in a study of the CDOM dominated Long Island Sound Estuary, that diverse phytoplankton assemblages create variability between spectral absorption and chlorophyll.

Bio-optical models describing phytoplankton for inland waters are highly site specific and models need to be 'tuned' for local conditions, explained in detail in Matthews (2017) and shown by Cherukuru et al. (2017) for specific inherent optical properties and spectral slopes of IOPs.

Coloured Dissolved Organic Matter (CDOM)

Ocean colour is mostly dominated by the concentration of phytoplankton and are often described as Case-I waters (Morel and Prieur (1977); Gordon and Morel (1983). Lakes and inland waterways however, are very commonly dominated by Coloured Dissolved Organic Matter (CDOM), the compounds of which are produced during the decay of plant matter and consist of various humic acids and fulvic acids or melanoids. Typical CDOM concentration ranges in absorption at 440 nm ranges from 0 to $0.16m^{-1}$ in the open oceans, but from 0.004 to $3.82m^{-1}$ in coastal areas and from 0.06 to $19.1m^{-1}$ in inland waters (Kirk, 1983). Furthermore, the absorption range of CDOM has been found to span 4 orders of magnitude in a single inland lake (Gons et al., 2008).

Scattering of CDOM is small and commonly ignored, yet fluorescence may be significant and should be accounted for in radiative transfer models at high concentrations (Pozdnyakov et al., 2002). Although CDOM is an important water quality characteristic, CDOM fluorescence is not well studied in inland waters or included into routine water water quality monitoring programs (Olmanson et al., 2016), and a bio-optical model that describes CDOM fluorescence is lacking (Kutser et al., 2017). However, CDOM is a major optical component of rivers and inland water and as such it is necessary to describe the optical characteristics and their effect on remote sensing reflectance if remote sensing is going to be used to monitor them (Mouw et al., 2015). Efforts to measure and monitor the impact of elevated nutrient and organic loads in the Swan River are discussed later in this chapter and the detailed bio-optical model describing CDOM is explained in Chapter 5.

Total Suspended Sediment (TSS) and Non-algal Particles (NAP)

All water bodies have a number of different types of suspended particles ranging from soil and sand from rain runoff, silt disturbed from the bottom to phytoplankton, bacteria and other dead cells. The sum of all these particulates is the Total Suspended Sediment (TSS) or often referred to as Total Suspended Matter (TSM).

The size distribution of TSS is roughly hyperbolic (Bader, 1970) and varies greatly depending on water body type, location and environmental conditions. Although the size distribution of particles is wide in range, small particles do not backscatter as efficiently as larger particles and as such, backscattering in natural waters are most frequently

dominated by particles with a diameter greater than $2\mu m$ (Jerlov, 1976). The total backscattering due to TSS ranges from about 0.2% to 3% (Chami et al., 2005; Antoine et al., 2011) for oceanic waters. The total scattering for inland waterways is much more site specific and typical values are much harder to report (e.g. Ogashawara et al., 2017b).

TSS without phytoplankton is known as detritus or non-algal particles, and the inorganic fraction of TSS is tripton. The absorption of detritus and tripton can be modelled using a similar bio-optical model to CDOM but with a spectral slope typically much less than for CDOM (Ogashawara et al., 2017b).

2.4.3 Semi-analytical and Quasi-analytical Models

Semi-analytical and quasi-analytical models describe IOPs as a function of water's AOPs, usually the remote sensing reflectance. One of the first semi-analytical optical models is described in Gordon et al. (1975) and Gordon et al. (1988) which defines the remote sensing reflectance just below the water surface as a function of the absorption to backscattering ratio. Inversion of the optical model allows the optical properties of the water to be derived from the sub-surface remote sensing reflectance. The details of how the the IOPs can be derived from an optical model though mathematical inversion are discussed in detail in the following chapters.

The first multi-spectral method of deriving absorption and chlorophyll-a from the Moderate-Resolution Imaging Spectrometer (MODIS) satellite was developed by Carder et al. (1999). This model was one of the early models able to produce daily global phytoplankton and chlorophyll estimates. One of the limitations of the MODIS sensor and the Carder et al. (1999) model is that is it not possible to separate the CDOM and detritus absorption spectra, which potentially reduces the accuracy of the phytoplankton retrieval.

The Quasi-Analytical Algorithm (QAA) was developed by Lee et al. (2002) to derive inherent optical properties of optically deep waters from remote sensing reflectance. The model takes a two step approach to deriving IOPs; the first step derives the total absorption and backscattering coefficients and the second step decomposes the total coefficients into the optically active constituent absorption and backscattering coefficients. Unlike the Carder MODIS-specific model, QAA is adaptable to both multispectral and hyperspectral instrument data, making it adaptable for any radiometric sensor, from satellite

to field instruments (IOCCG, 2000).

With advances in sensor technology, greater spectral bandwidth is available and more sophisticated models have been developed to make use of this information. With increased spectral resolution comes the ability to discern between a greater number of IOPs that can be considered spectrally similar by means of spectral pattern matching. Five such models are HOPE (Lee et al., 1999), BRUCE (Klonowski et al., 2007), SAMBUCA (Brando and Dekker, 2003), CRISTAL (Mobley and Bisset, 2011), and ALUT (Hedley et al., 2009), all of which are able to retrieve IOP estimates as well as bathymetric depth in shallow water environments.

CRISTAL forward estimates remote sensing reflectance from many different combinations of IOPs and environmental conditions, using the commercially available software Hydrolight (Mobley and Sundman, 2001). The inverse of the process, finding IOPs from remote sensing reflectance, is then achieved by an exhaustive search through a lookup table of reflectance IOP pairs. HOPE removes the requirement of a lookup table by fitting a semi-analytical mathematical model to reflectance data produced by Hydrolight, which reduces the computational requirement and processing time. The inverse process is then achieved through the use of a predictor-corrector algorithm which matches the best combination of IOPs and bottom depth from the model with measured remote sensing reflectance.

ALUT takes a hybrid approach of both CRISTAL and HOPE by producing an adaptive lookup table generated from HOPE. The adaptive lookup table is optimised and reduced in size compared to CRISTAL by pruning the lookup table so that the reflectance data is equidistant in reflectance spectra (Hedley et al., 2009). This results in a more efficient, smaller and faster lookup table than CRISTAL.

Both BRUCE and SAMBUCA are canonical variants of HOPE. BRUCE has been optimised to retrieve bathymetric depth as well as benthic class by finding the best match of different end-members of benthic spectra (Klonowski et al., 2007). SAMBUCA has been optimised to retrieve SIOPS by differentiating the spectral properties of the algal and non-algal particles.

Dekker et al. (2011) compare all these models for accuracy and efficiency for bathymetry mapping, with a view to resource management application and concludes that none of

the models compared are optimal for all situations. However, this intercomparison was conducted in a shallow water coastal environment and there still remains a paucity of information on the performance of these models in inland waterways such as rivers.

2.4.4 Uncertainty in Bio-optical Models

Key to understanding remote sensing and optical model products is the estimation of uncertainties associated with the inputs and algorithm parameters; this applies to both satellite (or airborne) and in situ measurements (Bracher et al., 2017; Wang et al., 2005b; IOCCG, 2006). For example, semi-analytical models are affected by uncertainties in remote sensing reflectance but they are also influenced by uncertainties associated with the chosen relationship between Rrs and IOPs, and uncertainties resulting from the assumptions used in their formulation. The complex interaction among the water constituents, which is often intensified by anthropogenic actions, creates greater uncertainty in remote sensing models designed for inland waters (Ogashawara et al., 2017a).

It is a major gap in using ocean colour to estimate phytoplankton from space for a number of reasons including a lack of quantitative uncertainty estimates provided with satellite data and the in situ measurements used for validation (Bracher et al., 2017). This becomes a compounding, propagating issue in inversion modelling, and as Wang et al. (2005b) and IOCCG (2006) explain, data products retrieved from the inversion of in situ or remotely sensed ocean-colour data are generally distributed or reported without estimates of their uncertainties. It therefore remains a challenge to improve and develop methodologies for uncertainty quantification.

2.5 Phytoplankton in the Swan River

2.5.1 Ecological Issues in the Swan River

The Swan and Canning rivers flow through the centre of metropolitan Perth, a city of more than two million people. The Swan River is $72km$ long and together with the Canning and their tributaries, drain a catchment area of $2090km^2$. Algae are a natural part of the rivers and estuary and an important part of the ecosystem, as they are in waterways throughout the world.

The Department of Parks and Wildlife and The Swan River Trust identify a range of factors which have the potential to impact on the water quality and ecological health of the Swan River system (e.g. Swan River Trust, 2017; Department Of Parks And Wildlife, 2015; Swan River Trust, 2008; Swan River Trust, 2005). There is also a reasonably large body of literature describing zooplankton (Griffin et al., 2001) and phytoplankton species distribution in relation to organic and inorganic nutrient loading (e.g. Thompson and Hosja, 1996; Pennifold and Davis, 2001; Hamilton et al., 2006; Robson and Hamilton, 2003; Petrone, 2010; Fellman et al., 2011), oxygenation levels (e.g. Tweedley et al., 2016), and hydrological process (e.g. Chan and Hamilton, 2001; Chan et al., 2002; Hipsey et al., 2013) in the Swan River. Field monitoring and reporting focus on key analytes including nitrogen, dissolved organic nitrogen, soluble reactive phosphorus, silica, dissolved organic carbon, total suspended solids, alkalinity, chlorophyll-a, secchi depth, phytoplankton, dissolved oxygen, salinity, temperature and pH (Thompson et al., 2001; Department Of Water, 2016).

A non-nutrient contaminant measurement program was conducted by DPAW, along the Swann Canning river system, and in particular in the vicinity of Claisebook Cove (closest to Nile Street on the SCCP measurement program and a sample site for this thesis). The field monitoring and reporting focuses on key analytes including metals, petroleum hydrocarbons and nitrogen, dissolved organic nitrogen, soluble reactive phosphorus, silica, dissolved organic carbon, total suspended solids, alkalinity, chlorophyll-a, secchi depth, phytoplankton, dissolved oxygen, salinity, temperature and pH. Many of these contaminants bind to sediment particles and settle on to the riverbed, and contaminated sediments may be re-mobilised if disturbed through activities such as dredging. A number of reports are publically available throughout the DPAW website detailing the issues and monitoring processes along the river, including Thompson et al. (2001), Evans (2009), Foulsham et al. (2009), Nice (2013), Fisher (2013) and Department Of Water (2016).

In summary, vast tracts of the Riverpark's catchment area have been cleared for agriculture and development, allowing sediment, nutrients, and other contaminants to enter the waterway (Department Of Parks And Wildlife, 2015). Permanent changes to the groundwater and surface water drainage systems and reduced rainfall over time have resulted in excess nutrients (phosphorus and nitrogen) and organic loading from urban and rural catchments, promoting excess algal growth and lowering oxygen conditions which in turn contributes to fish kills. Contaminants such as heavy metals, pesticides and herbicides, also entering the waterway through the drainage network, can be directly toxic to organ-

isms, affect life cycles and enter the food chain.

Most algal blooms are harmless, they may discolour the water but do not pose a problem for the rivers, wildlife or humans; however on occasion they are toxic. John and Kemp (2006) report that bloom events of potentially toxic species increased in the Swan River over a 20 year period, and since 1993, blooms of potentially toxic Anabaena species have occurred in the Canning River. In 2000 the Swan River estuary also experienced a prolonged toxic bloom of the cyanobacteria Microcystis aeruginosa for the first time, influenced by the physical process in the estuary (Robson and Hamilton, 2003).

2.5.2 Seasonal and Site Variation in Phytoplankton

The Swan River is highly variable in phytoplankton species succession, both temporally and spatially. Some phytoplankton species can reproduce very rapidly, doubling their numbers in two hours to a few days under favourable conditions, and blooms can co-occur and overlap in both time and location (Swan River Trust, 2005; Huang et al., 2017).

The estuary has a highly seasonal hydrology and typical successions of various phytoplankton species are observed throughout the year (Thompson and Hosja, 1996; Chan and Hamilton, 2001; Brearley and Hodgkin, 2005). There are hundreds of species of algae in the river, demonstrated by Hipsey et al. (2016b) (see Appendix A), dominated by green diatom, dinoflagellate, chlorophyte, cyanobacteria and cryptophyte species and encompassing a broad range of sizes (picoplankton to micron) and shapes (flagellated, round, cylindrical, chain forming etc). Dominant species distribution and succession is evident in the Hipsey et al. (2016b) report; highly variably by both site and season, driven by seasonal rainfall, and the subsequent changes in the spatial distribution of salinity and nutrients (John, 1984; John, 1987; Hodgkin, 1987; Twomey and John, 2001; Chan and Hamilton, 2001; Latchford et al., 2003; Swan River Trust, 2008; Department Of Parks And Wildlife, 2015).

Frequent blooms of problematic dinoflagellate species are of particular concern in the mid-upper estuary reaches (20 to 40km from the mouth; sites NIL up to SUC), with chlorophyll-a concentration increasing over relatively short distances to more than double ($>20\mu g/\mathrm{L}$) that of the lower reaches (BLA to NAR) during bloom events (e.g. Swan River Trust, 2005). Modeling efforts (e.g. Hipsey et al., 2016b; Hipsey et al., 2016a;

Huang et al., 2017) also indicate phytoplankton complexity in the middle Swan region. Relatively low summertime phytoplankton activity and chlorophyll-a concentrations (0-10μg/L) in the lower estuary the lower estuary is attributed to nitrogen limitation, due to tidal flushing with marine waters (Thompson et al., 2001).

2.5.3 Swan River Monitoring Programmes

The Swan Canning Riverpark, under the management of DPAW, was established in 2006, and encompasses 72.1km^2 of public land and adjoining river reserve including the waterways and adjacent Crown land reserves. The department works closely with other State Government agencies, local government authorities, community groups and research institutions (such as CSIRO) to manage the health of the ecosystem. The current program guiding this is this the Swan Canning River Protection Strategy (SCRPS) through the Swan River Trust, released in 2015 and arising from the Swan and Canning Rivers Management Act 2006 (Department Of Parks And Wildlife, 2015). The SCRPS has a number of objectives focussed on water quality (e.g. extent and severity of low oxygen and algal blooms) and water flow management, foreshore condition, biological indicators including fish and seagrasses, and an overarching protection, management and communications strategy. The Strategy report (Department Of Parks And Wildlife, 2015). details the coordinated management approaches for the ecological health measures undertaken to complement water quality monitoring and reporting, and releases progress reports and newsletters on the department website to ensure effective communication to a wide range of stakeholders (e.g. Swan River Trust, 2017; Department Of Parks And Wildlife, 2015).

The SCRPS is informed by two predecessor programs and a number of research studies focused on the phytoplankton ecology of the Swan River and factors influencing growth and events. The Swan Canning Cleanup Program (SCCP) ran from 1999 - 2004, and was launched by the Swan River Trust to tackle the increasing incidences of algal blooms in the Swan Canning river system (Thompson et al., 2001). The SCCP informed the development of the Healthy Rivers Action Plan (Swan River Trust, 2008), 2008-2013, and which, when reviewed in 2014 was found to have been effective with 78% of targeted actions to improve water quality accomplished.

2.5.4 Optical Studies and Modelling in the Swan River

While there is a strong body of work around the drivers of various aspects of water quality, there remains little in terms of the role of the optical properties of the water, as determined by CDOM and TSS presence. Even less exists around the application of optical models and/or radiometric sensors (hand-held, airborne or satellite based) as a potential monitoring technique for the Swan River estuary, either in complement to existing and well establish field monitoring program methods (e.g. hand-held instrumentation) or on the wider spatial scale (airborne or satellite). Water optical properties determine the underwater light climate, which is important for plant growth as well as water appearance. In the Swan River estuary, the light climate varies considerably over the length of the domain and throughout the year Kostoglidis et al. (2005), and light attenuation (Kd) exhibits strong variability associated with pulses of CDOM-rich inflow water. Kostoglidis et al. (2005) demonstrate that CDOM is the most significant factor explaining variability in Kd, with contributions from TSS. Hipsey et al. (2016b) and Hipsey et al. (2016a) go some way to identify this gap in optical property knowledge by evaluating much of the existing body of work, to take a consensus view on the most appropriate model complexity and parameterisation approach for an "Estuarine Response Model" platform to assist decision making. They review modelling efforts to date, mainly around sediment, nutrient, oxygen, salinity fluxes, and the turbidity work of Kostoglidis et al. (2005), in an effort to assess the estuary's ability to respond to multiple stressors over the short and long term, and conclude that making targeted management action is compounded i) these models have either a short term focus or low level of predictability in terms of management priorities, and ii) bloom occurrence is not due to a single limiting factor (salinity, nutrient levels or light climate), but rather a "coalescence of variable factors", agreeing with the conclusions and findings of Hamilton et al. (2006) and Thompson (1998). A follow up report (Huang et al., 2017) around the validation of the Swan Canning Estuarine Response Model (SCERM v2), was unable to achieve good model performance for total chlorophyll-a retrieval, suggesting that an improvement to water quality algorithms (including sediment load and light) are required, among other reasons (e.g. sampling frequency, boundary marking). Huang et al. (2017) also recommend that i) higher frequency data, such as total chlorophyll-a are required in order to capture their variations and provide more information for model settings and validations, and ii) the spatial differences along the Swan need to be observed and accounted for in modelling efforts. However, it has already been noted in the Introduction (Chapter 1), and across multiple Swan River Trust reports (as previously referenced) that monitoring programs are expensive and time consuming, and to increase spatial and temporal cov-

erage will greatly increase the cost and effort expenditure.

It has also been highlighted in this chapter that satellites could (and increasingly do) provide a free or low-cost alternative source of data for monitoring programs, if an appropriate optical model can be applied to derive the required parameters, and if the measurement area is large enough to be captured by the sensor in sufficient detail (or at all). At its widest the Swan River is approximately 3km wide, but in the upper Swan (NIL and beyond) the river narrows considerably to around 300m and continues to get increasingly narrow to around 70m at the inland-most sampling site (SUC). Even if the Sentinel-2b sensor spatial resolution (10m visible bands) may just about capture this narrowest region of the river, deriving any meaningful data from this sensor would be severely hampered by overhanging vegetation and the considerable shadow from the river banks and urban construction.

2.6 Summary

Until such time that coastal and inland waters are adequately captured by high spatial resolution (open access) satellite missions, other approaches for optical monitoring the Swan River must be investigated and developed. The modelling work of Kostoglidis et al. (2005), Hipsey et al. (2016b), Hipsey et al. (2016a) and Huang et al. (2017) are somewhat unique in attempting to characterise phytoplankton dynamics in the Swan River partly in response to the underwater climate (in conjunction with other parameters). The most notable (local and national) study prior to these was conducted by CSIRO (Jernakoff et al., 1996) and (Hick, 1997) prior to the SCCP programme, evaluating the application and potential of airborne remote sensing techniques as a low cost means of detecting and monitoring (in near-real time) phytoplankton, in complement to traditional field measurements. The conclusions of the Swan River component of this study - that field measurements with hyperspectral instruments can suffice for monitoring programs (Jernakoff et al., 1996; Hick, 1997) – influenced the development of the SCCP strategy and underpins the objectives outlined in Section 1.4 for this doctorate thesis.

Chapter 3

Comparative Assessment: Mie Theory and FDTD Scattering Methods

3.1 Introduction

Characterisation of particle scattering phase functions is required when modelling the underwater light field in remote sensing oceanographic applications such as with Hydrolight or PlanarRad. Due to the difficulty in accounting for the natural variability in the size and shapes of the many different particle types, phase functions are often expressed by finding analytical solutions to coarse approximations (Mie theory, Mie, 1908; Aden–Kerker, Aden and Kerker, 1951; anomalous diffraction approximations, Hulst, 1957), as semi-analytical solutions (Fournier and Forand, 1994) or closest fit to empirical data (Petzold, 1972). The finite-difference time-domain Method (FDTD) was first published by Yee (1966) as a numerical solution to Maxwell's equations over a finite domain, or voxel, known as a 'Yee cell' and is commonly used in computational electrodynamics. The electric field components are defined around the edge of the cell and the magnetic fields form the normals to the face of the cell. A structure is created by defining the permeability, permittivity and conductivity of the cell and subsequent adjacent cells. A non-homogeneous structure can be made by defining unique dielectric quantities for each cell, forming a computational domain formed by a lattice of Yee cells. An example of this is shown in Figure 3.1. This model makes it possible to use the FDTD method to calculate the particle scattering phase functions for any shaped scattering particle, such as a phytoplankton cell and other hydrosol shapes. This chapter presents the method for calculating the scattering of algal cells using the FDTD method and aims to calculate the algal scattering phase functions of various algal shapes.

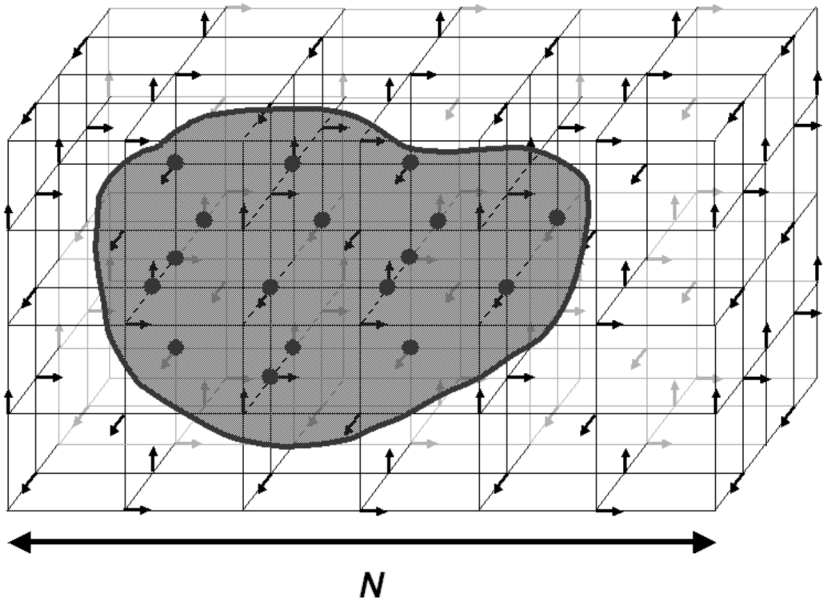

Figure 3.1: A grid made of Yee cells. The electric and magnetic field components, shown as arrows, are defined on the surface of the Yee cells. The complex index of refraction is defined at the location of the field components to define a particle of any shape (Hedley, 2012).

By defining a source electric field at time = 0 it is possible to calculate the magnetic field everywhere in the lattice from the electric field at time step $n + 1 = \Delta t$. Calculating the electric field at time $n + 2$ is then possible from the resultant magnetic field, and so on over subsequent iterations. The method is repeated until a steady state solution is reached. The scattered field is then calculated using a near-to-far-field transformation.

The FDTD technique can be used for any shaped scattering particle. This makes it particularly useful for finding phase functions of hydrosols. However, as the FDTD is a numerical technique, there is always a residual error due to discretising the computational domain. It is important to define the computational domain with sufficiently small quantisation to produce an error that falls within an acceptable tolerance. This may, however, require large amounts of computing resources; in particular, computer memory. We were provided access to a GPU based high performance computer, Fornax, constrained to a limited total run time.

Volten et al. (1998) present laboratory measurements of the scattering properties of 15 different phytoplankton species. The primary aim of the work described here was to:

1. Model the scattering of analogous phytoplankton cells presented in Volten et al. (1998).
2. Validate the ability of the FDTD method against results published in Volten et al. (1998).
3. Assess the ability of the FDTD method to model the effects of shape and internal phytoplankton structure.
4. Investigate the effect particle shape has on the forward:backward scattering ratio.
5. Investigate the usefulness of the FDTD method with respect to determining volume scattering functions for use in modelling R_{rs} for the Swan River.

3.1.1 Particle Scattering

This section will discuss the mechanisms for particle scattering and work towards the concept of the particle scattering phase function introduced in Section 5.1.5. Remote sensing reflectance is a function of the phase function of all the scattering mediums in a water column of interest. Knowing the phase function of all optical properties would make it possible to find an exact solution to the RTE. The focus of this thesis is to derive phytoplankton abundance from measuring the remote sensing reflectance. It is shown in later sections that the remote sensing reflectance is a function of absorption and scattering. The absorption properties of phytoplankton can be accurately by a dual-beam spectrophotometer (method discussed in Chapter 6). Particle scattering is much more difficult to measure at all angles due to the many orders of magnitude it changes across all angles and is outside the scope of this study. Models exist that describe the scattering of spherical particles, however, phytoplankton are rarely perfectly spherical and are too complex in shape and structure to model as such. Therefore, a new approach to modelling the scattering was investigated and presented in this chapter. The following section starts from first principles of Maxwell's equations and derives a special-case analytical solution (Mie theory) that describes particle scattering of homogeneous spheres. Later sections will derive a numerical solution to solving Maxwell's equations, the finite-difference time-domain (FDTD) method. Chapter 5 will demonstrate the use of the FDTD method to model the scattering of phytoplankton cells of arbitrary sizes

and shapes.

Maxwell's Equations

The fundamental theory that describes the behaviour of light is explained by Maxwell's equations. These four equations, shown in Table 3.1, explain the relationship between electricity and magnetism, and as such coined the term 'electromagnetic'.

Table 3.1: Maxwell's Equations

Differential Form	Integral Form	Significance
$\nabla \times \mathbf{E} = -\frac{\partial \mathbf{B}}{\partial t}$	$\oint_c \mathbf{E} \cdot d\ell = -\frac{d\Phi}{dt}$	Faraday's law
$\nabla \times \mathbf{H} = \mathbf{J} + \frac{\partial \mathbf{D}}{\partial t}$	$\oint_c \mathbf{H} \cdot d\ell = I + \int_s \frac{\partial \mathbf{D}}{\partial t} \cdot d\mathbf{s}$	Ampère's circuital law
$\nabla \cdot \mathbf{D} = \rho$	$\oint_s \mathbf{D} \cdot d\mathbf{s} = Q$	Gauss's law
$\nabla \cdot \mathbf{B} = 0$	$\oint_s \mathbf{B} \cdot d\mathbf{s} = 0$	No isolated magnetic charge

Maxwell's equations can be used to describe the absorption and scattering of light in any medium (Cheng, 1992). The differential form of the equations are particularly useful for numerical calculations, as they can be expressed conveniently in a discretised central-difference form. This will be shown in the following sections. In order to describe the scattering of light, it is convenient to represent the Maxwell's equations in their time harmonic form. That is to say, field vectors that are sinusoidal with respect to time can be represented as vector phases that are dependent on space coordinates but not on time. Maxwell's equations written in terms of vector field phasors are shown in Table 3.1 (Cheng, 1992).

Maxell's time-harmonic equations are written in the form:

$$\nabla \times \mathbf{E} = -i\omega\mu\mathbf{H} \tag{3.1a}$$

$$\nabla \times \mathbf{H} = \mathbf{J} + i\omega\epsilon\mathbf{E} \tag{3.1b}$$

$$\nabla \cdot \mathbf{E} = \frac{\rho}{\epsilon} \tag{3.1c}$$

$$\nabla \cdot \mathbf{H} = 0 \tag{3.1d}$$

Where ϵ is electrical permittivity, μ is magnetic permeability of the medium and ω is the angular frequency of the wave.

In a simple, non-conducting source-free medium – $\rho = \mathbf{J} = \epsilon = 0$ – the time-harmonic equations simplify to:

$$\nabla \times \mathbf{E} = -i\omega\mu\mathbf{H} \tag{3.2a}$$

$$\nabla \times \mathbf{H} = i\omega\epsilon\mathbf{E} \tag{3.2b}$$

$$\nabla \cdot \mathbf{E} = 0 \tag{3.2c}$$

$$\nabla \cdot \mathbf{H} = 0 \tag{3.2d}$$

These equations can be combined by taking the curl of Equation 3.2a and substituting in equation 3.2b.

$$\nabla \times \nabla \times \mathbf{E} = -\mu\frac{\partial}{\partial t}(\nabla \times \mathbf{H}) = \omega^2\mu\epsilon\frac{\partial^2\mathbf{E}}{\partial t^2}$$

Using a vector identity $\nabla \times \nabla \times \mathbf{E} = \nabla(\nabla \cdot \mathbf{E}) - \nabla^2\mathbf{E} = -\nabla^2\mathbf{E}$ because equation 3.2c $= 0$.

This yields the second-order partial differential equations in $\mathbf{E}$ and $\mathbf{H}$ which are the familiar homogeneous vector Helmholtz's equations.

$$\nabla^2\mathbf{E} + k^2\mathbf{E} = 0 \tag{3.3}$$

$$\nabla^2\mathbf{H} + k^2\mathbf{H} = 0 \tag{3.4}$$

Where $k = \omega\sqrt{\mu\epsilon}$.

3.1.2 General Scattering Problem

When describing the general scattering problem, it is convenient to define an orthogonal coordinate system which can be used to explain both the incident and scattered field. Considering a single scattering particle that is struck by a time-harmonic plane wave; the direction the wave travels along is the z-axis and the scattering particle is the origin (x, y, z). The basis vectors of the Euclidean space $\hat{\mathbf{e}}_x, \hat{\mathbf{e}}_y, \hat{\mathbf{e}}_z$ are positive in the x, y and z directions. At some point, the wave scatters at an angle ϕ with respect to the incident plane, the unit normal to the scattered direction is $\hat{\mathbf{e}}_r$. It is convenient to break the incident field in to orthogonal components with respect to the scattering plane. This gives two components: the parallel ($E_{||}$) and perpendicular ($E_{\perp}$) components.

$$\mathbf{E}_i = \left(E_{0||}\hat{\mathbf{e}}_{||i} + E_{0\perp}\hat{\mathbf{e}}_{\perp i}\right)\exp\left(ikz - i\omega t\right) = E_{||i}\hat{\mathbf{e}}_{||i} + E_{\perp i}\hat{\mathbf{e}}_{\perp i}$$

Where $k = \frac{2\pi N}{\lambda}$ is the wave number in the medium surrounding the particle; N is the refractive index of the surrounding medium; and λ is the wavelength in a vacuum.

The basis vectors are therefore:

$$\hat{\mathbf{e}}_{\perp i} = \sin\phi\hat{\mathbf{e}}_x - \cos\phi\hat{\mathbf{e}}_y$$
$$\hat{\mathbf{e}}_{||i} = \cos\phi\hat{\mathbf{e}}_x + \sin\phi\hat{\mathbf{e}}_y$$

Or in spherical polar coordinates:

$$\hat{\mathbf{e}}_{\perp i} = -\hat{\mathbf{e}}_\phi$$
$$\hat{\mathbf{e}}_{||i} = \sin\theta\hat{\mathbf{e}}_r + \cos\theta\hat{\mathbf{e}}_\theta$$

Multiplying by the x and y components, the parallel and perpendicular fields are:

$$E_{||i} = \cos\phi E_{xi} + \sin\phi E_{yi}$$
$$E_{\perp i} = \sin\phi E_{xi} - \cos\phi E_{yi}$$

At large distances from the particle ($kr \gg 1$), the 'far-field region', the scattered electric field $\mathbf{E}_s$ is approximately transverse ($\hat{\mathbf{e}}_r \cdot \mathbf{E}_s$) $\simeq 0$ and has the asymptotic form (Jackson, 1975):

$$\mathbf{E}_s \approx \frac{e^{ikr}}{-ikr}\mathbf{A} \quad kr \gg 1 \tag{3.5}$$

Therefore, the far-field scattered region is:

$$\mathbf{E}_s = E_{||s}\hat{\mathbf{e}}_{||s} + E_{\perp s}\hat{\mathbf{e}}_{\perp s}$$

The relationship between the incident and the scattered field, written in matrix form, is (Bohren and Huffman, 1983)

$$\begin{pmatrix} E_{||s} \\ E_{\perp s} \end{pmatrix} = \frac{e^{ik(r-z)}}{-ikr} \begin{pmatrix} S_2 & S_3 \\ S_4 & S_1 \end{pmatrix} \begin{pmatrix} E_{||i} \\ E_{\perp i} \end{pmatrix} \tag{3.6}$$

The elements of the matrix S_j are the amplitude components of the **scattering matrix**.

Poynting Vector

The Poynting vector describes the 'flow' of electromagnetic energy in W/m^2. When describing the scattering process the Poynting vector is the sum of the incident wave, scattered wave and the extinction field. The extinction field is a result of interaction between fields and the medium.

$$\mathbf{S} = \frac{1}{2}Re\{\mathbf{E}_2 \times \mathbf{H}_2^*\} = \mathbf{S}_i + \mathbf{S}_s + \mathbf{S}_{ext} \tag{3.7a}$$

$$\mathbf{S}_i = \frac{1}{2}Re\{\mathbf{E}_i \times \mathbf{H}_i^*\} \tag{3.7b}$$

$$\mathbf{S}_s = \frac{1}{2}Re\{\mathbf{E}_s \times \mathbf{H}_s^*\} \tag{3.7c}$$

$$\mathbf{S}_{ext} = \frac{1}{2}Re\{\mathbf{E}_i \times \mathbf{H}_s^* + \mathbf{E}_s \times \mathbf{H}_i^*\} \tag{3.7d}$$

Considering a non-absorbing material, if a detector is placed sufficiently far from the scattering particle and the detector's surface area ΔA is sufficiently small, $\mathbf{S}_s$ does not vary greatly. The detector only measures light from the scattered field provided it is not aiming at the source of the incident field. Therefore, substituting Equation (3.5) in to Equation (3.7) we get:

$$\mathbf{S}_s \cdot \hat{\mathbf{e}}_r \Delta A = \frac{k}{2\omega\mu} \frac{|\mathbf{A}|^2}{k^2} \Delta\Omega \tag{3.8}$$

Where $\Delta\Omega = \Delta A / r^2$ which is the solid angle subtended by the detector. If we place polarising lenses between the particle and the detector and record the measured irradiances, we can obtain the Stokes parameters of light scattered by the particle. They are:

$$I_s = \left\langle E_{\|s} E^*_{\|s} + E_{\perp s} E^*_{\perp s} \right\rangle \tag{3.9a}$$
$$Q_s = \left\langle E_{\|s} E^*_{\|s} - E_{\perp s} E^*_{\perp s} \right\rangle \tag{3.9b}$$
$$U_s = \left\langle E_{\|s} E^*_{\perp s} + E_{\perp s} E^*_{\|\|s} \right\rangle \tag{3.9c}$$
$$V_s = i \left\langle E_{\|s} E^*_{\perp s} - E_{\perp s} E^*_{\|\|s} \right\rangle \tag{3.9d}$$

The relationship between the scattering matrix and the Stokes parameters in matrix form is:

$$\begin{pmatrix} I_s \\ Q_s \\ U_s \\ V_s \end{pmatrix} = \frac{1}{k^2 r^2} \begin{pmatrix} S_{11} & S_{12} & S_{13} & S_{14} \\ S_{21} & S_{22} & S_{23} & S_{24} \\ S_{31} & S_{32} & S_{33} & S_{34} \\ S_{41} & S_{42} & S_{43} & S_{44} \end{pmatrix} \begin{pmatrix} I_i \\ Q_i \\ U_i \\ V_i \end{pmatrix} \tag{3.10}$$

This 4×4 matrix is the Mueller matrix and describes the scattering of light by a single particle. The Stokes parameters of randomly separated and oriented particles is the sum of the individual particles. The Mueller matrix describes the scattering event of an incident wave and the polarisation of the scattered light.

$$\frac{I_s}{I_i} = S_{11}, \quad \frac{Q_s}{I_i} = S_{21}, \quad \frac{U_s}{I_i} = S_{31}, \quad \frac{V_s}{I_i} = S_{41} \tag{3.11}$$

Because the scattered light is a function of ϕ the scattering angle, so is the degree of polarisation of the scattered field.

Scattering, Absorption and Extinction

If a finite volume of particles is illuminated by a beam of light, the rate at which the energy enters the volume is denoted by U_0 and the rate at which it enters a detector is

denoted by U. If $U_0 > U$ the volume has resulted in an extinction of the incident beam. If the volume surrounding the particles is non-absorbing, the unaccounted for energy is due to either scattering by the particles or by absorption of the particles. In the case of absorption, the light energy is transformed into other forms of energy. In the case of scattering, the extinction is dependent on the chemical composition of the particles, their size, shape, orientation, the surrounding medium, the number of particles and the polarisation state and frequency of the incident beam (Bohren and Huffman, 1983).

Considering a single particle illuminated by a plane wave; the net rate at which energy enters an imaginary unit sphere of radius r around the particle; then the net rate at which the wave enters the sphere of surface area A is:

$$W_a = -\oint \mathbf{S} \cdot \hat{\mathbf{e}}_r \, dA$$

Using the Poynting vector relationship shown in Equations (3.7).

$$W_a = W_i - W_s + W_{ext}$$

Where:

$$W_i = -\oint \mathbf{S}_i \cdot \hat{\mathbf{e}}_r \, dA, \quad W_s = -\oint \mathbf{S}_s \cdot \hat{\mathbf{e}}_r \, dA, \quad W_{ext} = -\oint \mathbf{S}_{ext} \cdot \hat{\mathbf{e}}_r \, dA \tag{3.12}$$

W_i vanishes for any non-absorbing medium: W_s is the rate at which energy is scattered across the surface of the imaginary sphere. Therefore, W_{ext} is the sum of the energy absorption rate and the energy scattering rate:

$$W_{ext} = W_a + W_s \tag{3.13}$$

Taking the incident electric field to be polarised along the x-axis $E_i = E\hat{\mathbf{e}}_x$ and choosing a distance from the particle r such that the distance is considered to be in the far-field region, the scattered electric field is:

$$E_s \approx \frac{e^{ik(r-z)}}{-ikr}\mathbf{X}E, \quad H_s \approx \frac{k}{\omega\mu}\hat{\mathbf{e}}_r \times \mathbf{E}_s \tag{3.14}$$

Where $\mathbf{X}$ is related to the scattering elements by:

$$\mathbf{X} = (S_2 \cos\phi + S_3 \sin\phi)\hat{\mathbf{e}}_{||s} + (S_4 \cos\phi + S_1 \sin\phi)\hat{\mathbf{e}}_{\perp s} \tag{3.15}$$

And, after a considerable amount of algebraic manipulation (Bohren and Huffman, 1983), the cross-section is obtained, which is the ratio of the net energy rate to the incident energy, and has the dimensions of area:

$$W_{ext} = I_i \frac{4\pi}{k^2} Re\{(\mathbf{X} \cdot \hat{\mathbf{e}}_x)_{\theta=0}\}$$

$$C_{ext} = \frac{W_{ext}}{I_i} = \frac{4\pi}{k^2} Re\{(\mathbf{X} \cdot \hat{\mathbf{e}}_x)_{\theta=0}\} \tag{3.16}$$

And following on from Equation (3.13) the extinction cross-section may be written as the sum of the absorption cross-section C_{abs} and the scattering cross-section C_{sca}

$$C_{ext} = C_{abs} + C_{sca} \tag{3.17}$$

Substituting:

$$C_{abs} = \frac{W_{abs}}{I_i} \quad C_{sca} = \frac{W_{sca}}{I_i}$$

We end with:

$$C_{sca} = \int_0^{2\pi} \int_0^{\pi} \frac{|\mathbf{X}|^2}{k^2} \sin\theta \, d\theta \, d\phi = \int_{4\pi} \frac{|\mathbf{X}|^2}{k^2} \, d\Omega \tag{3.18}$$

Finally making $\frac{|\mathbf{X}|^2}{k^2 C_{sca}} = p$ and substitute, the solution is the definition of the phase function:

$$\int_{4\pi} = p\, d\Omega = 1 \tag{3.19}$$

Which describes the normalised distribution of scattered light over a unit sphere.

3.1.3 Mie Theory

Mie theory is an analytical solution to Maxwell's equations that describes scattering from homogeneous spheres that are much larger than the wavelength of the scattered light. A full derivation of Mie theory is exhaustive and shown in Bohren and Huffman (1983). A summarised version is presented here as Mie theory will be used to compare and check results from the numerical solution to FDTD.

Solution to scattering of spheres

The analytical solution to Mie scattering begins with time-harmonic Maxwell's equations shown in Equation (3.3). That is to say that the electromagnetic field in a linear, isotropic, homogeneous medium must satisfy the wave equation:

$$\nabla^2\mathbf{E} + k^2\mathbf{E} = 0, \quad \nabla^2\mathbf{H} + k^2\mathbf{H} = 0$$

Where $k^2 = \omega^2\epsilon\mu$

And remembering:

$$\nabla \cdot \mathbf{E} = 0, \quad \nabla \cdot \mathbf{H} = 0$$

And that $\mathbf{E}$ and $\mathbf{H}$ are not independent:

$$\nabla \times \mathbf{E} = i\omega\mu\mathbf{H}, \quad \nabla \times \mathbf{H} = -i\omega\epsilon\mathbf{E}$$

Given the scalar function ψ and an arbitrary constant vector $\mathbf{c}$, we construct a vector function $\mathbf{M}$

$$\mathbf{M} = \nabla \times (\mathbf{c}\psi)$$

The divergence of the curl of any vector function vanishes:

$$\nabla \cdot \mathbf{M} = 0$$

Using the vector identities:

$$\nabla \times (\mathbf{A} \times \mathbf{B}) = \mathbf{A}(\nabla \cdot \mathbf{B}) - \mathbf{B}(\nabla \cdot \mathbf{A}) + (\mathbf{B} \cdot \nabla)\mathbf{A} - (\mathbf{A} \cdot \nabla)\mathbf{B}$$
$$\nabla(\mathbf{A} \cdot \mathbf{B}) = \mathbf{A} \times (\nabla) \times \mathbf{B}) + \mathbf{B} \times (\nabla \times \mathbf{A}) + (\mathbf{B} \cdot \nabla)\mathbf{A} + (\mathbf{A} \cdot \nabla)\mathbf{B}$$

We obtain:

$$\nabla^2\mathbf{M} + k^2\mathbf{M} = \nabla \times \left[c\left(\nabla^2\psi + k^2\psi\right)\right] \tag{3.20}$$

Therefore, $\mathbf{M}$ satisfies the vector wave equation if ψ is a solution to the scalar wave equation:

$$\nabla^2\psi + k^2\psi = 0$$

If we take:

$$\mathbf{N} = \frac{\nabla \times \mathbf{M}}{k}$$

With zero divergence:

$$\nabla^2\mathbf{N} + k^2\mathbf{N} = 0$$

And:

$$\nabla \times \mathbf{N} = k\mathbf{M}$$

The purpose of the derivation so far is to show that it is possible to construct two equations that satisfy the required properties of the electromagnetic field. Therefore, the solution scheme becomes the simpler problem of finding solutions to the scalar function ψ. As we are looking to solve the problem of scattering by a sphere, it is convenient to choose a function ψ that satisfies the wave equation in spherical polar coordinates. Therefore, it makes sense to choose a constant vector $\mathbf{c}$ to be the radius vector $\mathbf{r}$:

$$\mathbf{M} = \nabla \times (\mathbf{r}\psi) \tag{3.21}$$

$\mathbf{M}$ is a solution to the vector wave equation in spherical polar coordinates. The scalar wave equation in spherical polar coordinates is:

$$\frac{1}{r^2}\frac{\partial}{\partial r}\left(r^2\frac{\partial\psi}{\partial r}\right) + \frac{1}{r^2\sin\theta}\frac{\partial}{\partial\theta}\left(\sin\theta\frac{\partial\psi}{\partial\theta}\right) + \frac{1}{r^2\sin\theta}\frac{\partial^2\psi}{\partial\phi^2} + k^2\psi = 0 \tag{3.22}$$

Using the method of separation of variables to see the particular solutions to Equation (3.22) of the form:

$$\psi(r,\theta,\phi) = R(r)\Theta(\theta)\Phi(\phi)$$

When substituted into Equation (3.22) this yields the three separated equations:

$$\frac{d^2\Phi}{d\phi^2} + m^2\Phi = 0 \tag{3.23a}$$

$$\frac{1}{\sin\theta}\frac{d}{d\theta}\left(\sin\theta\frac{d\Theta}{d\theta}\right) + \left[n(n+1) - \frac{m^2}{\sin^2\theta}\right]\Theta = 0 \tag{3.23b}$$

$$\frac{d}{dr}\left(r^2\frac{dR}{dr}\right) + \left[k^2r^2 - n(n+1)\right]R = 0 \tag{3.23c}$$

The separation constants m and n are determine by the subsidiary conditions that ϕ must satisfy. The linearly independent solutions to the first equation for a given m and Φ_m are:

$$\Phi_e = \cos m\phi \quad \phi_o = \sin m\phi \tag{3.24}$$

Where the subscripts e and o denote even and odd.

The solutions to the second equation that are finite at $\theta = 0$ and $\theta = \phi$ are the associated **Legendre functions** of the first kind, $P_n^m(\cos\theta)$, of degree n and order m, where $n = m, m+1, ...$

$$\int_{-1}^{1} P_n^m(\mu) P_{n'}^m(\mu) d\mu = \delta_{n'n} \frac{2}{2n+1} \frac{(n+m)!}{(n-1)!} \tag{3.25}$$

The linearly independent solutions are the **spherical Bessel functions** (j_n, y_n). As linear combinations of j_n and y_n, the **spherical Hankel** (h_m) functions, are also solutions to the third equation.

Spherical Bessel functions of the first and second kind are:

$$j_n(\rho) = \sqrt{\frac{\pi}{2\rho}} J_{n+\frac{1}{2}}(\rho) \tag{3.26a}$$

$$y_n(\rho) = \sqrt{\frac{\pi}{2\rho}} Y_{n+\frac{1}{2}}(\rho) \tag{3.26b}$$

The solution to the third equation in Equations (3.23) is any linear combination of spherical Bessel functions. Two combinations of linearly independent Bessel functions of the third kind are the spherical Hankel functions.

Spherical Hankel functions are:

$$h_n^{(0)}(\rho) = j_n(\rho) + i y_n(\rho) \tag{3.27a}$$

$$h_n^{(2)}(\rho) = j_n(\rho) - i y_n(\rho) \tag{3.27b}$$

Now we have a series expansion functions that satisfy the scalar wave equation in spherical polar coordinates:

$$\psi_{emn} - \cos m\psi P_n^m z_n, \quad \psi_{emn} - \sin m\psi P_n^m z_n$$

Where z_n is any of the four Bessel functions

The vector spherical harmonics generated by ϕ_{emn} and ϕ_{omn} are:

$$\begin{aligned}
\mathbf{M}_{emn} &= \nabla \times (\mathbf{r}\psi_{emn}) \\
\mathbf{M}_{omn} &= \nabla \times (\mathbf{r}\psi_{omn}) \\
\mathbf{N}_{emn} &= \frac{\nabla \times \mathbf{M}_{emn}}{k} \\
\mathbf{N}_{omn} &= \frac{\nabla \times \mathbf{M}_{omn}}{k}
\end{aligned}$$

Defining two angle-dependent functions:

$$\pi_n = \frac{P_n^1}{sin\theta}, \quad \tau_n = \frac{dP_n^1}{d\theta}$$

It is possible to write the vector spherical harmonics in component form, where $m = 1$:

$$\begin{aligned}
\mathbf{M}_{o1n} &= \cos\phi\pi_n(\cos\theta)z_n(\rho)\hat{\mathbf{e}}_\theta - \sin\phi\tau_n(\cos\theta)z_n(\rho)\hat{\mathbf{e}}_\phi \\
\mathbf{M}_{e1n} &= -\cos\phi\pi_n(\cos\theta)z_n(\rho)\hat{\mathbf{e}}_\theta - \cos\phi\tau_n(\cos\theta)z_n(\rho)\hat{\mathbf{e}}_\phi
\end{aligned}$$

$$\begin{aligned}
\mathbf{N}_{o1n} = \sin\theta n(n+1)\sin\theta\pi_n(\cos\theta)\frac{z_n(\rho)}{\rho}\hat{\mathbf{e}}_r + \sin\phi\tau_n(\cos\theta)\frac{[\rho z_n(\rho)]'}{\rho}\hat{\mathbf{e}}_\theta \\
+ \cos\phi\pi_n(\cos\theta)\frac{[\rho z_n(\rho)]'}{\rho}\hat{\mathbf{e}}_\phi \\
\mathbf{N}_{eln} = \cos\theta n(n+1)\sin\theta\pi_n(\cos\theta)\frac{z_n(\rho)}{\rho}\hat{\mathbf{e}}_r + \cos\phi\tau_n(\cos\theta)\frac{[\rho z_n(\rho)]'}{\rho}\hat{\mathbf{e}}_\theta \\
+ \sin\phi\pi_n(\cos\theta)\frac{[\rho z_n(\rho)]'}{\rho}\hat{\mathbf{e}}_\phi
\end{aligned}$$

Expansion of a plane wave in vector spherical harmonics

Considering the scattering of a plane x-polarised wave in spherical polar coordinates, the incident field is given by the equation:

$$\mathbf{E}_i = E_0 e^{ikr\cos\theta}\hat{\mathbf{e}}_x \tag{3.28}$$

Where:

$$\hat{\mathbf{e}}_x = \sin\theta\cos\phi\hat{\mathbf{e}}_r + \cos\theta\cos\phi\hat{\mathbf{e}}_\theta - sin\phi\hat{\mathbf{e}}_\phi \tag{3.29}$$

We expand Equation 3.28 in vector spherical harmonics:

$$\mathbf{E}_i = \sum_{m=0}^{\infty}\sum_{n=m}^{\infty}\left(B_{emn}\mathbf{M}_{emn} + B_{omn}\mathbf{M}_{omn} + A_{emn}\mathbf{N}_{emn} + A_{omn}\mathbf{N}_{omn}\right) \tag{3.30}$$

Where $A_{emn}, A_{omn}, B_{emn}$ and B_{omn} are the expressions describing the expansion coefficients required. With considerable mathematical manipulation shown in (Bohren and Huffman, 1983, 90–93) the expansion of the incident electric field vector as a plane wave in vector spherical harmonics is:

$$\mathbf{E}_i = E_0\sum_{n=1}^{\infty} i^n\frac{2n+1}{n(n+1)}\left(\mathbf{M}_{o1n}^{(1)} - i\mathbf{N}_{e1n}^{(1)}\right) \tag{3.31}$$

The corresponding incident magnetic field is obtained by taking the curl of Equation (3.31).

$$\mathbf{H}_i = \frac{-k}{\omega\mu}E_0\sum_{n=1}^{\infty} i^n\frac{2n+1}{n(n+1)}\left(\mathbf{M}_{e1n}^{(1)} - i\mathbf{N}_{o1n}^{(1)}\right) \tag{3.32}$$

It is possible to span the scattered electromagnetic field $\mathbf{E}_s, \mathbf{H}_s$ and the field inside the particle $\mathbf{E}_1, \mathbf{H}_1$ by imposing the boundary conditions:

$$(\mathbf{E}_i + \mathbf{E}_s - \mathbf{E}_1)\times\hat{\mathbf{e}}_r = (\mathbf{H}_i + \mathbf{H}_s - \mathbf{H}_1)\times\hat{\mathbf{e}}_r = 0 \tag{3.33}$$

Inside the particle:

$$\mathbf{E}_1 = \sum_{n=1}^{\infty} E_n \left(c_n \mathbf{M}_{o1n}^1 - i d_n \mathbf{N}_{e1n}^{(1)} \right) \tag{3.34}$$

$$\mathbf{H}_1 = \frac{-k_1}{\omega \mu_1} \sum_{n=1}^{\infty} E_n \left(d_n \mathbf{M}_{e1n}^1 - i c_n \mathbf{N}_{o1n}^{(1)} \right) \tag{3.35}$$

Where:

$$E_n = i^n E_o \frac{2n+1}{n(n+1)}$$

And μ_1 is the permeability of the sphere. Again, rigorous mathematical manipulation (Bohren and Huffman, 1983) shows the expansion of the scattered field is:

$$\mathbf{E}_s = \sum_{n=1}^{\infty} E_n \left(i a_n \mathbf{N}_{e1n}^{(3)} - b_n \mathbf{M}_{o1n}^{(3)} \right) \tag{3.36}$$

$$\mathbf{H}_s = \frac{k}{\omega \mu} \sum_{n=1}^{\infty} E_n \left(i b_n \mathbf{N}_{o1n}^{(3)} + a_n \mathbf{M}_{e1n}^{(3)} \right) \tag{3.37}$$

3.1.4 Finite-Difference Time-Domain (FDTD)

In the following section, it will be shown, that by defining a source electric field at time=0 it is possible to calculate the magnetic field everywhere in the lattice from the electric field at time step $n+1 = \Delta t$. Calculating the electric field at time $n+2$ is then possible from the resultant magnetic field and so on over subsequent iterations. The algorithm is repeated until a steady state solution is reached. The scattered field is then calculated using a near-to-far-field transformation.

The FDTD technique can be used for any shaped scattering particle. This, potentially, makes it particularly useful for finding phase functions of hydrosols such as phytoplankton cells that are highly non-spherical. However, the FDTD is a numerical technique and there is always a computational error due to discretising the computational domain. It is important to define the computational domain with sufficiently small quantisation to produce an error that falls within acceptable tolerance. This may, however, require large amounts of computing resources; in particular, computer memory.

Derivation of the FDTD Equations

The first step in the FDTD method is to convert the vector form of Ampère's and Faraday's laws into a derivative form by taking the curl of each side of both equations.

Beginning with:

$$\nabla \times \mathbf{E} = -\mu \frac{\mathbf{H}}{\partial t} \quad , \quad \nabla \times \mathbf{H} = \sigma \mathbf{E} + \frac{\partial \mathbf{E}}{\partial t}$$

$$\begin{aligned} \left(\frac{\partial E_z}{\partial y} - \frac{\partial E_y}{\partial z}\right)\hat{\mathbf{x}} - \left(\frac{\partial E_z}{\partial x} - \frac{\partial E_x}{\partial z}\right)\hat{\mathbf{y}} + \left(\frac{\partial E_y}{\partial x} - \frac{\partial E_x}{\partial y}\right)\hat{\mathbf{z}} = \\ -\mu\left[\frac{\partial H_X}{\partial t}\hat{\mathbf{x}} + \frac{\partial H_Y}{\partial t}\hat{\mathbf{y}} + \frac{\partial H_z}{\partial t}\hat{\mathbf{z}}\right] \end{aligned} \tag{3.38}$$

$$\left(\frac{\partial E_z}{\partial y} - \frac{\partial E_y}{\partial z}\right) = -\mu \frac{\partial H_X}{\partial t} \tag{3.39a}$$

$$-\left(\frac{\partial E_z}{\partial x} - \frac{\partial E_x}{\partial z}\right) = -\mu \frac{\partial H_Y}{\partial t} \tag{3.39b}$$

$$\left(\frac{\partial E_y}{\partial x} - \frac{\partial E_x}{\partial y}\right) = -\mu \frac{\partial H_z}{\partial t} \tag{3.39c}$$

And:

$$\begin{aligned} \left(\frac{\partial H_z}{\partial y} - \frac{\partial H_y}{\partial z}\right)\hat{\mathbf{x}} - \left(\frac{\partial H_z}{\partial x} - \frac{\partial H_x}{\partial z}\right)\hat{\mathbf{y}} + \left(\frac{\partial H_y}{\partial x} - \frac{\partial H_x}{\partial y}\right)\hat{\mathbf{z}} = \\ \sigma\left[E_x + E_y + E_z\right] + \epsilon\left[\frac{\sigma E_z}{\partial t}\hat{\mathbf{x}} + \frac{\partial E_y}{\partial t}\hat{\mathbf{y}} + \frac{\partial E_z}{\partial z}\hat{\mathbf{z}}\right] \end{aligned} \tag{3.40}$$

Any solution to the field equation can now be expanded in an infinite series of the above vector harmonic equations.

Discretising the FDTD grid

The next step is to derive the difference equations for both the electric and magnetic field over a finite volume. This is done by defining a unit cube in the (x, y, z) planes and

defining the orthogonal components on the cell.

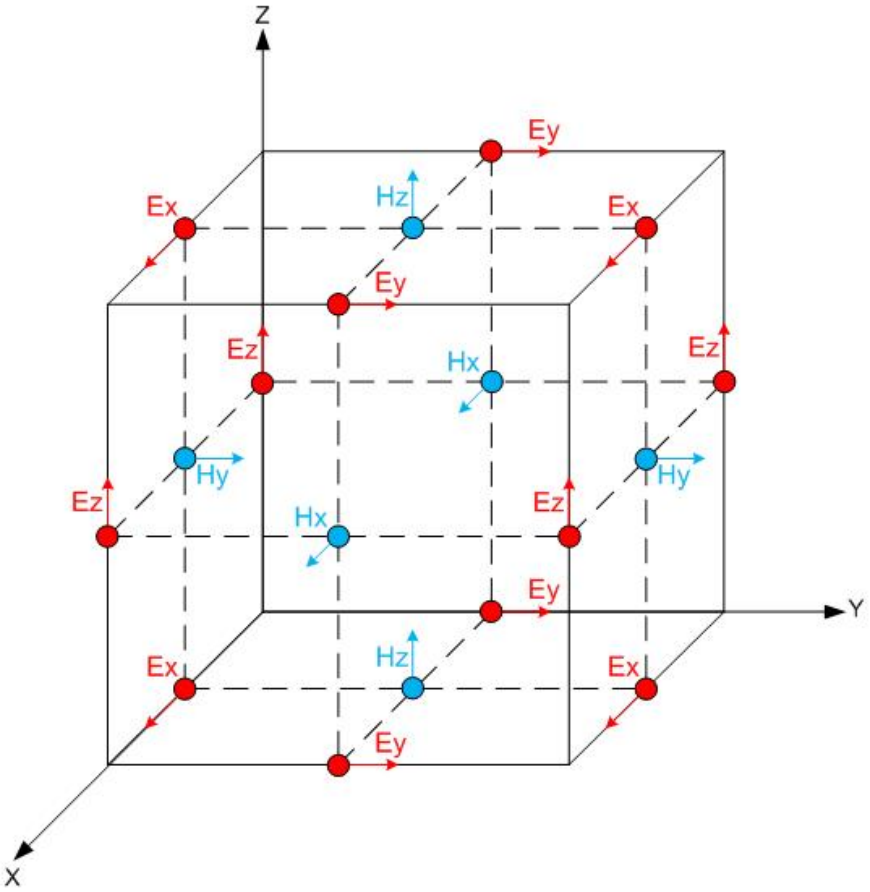

Figure 3.2: Yee cell with the orthogonal electric and magnetic field vectors mapped to its surface.

$$\left[\frac{E^n_{z(i,j+1,k)} - E^n_{z(i,j,k)}}{\Delta y} - \frac{E^n_{y(i,j,k+1)} - E^n_{y(i,j,k)}}{\Delta z}\right] = -\mu_{(i,j,k)}\left[\frac{H^{n+\frac{1}{2}}_{x(i,j,k)} - H^{n-\frac{1}{2}}_{x(i,j,k)}}{\Delta t}\right] \tag{3.41a}$$

$$-\left[\frac{E^n_{z(i+1,j,k)} - E^n_{z(i,j,k)}}{\Delta x} - \frac{E^n_{x(i,j,k+1)} - E^n_{x(i,j,k)}}{\Delta z}\right] = -\mu_{(i,j,k)}\left[\frac{H^{n+\frac{1}{2}}_{y(i,j,k)} - H^{n-\frac{1}{2}}_{y(i,j,k)}}{\Delta t}\right] \tag{3.41b}$$

$$\left[\frac{E^n_{y(i+1,j,k)} - E^n_{y(i,j,k)}}{\Delta x} - \frac{E^n_{x(i,j+1,k)} - E^n_{x(i,j,k)}}{\Delta y}\right] = -\mu_{(i,j,k)}\left[\frac{H^{n+\frac{1}{2}}_{z(i,j,k)} - H^{n-\frac{1}{2}}_{z(i,j,k)}}{\Delta t}\right] \tag{3.41c}$$

Where time $= (n) \times \Delta t$.

$$\left[\frac{H^{n+\frac{1}{2}}_{z(i,j,k)} - H^{n+\frac{1}{2}}_{z(i,j-1,k)}}{\Delta y} - \frac{H^{n+\frac{1}{2}}_{x(i,j,k)} - H^{n+\frac{1}{2}}_{x(i,j,k-1)}}{\Delta z}\right] = \sigma_{(i,j,k)}\left[\frac{E^{n+1}_{x(i,j,k)} - E^n_{x(i,j,k)}}{2}\right] + \epsilon_{(i,j,k)}\left[\frac{E^{n+1}_{x(i,j,k)} - E^n_{x(i,j,k)}}{\Delta t}\right] \tag{3.42a}$$

$$-\left[\frac{H^{n+\frac{1}{2}}_{z(i,j,k)} - H^{n+\frac{1}{2}}_{z(i-1,j,k)}}{\Delta x} - \frac{H^{n+\frac{1}{2}}_{x(i,j,k)} - H^{n+\frac{1}{2}}_{x(i,j,k-1)}}{\Delta z}\right] = \sigma_{(i,j,k)}\left[\frac{E^{n+1}_{y(i,j,k)} - E^n_{y(i,j,k)}}{2}\right] + \epsilon_{(i,j,k)}\left[\frac{E^{n+1}_{y(i,j,k)} - E^n_{y(i,j,k)}}{\Delta t}\right] \tag{3.42b}$$

$$\left[\frac{H^{n+\frac{1}{2}}_{y(i,j,k)} - H^{n+\frac{1}{2}}_{y(i-1,j,k)}}{\Delta x} - \frac{H^{n+\frac{1}{2}}_{x(i,j,k)} - H^{n+\frac{1}{2}}_{x(i,j-1,k)}}{\Delta y}\right] = \sigma_{(i,j,k)}\left[\frac{E^{n+1}_{z(i,j,k)} - E^n_{z(i,j,k)}}{2}\right] + \epsilon_{(i,j,k)}\left[\frac{E^{n+1}_{z(i,j,k)} - E^n_{z(i,j,k)}}{\Delta t}\right] \tag{3.42c}$$

Where time $= (n + \frac{1}{2}) \times \Delta t$.

Solving the FDTD equations is a matter of iteratively walking through the solutions, alternating between the electric field and the magnetic field. Taking the solution of one and passing it on as the initial condition of the next. The many iterations that are required for this method would take a desktop computer's central processing unit (CPU) quite a long time to iterate through. A method and tool (RTCode) for solving this method on a GPU was developed by Hedley (2012) which greatly decreases the time required to converge to a solution. This tool was used to produce the particle scattering results shown in Chapter 5.

3.1.5 FDTD Scattering Modelling of Hydrosols

The reflectance, and reflectance models (HOPE etc.) depend on the IOPs, 'a' and 'b', thus appropriate and accurate models of the 'a' and 'b' processes are important. Investigating and understanding the scattering process of hydrosols of complex shapes is quite challenging. There are well-established models of scattering of relatively simple structures and shapes, some of which are described in this chapter. It was considered whether or not the Swan River had particularly non-spherical particles and if that would greatly affect the reflectance model inversion results. A question still remained whether or not the scattering models could accurately model the scattering despite them being a crude approximation to the shape and structure of typical phytoplankton. An added complication is that the difficulty is, measuring the scattering of particles at all angles is extremely difficult to do accurately. In the field it is difficult to isolate phytoplankton particles from other particles. Making measurements in the laboratory is also quite difficult, especially in the forward scattering angles. This is in part due to many orders of magnitude the scattering energy changes over the forward-facing to back-facing angles. There are both field-based and laboratory specialist equipment that can measure particle scattering, however none could be made available for this project.

The opportunity to investigate a new approach to scattering of hydrosols presented itself through collaboration with Environmental Computing Sciences (ECS). The FDTD method is described in detail in Chapter 2 and the software (RTCode) to execute this method, specifically using GPUs, was made available for this project. The software itself does not model hydrosols but provides tools for modelling the scattering of any abstract shape by defining the lattice structure (Yee cell) in a text file along with the complex refractive index of the scattering lattice layers. Quite some effort was assigned to building scripting tools that could model different shapes with multiple layers that RTCode

could use in scattering calculations. Python scripts were designed to define cell structures in a format that the software tool Gmsh[1] could read. Gmsh was used to visualise and further build Platonic solids, as well as the more complex phytoplankton cell analogues. Further scripts[2] were written to interface with RTCode that made it possible to define the other cell properties, such as size, rotation and refractive index of all the layers, and execute multiple 'batch runs' of the scattering calculations. Furthermore, as the calculations require a very large amount of computer resources, access to the GPU supercomputer Fornax was granted by Pawsey Supercomputing Centre, Perth, Western Australia. Special scripts and compile tools were developed in order for the code to run on the specialist computer and interface correctly with the job scheduler and file system.

The following section presents the preliminary results of building and running the software tools and workflows that enabled the scattering of virtualised phytoplankton cells. The results provide a 'sanity check' to make sure the outputs from RTCode and other software tools developed to work alongside it were sensible. A full description of the phytoplankton modelling, including results of the simulations, is presented in Chapter 5, originally written, submitted and presented as an oral presentation at the international Ocean Optics Conference XXI in Glasgow (Marrable et al., 2012). The first test was designed to test that RTCode could replicate the scattering results for a sphere, as predicted by Mie theory. Other tests were designed to evaluate whether or not non-spherical shapes could be accurately modelled using Mie theory.

[1] `http://gmsh.info/`
[2] `https://code.launchpad.net/dalecppt`

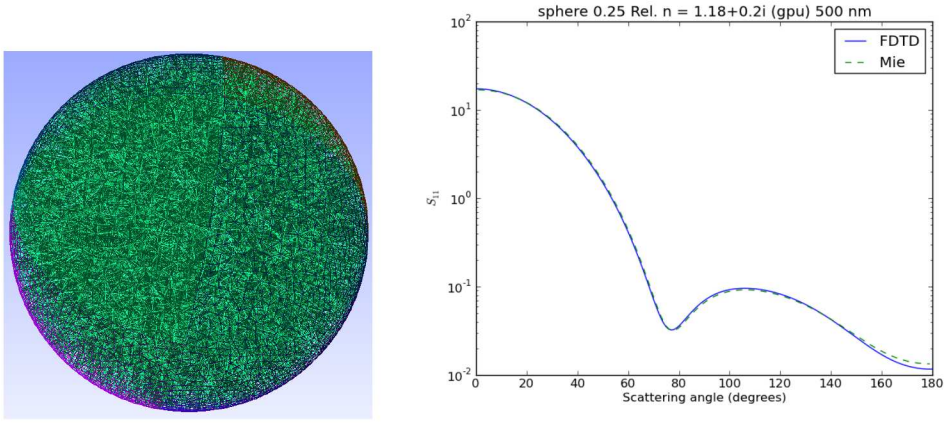

Figure 3.3: (Left) Representation of a spherical particle with uniform refractive index. (Right) Scattering phase functions derived using the FDTD method compared with Mie theory for an equivalent volume sphere for the S_{11} Mueller matrix scattering element. The figure shows that both methods closely agree. The small differences that can be seen in the backscattering are due to the discretisation of the grid to approximate a perfect sphere.

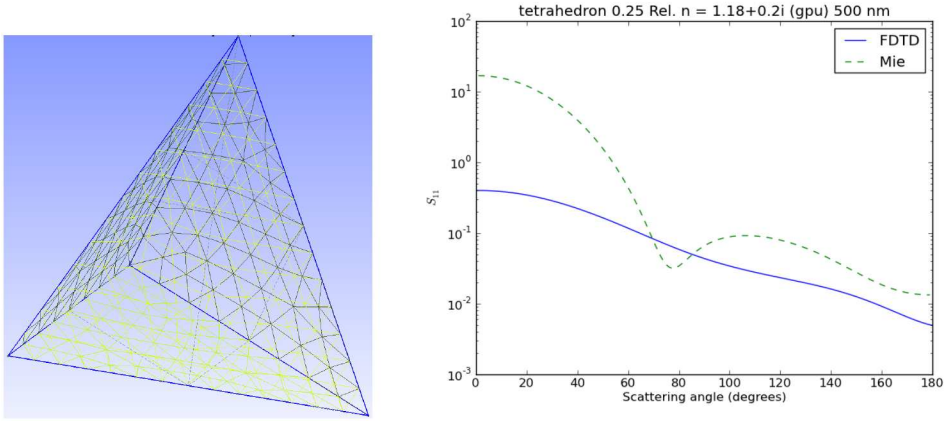

Figure 3.4: (Left) Representation of a tetrahedron shaped particle with uniform refractive index. (Right) Scattering phase functions derived using the FDTD method compared with Mie theory for an equivalent volume sphere for the S_{11} Mueller matrix scattering element for a single scattering angle. The figure shows that both methods do not agree and that Mie theory does not accurately model the scattering of the highly aspherical particle.

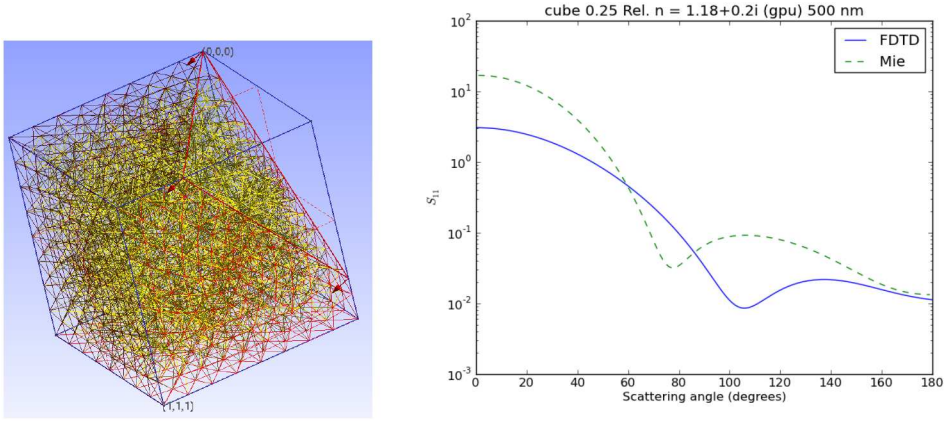

Figure 3.5: (Left) Representation of a cube shaped particle with uniform refractive index. (Right) Scattering phase functions derived using the FDTD method compared with Mie theory for an equivalent volume sphere for the S_{11} Mueller matrix scattering element for a single scattering angle. The figure shows that both methods do not agree and that Mie theory does not accurately model the scattering of the highly aspherical particles.

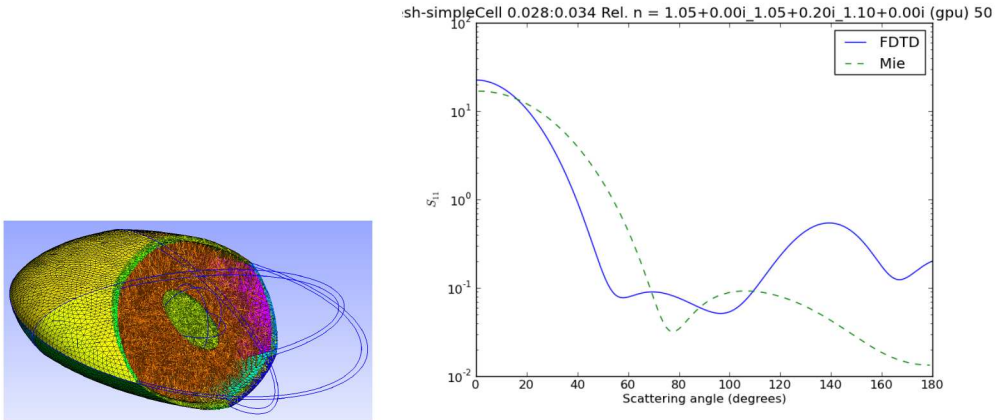

Figure 3.6: (Left) Representation of a multi-layered virtual phytoplankton cell with a cell wall, cytoplasm and nucleus all modelled with different refractive indices. (Right) Scattering phase functions derived the FDTD method with Mie theory for the S_{11} Mueller matrix scattering element for a single scattering angle.

It was expected that Mie theory would produce the same results as FDTD for a spherical particle, regardless of the scattering angle. These were the results produced from RTCode and the other scripting tools and, therefore, gave good indication that the tools were working correctly (Figure 3.3). The non-spherical shapes (figures 3.4, 3.5 and 3.6) showed significant differences between the Mie theory and the FDTD method. This was expected, as Mie theory is an exact solution of electromagnetic scattering for perfect spheres only. It should be noted that calculating the scattering for a single incident angle only is not a reliable method for calculating volume scattering functions for collections of particles compromising of different sizes and shapes. Volume scattering functions for natural water bodies are functions of an ensemble scattering of many particle shapes, sizes and orientations. This is addressed later in this chapter which presents results for simulations run for many size and orientation perturbations, based on cell population size distribution data. At the time of producing the figures presented here, access to enough computing resources to make the repeat measurements was not available. These initial data were used as a proof of concept and contributed to the application for time to run more comprehensive simulations on the Fornax supercomputer at the Pawsey Supercomputing Centre. As noted in an early section, a full description of those simulations is presented in Chapter 5.

3.2 Method

3.2.1 Particle Shape

Ten of the phytoplankton presented in Volten et al. (1998) (Table 3.2) were approximated by three basic shapes: a sphere, a rounded cylinder and a sickle shape. The sphere and the rounded cylinder shapes were modelled programmatically, while the sickle shape was built in the 3D–modelling program Blender[3] and exported in a file format that could be used with the FDTD solver using Gmsh[4].

3.2.2 Phytoplankton Internal Structure

Data on the complex refractive index (RI) of phytoplankton is scarce. Furthermore, data on the refractive index of individual internal structures are extremely difficult to find. Therefore, the approach taken was to assume the refractive index data in Volten et al.

[3]http://www.blender.org
[4]http://geuz.org/gmsh

Table 3.2: Summary of the phytoplankton properties modelled. Reproduced in part from Volten et al. (1998)

Name of Hydrosol	Cell Shape	Structural Features	Cell Radius (μm)	Cell Radius Variance (μm)	Refractive Index
Microcystis aeruginosa	Sphere	No gas vac	5.23	0.500	$1.04 - 0.000i$
Microcystis sp.	Sphere	Gas vac	1.87	0.063	$1.02 - 0.001i$
Prochlorothrix hollandica	Cylinder	Filamentous	1.55	0.080	$1.24 - 0.006i$
Oscillatoria amoena	Cylinder	Filamentous	2.58	0.002	$1.05 - 0.004i$
Oscillatoria agardhii	Cylinder	Filamentous with gas vac	1.64	0.044	$1.05 - 0.000i$
Melosira granulata	Cylinder	Filamentous	3.74	0.004	$1.02 - 0.002i$
Asterionella formosa	Cylinder	Star-shaped col	4.23	0.010	$1.03 - 0.003i$
Selenastrum capricornutum	Sickle		1.09	0.037	$1.24 - 0.020i$
Emiliania huxleyi	Sphere	Calcite mantel	1.90	0.070	$1.04 - 0.000i$
Emiliania huxleyi	Sphere	No calcite mantel	1.80	0.002	$1.04 - 0.042i$

(1998) represented the mean refractive index of the object. A simple two–component model was designed which broke the virtual phytoplankton cell into gas vacuoles and non-gas material. The mean refractive index was reduced to the sum of the two components. The refractive index of gas was assumed to be $1.00 - 000i$. Therefore the non-gas material was calculated using the following simple formula.

$$RI_{non-gas} = \frac{RI - \%ofgas \times 1.00}{\%ofnon - gas} \tag{3.43}$$

Table 3.3: Ratio of gas vacuoles to volume of plankton cell. Reproduced from Smith and Pete (1967)

Name of Hydrosol	Width of Gas Cylinders	Range of Lengths	Mean % Volume	Mean RI	non-gas RI
Oscillatoria agardhii	70mu	100–500	39	$1.05 - 0.000i$	$1.08 - 0.000i$
Microcystis aeruginosa	75mu	100–500	30*	$1.04 - 0.000i$	$1.06 - 0.000i$
Mircrocystis sp.	75mu*	100–500*	30*	$1.02 - 0.000i$	$1.03 - 0.001i$

3.2.3 Model Run

To find the scattering of the distribution of a species, the model was run hundreds of times and the average of all the runs was taken to be the mean scattering of the particle distribution. For each run, a random number was generated from a statistical distribution with a mean value centred around the mean particle size and with a variance that corresponded to the variance of phytoplankton size shown in Table 3.2. This random number was used to build an analogous phytoplankton cell with the size of the randomly generated number and material properties that corresponded with that species RI shown in Table 3.2. Each time a new simulation was executed, the cell was randomly rotated

with respect to the incident light. This process was repeated until the average of all the runs converged to a small tolerance of change. A tolerance was chosen at a compromise between modelling accuracy and the time required to reduce the residual error between the mean value and the subsequent model run. This process was repeated for all of the species presented in Table 3.2 and using the gas vacuoles data presented in Table 3.3 where appropriate.

The integral of the phase function over solid angle should sum to unity. Furthermore, the phase function can be expressed as:

$$p(\theta) = \frac{S_{11}(\theta)}{k^2 \times C_{scat}} \tag{3.44}$$

Where:

$$k = \frac{2\pi}{\lambda} \tag{3.45}$$

And C_{scat} is the scattering cross-section. Therefore, the irradiance scattering was normalised by numerically integrating the over all angles and dividing by the result. For further quality control, the integral was checked to see that it was equal to $k^2 \times C_{scat}$. Volten et al. (1998) scale the scattering curves to match Petzold (1972) phase functions at 90°. In order to be consistent with the definition of the phase function presented in Bohren and Huffman (1983), the empirical results presented in Volten et al. (1998) were rescaled to match FDTD results at 90°.

Every time an FDTD run was executed, a Mie calculation was performed for a sphere of equal volume as the particle that was being modelled – regardless of particle shape. This was done in order to compare the FDTD method to Mie. In order to reduce clutter, only the average of the Mie runs are shown (figures 3.7–3.12).

Volten et al. (1998) results were measured at a wavelength of 633 nm in air and the refractive index of the cells is given relative to water. The FDTD model does not include the air-water interface, therefore, to enable direct comparison of FDTD and Volten et al. (1998) results, the FDTD model wavelength was calculated at 475 nm which is approximately 633 nm divided by the refractive index of water (1.33).

3.3 Results

The following section presents the S_{11} scattering and the $\frac{S_{11}}{S_{12}}$ scattering for all the modelled phytoplanktion species (figures 3.7–3.16). These data are compared to both Mie predicted results and those presented in Volten et al. (1998).

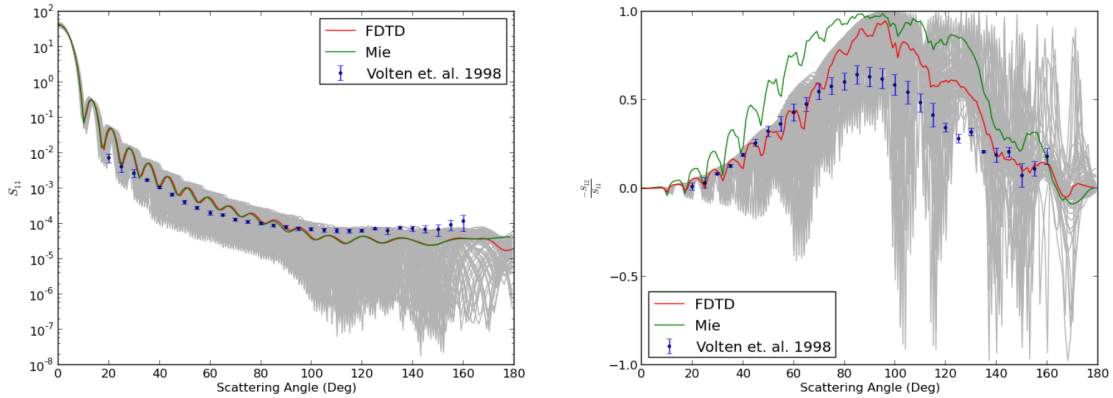

Figure 3.7: (Left) S_{11} and; (right) $\frac{S_{11}}{S_{12}}$ scattering of *Microcystis-aeruginosa*. Grey curves show the scattering for individual runs of FDTD. The red curve is the average of those runs. The green curve shows the Mie scattering for a sphere of equivalent volume to the algal cell. The blue dots show the results presented in Volten et al. (1998).

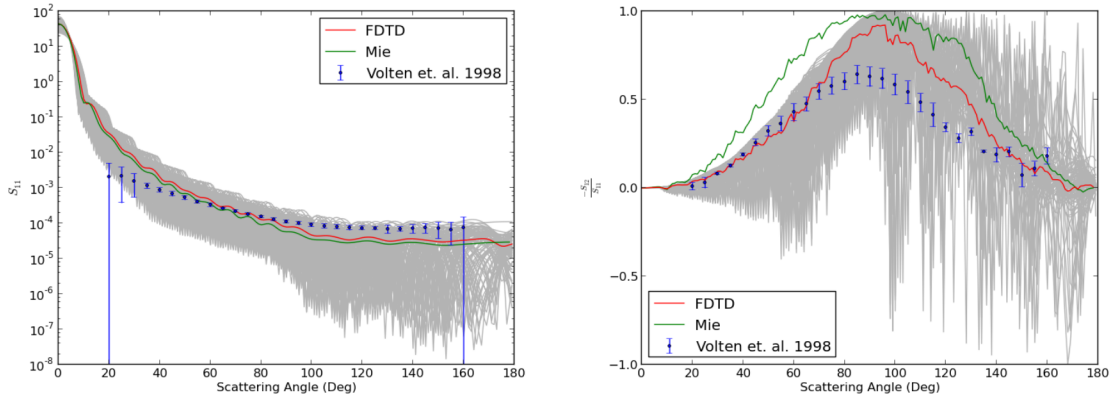

Figure 3.8: (Left) S_{11} and; (right) $\frac{S_{11}}{S_{12}}$ scattering of *Microcystis-sp.* Grey curves show the scattering for individual runs of FDTD. The red curve is the average of those runs. The green curve shows the Mie scattering for a sphere of equivalent volume to the algal cell. The blue dots show the results presented in Volten et al. (1998).

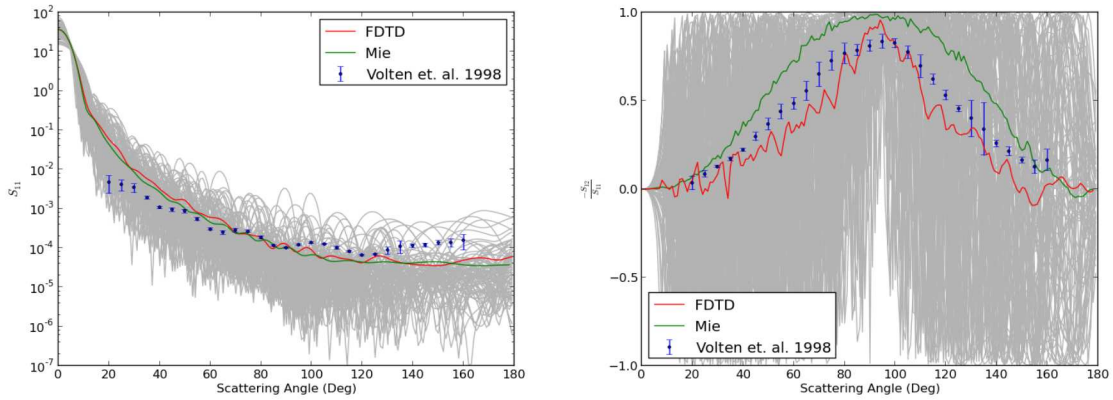

Figure 3.9: (Left) S_{11} and; (right) $\frac{S_{11}}{S_{12}}$ scattering of *Prochlorothrix-hollandica*. Grey curves show the scattering for individual runs of FDTD. The red curve is the average of those runs. The green curve shows the Mie scattering for a sphere of equivalent volume to the algal cell. The blue dots show the results presented in Volten et al. (1998).

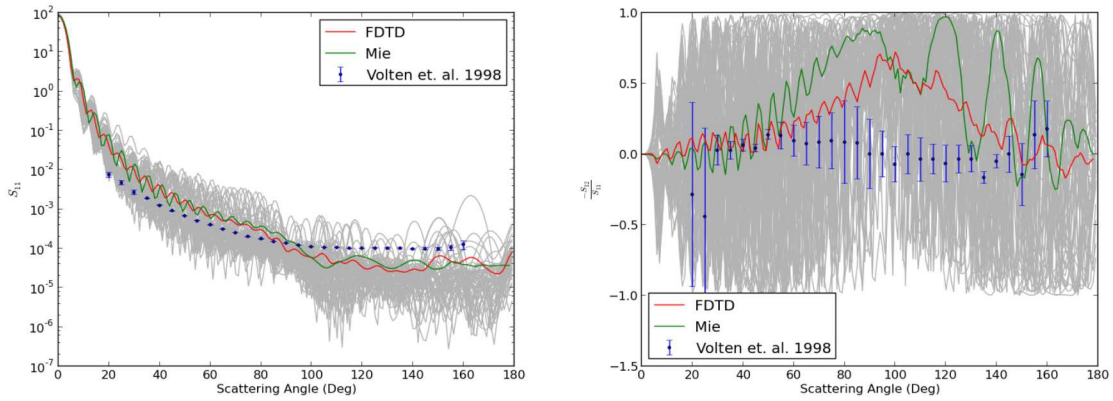

Figure 3.10: (Left) S_{11} and; (right) $\frac{S_{11}}{S_{12}}$ scattering of *Oscillatoria-amoena*. Grey curves show the scattering for individual runs of FDTD. The red curve is the average of those runs. The green curve shows the Mie scattering for a sphere of equivalent volume to the algal cell. The blue dots show the results presented in Volten et al. (1998).

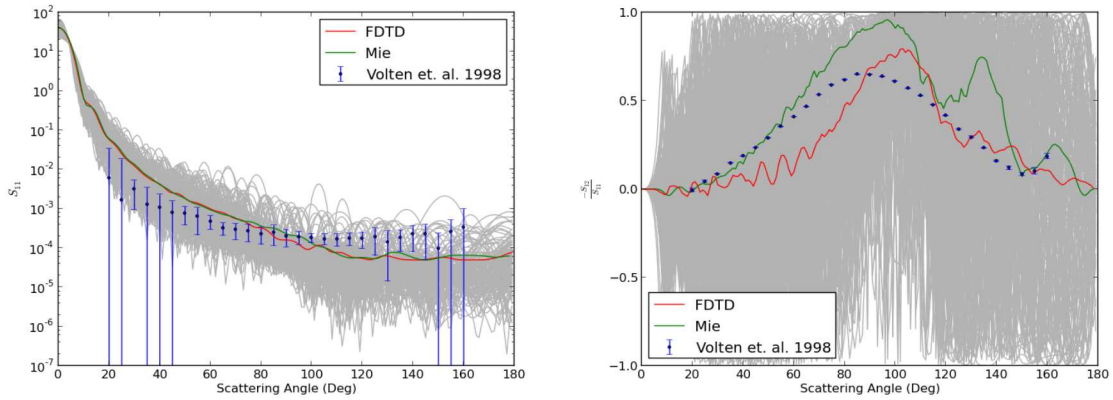

Figure 3.11: (Left) S_{11} and; (right) $\frac{S_{11}}{S_{12}}$ scattering of *Oscillatoria-agarhii*. Grey curves show the scattering for individual runs of FDTD. The red curve is the average of those runs. The green curve shows the Mie scattering for a sphere of equivalent volume to the algal cell. The blue dots show the results presented in Volten et al. (1998).

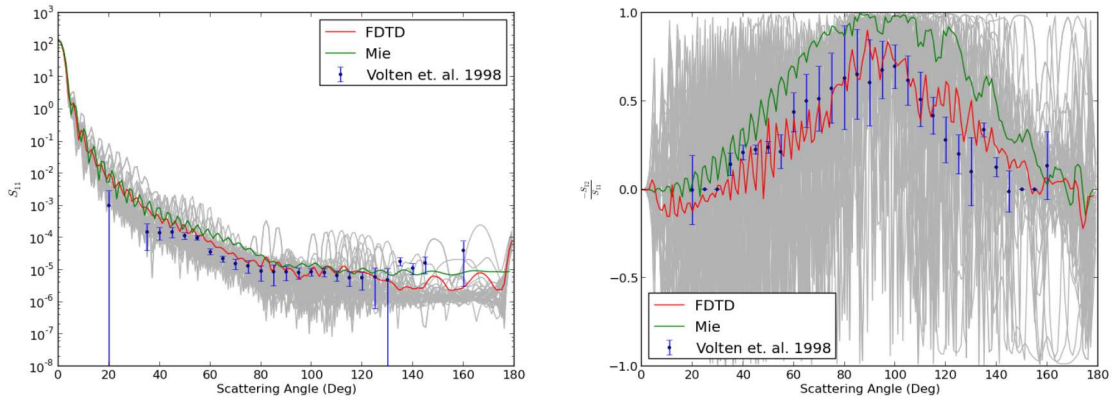

Figure 3.12: (Left) S_{11} and; (right) $\frac{S_{11}}{S_{12}}$ scattering of *Melosira-granulata*. Grey curves show the scattering for individual runs of FDTD. The red curve is the average of those runs. The green curve shows the Mie scattering for a sphere of equivalent volume to the algal cell. The blue dots show the results presented in Volten et al. (1998).

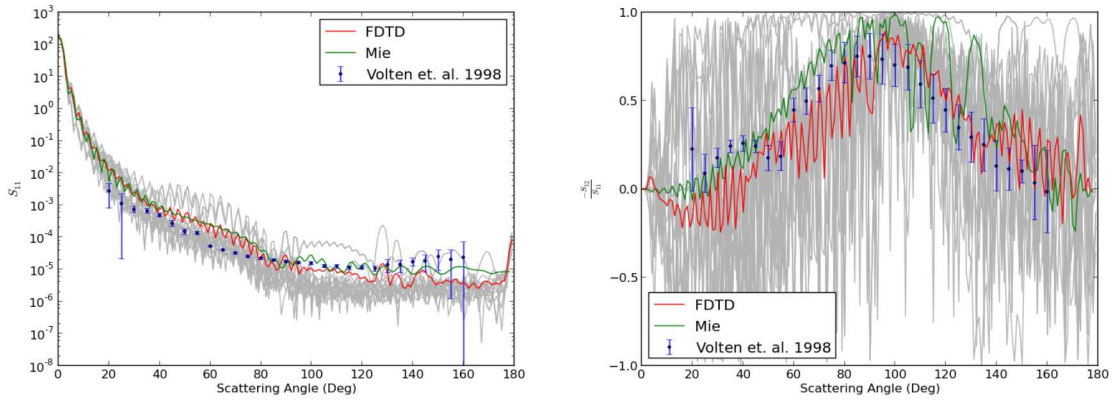

Figure 3.13: (Left) S_{11} and; (right) $\frac{S_{11}}{S_{12}}$ scattering of *Asterionella-formosa*. Grey curves show the scattering for individual runs of FDTD. The red curve is the average of those runs. The green curve shows the Mie scattering for a sphere of equivalent volume to the algal cell. The blue dots show the results presented in Volten et al. (1998).

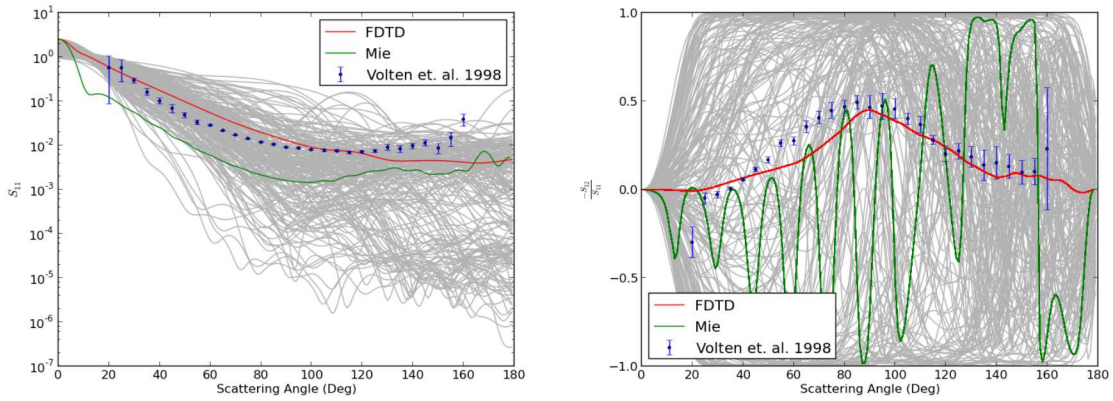

Figure 3.14: (Left) S_{11} and; (right) $\frac{S_{11}}{S_{12}}$ scattering of *Selenastrum-capricornutum*. Grey curves show the scattering for individual runs of FDTD. The red curve is the average of those runs. The green curve shows the Mie scattering for a sphere of equivalent volume to the algal cell. The blue dots show the results presented in Volten et al. (1998).

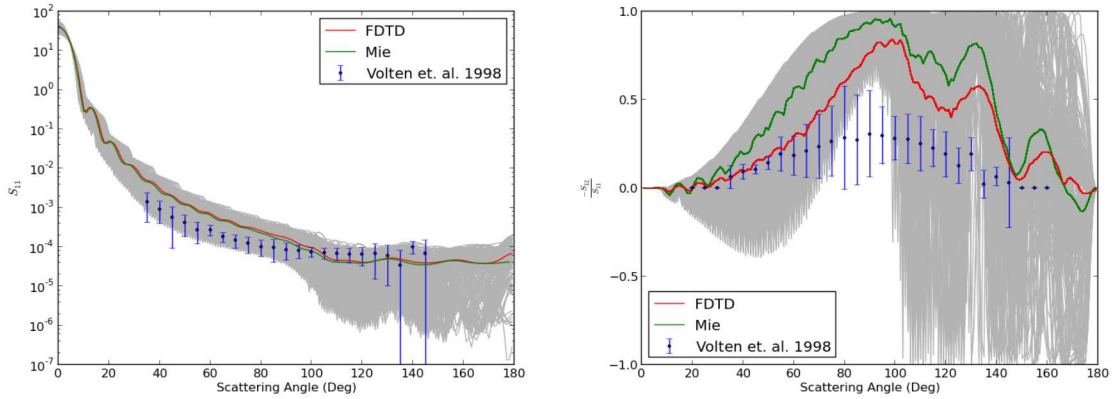

Figure 3.15: (Left) S_{11} and; (right) $\frac{S_{11}}{S_{12}}$ scattering of *Emiliana-huxleyi* without coccospheres. Grey curves show the scattering for individual runs of FDTD. The red curve is the average of those runs. The green curve shows the Mie scattering for a sphere of equivalent volume to the algal cell. The blue dots show the results presented in Volten et al. (1998).

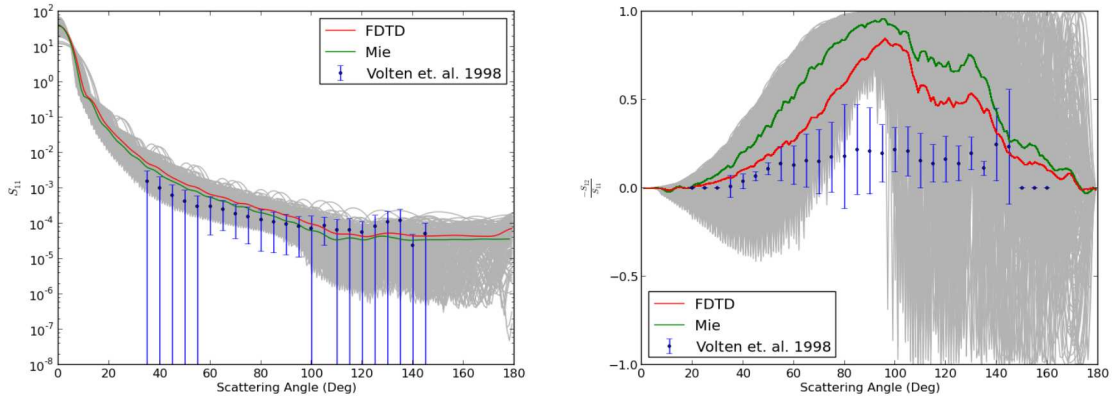

Figure 3.16: (Left) S_{11} and; (right) $\frac{S_{11}}{S_{12}}$ scattering of *Emiliana-huxleyi* with coccospheres. Grey curves show the scattering for individual runs of FDTD. The red curve is the average of those runs. The green curve shows the Mie scattering for a sphere of equivalent volume to the algal cell. The blue dots show the results presented in Volten et al. (1998).

Table 3.4: FDTD and Mie Calculated Scattering Fractions of Hydrosols

Name of Hydrosol	Cell Radius (μm)	Cell Radius Variance (μm)	Refractive Index	Scattering Fraction FDTD	Scattering Fraction Mie
Microcystis aeruginosa	5.23	0.500	$1.04 - 0.000i$	5.026×10^{-5}	4.994×10^{-5}
Microcystis sp.	1.87	0.063	$1.02 - 0.001i$	2.693×10^{-4}	4.977×10^{-4}
Prochlorothrix hollandica	1.55	0.080	$1.24 - 0.006i$	3.834×10^{-4}	4.960×10^{-4}
Oscillatoria amoena	2.58	0.002	$1.05 - 0.004i$	3.473×10^{-4}	4.982×10^{-4}
Oscillatoria agardhii	1.64	0.044	$1.05 - 0.000i$	4.997×10^{-4}	4.996×10^{-4}
Melosira granulata	3.74	0.004	$1.02 - 0.002i$	6.371×10^{-5}	2.660×10^{-4}
Asterionella formosa	4.23	0.010	$1.03 - 0.003i$	7.072×10^{-5}	2.666×10^{-4}
Selenastrum capricornutum	1.09	0.037	$1.24 - 0.020i$	4.164×10^{-4}	5.120×10^{-4}
Emiliania huxleyi	1.90	0.070	$1.04 - 0.000i$	4.429×10^{-4}	5.160×10^{-4}
Emiliania huxleyi	1.80	0.002	$1.04 - 0.042i$	4.164×10^{-4}	5.199×10^{-4}

As the calculated scattering fractions were two to three orders of magnitude smaller than measured by Petzold (1972), an investigation was conducted into what the expected scattering of the particles was predicted by Mie. Moreover, to check that if the very small scattering fractions were due to the size of the particles modelled in this study. For each hyrdrosol in Table 3.4, Mie theory was used to calculate the scattering fraction for a range of particles sizes between 0.02×10^{-6} m and 6.0×10^{-6} m. The scattering fraction averaged over the cell radius variance was also calculated, using FDTD and Mie, for each cell (figures 3.17–3.26).

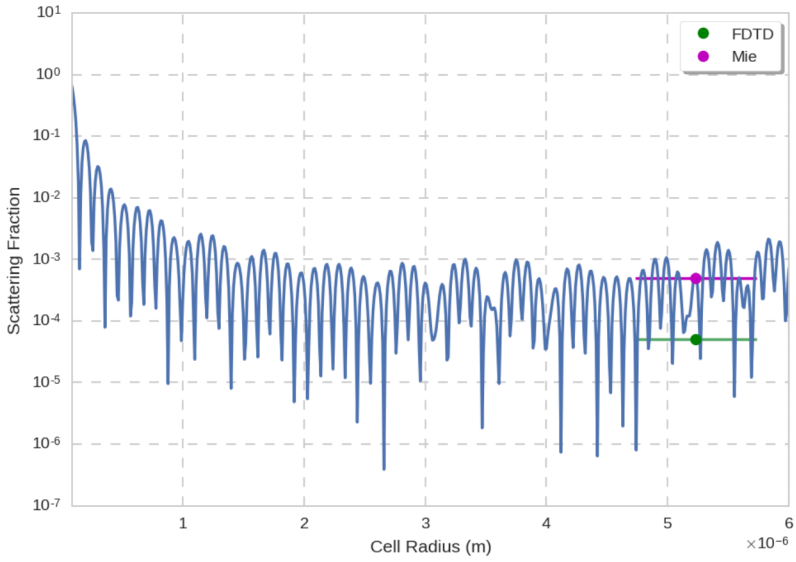

Figure 3.17: The blue line shows the scattering fraction, predicted by Mie, over the range 0.02×10^{-6} m and 6.0×10^{-6} m. The green and magenta marks show the scattering fraction averaged over the cell radius variance for *Microcystis-aeruginosa* calculated using FDTD and Mie respectively.

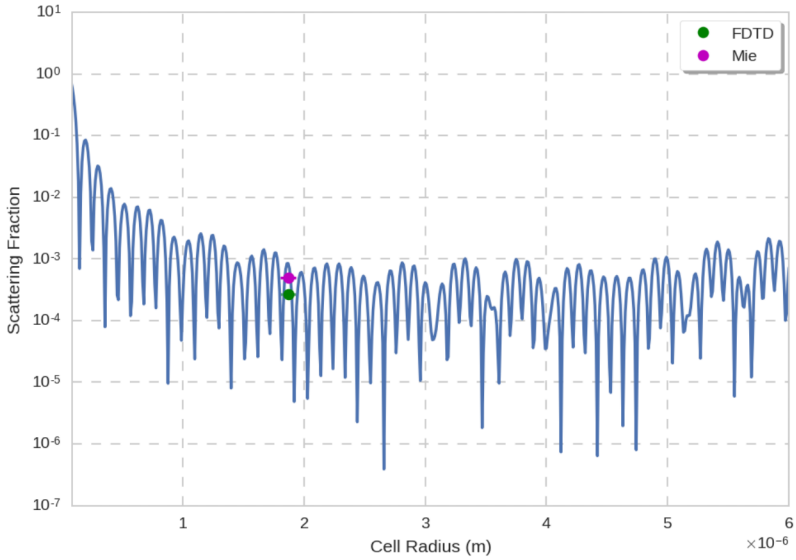

Figure 3.18: The blue line shows the scattering fraction, predicted by Mie, over the range 0.02×10^{-6} m and 6.0×10^{-6} m. The green and magenta marks show the scattering fraction averaged over the cell radius variance for *Microcystis-sp.* calculated using FDTD and Mie respectively.

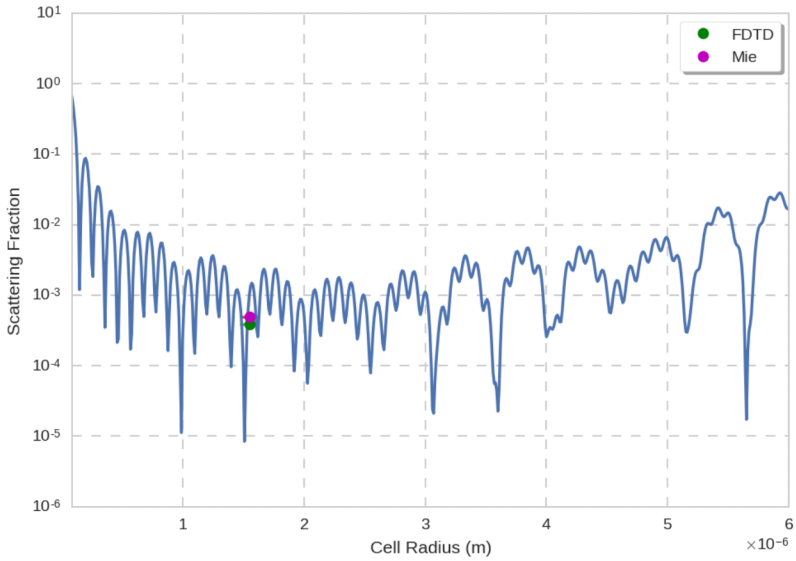

Figure 3.19: The blue line shows the scattering fraction, predicted by Mie, over the range 0.02×10^{-6} m and 6.0×10^{-6} m. The green and magenta marks show the scattering fraction averaged over the cell radius variance for *Prochlorothrix-hollandica* calculated using FDTD and Mie respectively.

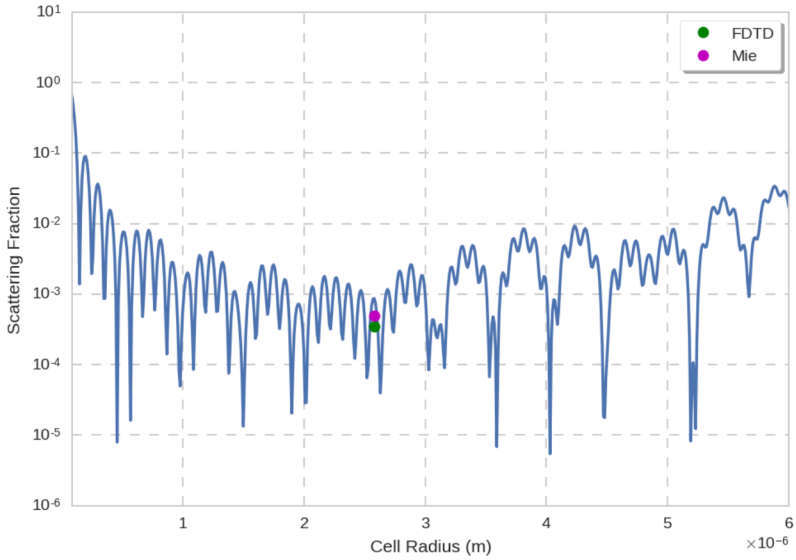

Figure 3.20: The blue line shows the scattering fraction, predicted by Mie, over the range 0.02×10^{-6} m and 6.0×10^{-6} m. The green and magenta marks show the scattering fraction averaged over the cell radius variance for *Oscillatoria-amoena* calculated using FDTD and Mie respectively.

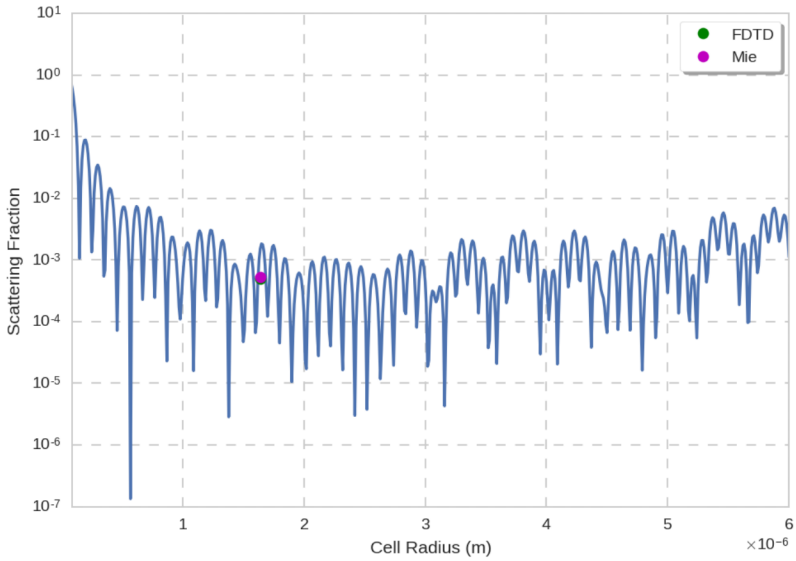

Figure 3.21: The blue line shows the scattering fraction, predicted by Mie, over the range 0.02×10^{-6} m and 6.0×10^{-6} m. The green and magenta marks show the scattering fraction averaged over the cell radius variance for *Oscillatoria-agardhii* calculated using FDTD and Mie respectively.

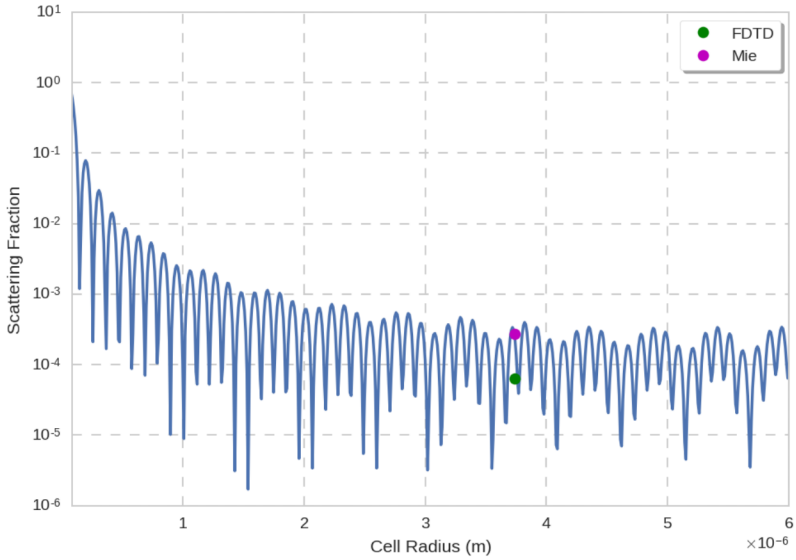

Figure 3.22: The blue line shows the scattering fraction, predicted by Mie, over the range 0.02×10^{-6} m and 6.0×10^{-6} m. The green and magenta marks show the scattering fraction averaged over the cell radius variance for *Melosira-granulata* calculated using FDTD and Mie respectively.

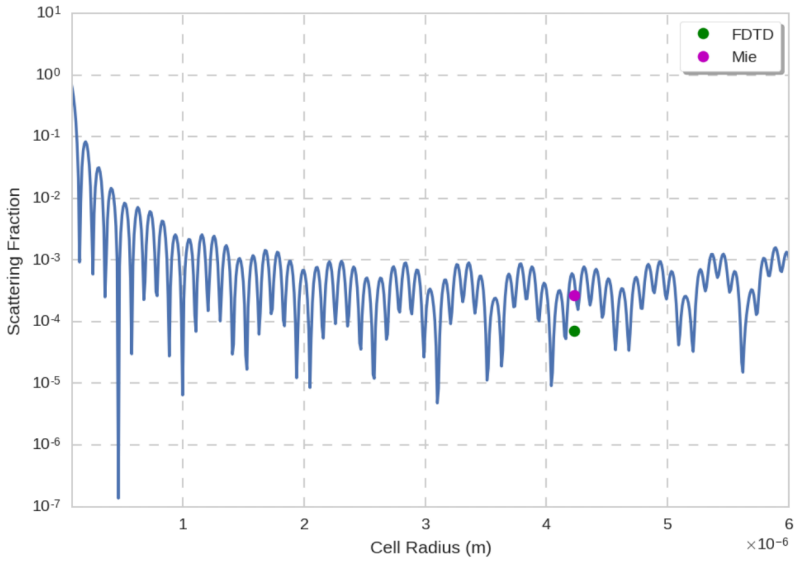

Figure 3.23: The blue line shows the scattering fraction, predicted by Mie, over the range 0.02×10^{-6} m and 6.0×10^{-6} m. The green and magenta marks show the scattering fraction averaged over the cell radius variance for *Asterionella-formosa* calculated using FDTD and Mie respectively.

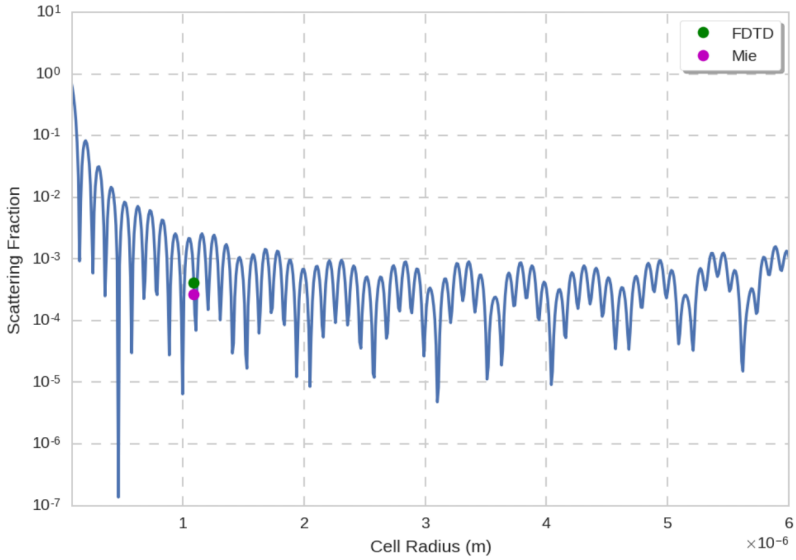

Figure 3.24: The blue line shows the scattering fraction, predicted by Mie, over the range 0.02×10^{-6} m and 6.0×10^{-6} m. The green and magenta marks show the scattering fraction averaged over the cell radius variance for *Selenastrum-capricornutum* calculated using FDTD and Mie respectively.

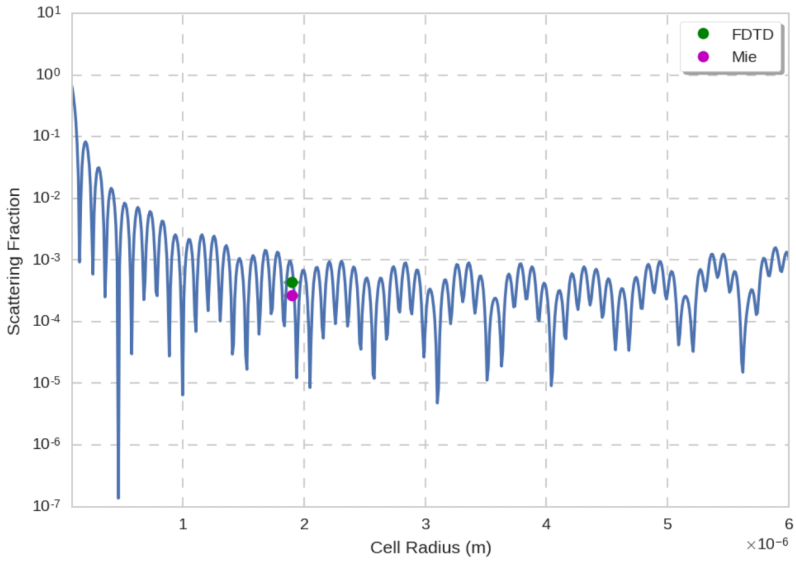

Figure 3.25: The blue line shows the scattering fraction, predicted by Mie, over the range 0.02×10^{-6} m and 6.0×10^{-6} m. The green and magenta marks show the scattering fraction averaged over the cell radius variance for *Emiliania-huxleyi* with calcite, calculated using FDTD and Mie respectively.

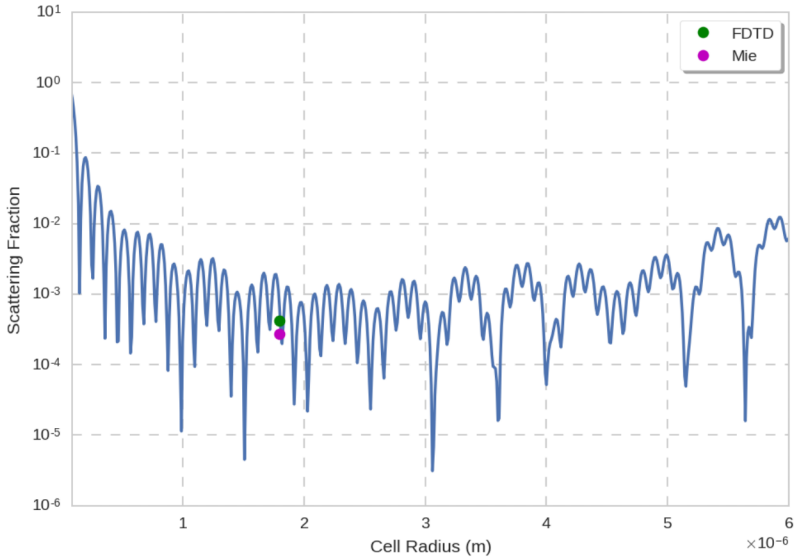

Figure 3.26: The blue line shows the scattering fraction, predicted by Mie, over the range 0.02×10^{-6} m and 6.0×10^{-6} m. The green and magenta marks show the scattering fraction averaged over the cell radius variance for *Emiliania-huxleyi* without calcite, calculated using FDTD and Mie respectively.

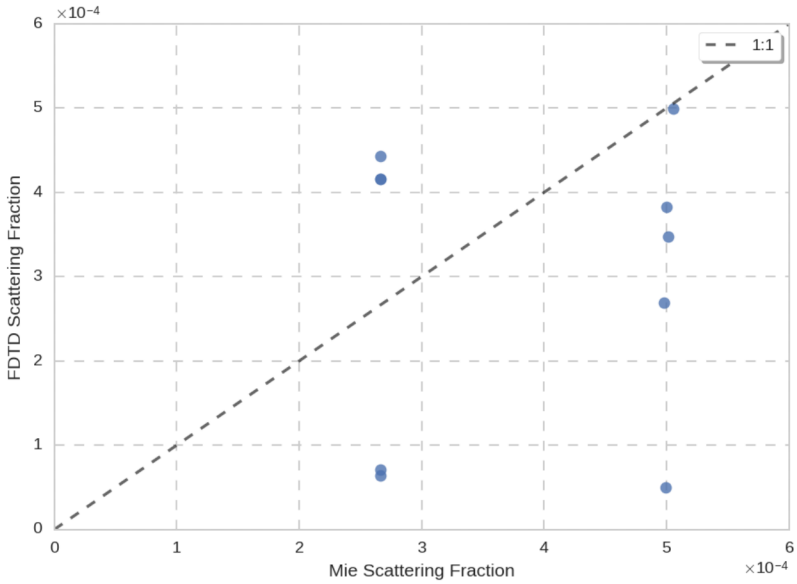

Figure 3.27: The scattering fractions of all the hydrosols in Table 3.2, predicted by FDTD and Mie theories, compared with each other.

Figure 3.27 shows the difference in scattering fraction predicted by both FDTD and Mie

theories. Although there are differences in between the two, they are both many orders of magnitude smaller than Petzold (1972).

3.4 Discussion

Although a single FDTD simulation (grey curves, figures 3.8–3.15), can show a large difference in scattering when compared to what Mie theory predicts, averaging the ensemble simulations together converges the results towards Mie theory calculations. The exception being *Selenastrum capricornutum* Figure 3.14 which is a sickle shaped cell. This suggests that the shapes that differ significantly from spherical shapes may not be as accurately modelled with Mie as with FDTD. Furthermore, Figure 3.14 shows that FDTD results agree more closely with Volten et al. (1998) than Mie. However, when considering the scattering fractions presented in Table 3.4 the scattering fractions of *Selenastrum capriconutum* predicted by both Mie and FDTD agree very closely with each other.

All of the results here show that there is a difference between the modelled scattering (both Mie and FDTD) and the scattering measured by Volten et al. (1998). As expected, the Mie-calculated scattering and the FDTD-modelled scattering agree very well for spherical particles (figures 3.7, 3.8, 3.16 and 3.15), especially in the forward-scattering directions. The greatest differences in the backscattering were in the direction close to 180°.

In the case of rounded cylinders (figures 3.9, 3.10, 3.11, 3.12 and 3.13), there was only a small disagreement between Mie and FDTD results. Both results showed differences between both simulations and Volten et al. (1998).

Possibly the most interesting results are that the FDTD modelled scattering more closely agrees with the experimental results for the highly aspherical sickle-shaped cell, where it was found that there was a larger degree of difference between FDTD and Mie. This seems intuitive, as it is the least spherical of the shapes modelled and Mie is applicable only to spherical scatterers. This may be evidence that FDTD is useful and accurate for modelling shapes that differ greatly from a sphere.

Figures 3.7–3.15 also show the individual FDTD runs (light-grey) for each rotation and random size. It can be clearly seen in all plots that the variance in scattering, related

to the spread in the light grey curves at each scattering angle, is much smaller in the forward-scattering direction. All shapes showed the greatest variance in the backscattering directions, often by a few orders of magnitude.

Differences in backscattering may be for a few different reasons. Due to internal wave reflections at boundaries of discontinuity, such as the edge of the cell boundary, it can take a long time for modelled internal waves to extinguish compared to the time it takes for the waves scattering from the surface of the cell. If insufficient time was given for FDTD to reach a steady state, it is possible that there could be some energy lost after the far-field transformation. The time allocated to the simulation was, in part, limited to the run-times allocated to the project on the supercomputer.

Further differences due to structure may be due to the discretisation of the three-dimensional structure. It is impossible to make a perfectly smooth surfaces using cube voxels. However, this error should be relatively small, as voxel sizes were chosen that are much smaller than the wavelength of interest. A much larger effect is likely present on the rounded cylinder shapes used to model the filamentous algae species. The dimensions of length-to-width ratio of the filamentous species are much greater than it is possible to build on the current generation of graphics cards, due to the limitation of their available memory, related to the number of discrete voxels required.

Another limitation of the models presented here is the ability to accurately model the material properties of the cells. A simple homogeneous or even two-part volume structure is not sufficient enough to represent a single algal cell accurately. It may be the case that a two-part or three-part model may be sufficient for modelling bulk scattering distributions, as differences in different algal cells may average out in phytoplankton communities. More investigation on this is required as it is difficult to find much empirical literature on this topic. The FDTD model has shown to be a useful tool when investigating the differences that shape and material structures can make on scattering; in particular, the forward-to-backscattering ratio. This ratio is used directly in forward-modelling IOPs of water in Hydrolight and PlanarRad.

When considering scattering fractions of different particle sizes, figures 3.17–3.26, with the same refractive indices in Table 3.4, all of the scattering fractions are orders of magnitude lower than particles of much smaller size. Considering the estimated particle scattering fraction from Petzold (1972) measurements is $\sim$0.018, it is likely that the scattering was

due to particles much smaller than those modelled in this chapter. Furthermore, even though there were differences between Mie and FDTD simulations, figures 3.17–3.26 show that the particle size is the most significant factor in calculating the scattering affects.

3.5 Summary

The FDTD model shows differences in the scattering predicted by Mie theory and measured by Volten et al. (1998). FDTD modelling shows that internal structure and material properties affects the scattering phase function. The FDTD method agrees closely with both Mie and laboratory measured scattering in the forward direction of all shapes but may struggle at backscattering directions close to 180°. This is more a limitation of current generation hardware and the ability to accurately model the volume rather than the FDTD calculation itself.

The differences between the FDTD method and Mie theory are small, for equivalent volume particles, when compared to the differences in scattering due to change in size makes. Therefore, Mie theory may be a suitable approximation for estimating the scattering fraction of hydrosols.

Considering that the FDTD results, for the most aspherical particle *Selenastrum capricornutum* (Figure 3.14), agreed more closely than Mie, FDTD shows promise of being a very useful tool for modelling the scattering effects due to different shapes and internal structures. However, further investigation into these differences is required before the FDTD method can be used for modelling the specific scattering effects of shape and internal cell structure of algae. In order to investigate this further, more data on the refractive index of cell structures of different algal cells is required.

Chapter 4

Phytoplankton Culturing and Absorption

4.1 Introduction

Advances in chromatography, and the ability to purify and crystallise chlorophylls (Mackinney, 1941; Zscheile, 1941), has made it possible to rapidly separate and quantitate the many pigments found inside a single species of phytoplankton. This ability has also spawned the field of chemotaxonomy, which has developed the ability to distinguish classes of microalgae.

There are four major and taxonomically significant pigments in phytoplankton divisions: chlorophylls, carotenes, xanthophylls and biliproteins. All contain many subclasses of pigments. In particular, cyanobacteria, such as blue-green algae, is known to contain chlorophyll-a, β-carotene, zeaxanthin, allophycocyanin, phycocyanin and phycoerythin (Cox, 1993), all of which make the identification of cyanobacteria identifiable through high pressure liquid chromatography (HPLC) and, because these pigments are photosynthetic in the visible spectra, they are also detectable through radiometric measurements.

This chapter describes the processing of culturing three different species of algae and measuring their absorption properties. At this time, mono-cultures native to the Swan River were not available. Therefore, cultures with different absorption properties were used to develop algorithms for inverting the optical model as well as developing laboratory techniques. Although the mono-culture results were unused in the optical model, in favour for using in situ measurements of phytoplankton absorption, the results were used

to help develop the algorithms.

4.1.1 Phytoplankton Classification

The term 'algae' has no formal taxonomic definition. The origin of the term comes from the Latin word *alga*, which means seaweed. The term algae is routinely used in biology to describe polyphyletic organisms. Generally speaking, algae is considered to be a group of aquatic, photosynthetic, eukaryotic organisms and can be unicellular or multicellular (Barsanti and Guarltieri, 2006). The term 'phytoplankton' refers to microalgae which are buoyant and usually found in the upper part of the water column. Microalgae are the focus of this thesis and the term algae and phytoplankton may be used interchangeably. This thesis is not concerned with benthic macroalgae.

Most algae are aquatic; however, a considerable number of algae are subaerial and have adapted to life on land. Aquatic algae can be both planktonic, living suspended in lighted water columns; or benthic, attached to the bottom of shallow-water areas. Algae are diverse in size, ranging from 0.2 μm in diameter in the case of picoplankton, to 60 m in length, in the case of giant kelp (Barsanti and Guarltieri, 2006).

A classification scheme can be very difficult to define due to the polyphyletic nature of the term 'algae' and because taxonomy is under constant and rapid revision. Table 4.1 shows kingdom, division and class of different classes of phytoplankton.

Table 4.1: Different Classes of Phytoplankton. Reproduced from Barsanti and Guarltieri (2006)

Kingdom	**Division**	**Class**
Prokaryota eubacteria	Cyanophyta	Cyanophyceae
	Prochlorophyta	Prochlorophyceae
	Glaucophyta	Glaucophyceae
	Rhodophyta	Bangiophyceae
		Florideophyceae
	Heterokontophyta	Chrysophyceae
		Xanthophyceae
		Eustigmatophyceae
		Bacillariophyceae
		Raphidophyceae
		Dictyochophyceae
		Phaeophyceae
	Haptophyta	Haptophyceae
	Cryptophyta	Cryptophyceae
Eukaryota	Dinophyta	Dinophyceae
	Euglenphyta	Prasinophyceae
	Chlorarachniophyta	Chlorarachniophyceae
	Chlorophyta	Prasinophyceae
		Chlorophyceae
		Ulvophyceae
		Cladophorophyceae
		Bryopsidophyceae
		Zygnematophyceae
		Trentepohliophyceae
		Klebsormidiophyceae
		Charophyceae
		Dasycladophyceae

4.1.2 Photosynthetic Pigments

As with all plants, algae use photosynthesis to convert light energy and carbon molecules into chemical energy. Algae use light-harvesting pigments to assist in this process. These pigments can be classified as chlorophylls, carotenoids or biliproteins. Chlorophylls are greenish pigments which contain a porphyrin ring from which electrons are free to migrate. This ring can gain or lose electrons easily and has the potential to provide energised electrons to other molecules. This is the fundamental process by which chlorophyll 'captures' the energy of light. All plants that photosynthesise contain chlorophyll-*a*, the primary, most abundant, pigment in photosynthetic algae. Chlorophyll-*b* is a less abundant pigment and helps the plant increase the range of light it can use for energy. Another form of chlorophyll is chlorophyll-*c* which is found only in dinoflagellates and some diatoms. It is primarily chlorophyll which gives plants, including algae, their green colour. Table 4.2 shows a list of different classes of algae. It shows that all classes have chlorophyll-*a* however the accessory pigments vary across the classes.

Carotenoids contain the compound carotene which gives the usual red, orange and yellow colours. Carotenoids are organic compounds that are non-soluble and cannot transfer the energy from sunlight directly in the photosynthesis process. Instead, they must pass their absorbed energy to chlorophyll. For this reason, they are commonly referred to as 'accessory pigments'.

Biliproteins are water-soluble and are found in the cytoplasm of the chloroplast. Biliproteins are commonly found in cyanobacteria and in rhodophyta (red algae).

Table 4.2: Photosynthetic pigments found in different classes of algae. The markers; ⊗ indicates an important pigment; + indicates the pigment is present and ± indicates the pigment occurs rarely. (reproduced from Hoek et al., 1995)

	Cyanophyta	Prochlorophyta	Glaucophyta	Rhodophyta	Heterokontophyta/Chrysophytceae	Heterokontophyta/Xanthophyceae	Heterokontophyta/Eustigmatophyceae	Heterokontophyta/Bacillariophyceae	Heterokontophyta/Raphidophyceae	Heterokontophyta/Dictyochophyceae	Heterokontophyta/Phaeophyceae	Haptophyta	Cryptophyta	Dinophyta I	Dinophyta II	Euglenophyta	Chlorarachniophyta	Chlorphyta
Chlorophylls																		
Chlorophyll-*a*	⊗	⊗	⊗	⊗	⊗	⊗	⊗	⊗	⊗	⊗	⊗	⊗	⊗	⊗	⊗	⊗	⊗	⊗
Chlorophyll-*b*		⊗														⊗	⊗	⊗
Chlorophyll-c_1					⊗	+		⊗	⊗		⊗	⊗			⊗			
Chlorophyll-c_2					⊗	+		⊗	⊗	⊗	⊗	⊗			⊗			±
Chlorophyll-c_3					±			⊗			⊗							
Phycobilins																		
Phycocyanin	⊗		⊗	⊗									⊗					
Allophycocyanin	⊗		⊗	⊗														
Phycoerythrin	⊗			⊗									⊗					
Carotenes																		
α-carotene				⊗	+							+	⊗		+			±
β-carotene	⊗	⊗	⊗	⊗	⊗	⊗	⊗	⊗	⊗	⊗	⊗	⊗	±	⊗	⊗	⊗		⊗
γ-carotene																±		±
ε-carotene					+			+			+		±					
Xanthophylls																		
Zeaxanthin	⊗	⊗	⊗	⊗	+		±		+		±		+			±		+
Echinenone	⊗	+						+				+		+		±		±
Canthaxanthin	⊗					+	+				+		+					
Myxoxanthophyll	⊗																	
Oscillaxanthin	⊗																	
α-cryptoxanthin				±	+		±					+						
β-cryptoxanthin	+	+	+	±		±		±	±							±		±
Isocryptoxanthin	+	+																
Mutachrome	+	+																

4.1.3 Harvesting Light Energy

Plants that are able to synthesize food from carbon dioxide using light as an energy source are called photoautotrophs. In the case of algae, oxygen is released as a product of photosynthesis. This is called oxygenic photosynthesis. The process in which carbon dioxide is converted into sugars is called 'carbon fixation'. Carbon fixation is a redox reaction; therefore, a source of electrons is needed to convert carbon dioxide into carbohydrate. The general equation for photosynthesis is:

$$2nCO_2 + 2nH_2O + photons \rightarrow 2(CH_2O)_n + O_2 + 2nA$$

Carbon dioxide + electron donor + light energy → carbohydrate + oxygen + oxidised electron donor

Photosynthesis takes place within the algae cells in the chloroplasts. All light-harvesting pigments are known to be bound to proteins found within cell membranes, called thylakoids. Thylakoids are tightly folded into cylindrical sheets giving them large surface areas, so they are capable of absorbing a larger amount of light than if they were not. However, in the case of cyanobacteria the thylakoids generally lie in concentric rings in the cytoplasm, although there are a few exceptions (Graham and Wilcox, 2000).

It is this process of photosynthesis which explains the existence of these pigments, within the cells, which are responsible for absorbing particular wavelengths from the incoming sunlight radiation. The absorption of these wavelengths is what gives the absorption signal a particular spectral shape or 'spectral features'.

4.2 Algal-Culturing Techniques

Three species of algae were chosen for culture and obtained from the Murdoch University Microalgae Culture Collection. Details of the species of algae used in this study are described in Table 4.4. These species were chosen as they were inexpensive and readily available. The three species cultured are not native to the Swan or Canning rivers but were cultured in order to test the viability of setting up a culturing laboratory for further investigation of Swan and Canning specific cultures.

Seawater used for media preparation was obtained from Hillarys Boat Beach (Perth, Western Australia) and was stored in 10 000 L holding tanks at Murdoch University.

The seawater was charcoal-treated overnight by adding 10 g of activated charcoal to 10 L of seawater. After treatment, the water was filtered twice through triple thickness Whatman No.1 filter paper, followed by a 0.45 μm Whatman nitrocellulose membrane filter. The seawater was then stored at 4 °C in polycarbonate containers in the dark.

Cultures were maintained in 100 mL of culture medium and stored in 250 mL conical flasks. Cultures were grown at 25 °C in constant temperature growth rooms at approximately 10 Wm^{-2} ambient light provided by a combination of cool white and day light fluorescent lights. All cultures were grown in f/2 medium, Table 4.3 (Andersen, 2005). Silicon was added to MUR-158. MUR-158 and CCMP-1211 were grown at 3.3% NaCl salinity and MUR-29 were grown at 12.5% NaCl salinity.

Table 4.3: Phytoplankton Culture Medium Recipe f/2

Component	Stock Solution ($gL^{-1}dH_2O$)	Quantity Used
$NaNO_3$	75	1 mL
$NaH_2PO_4.1H_2O$	5	1 mL
Trace Metal Mix		
$Na_2EDTA.2H_2O$	0.4725	3.15 g
$FeCL_3.6H_2O$	0.61	4.36 g
$MnCL_2.4H_2O$	180	1 mL
$ZnSO_4.7H_2O$	22	1 mL
$CoCl_2.6H_2O$	10	1 mL
$CuSO_4.5H_2O$	9.8	1 mL
$Na_2MoO_4.2H_2O$	6.3	1 mL
Vitamin Mix		
Cyanocobalamin (vitamin B_{12})	1	200 mg
Thiamine HCL (vitamin B_1)	1	1 mL
Biotin (vitamin H)	1	1 mL

Cell counts were taken daily in order to keep track of growth rate, growth phase and culture volume. Subcultures were performed every few days in the log phase of growth until spectrophotometric analysis. Subculturing was performed using aseptic microbiological techniques outlined in Andersen (2005) by transferring culture into fresh, pre-sterilised medium.

4.3 Algal Spectral Absorption in Optical Model

Ultimately, the algal absorption results were not used in the model inversion as originally planned but are presented here to illustrate the different absorption characteristics that algae from different classes have as a result of the different photosynthetic pigments. The original vision of the project was to build a spectral library of mono-cultures found in the Swan and Canning Rivers. In practice, the amount of time it took to grow the cultures in the laboratory detracted far too much time from the modelling, algorithm development and fieldwork requirements of the project. Furthermore, early in the algorithm development stage of the project, it was found that chlorophyll-a and CDOM absorption features were so dominant in the measured reflectance spectra that differences in species due to accessory pigments made very little difference to the inversion results. It was found that it was far more important to accurately measure the reflectance, being careful to keep the sun and sensor viewing geometry correct without corrupting measurements through sunglint, foam or debris. This is discussed in more detail in later chapters. This ultimately led to the decision to refocus the project on field measurements and algorithm development. The field results presented in Chapter 6 used phytoplankton pigment spectra taken from the river during the field campaigns and measured in the laboratory.

In Chapter 5, it is identified that there were three possible optical models that could be used for model inversion. Two were published and one was being developed in-house. Time was spent coding all three models in Python and testing their suitability for the project. The following chapter shows the major results of this investigation. These results were used to decide which model was the most suitable model to use for the subsequent field campaigns.

Over the course of the project there were many opportunities to make radiometric measurements at the water sampling locations along the Swan River. It was not possible to measure a complete transect on these field trips due to the speed the Swan River Trust boat which was far too high for making underway measurements. It was possible to make measurements at the sample locations while the boat was stationary and water samples were being collected. This provided an opportunity, however, to test and develop workflows as well as make adjustments to equipment and the processing software. The results for these measurements are shown in Section 6.7.2.

The work presented in this chapter so far was used as a development platform to get

the necessary tools and workflows together in order to complete a full underway transect between the first and final water sampling locations. A boat was secured for use on one occasion that, unlike the Swan River Trust boat, could make way at the optimal speed (approx. 3–5 knots, depending on traffic) for radiometric measurements. The results of this transect including the in situ measurements of the IOPs are presented in the last part of Chapter 6, Section 6.7.14. Access to this boat, unfortunately, was not available for any other field campaigns.

This section presents the absorption due to pigments of three different species of algae. These particular species were chosen as they were readily available from the Murdoch University culturing laboratory and were considered as potentially the closest type to what might be found in the Swan River (personal communication Michael Borowitzka). The phytoplankton presented in Table 4.4 were used to produce the absorption plots show in Figure 4.1. A detailed description of the methodology used to measure the phytoplankton absorption of these samples as well as the those collected in the field campaign are described in Section 6.5.

Table 4.4: Phytoplankton culture details

Species/class	Culture Collection Number	Source
Pleurochrysis sp.	CCMP-1211	Hawaii, North Pacific
Dunaliella salina	MUR-8	Hutt Lagoon, Western Australia
Diatoms	MUR-158	unknown

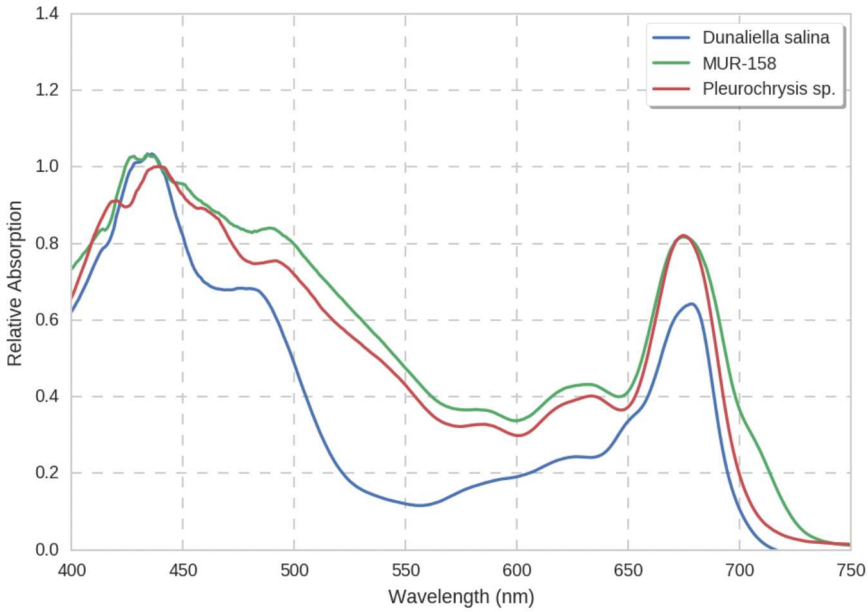

Figure 4.1: The relative absorption of the cultures grown in the lab. The absorption has been normalised at 440 nm

4.4 Summary

The research methods discussed in this chapter began by discussing the methods used to culture algae for spectral absorption characterisation. The results of the spectral absorption measurements are shown in Figure 4.1. Although these measurements were not utilised in the inversion of Swan River data, the methodologies of measuring the absorption of different phytoplankton were used to measure the in situ phytoplankton spectra at the validation sites along the transect. Furthermore, these spectra were utilised in the sensitivity analysis comparing different phytoplankton absorption spectra in the presence of high CDOM and presented in Figure 7.1.

Chapter 5

Development of Numerical Techniques for Solving the Optical Model

5.1 Introduction

Radiative transfer describes the change of energy of light as it passes through a medium. A fundamental understanding of this phenomenon is required to predict the behaviour of the underwater light field and the processes affecting it. The following subsections define terms, units and coordinates required to understand the radiative transfer equation.

5.1.1 Light

In this thesis, the term 'light' refers to a subset of wavelengths that make up the electromagnetic spectrum. In general, this thesis is concerned with wavelengths of light that range from the infrared to the ultraviolet, approximately 380–750 nm.

All units used in this document are shown in Table 5.1, unless otherwise stated.

5.1.2 Coordinate System

The coordinate system used in this thesis follows the system used in Mobley (1994), shown in Figure 5.1.

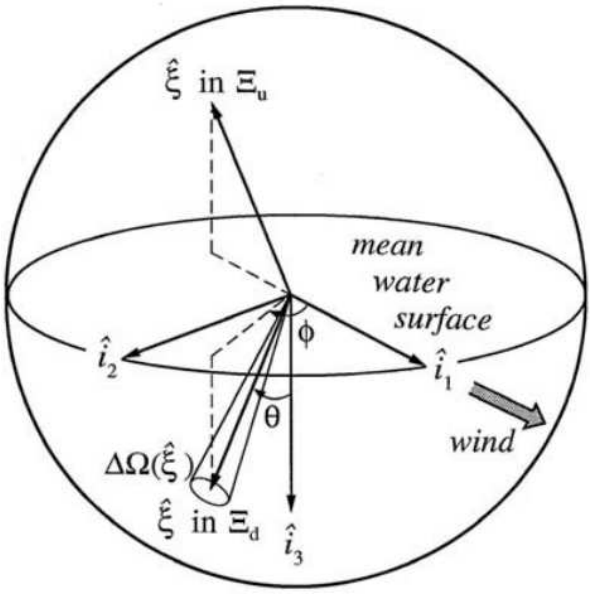

Figure 5.1: Definition of the polar coordinates (θ, ϕ) and of the upward (Ξ_u) and downward (Ξ_d) hemispheres of directions. $\Delta\Omega(\hat{\xi})$ is an element of solid angle centred on $\hat{\xi}$.

5.1.3 Radiometry

Considering a beam of light passing through a finite volume of water, the radiant energy of the beam is defined in units of 'per unit volume' – or the energy density.

Radiance

The amount of power that an object emits (or reflects) in a particular direction is described by the quantity **radiance**. Radiance is a geometrical and spectral quantity and is, therefore, a function of angle and frequency. It is defined as:

$$L(\vec{x}, t, \hat{\xi}, \lambda) = \frac{\partial^4 Q}{\partial t \partial A \partial \Omega \partial \lambda} \quad (Wm^{-2}sr^{-1}nm^{-1}) \tag{5.1}$$

Where:

L is radiance $(Wm^{-2}sr^{-1}nm^{-1})$
$\vec{x}$ is the position vector of a detector $\vec{x} = (x_1\hat{\mathbf{i}} + x_2\hat{\mathbf{j}} + x_3\hat{\mathbf{k}})$
Q is spectral energy (J)
$\hat{\xi}$ is the direction of travel of the wave
λ is the wavelength (nm)

t is time (s)
A is the area of the water surface (m^2)
Ω is the solid angle (sr)

Irradiance

The amount of power per unit area incident on a surface is called **irradiance**. Most commonly, the amount of power reaching a surface is considered incident irradiance arriving at a flat surface as a plane wave, and therefore, often considered irradiance over a hemisphere. In terms of passive remote sensing, the incident source of irradiance is solar irradiance (the sun) usually described as downwelling scalar irradiance (E_d) and is defined as:

$$E_d(\vec{x}, t, \lambda) = \int_0^{2\pi} \int_0^{\frac{\pi}{2}} L(\vec{x}, t, \theta, \phi, \lambda) \sin\theta d\theta d\phi \quad (Wm^{-2}nm^{-1}) \tag{5.2}$$

Where:
E_d is irradiance $(Wm^{-2}nm^{-1})$ in the direction θ
$\vec{x}$ is the position vector of a detector $\vec{x} = (x_1\hat{\mathbf{i}} + x_2\hat{\mathbf{j}} + x_3\hat{\mathbf{k}})$
$\hat{\xi}$ is the direction of travel of the wave
t is time (s)
A is the area of the surface (m^2)
Ω is the solid angle (sr)
L is radiance $(Wm^{-2}sr^{-1}nm^{-1})$
λ is the wavelength (nm)
θ is the zenith angle *radian*
ϕ is the azimuth angle *radians*

The upwelling scalar irradiance (E_u) is defined in much the same way. The difference between radiance and irradiance is the dependence that radiance has on the viewing solid angle. Measuring the downwelling radiance over the complete hemisphere, would lead to the definition of downwelling scalar irradiance. That is to say, integrating radiance over $\phi : 0- > 2\pi$ and $\theta : 0- > \frac{pi}{2}$ would yield upwelling scalar irradiance:

$$E_u(\vec{x},t,\lambda) = \int_0^{2\pi}\int_{\frac{\pi}{2}}^{\pi} L(\vec{x},t,\theta,\phi,\lambda)\sin\theta d\theta d\phi \quad (Wm^{-2}nm^{-1}) \tag{5.3}$$

So far, the definitions presented here have assumed that the surface is illuminated equally from all photons of light, regardless of their incident angle. In practice, irradiance is often measured with a detector that has a flat collection surface. In this case, the effective area a beam of light makes with the detector is $\Delta A|\cos\theta|$, where ΔA is the collection surface of the detector (such as the DALEC). That is to say that, light entering a detector's collection surface at an angle θ from the axis of the instrument, projects a larger surface area than a beam of light parallel with the axis of the instrument. This results in a detector response directly proportional to the cosine of the angle θ the light makes with the instrument.

In this case, equations (5.2) and (5.3) must take in to account the **cosine response** of the detector and are slightly modified to be:

$$E_d(\vec{x},t,\lambda) = \int_0^{2\pi}\int_0^{\frac{\pi}{2}} L(\vec{x},t,\theta,\phi,\lambda)|\cos\theta|\sin\theta d\theta d\phi \tag{5.4}$$

and

$$E_u(\vec{x},t,\lambda) = \int_0^{2\pi}\int_{\frac{\pi}{2}}^{\pi} L(\vec{x},t,\theta,\phi,\lambda)|\cos\theta|\sin\theta d\theta d\phi \tag{5.5}$$

Equations 5.4 and 5.5 are the vector irradiances. Some instruments are designed to be equally sensitive to photons from all directions. However, the instrument used for this study was not; therefore equations (5.4) and (5.5) are used to calculate vector irradiance for all measurements.

Table 5.1: Physical quantities and their units

Quantity	Unit	Symbol
length	metre	m
mass	kilogram	kg
time	second	s
temperature	kelvin	K
plane angle	radian	rad
solid angle	steradian	sr

5.1.4 Radiative Transfer Equation

Conservation of Energy

The following section will continue to define some fundamental quantities and principles that are required to define the radiative transfer equation.

When a small collimated beam of light (Φ_i) enters a volume of water, only three processes can occur. Some of the beam (Φ_a) may be absorbed by the medium, some of the beam may be scattered (Φ_s) by the medium and the remaining beam (Φ_t) is transmitted unaffected.

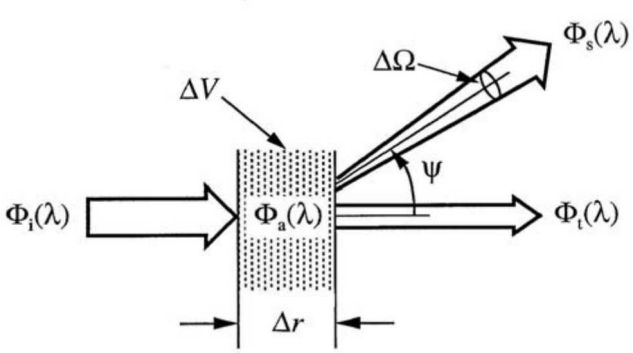

Figure 5.2: The transmitance, scatterance and absorptance of a collimated beam of light through a small volume of water (Mobley, 1994).

$$\Phi_i = \Phi_a + \Phi_s + \Phi_t$$

The fraction of power that is absorbed within the volume is the **spectral absorptance**, defined as:

$$A(\lambda) = \frac{\Phi_a(\lambda)}{\Phi_i(\lambda)}$$

The fraction of power that is scattered out of the volume is the **spectral scatterance**, defined as:

$$B(\lambda) = \frac{\Phi_s(\lambda)}{\Phi_i(\lambda)}$$

The fraction of power that is transmitted through the volume is the **spectral transmittance**, defined as:

$$T(\lambda) = \frac{\Phi_t(\lambda)}{\Phi_i(\lambda)}$$

And, by conservation of energy, $A(\lambda) + B(\lambda) + T(\lambda) = 1$

5.1.5 Inherent Optical Properties

The inherent optical properties (IOPs) of a water column are defined as the spectral absorption $a(\lambda)$ and spectral scattering $b(\lambda)$ coefficients. They are the absorptance and scatterance per unit distance in the medium and are defined as:

$$a(\lambda) = \lim_{\Delta r \to 0} \frac{A(\lambda)}{\Delta r} \quad (m^{-1}) \tag{5.6a}$$

$$b(\lambda) = \lim_{\Delta r \to 0} \frac{V(\lambda)}{\Delta r} \quad (m^{-1}) \tag{5.6b}$$

$$c(\lambda) = a(\lambda) + b(\lambda) \quad (m^{-1}) \tag{5.6c}$$

Where:

c is the spectral attenuation coefficient (m^{-1})
λ is the wavelength (nm)
r is the beam of light path length (m)
V is the volume of water (m^{-3})

When modelling or predicting IOPs, it is common and useful to break the absorption

and scattering down into the contributions from each of the water's constituents. It is usually these individual contributions that are of interest. For example, the absorption of light due to phytoplankton, as shown in the following section, can be used to characterise the concentration levels of phytoplankton present in the water body. Other important IOPs include; absorption due to coloured dissolved organic material and scattering due to suspended particles. All of these IOPs are commonly used in water quality measurements and used in environmental monitoring of water bodies. The individual IOPs contribute to the total IOPs by:

$$a(\vec{x}, t, \lambda) = \sum_{i=1}^{N_a} a_i(\vec{x}, t, \lambda) \tag{5.7a}$$

$$b(\vec{x}, t, \lambda) = \sum_{i=1}^{N_s} b_i(\vec{x}, t, \lambda) \tag{5.7b}$$

Where:

N_a is the number of absorbing substances
N_b is the number of scattering substances
$\vec{x}$ is the position vector $(x_1\hat{\mathbf{i}} + x_2\hat{\mathbf{j}} + x_3\hat{\mathbf{k}})$
t is time (s)
λ is the wavelength (nm)

While equations 5.7a and 5.7b show that the IOPs vary in position and over time, single measurements of a water body which are being studied are usually a snapshot of position in time. As such, the units of position and time are often dropped.

Section 5.1.5 defines the remote sensing reflectance as a function of IOPs. Mathematical inversion of an optical model along with measurements of remote sensing reflectance will be used to infer the concentration of IOPs, in particular, phytoplankton absorption. Chapter 3 will describe this process and how it was used to measure the remote sensing reflectance of the Swan River with the DALEC and estimate the concentration of phytoplankton.

Another essential property is the **spectral single-scattering albedo**, defined as:

$$\omega_0(\lambda) = \frac{b(\lambda)}{c(\lambda)} \tag{5.8}$$

The spectral single-scattering albedo is the probability that a photon will be scattered, rather than absorbed, in an interaction. The term **bottom albedo** is often used to describe the 'colour' of a benthic substrate.

Volume Scattering Function

The volume scattering function is a fundamental IOP that describes the intensity of scattering for a given angle ψ and is described by $\beta(\psi, \lambda)$. Using the previous definition of scatterance over a finite volume ΔV, scattered into a solid angle $\Delta\Omega$, the spectral volume scattering function is defined as:

$$\beta(\psi, \lambda) = \lim_{\Delta r \to 0} \lim_{\Delta\Omega \to 0} \frac{\Phi_s(\psi, \lambda)}{\Phi_i(\lambda)\Delta r \Delta\Omega} \quad (m^{-1}sr^{-1}) \tag{5.9}$$

Integrating $\beta(\psi, \lambda)$ over all solid angles gives the total scattered power per unit volume of water, which is the same definition as the spectral scattering coefficient shown in equation (5.6).

$$b(\lambda) = \int \beta(\psi, \lambda) d\Omega = 2\pi \int_0^\pi \beta(\psi, \lambda) \sin\psi d\psi \quad (m^{-1}) \tag{5.10}$$

Dividing the spectral volume scattering function by the scattering coefficient yields the spectral volume scattering phase function.

$$\tilde{\beta}(\psi, \lambda) = \frac{\beta(\psi, \lambda)}{b(\lambda)} \quad (sr^{-1}) \tag{5.11}$$

The phase function is essentially the normalised spectral volume scattering function and describes the distribution of energy over the scattering angle, and as such, should integrate to = 1.

$$2\pi \int_0^\pi \tilde{\beta}(\psi, \lambda) \sin\psi d\psi = 1 \tag{5.12}$$

It was be shown in Chapter 3 that the volume scattering function can also be found by considering time-harmonic Maxwell's equations. This, in fact, provides a way of checking numerical calculations and is used in Chapter 3 in order to validate the results of modelled phase functions of algal cells.

As remote sensing reflectance is the quantity that is used in this study to characterise the IOPs, it is convenient to separate the total scattering coefficient into forward (b_f), and backscattering coefficients (b_b).

$$b_f(\lambda) = 2\pi \int_0^{\frac{\pi}{2}} \beta(\psi, \lambda) \quad (m^{-1}) \tag{5.13a}$$

$$b_b(\lambda) = 2\pi \int_{\frac{\pi}{2}}^{\pi} \beta(\psi, \lambda) \quad (m^{-1}) \tag{5.13b}$$

It will be shown in later sections that the measurement used in this thesis, i.e. remote sensing reflectance to derive phytoplankton abundance, is a function of absorption and backscatter. It was shown in Chapter 3 that the abundance of phytoplankton can be estimated by considering its contribution to the total absorption and scattering. For this reason, it is important to characterise the absorption and scattering processes in radiative transfer theory.

Apparent Optical Properties

Apparent optical properties (AOPs) are a function of both the IOPs and the light field in which they are measured. For an AOP to be a useful descriptor of a water body, it must show regular features and be stable for the period of measurement. Traditionally, direct measurement of IOPs has been difficult, especially when discussing oceanography. Generally, it is the AOPs that are measured and as they are a function of IOPs, they can be useful in describing the bulk properties of a water column. Satellite observations are only able to directly measure AOPs. For this reason, a few useful AOPs have been defined. The **spectral irradiance reflectance** at depth z is the ratio of spectral upwelling to downwelling irradiance:

$$R(z,\lambda) = \frac{E_u(z,\lambda)}{E_d(z,\lambda)} \tag{5.14}$$

The **spectral remote sensing reflectance** R_{rs} is defined as:

$$R_{rs}(\theta,\phi,\lambda) = \frac{L(0^+,\theta,\phi,\lambda)}{E_d(0^+,\lambda)} \tag{5.15}$$

Where depth 0^+ indicates just above the water surface. The remote sensing reflectance is a measure of how much downwelling irradiance is scattered back through the water and exits the surface. The scattering is due to water, phytoplankton and other suspended particles.

Other commonly used AOPs are the **diffuse attenuation coefficients**, particularly the downwelling spectral diffuse attenuation coefficient $K_d(z,\lambda)$. If we consider the depth dependence of E_d and assume that it decreases exponentially with depth[1]. Then we can write E_d as:

$$E_d(z,\lambda) = E_d(0,\lambda)\exp\left[-\int_0^z K_d(z',\lambda)dz'\right] \tag{5.16}$$

Solving for K_d yields (Smith and Baker, 1978):

$$K_d(z,\lambda) = -\frac{d\ln E_d(z,\lambda)}{dz} = -\frac{1}{E_d(z,\lambda)}\frac{dE_d(z,\lambda)}{dz} \quad (m^{-1}) \tag{5.17}$$

Other diffuse attenuation coefficients or 'K-functions' can be defined in a similar fashion. K-functions are strongly affected by phytoplankton chlorophyll concentration and, therefore, can be used as an indicator of phytoplankton biomass. There are commercially available instruments that can measure K-functions.

[1]True only far from both the surface, the bottom.

Absorption and Scattering of Pure Water

The scattering of photons in pure water is due to refraction. When a photon passes through water it experiences small changes in the refractive index of the water. These small changes are usually a result of small thermal fluctuations through the medium. When a photon experiences a change in the refractive index, its phase velocity is altered, causing a change in direction, as the wavelength is altered but its frequency remains the same. If there were no changes in the refractive index through the water, there would be no scattering of light at all.

Smith and Baker (1981) made careful indirect measurements of the absorption of pure water, by measuring the K_d of extremely clear natural waters. Pope and Fry (1997) have made laboratory measurements of pure water absorption using an integrating cavity absorption meter, shown in Figure 5.3. More recently, field measurements similar to those of Smith and Baker (1981) have been carried out by Morel et al. (2007) in the hyperoligotrophic waters in the South Pacific in an attempt to determine an upper bound limit to the absorption coefficients in the UV domain.

The scattering of pure water can be shown to be (Mobley, 1994):

$$b_w(\lambda) = 16.06 \left(\frac{\lambda_0}{\lambda} \right)^{4.32} \beta_w(90^\circ, \lambda_0) \quad (m^{-1}) \tag{5.18}$$

Morel (1974) shows that a sodium chloride solution of 0.035‰ of water, which is approximately the same salinity as sea water, scatters light 1.18–1.20 times as much as pure water.

It is very difficult to make measurements of the absorption or scattering of pure water for the following reasons: Precise calibration of optical equipment is difficult do the large orders of magnitude differences between incident and scattered fields; the presence of stray light is difficult to eliminate; purification of water is difficult and electronic sensors sensitive enough to the large change in scattering energy are difficult to make. For these reasons, when modelling radiative transfer the published values of absorption and scattering are used.

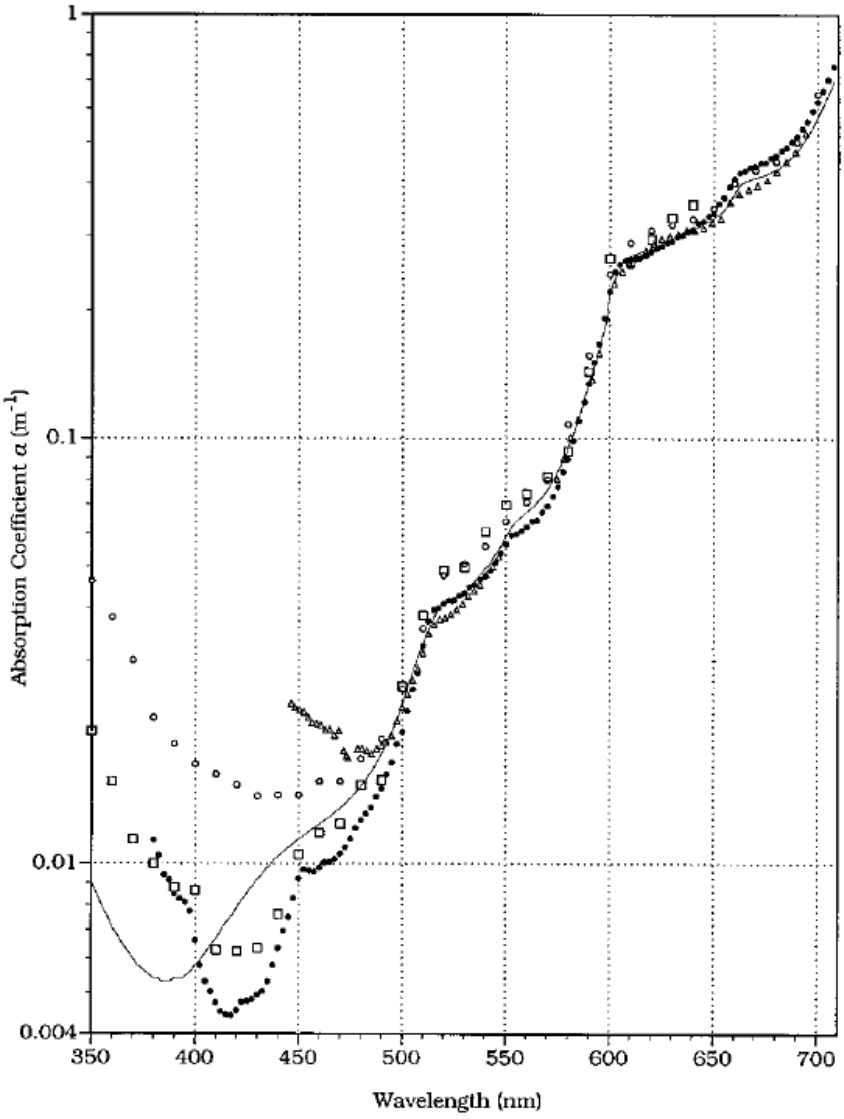

Figure 5.3: Historical data of the pure water absorption coefficient. Open circles (○) represent Smith and Baker (1981), closed circles (●) represent Pope and Fry (1997). Figure taken from Pope and Fry (1997).

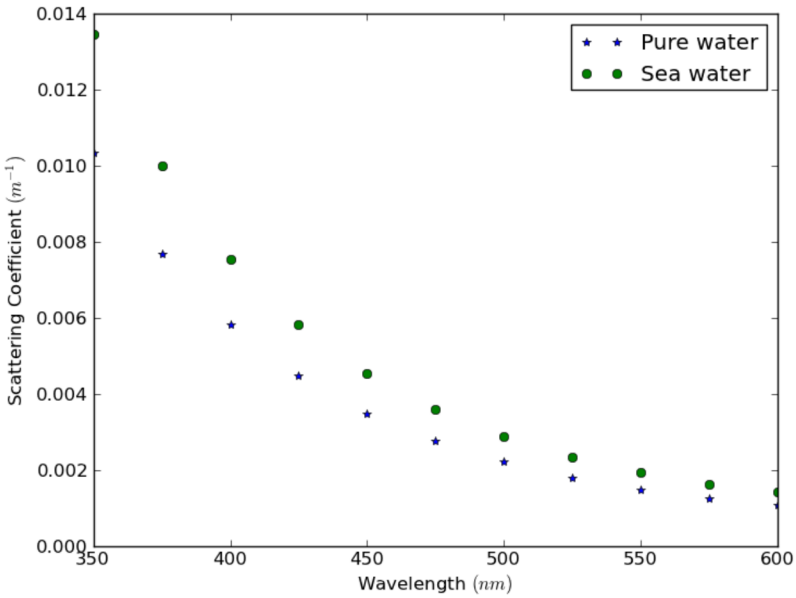

Figure 5.4: Scattering of pure water and sea water. Pure sea water consists of salts, which average about 35‰ by weight. These salts increase scattering above that of pure water by about 30% (Mobley, 1994).

Absorption and scattering of phytoplankton

The spectral absorption and scattering due to phytoplankton is very difficult to characterise. One reason for this is the complex chemical make-up of cells and the complex structure of the cells themselves. These complex structures are so varied between different classes that a simple bio-optical model is difficult to define. The other reason cells are difficult to characterise in terms of their scattering and absorption is due to the large variability in community size, structure and composition.

At the most fundamental level, the absorption and scattering of light can be described by solving Maxwell's equations for electromagnetics for light passing through a medium. Analytical solutions to Maxwell's equations are very difficult. One solution, however, is Mie theory, after Mie (1908), who found a solution for homogenous spherical particles. Although Mie theory has been used in an attempt to describe scattering by phytoplankton, cells in nature are much more complicated than Mie theory allows for (Quirantes and Bernard, 2004). Mie theory is presented in full later in this chapter and used in Chapter 5 to compare different scattering models.

Another approach to characterising the absorption and scattering process in cells is the anomalous diffraction approximation (ADA) (Hulst, 1957). In general, the ADA is only valid for small angles but, unlike Mie theory can be used to explain scattering by non-spherical particles. A study by Morris and Jennings (1977) found that the ADA was useful when considering large cells with little internal features, but with optically significant cell walls or membranes. This limits the validity of the model to only a few species, mostly bacteria.

The absence of a suitable analytical solution leaves only numerical solutions or empirical modelling as a practical approach. One such numerical solution is the finite-difference time-domain (FDTD) method. Chapter 5 describes this method in detail and uses it to model the scattering of different algal cells with more complex structures than other traditional methods. These results are compared with laboratory measurements made by Volten et al. (1998).

The absorption of phytoplankton is mostly due to the organisms' photosynthetic pigments, of which chlorophyll is the most dominant. Chlorophyll absorbs predominantly in the blue and red bands of the visible spectrum, with very little absorption in the green. Accessory pigments are often present altering the total spectral absorption slightly and

can potentially be used as 'marker' pigments to identify a group of species that a sample of phytoplankton may belong to. Chlorophyll, however, remains the most optically significant pigment and, as such, its concentration is often used to estimate phytoplankton abundance. Figure 5.5 shows to different classes of phytoplankton, with different accessory pigments, have unique spectral absorption shapes. Figure 5.6 shows that different phytoplankton classes, with different shapes and structures, results in unique spectral scattering shapes. Furthermore, the concentration of phytoplankton can also vary the spectral attenuation and absorption as shown in figures 5.10 and 5.11 respectively. This large variability becomes a challenge when modelling the remote sensing reflectance and, is a large source of uncertainty when estimating the phytoplankton concentration from remote sensing reflectance measurements.

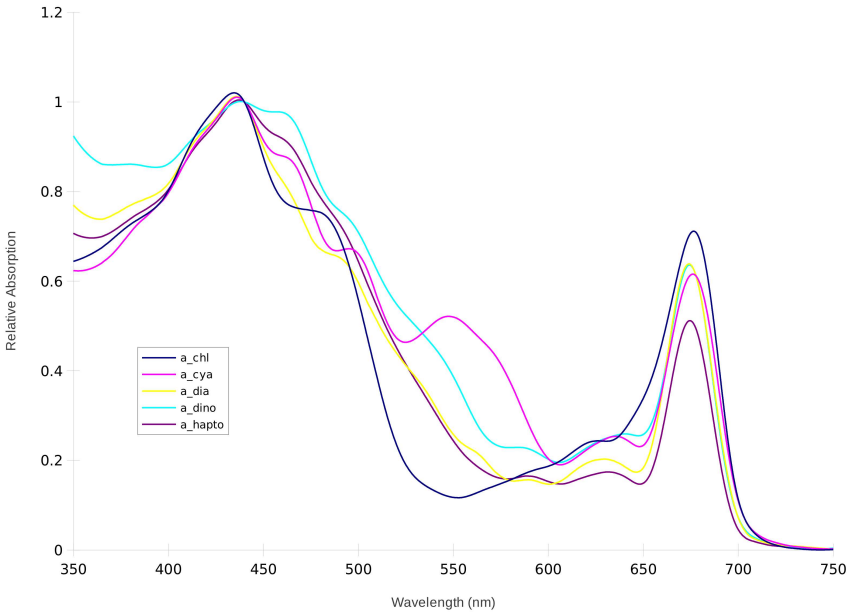

Figure 5.5: Spectral absorption of five different phytoplankton classes. Different accessory pigments result in unique absorption characteristics.

There are a few factors, however, affecting the absorption of phytoplankton. The most significant being the size, density and distribution in a water column, as well as pigment packaging, self-shading and multiple scattering. Trying to account for all of this variability is extremely difficult to model. Attempts have been made to derive relationships theoretically, semi-empirically and empirically.

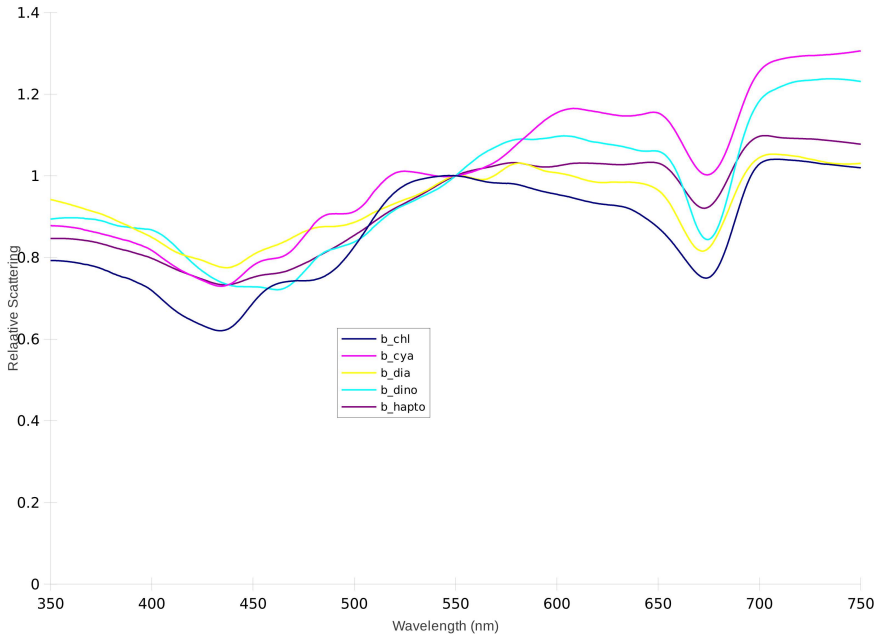

Figure 5.6: Spectral scattering of five different phytoplankton classes. Differences in both shape and chemical composition are responsible for unique scattering characteristics.

Absorption of Dissolved Organic Material

Most water bodies found in nature include some amount of dissolved organic compounds, often as a result of rotting vegetation or water run-off over wetlands and tree roots. The organic compounds mostly consist of fulvic and humic acids. They are usually brown in colour and make the water a yellow–brown colour. The dissolved organic compounds are often – in the general sense – referred to as yellow matter; gelbstoff; gilvin; coloured dissolved organic matter; or chromophoric dissolved organic matter and are often given the acronym CDOM. As CDOM is dissolved in the water it has little to no effect on scattering (except by possibly changing the refractive index of the water) but, rather, absorbs heavily in the blue part of the spectrum.

However, the most accepted model for describing CDOM absorption, and the model used by Lee et al. (1999) as described byBricaud et al. (1981):

$$a_{CDOM}(\lambda) = A_0 \exp^{(-S_{CDOM}(\lambda_0 - \lambda))} \tag{5.19}$$

Where A_0 and S_{CDOM} are modelled parameters found through regression analysis, λ is the wavelength and λ_0 is a reference wavelength. An example using this model can

be seen in Figure 5.7 which shows how CDOM absorbs heavily in the blue part of the spectrum. This is what gives it a yellow colour. It is this bio-optical model that is used when modelling CDOM for inputs into PlanarRad, the radiative transfer model which is describe in detail in further sections.

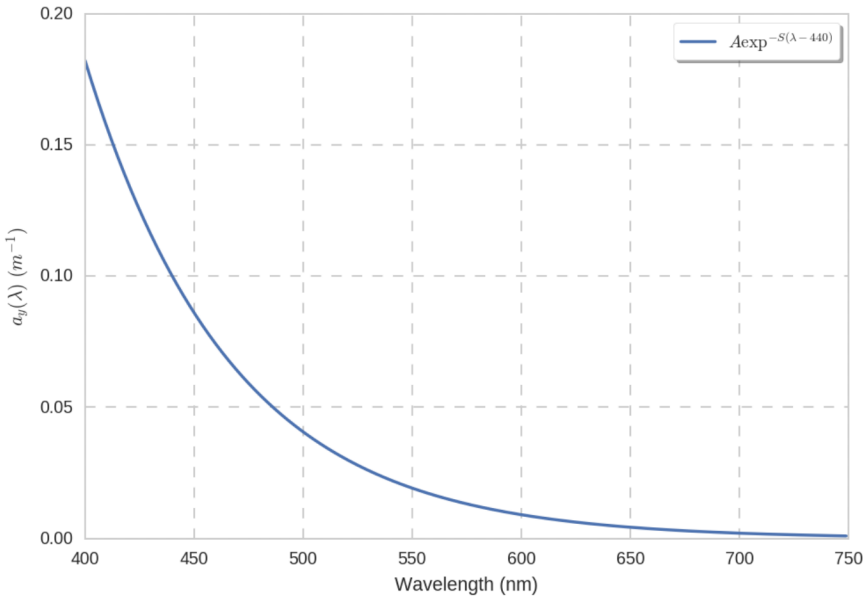

Figure 5.7: The absorption coefficient of CDOM modelled using Equations 5.19. In this model instance, A = 0.1, S = 0.015 and the reference wavelength was set to 440 nm.

Although this model was originally designed for case 1 ocean colour, regional tuning of slope parameters have been successful in various case 2 systems (e.g. Wang et al., 2005a; Kuchinke et al., 2009; Naik et al., 2011).

Absorption of Non-algal Particles (a_{nap})

Particles that do not include phytoplankton are known as non-algal particles (a_{nap}) and is sometimes referred to as tripton. This can include silt and minerals, as well as the detritus material from the algal cells. The absorption of a_{nap} can be modelled using a similar bio-optical model to CDOM but with a spectral slope typically much less than for CDOM.

$$a_{nap}(\lambda) = B_0 \exp^{(-S_{nap}(\lambda_0 - \lambda))} \tag{5.20}$$

Absorption of Gelbstoff

Gelbstoff literally means "yellow stuff" in German. Originally used to described CDOM, in this thesis it is used to describe the total contribution of CDOM and a_{nap} to the 'yellow stuff' budget.

$$a_g(\lambda) = A_0 \exp^{(-S_{CDOM}(\lambda_0 - \lambda))} + B_0 \exp^{(-S_{nap}(\lambda_0 - \lambda))} \tag{5.21}$$

Scattering of Suspended Particles

Most water bodies have a certain amount of suspended particles in the water contributing to the total scattering of light. The particles usually include both minerals, phytoplankton and other non-algal particles. As the backscattering of suspended particles (b_{bp}) is an IOP that contributes to the remote sensing reflectance, it is useful to model the spectral backscattering. Lee et al. (1999) describes such a model:

$$b_{bp} = X \left(\frac{400}{\lambda} \right)^Y \tag{5.22}$$

Where:

$X = b_{bp}(400)$
$Y \approx 3.44[1 - 3.17 \exp^{(-2.01\chi)}]$
$\chi = \frac{R_{rs}^{in}(440)}{R_{rs}^{in}(490)}$

Figure 5.8 shows and modelled particle scattering spectrum using Equation (5.22). This is the model for particle scattering used for inputs into PlanarRad, the radiative transfer model which is describe in detail in further sections.

Specific Inherent Optical Properties

Specific Inherent Optical Properties (SIOPs) are parameters that relates the spectral absorption and scattering of an IOP to a physical concentration level, such as chlorophyll-a concnetration from $a_\phi(440)$. The relationship between spectral absorption and cell size of phytoplankton investigated in Morel and Bricaud (1981) is presented in Figure 5.9.

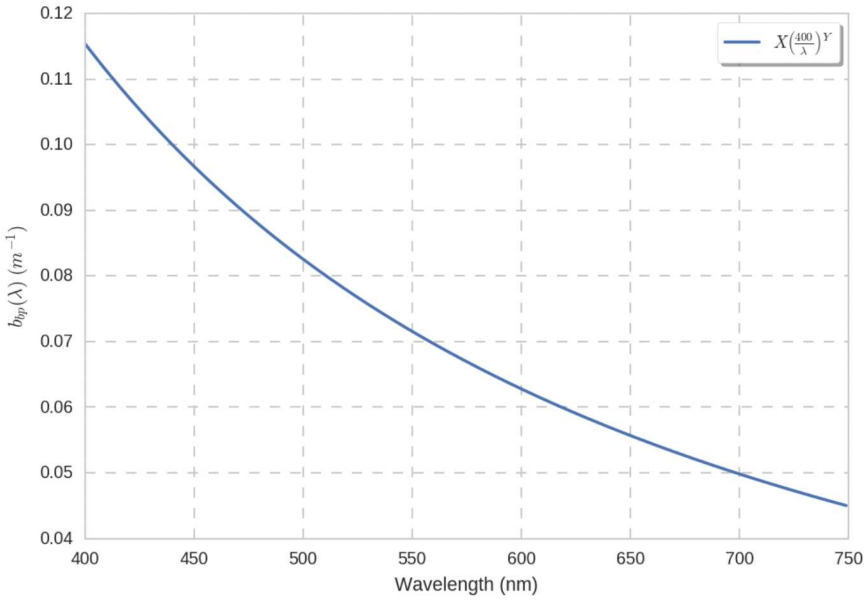

Figure 5.8: The scattering coeffecient of b_{bp} modelled using Equations 5.22. In this model instance, X = 0.1, Y = 1.5 and the reference wavelength was set to 400 nm.

Variations in the spectral absorption values for different concentrations of eight different phytoplankton have been investigated by Sathyendranath et al. (1987) and shown to have the relationship:

$$a_i^*(\lambda) = \frac{a_i(\lambda) - a_i(737)}{C_i} \tag{5.23}$$

Where C_i is the chlorophyll concentrations of the respective cultures.

Furthermore, Bricaud et al. (1988) investigate the absorption, attenuation and scattering coefficients per unit of chlorophyll-a concentration over the range (340–740) nm.

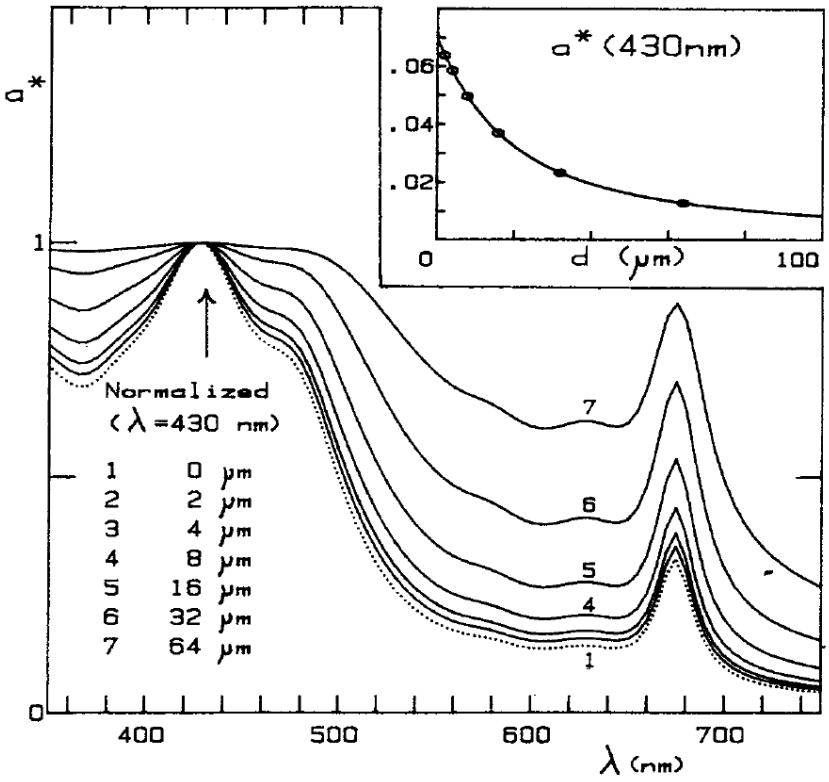

Figure 5.9: Change in spectral absorption values with variable cell size (Morel and Bricaud, 1981).

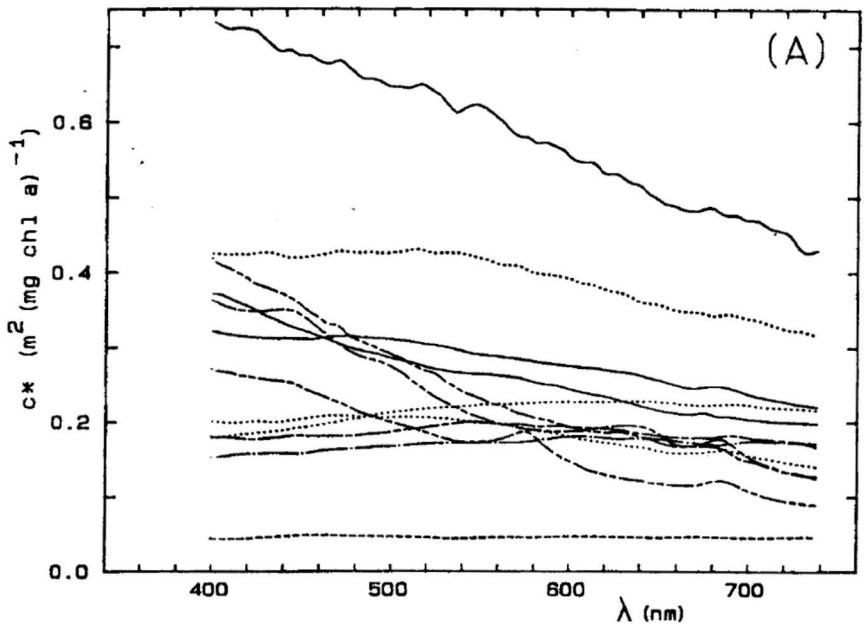

Figure 5.10: The spectral relationship between attenuation and chlorophyll-*a* concentration (Bricaud et al., 1988).

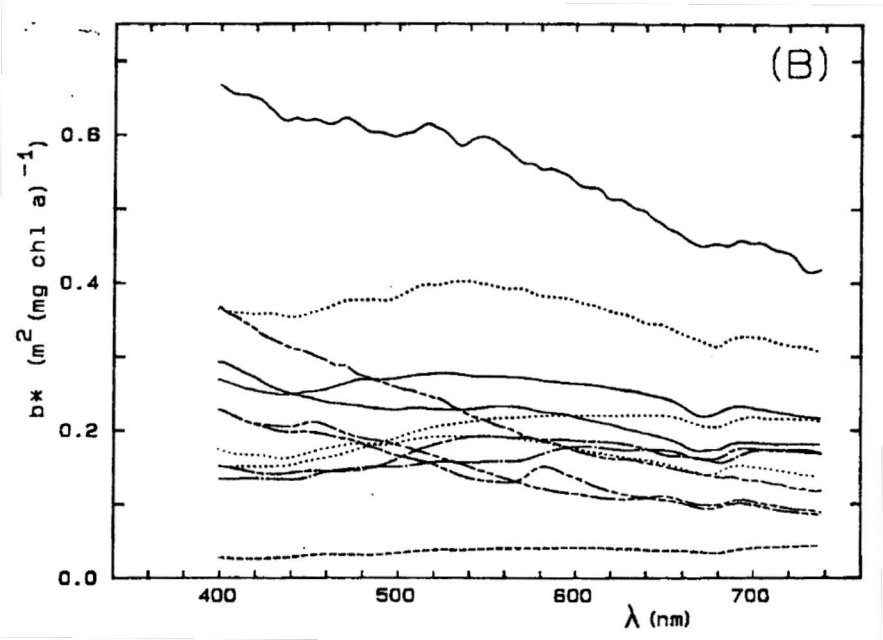

Figure 5.11: The spectral relationship between scattering and chlorophyll-*a* concentration Bricaud et al. (1988).

If the relationships between the absorption and scattering of SIOPs and IOPs are understood. The specific concentration of those IOPs can be derived by optical measurements.

5.1.6 Characterising Volume Scattering Functions

Petzold's Measurements of Volume Scattering Functions

As mentioned previously, measuring the volume scattering functions of oceanic water is problematic, due to the difficulty of designing electronic equipment that can measure the orders of magnitude change in scattering over very small angles. Furthermore, the issues of multiple scattering, internal scattering of the instrument and precise measurement of viewing geometry also present significant problems. However, instruments – such as the ECO VSF (WET Labs) – have been developed in an attempt to characterise this phenomena. The most widely cited measurements of volume scattering functions of oceanic waters are those made by Petzold (1972) which were carefully made at three different sites of three different water types: clear; productive coastal; and turbid waters, at the Bahamas, California and San Diego, respectively.

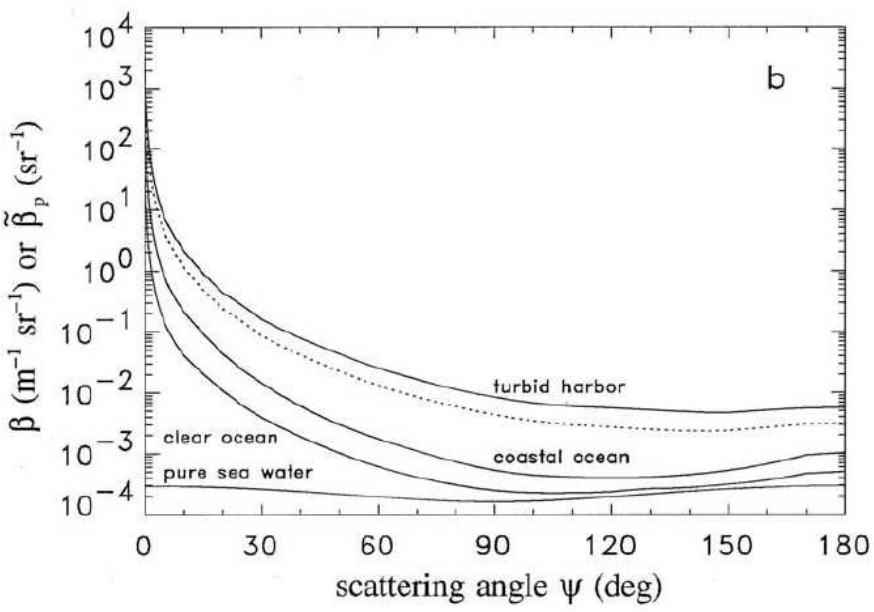

Figure 5.12: Measured volume scattering functions from the three different natural waters (Petzold, 1972), and the computed volume scattering function for pure sea water (Mobley, 1994). The dotted line is the particle phase function in Table 3.10 (Mobley, 1994).

The volume scattering functions presented in Figure 5.12 are commonly used in radiative transfer calculations. It is important to recognise, however, that scattering values may

deviate from these values significantly in waters dominated by large or small particles. This is very much due to the very limited data set available when considering the wide variety and combinations of water types commonly found around the world.

Fournier-Forand Volume Scattering Function

In an attempt to approximate an analytical phase function of particles that have a hyperbolic (Junge) particle size distribution, Fournier and Forand (1994) derived an analytical form of volume scattering function based on the anomalous diffraction approximation of Mie theory. In the latest form presented in Fournier and Jonasz (1999):

$$\tilde{\beta}(\theta) = \frac{1}{4\pi(1-\delta)^2\delta^\nu}\left[\nu(1-\delta) - (1-\delta^\nu) + [\delta(1-\delta^\nu) - \nu(1-\delta)]\sin^{-2}\left(\frac{\theta}{2}\right)\right] + \frac{1-\delta_{180}^\mu}{16\pi(\delta_{180}-1)\delta_{180}^\mu 2\cos^2\theta - 1} \tag{5.24}$$

Where:

$$\mu = \frac{3-\mu}{2} \tag{5.25}$$

And:

$$\delta = \frac{4}{3(n-1)^2}\sin^2\left(\frac{\theta}{3}\right) \tag{5.26}$$

Where n is the real index of refraction of the particles, μ is a spectral slope parameter and δ_{180} is δ evaluated at $\theta = 180°$. Equation 5.24 can be integrated to obtain the backscatter fraction:

$$\frac{b_b}{b} = 1 - \frac{1-\delta_{90}^{\nu+1} - 0.5(1-\delta_{90}^\nu)}{(1-\delta_{90})\delta_{90}^\nu} \tag{5.27}$$

Where δ_{90} is δ evaluated at 90°.

The Fournier-Forand phase functions, shown in Figure 5.13 are able to reproduce the shapes of ocean phase functions. However, for the reasons already discussed, it is difficult to validate, particularly at near forward-scattering angles. The advantage over Petzold's phase functions is that they can be produced for a known backscatter fraction. If the backscatter fraction is known, the Fournier-Forand method can be used to generate a complete phase function.

5.1.7 Radiative Transfer Equation

The following section of this chapter's goal is to develop a radiative transfer equation that can be used to model the underwater light field of a water body. To achieve this, a few constraints need to be defined. Firstly, the theory developed here will be restricted to 'plane–parallel' water bodies as described by Mobley (1994). The plane–parallel model assumes that the water body has no horizontal variations in the inherent optical properties. The inherent optical properties may significantly vary with depth. The full radiative transfer equations is an important tool in understanding the underwater light field and how solar radiation passes through a water column and is reflected back up through the water surface. The radiative transfer equation can be used to calculate the remote sensing reflectance (along with other quantities) by providing IOPs and VSFs as inputs. In this study, a solution to the inverse problem is required. The remote sensing reflectance can be measured, however, it is the IOPs that are desired an an output. The full and complex radiative transfer equation will be developed in this section. In later sections of this chapter, it will be shown that software tools that solve the radiative transfer equation for remote sensing reflectance, have been used to develop simpler, less computationally burdened models. These simpler models, unlike the full radiative transfer equation, can be inverted using mathematical optimisations techniques to obtain IOP concentrations from remote sensing reflectance inputs. Hence, providing a solution to the inverse problem stated previously.

The first consideration is the boundary conditions. It is assumed that the water body is infinite in the horizontal plane, so the two boundaries that need to be considered are the air–water boundary and the bottom surface – these are the upper and lower boundaries shown in Figure 5.14.

Figure 5.14 shows an infinitesimally thin surface 'slab' denoted by $S[a, w]$ between the air and water at depth $a = 0$.

Another useful quantity to define is the **optical depth**, defined as:

$$\zeta = \int_0^z c(z')dz' \tag{5.28}$$

Where $c(z')$ is the attenuation coefficient and z is the geometric depth. As $c(z')$ is in units per metre and geometric depth is in units of metre, the optical depth is dimensionless.

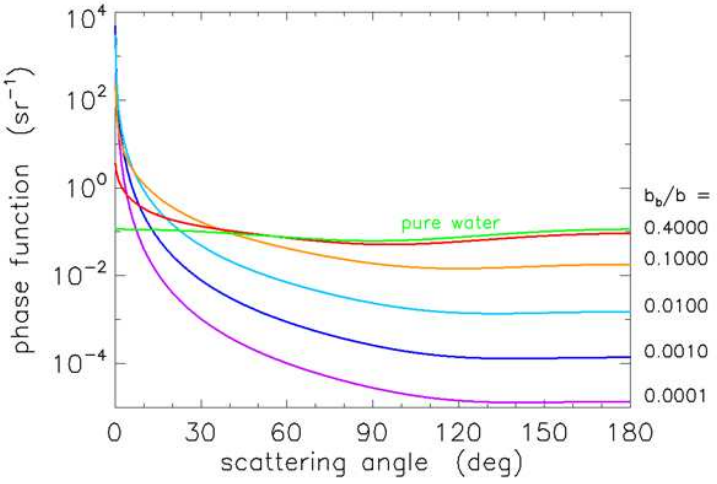

Figure 5.13: Fournier-Forand phase functions for selected backscatter fractions.

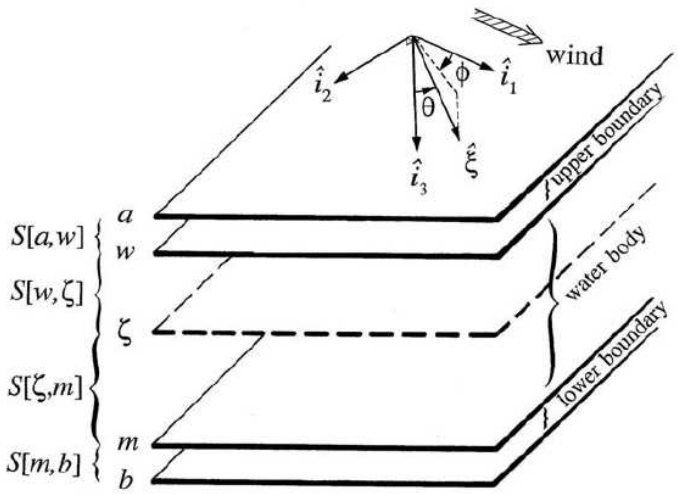

Figure 5.14: Representation of a plane–parallel water body (Mobley, 1994).

If the maximum depth of interest is denoted by m and the bottom b, then the lower boundary slab is denoted by $S[m, b]$. The lower boundary can either be infinitesimally thin or a finite thick slab of water below the greatest depth of interest.

Interaction Across the Air–Water Interface

Considering the air-incident radiance on the surface, $L(a, \hat{\xi}), \hat{\xi} \epsilon \Xi_d$, and the water-incident radiance, $L(w, \hat{\xi}), \hat{\xi} \epsilon \Xi_u$, there are two incident radiances on the slab $S[a, w]$. The interaction principle for radiance defines four radiance transfer functions for $S[a, w]$ from the functions:

Air-incident:

$$L(a, \hat{\xi}) = \int_{\Xi_u} L(w, \xi')t(w, a, \hat{\xi}' \to \hat{\xi})d\Omega(\hat{\xi}') + \int_{\Xi_d} L(a, \xi')r(a, w, \hat{\xi}' \to \hat{\xi})d\Omega(\hat{\xi}') \quad for\ \hat{\xi} \epsilon \Xi_u \tag{5.29a}$$

Water-incident:

$$L(w, \hat{\xi}) = \int_{\Xi_u} L(w, \xi')r(w, a, \hat{\xi}' \to \hat{\xi})d\Omega(\hat{\xi}') + \int_{\Xi_d} L(a, \xi')t(a, w, \hat{\xi}' \to \hat{\xi})d\Omega(\hat{\xi}') \quad for\ \hat{\xi} \epsilon \Xi_d \tag{5.29b}$$

The left and right terms of both equations with t and r, denote the radiance that is transmitted, or reflected, respectively.

Following the same principle, it is possible to obtain the irradiance transfer functions by multiplying equation (5.29a) by $|\hat{\xi} \cdot \hat{i}_3|$ and integrating over Ξ_u and by multiplying equation (5.29b) by $|\hat{\xi} \cdot \hat{\xi}\hat{i}_3|$ and integrating over Ξ_d:

$$E_u(a) = E_u(w)t(w, a) + E_d(a)r(a, w) \tag{5.30}$$

$$E_d(w) = E_u(w)r(w, a) + E_d(a)t(a, w) \tag{5.31}$$

$$t(w,a) = \frac{1}{E_u(w)} \int_{\Xi_u} \left[\int_{\Xi_u} L(w,\hat{\xi}') t(w,a,\hat{\xi}' \to \hat{\xi}) d\Omega(\hat{\xi}') \right] |\hat{\xi} \cdot \hat{i}_3| d\Omega(\hat{\xi}) \tag{5.32a}$$

$$r(a,w) = \frac{1}{E_d(a)} \int_{\Xi_u} \left[\int_{\Xi_d} L(a,\hat{\xi}') t(a,w,\hat{\xi}' \to \hat{\xi}) d\Omega(\hat{\xi}') \right] |\hat{\xi} \cdot \hat{i}_3| d\Omega(\hat{\xi}) \tag{5.32b}$$

$$r(w,a) = \frac{1}{E_u(w)} \int_{\Xi_d} \left[\int_{\Xi_u} L(w,\hat{\xi}') r(w,a,\hat{\xi}' \to \hat{\xi}) d\Omega(\hat{\xi}') \right] |\hat{\xi} \cdot \hat{i}_3| d\Omega(\hat{\xi}) \tag{5.32c}$$

$$t(a,w) = \frac{1}{E_d(a)} \int_{\Xi_d} \left[\int_{\Xi_d} L(a,\hat{\xi}') t(a,w,\hat{\xi}' \to \hat{\xi}) d\Omega(\hat{\xi}') \right] |\hat{\xi} \cdot \hat{i}_3| d\Omega(\hat{\xi}) \tag{5.32d}$$

Equations 5.29 and 5.32 describe everything that is needed to model the interaction of light at the air–water interface.

Fesnel Reflection

When the air–water interface is flat, the reflection and transmission of a beam across the surface can be easily described using geometrical optics. The partial transmission and reflection of light from one medium to another, as a function of their refractive indices, can be described using Fresnel's equation [unpolarised case]:

$$r(\theta') = r(\hat{\xi} \cdot \hat{n}) = \frac{1}{2} \left\{ \left[\frac{\sin(\theta' - \theta_t)}{\sin(\theta' + \theta_t)} \right]^2 \left[\frac{\tan(\theta' - \theta_t)}{\tan(\theta' + \theta_t)} \right]^2 \right\} \tag{5.33}$$

Where:

$$\theta_r = \cos^{-1} |\hat{\xi}' \cdot \hat{n}| = \theta'$$
$$\theta_t = \sin^{-1}(n_w \sin\theta')$$

And n_w is the refractive index of water, $\hat{n}$ is the unit normal vector to the surface, and assuming the refractive index of air = 1.0.

Surface Topology

The Fresnel equation, Equation 5.33, is a special case and not very useful for modelling real water body surfaces that usually present waves, due to wind, capillary and gravitational processes. There is no analytical case that can describe this kind of surface so numerical techniques need to be employed.

The most common form of modelling an air–water surface transmission is to use Monte Carlo methods to statistically estimate a solution. A complete description of the process is outlined in Mobley (1994); however, an overview will be presented here.

Consider a sea surface that is covered by wind-induced waves that are free from white caps. The Monte Carlo method of tracing light beams through the air–water interface first requires a realistic model of the sea surface. A surface can be constructed using the wave slope wind speed law described by Cox and Munk (1954).

At some position, the water surface elevation η changes, due to wind blowing across the surface. The upwind and crosswind slopes of the water surface are:

$$\eta_u = \frac{\partial \eta}{\partial x_1}$$
$$\eta_c = \frac{\partial \eta}{\partial x_2}$$

Slopes η_u and η_c vary randomly described by a normal distribution with zero mean and variances described by:

$$\sigma_u^2 = a_u U \quad where \quad a_u = 3.16 \times 10^{-3} sm^{-1}$$
$$\sigma_c^2 = a_c U \quad where \quad a_c = 1.93 \times 10^{-3} sm^{-1}$$

Where U is the wind speed in metres per second measured at 12.5 m above the mean sea level.

This relationship between wind speed and surface slope can be used to generate a large number of random capillary wave surfaces. The process of which is described in detail in Mobley (1994).

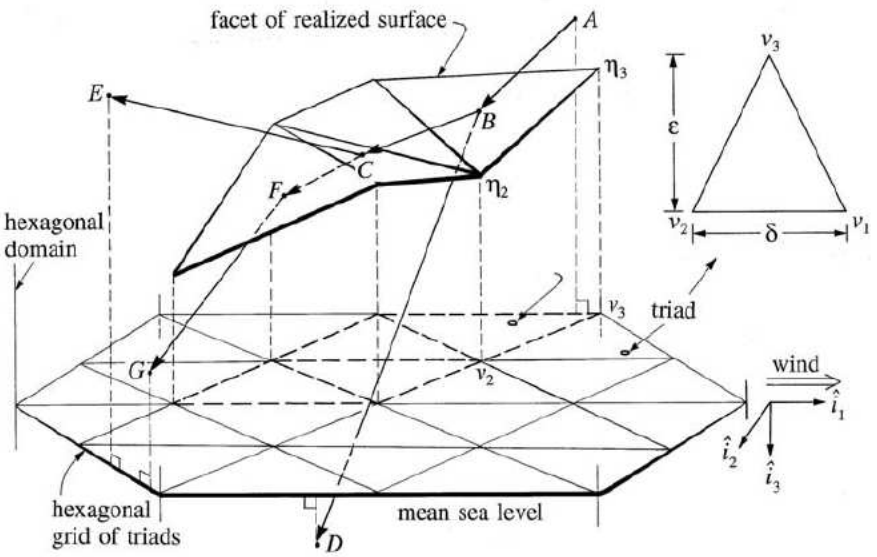

Figure 5.15: Model of the sea surface as a hexagonal grid of triangular wave facets (Mobley, 1994).

Figure 5.15 shows one possible realisation of a wave surface. A complete sea surface topology is created by repeating this process to create an ensemble average. The two-dimensional probability distribution is described by:

$$p(\eta_u, \eta_c) = \frac{1}{2\pi\sigma_u\sigma_c} \exp\left[-\frac{1}{2}\left(\frac{\eta_u^2}{\sigma_u^2} + \frac{\eta_c^2}{\sigma_c^2}\right)\right] \tag{5.34}$$

Once a suitable water surface is constructed, it is possible to proceed with the ray-tracing algorithm as shown in the following steps:

1. Construct the sea surface using the technique outlined above.
2. Trace randomly generated parent light rays over, under and through the realised surface toward their ultimate destinations.
3. Assign radiant energy content to each processed daughter ray.
4. Store the daughter rays (for multiple scattering processes) for later processing by repeating steps (1) and (2).
5. Accumulate the assigned ray energies of the daughter rays to obtain associated reflectance and transmittance properties of the surface.

6. Continue until changes in the ratio of the total amount of reflected radiant power $S(\omega)$ from a small neighbourhood converges some defined limit.

It is important to store the daughter waves and reprocess them by repeating steps (1) and (2) to account for multiple scattering. Rays in the most simple case will pass from the air through the water. However, it is shown in Figure 5.16 how rays can be reflected and transmitted off multiple surfaces.

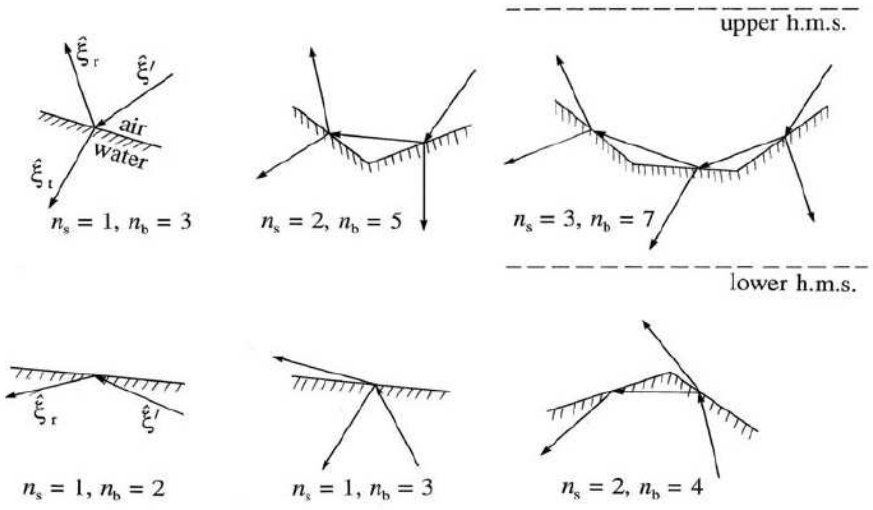

Figure 5.16: Schematic diagrams of common water-surface scattering events (Mobley, 1994). n_s and n_b show the total number of rays involved in the scattering event.

The incident radiant power is:

$$\Phi(I) = L(\hat{\xi}')\Delta\Omega\Delta A$$

And the upward emergent power $\Phi(R, \omega)$ through the surface of the horizontal monitoring surface $S(\omega)$ is given by:

$$\begin{aligned}\Phi(R, \omega) &= \Phi(I) r_+(\hat{\xi}', \omega) \\ &= (\hat{\xi}')\Delta\Omega\Delta A r_+(\hat{\xi}', \omega)\end{aligned}$$

The ensemble average is found by solving for $r_+(\hat{\xi}', \omega)$ and dividing through by $|\hat{\xi}' \cdot \hat{k}|$.

$$\mathscr{E}_\omega\left\{r_+(\hat{\xi}',\omega)\right\} = \frac{\mathscr{E}_\omega\left\{\frac{\Phi(R,\omega)}{\left(\frac{\Delta A}{|\hat{\xi}'\cdot\hat{k}|}\right)}\right\}}{L(\hat{\xi}')\Delta\Omega|\hat{\xi}'\cdot\hat{k}|} = r_+(\hat{\xi}') \tag{5.35}$$

The values of $r_-(\hat{\xi}')$ and $t_\pm(\hat{\xi}')$ are found in a similar way. Then $r_\pm(\hat{\xi}')$ and $t_\pm(\hat{\xi}')$ can be regarded as the functions that describe the reflective and transmissive properties of the mean horizontal surface of a wind-roughened water surface. The reflectance and transmission can be modelled for a range of wind, sun and surface conditions (Mobley, 1999) providing a useful lookup table for quick calculation of transmitted light[2]. An example of this is shown in Figure 5.17.

[2]This is mentioned here as it is used in calculations to estimate the remote sensing reflectance in later chapters.

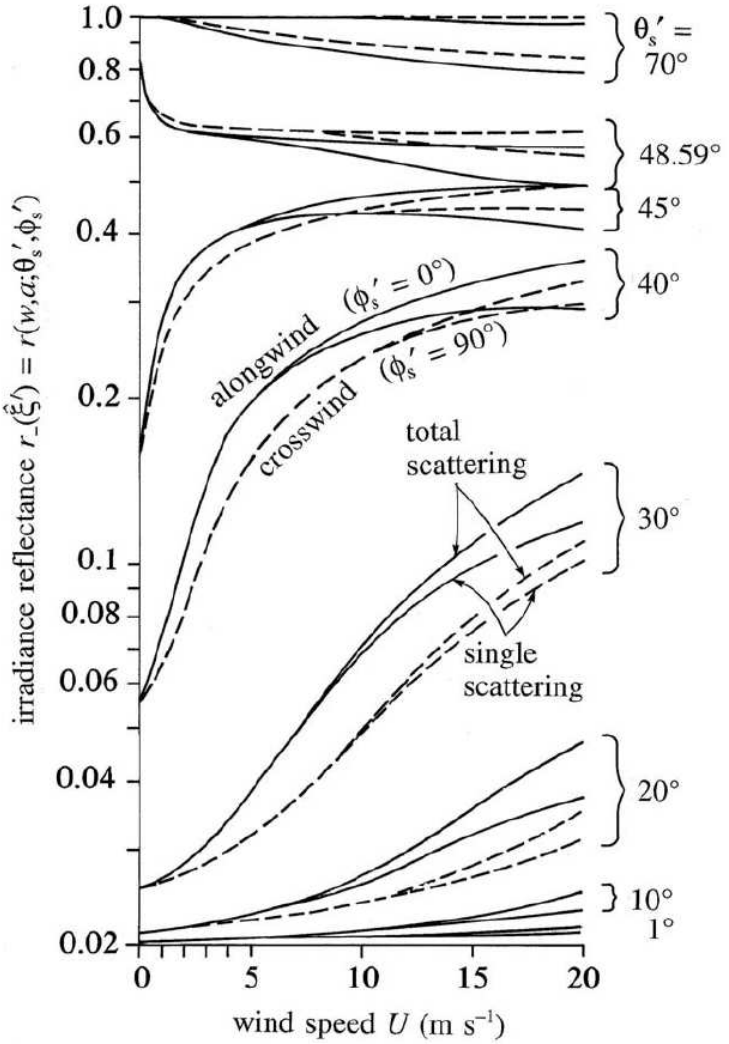

Figure 5.17: Reflectances for random capillary waves and water-incident light rays from distant point sources. For each group of θ'_s curves, the solid lines are for $\phi'_s = 0°$ (nadir), and the dashed curves are for $\phi_s = 90°$ (source at right angles to the wind direction). For each pair of solid curves or pair of dashed curves, the top curve is for the total scattering and the bottom curve is for single scattering only (Mobley, 1999).

The wave model described here has some limitations. The first one is that the model does not include the effects of gravity waves, tide, swell, internal waves or shallow water waves. This is due to computational limitations. The inclusion of gravity waves is discussed in Mobley (1994). There are a number of different stochastic wave distributions that can be used to generate a surface realisation. The (Joint North Sea Wave Project) JONSWAP and the Pierson-Moskowitz (Pond and Pickard, 1983) are two popular wave spectra in oceanography. These spectra were designed for waves generated from wind blown over large distances (fetch) and were used for modelling the sea state effects on radar. Wave spectra that focuses on the effect at visible wavelengths still requires some work.

It should also be noted that any realisation is a snapshot in time and, therefore, does not consider temporal effects. Such effects include time-dependent wave focusing, which may be important to some organisms. The lensing effect of the moving water surface can cause fluctuations of many times the average energy value over less than a second.

Furthermore, the effects of foam and white caps are not modelled by any of the traditional wave spectra but may have a significant effect on radiative transfer. This is also an area requiring more research.

Bottom Surfaces

The bottom surface is the lower boundary of the radiative transfer equation and is described using Equation 5.8. Common bottom classes include; sand, seagrass, rocks and coral. It is possible to break these classes into subclasses that each have different spectral properties. Identifying these spectral properties and classifying benthos based on these spectral properties is currently the subject of further remote sensing research in the field of benthic habitat mapping. Figure 5.18 shows an example of six spectrally different surfaces. As the Swan River is predominantly optically deep, i.e. the bottom surface cannot be seen, a completely black surface is used in modelling. The exception being, a small section between the two of the sample locations BLA and ARM. In this region, the bottom surface is all sand and therefore a sand reflectance is used for the HOPE model inputs in this corresponding area.

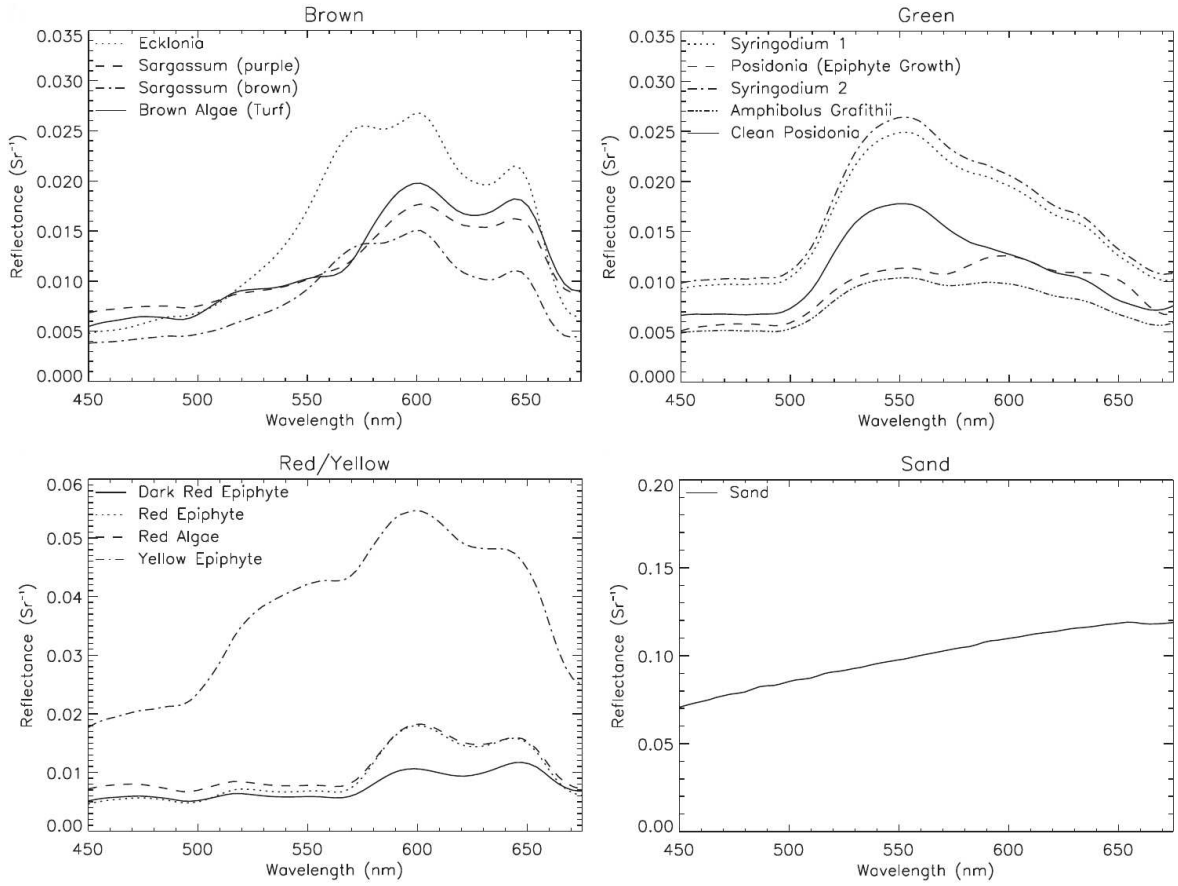

Figure 5.18: Spectral values of the albedo for various colour substratum (Fearns et al., 2011).

Generalised Radiative Transfer Equation

Putting all of the information together from the previous sections, it is possible to define a generalised radiative transfer equation. Chapter 5 of *Light and Water: Radiative Transfer in Natural Waters* (Mobley, 1999) shows in detail how to derive this equation.

$$\mu \frac{dL(z,\hat{\xi},\lambda)}{dz} = -c(z,\lambda)L(z,\hat{\xi},\lambda) + \int_{\Xi} L(z,\hat{\xi}',\lambda)\beta(z,\hat{\xi}' \rightarrow \hat{\xi},\lambda)d\Omega(\hat{\xi}') + S(z,\hat{\xi},\lambda) \quad (5.36)$$

It is this general form of the RTE that many modelling tools, such as Hydrolight and PlanarRad, attempt to solve for remote sensing reflectance given IOPs and VSFs as inputs. The $S(z,\hat{\xi},\lambda)$ term is a source term and accounts for IOP fluorescence. This term is not calculated in PlanarRad used for this study and is a limitation of the software tool.

5.1.8 Solution to the Radiative Transfer Equation

The most common way of solving the RTE is by using Monte Carlo techniques. Monte Carlo methods use ray-tracing methods to calculate the probability of an event occurring and are commonly used as they are quite simple to implement but can be computationally inefficient. Another popular numerical method for solving the RTE is the invariant imbedding technique. A detailed description of this method of solving the RTE is described in Chapter 8 of Mobley (1999) and will not be discussed here, other than to note that the very popular numerical modelling package Hydrolight uses these techniques. Hydrolight was written by Curtis Mobley and has become the industry standard in modelling underwater light fields. PlanarRad (Hedley, 2008) is an open source implementation of Hydrolight that uses the same solution methods and produces the same solutions as Hydrolight. This thesis uses PlanarRad for the numerical modelling of remote sensing reflectance.

5.2 Modelling the Radiative Transfer Equation

Previous sections described the development of the RTE and mentioned two popular tools used to solve the RTE which are very useful for calculating the spectral reflectance of a water body based on a range of water properties and environmental inputs. In practice, it is often the case that it is those inputs that are of interest and the inverse problem presents itself. That is, the water colour can be measured and it is the water

properties that need to be known. In the case of this body of work, the remote sensing reflectance of the Swan and Canning rivers can be measured, but it the absorption due to phytoplankton abundance that is required.

One solution to this problem would be to run PlanarRad many times for many combinations of IOP and environmental inputs and then match the measurements with the closet output from PlanarRad i.e. create a lookup table. The inputs required to produce that output could be inferred as the water property inputs that would reproduce the measurement. One problem with this approach is that there are a very large number, range and combinations of inputs that could be used to generate a very large number of outputs. PlanarRad (and Hydrolight) are already very computationally intensive and take a long time to run simulations. Furthermore, the size of the lookup table very quickly becomes large and difficult to load into a computer's memory, so searches can become slow. One solution to this problem has been developed by Hedley et al. (2009) by creating an adaptive lookup table which significantly reduces the search time. This does not negate the problem that generating the lookup table is very computationally expensive and time consuming. In fact, Hedley et al. (2009) generates the lookup table using a semi-analytical model rather than the full RTE.

Another and more commonly used approach is to use a simpler semi-analytical or quasi-analytical model of the full RTE. One of these simpler models has the advantage of being much faster to solve and computationally and mathematically much simpler. A semi-analytical or quasi-analytical model is much more constrained than the full RTE and usually requires some assumptions and/or approximations for the inputs. PlanarRad or Hydrolight provide accurate tools that can be used to build such a simpler and more constrained model that is easier to solve.

Many remote sensing reflectance models have been based on the work produced by Gordon et. al. (1988). This work was one of the first to describe upwelling spectral radiance at the water surface as a function of phytoplankton pigment concentration. Gordon et. al. (1988) show that the remote sensing reflectance is some function of absorption and backscatter as follows:

$$R_{rs}(\lambda) = f\left\{\frac{b_b(\lambda)}{a(\lambda) + b_b(\lambda)}\right\} \tag{5.37}$$

Where $a(\lambda)$ is the total spectral absorption and $b(\lambda)$ is the total spectral backscatter.

Most of these simpler models are, in part, an attempt to accurately estimate Gordon's remote sensing function f and represent the function in terms of the water's IOPs. The model used in this proposal is based on work by Lee et al. (1999). This model (HOPE) is a refinement on a previous model of Lee et al. (1998) and was developed using both computer-simulated data and field-measured data. The model was refined using Monte Carlo and Hydrolight calculations and defines the remote sensing reflectance as:

$$R_{rs}(\lambda) = f[a(\lambda), \beta(\lambda), \rho(\lambda), H, \theta_w, \theta, \phi] \tag{5.38}$$

Where f is a function of:

H, the bottom depth (m)
$\rho(\lambda)$, the bottom reflectance
$a(\lambda)$, the total absorption (m^{-1})
$\beta(\lambda)$, the volume scattering function (m^{-1})
θ_w, the subsurface solar zenith angle (rad)
θ, the subsurface viewing angle from the solar plane (rad)
ϕ, the viewing azimuth angle from the solar plane (rad)

All these parameters can be measured in the field. Furthermore, the authors show that $a(\lambda)$ and $b(\lambda)$ is the absorption and backscatter due to IOPs and that the spectrum of each IOP can be parameterised using parameter coefficients. This allows modelling and retrieval of specific absorption and backscatter spectra via single value parameters using bio-optical models. This is described in detail in Section 5.3.1.

HOPE has been used successfully and validated for ocean and coastal waters (Lee et. al., 1999). Inland waters high in CDOM, such as the Swan and Canning rivers, are more optically complex than the model was originally designed for. The current model uses semi-empirical data taken from the Atlantic Ocean around Florida, USA (Lee et. al., 1999). Furthermore the model was developed for reflectances measured with the sun at nadir angle. In this study, a transect of the Swan River takes approximately six hours. The sun is at nadir for only a fraction of this time, ignoring seasonal angular effects.

In 2008, field trials of the DALEC showed that HOPE can model the spectral features of the measured reflectance, between 400 nm and 650 nm in low concentrations of CDOM (Marrable, 2008). However, for wavelengths greater than 650 nm, i.e. these that are im-

portant for information regarding the red end of the spectrum and particulate scattering, the model is not an acceptable fit. Furthermore, in the presence of high concentrations of CDOM, the model does not fit at well any wavelengths. There was enough evidence to show that IOP retrieval from measured remote sensing reflectance was in fact possible but further research was required. The field trials did not cover the full range of the river and limited in situ measurements were made. It was concluded that a greater number and range of in situ measurements were required as well as a greater assessment of the optical model and available optical models. For this reason, 3 more optical models are assessed in the thesis.

5.3 Remote Sensing Optical Models

Since Gordon et al. (1988) first published a semi-analytical model of ocean colour, various remote sensing optical models ('optical models' for brevity) have been presented as incremental improvements have been made. This chapter investigates the ability of a number of optical models to accurately model the remote sensing reflectance of the Swan River. The models presented here were originally designed for inversion of ocean reflectance data; therefore, their suitability to model the generally higher attenuating water found in the Swan and Canning rivers is still unknown. An investigation into the performance of each optical model is presented further in the following sections.

5.3.1 HOPE

Hydrolight is a very useful tool for forward modelling of light. That is to say that, if the boundary conditions and all of the IOPs are known, Hydrolight will describe the light distribution at any point in the water column or just above the water surface. It is usually the case that when making measurements in the field, the inverse problem presents itself. That is to say, the light field is measured and it is the IOPs that are the required solution.

HOPE uses a quasi-single-scattering theory (presented in Gordon et al., 1975) and Hydrolight to develop a semi-analytical model for describing the remote sensing reflectance. As mentioned earlier, remote sensing reflectance is an AOP and is a function of IOPs – including phytoplankton absorption, which is the focus of this thesis. HOPE is described by:

$$r_{rs} = r_{rs}^{dp}\left(1 - \alpha_0 \exp\left\{-\left[\frac{1}{\cos(\theta_w)} + D_0(1 + D_1 u)^{0.5}\kappa H\right]\right\}\right) + \alpha_1 \rho \exp\left\{-\left[\frac{1}{\cos(\theta_w)} + D_0'(1 + D_1' u)^{0.5}\right]\kappa H\right\} \tag{5.39}$$

Where:

$$r_{rs}^{dp} = (g_0 + g_1 u^{g_2})u \tag{5.40}$$

And:

$$u = \frac{b_b}{a + b_b} \tag{5.41}$$

$$\kappa = a + b_b \tag{5.42}$$

The terms $g_0, g_1, g_2, \alpha_0, \alpha_1, D_0, D_1, D_0', D_1'$ are the model parameters and were solved by fitting those values to a large generated set of r_{rs} values. The model parameters are[3]:

$$\begin{aligned} g_0 &= 0.089, \quad g_1 = 0.125, \quad g_2 = 1 \\ \alpha_0 &= 1, \quad \alpha_1 = \frac{1}{\pi} \\ D_0 &\approx 1.03, \quad D_1 \approx 2.4 \\ D_0' &\approx 1.04, \quad D_1' \approx 5.4 \end{aligned}$$

This gives:

$$r_{rs} = r_{rs}^{dp}\left(1 - \exp\left\{-\left[\frac{1}{\cos(\theta_w)} + 1.03(1 + 2.4u)^{0.5}\kappa H\right]\right\}\right) + \frac{1}{\pi}\rho \exp\left\{-\left[\frac{1}{\cos(\theta_w)} + 1.04(1 + 5.4u)^{0.5}\right]\kappa H\right\} \tag{5.43}$$

With:

$$r_{rs}^{dp} \approx (0.089 + 0.125u)u \tag{5.44}$$

The relationship between the above water remote sensing reflectance and the subsurface

[3] g_0 and g_1 have been updated here in accordance with Lee et al. (2009), not the original values presented in Lee et al. (1999).

remote sensing surface is:

$$R_{rs} = \frac{\zeta r_{rs}}{1 - \Gamma r_{rs}} \tag{5.45}$$

Where:

$$R_{rs} \approx \frac{0.5 r_{rs}}{1 - 1.5 r_{rs}} \tag{5.46}$$

The IOPs, a and b_b embedded in equations 5.41 and 5.42. The individual IOPs are parameterised by:

$$a = a_\phi + a_g + a_w \tag{5.47a}$$
$$b_b = \varepsilon(\lambda) b_{bp} + b_{bw} \tag{5.47b}$$

Where:

$$\varepsilon(\lambda) \approx 1.0 + [0.1 + 0.8 b_{bp}(\lambda)/b_b(\lambda) \sin(\theta) \sin(\theta_w)] \tag{5.48}$$

And:

$$a_\phi(\lambda) = P[a_0(\lambda) + a_1(\lambda) ln(P)] \tag{5.49}$$

$$a_g(\lambda) = G \exp[-S(\lambda - 440)] \tag{5.50}$$

$$b_{bp} = X \left(\frac{400}{\lambda} \right)^Y \tag{5.51}$$

And the bottom reflectance is parametrised by:

$$\rho(\lambda) = B \rho_{sd}(\lambda) \tag{5.52}$$

This gives the parameters P, G, S, X, Y, H and B as scalar parameters the model can be inverted for. The coefficients in Equation 5.49, a_0 and a_1, are tabulated values from Lee (1994).

limitations

HOPE was designed for retrieving shallow water ocean bathymetry. The benthic substrate in shallow water can be very bright, and where this is the case, it can be difficult to retrieve water column parameters, as their brightness is weak in comparison. Further-

more, if the benthic colour is similar in colour to the in-water constituent of interest, it can be difficult to distinguish between them. For example, it can be difficult to estimate phytoplankton concentrations in the water column in the presence of macroalgae on the seafloor. This is because their colour are both dominated by chlorophyll i.e. they are both green.

5.3.2 BRDF Corrected Optical Model

HOPE was designed by forward modelling ocean reflectance in Hydrolight and curve fitting a number of model coefficients. One of the forward model constraints is the solar and sensor geometry. The model coefficients published in Lee et al. (1999) were calculated with the sun position at nadir. The bi-directional reflectance distribution function (BRDF) corrected model published in Lee et al. (2011), presents a method suitable for optically deep[4] water that corrects for variations in angular geometry. Furthermore, unlike HOPE, the BRDF-corrected model coefficients are a function of the above-water remote sensing reflectance directly and thereby avoids the need to calculate the subsurface remote sensing reflectance, then the effects of the air–water interface. A summary is presented below:

$$R_{rs}(\lambda,\Omega) = \left(G_0^w(\Omega) + G_1^w(\Omega)\frac{b_{bw}(\lambda)}{\kappa(\lambda)}\right)\frac{b_{bw}(\lambda)}{\kappa(\lambda)} + \left(G_0^p(\Omega) + G_1^p(\Omega)\frac{b_{bp}(\lambda)}{\kappa(\lambda)}\right)\frac{b_{bp}(\lambda)}{\kappa(\lambda)} \quad (5.53)$$

Where $\kappa = a + b_b$.

The G coefficients are dependent on angular geometry and phase function and independent of absorption and backscattering coefficients. The G model coefficients are derived from numerically simulated remote sensing reflectance. The numerical simulations presented by Lee et al. (2011) use two phase functions, 1% Petzold averaged and Fournier-Forand for minerals and phytoplankton, respectively. A sample number of G coefficients reproduced from Lee et al. (2011) are presented in Table 5.2

[4]Where bottom contributions are negligible.

Table 5.2: Sample Values of $G_0^w(\Omega), G_1^w(\Omega), G_0^p(\Omega), G_1^p(\Omega)$ for Angular R_{rs}. Reproduced from Lee et al. (2011)

θ_S	0°	0°	15°	30°	0°	15°	30°
θ_v	0°	30°	30°	30°	40°	40°	40°
ψ	0°	90°	90°	90°	135°	135°	135°
G_w^0	0.0604	0.0596	0.0590	0.0584	0.0581	0.0614	0.0624
G_w^1	0.0406	0.0516	0.0562	0.0601	0.0581	0.0524	0.0524
G_p^0	0.0402	0.0408	0.0411	0.0418	0.0414	0.0425	0.0434
G_p^1	0.1310	0.1420	0.14161	0.1492	0.1458	0.1408	0.1406

limitations

The BRDF corrected model works for optically deep water only and does not work if the bottom reflectance contributes to the remote sensing reflectance.

5.3.3 BRUCE-LUT Optical Model

The next model investigated for the project is an unpublished (at the time of writing) Klonowski model that includes BRDF-corrected coefficients and a variable, retrievable particle scattering fraction. The particle scattering fraction should allow the model to vary the contribution of particle backscattering to total backscattering. This model was selected for testing as the Swan River as the optical properties vary greatly along the lengths of the river (Marrable, 2008). A summary of the model is presented below:

The subsurface remote sensing reflectance is described by:

$$r_{rs}^{dp} = gu \tag{5.54}$$

Where:

$$u = \frac{b_b}{a + b_b} \tag{5.55}$$

And:

$$g = g_w \frac{b_{bw}}{b_b} + g_p \frac{b_{bp}}{b_b} \tag{5.56}$$

g_p is expressed as:

$$g_p = G_0 \left[1 - G_1 \exp\left(-G_2 \frac{b_{bp}}{a + b_b} \right) \right] \tag{5.57}$$

And:

$$r_{rs} = (p_0 u + p_1 u^2 + p_2 u^3 + p_3 u^4) \tag{5.58}$$

p_i are coefficients expressed a functions of $\frac{b_{bp}}{b_p}$.

$$p_0 = \alpha_0 + \alpha_1 \ln\left(\frac{b_{bp}}{b_p}\right) + \alpha_2 \ln\left(\frac{b_{bp}}{b_p}\right)^2 \tag{5.59a}$$

$$p_1 = \beta_0 + \beta_1 \ln\left(\frac{b_{bp}}{b_p}\right) + \beta_2 \ln\left(\frac{b_{bp}}{b_p}\right)^2 + \beta_2 \ln\left(\frac{b_{bp}}{b_p}\right)^3 \tag{5.59b}$$

$$p_2 = \gamma_0 + \gamma_1 \ln\left(\frac{b_{bp}}{b_p}\right) + \gamma_2 \ln\left(\frac{b_{bp}}{b_p}\right)^2 + \gamma_3 \ln\left(\frac{b_{bp}}{b_p}\right)^3 + \gamma_4 \ln\left(\frac{b_{bp}}{b_p}\right)^4 \tag{5.59c}$$

$$p_3 = \delta_0 + \delta_1 \ln\left(\frac{b_{bp}}{b_p}\right) + \delta_2 \ln\left(\frac{b_{bp}}{b_p}\right)^2 + \delta_3 \ln\left(\frac{b_{bp}}{b_p}\right)^3 + \delta_4 \ln\left(\frac{b_{bp}}{b_p}\right)^4 + \delta_5 \ln\left(\frac{b_{bp}}{b_p}\right)^5 \tag{5.59d}$$

And the above-water remote sensing reflectance (R_{rs}) is related to the subsurface remote sensing reflectance r_rs by:

$$R_{rs} = \frac{\zeta r_{rs}}{1 - \Gamma r_{rs}} \tag{5.60}$$

With:

$$\zeta = \zeta'_0 + \zeta'_1 \ln\left(\frac{b_{bp}}{b_p}\right) + \zeta'_2 \ln\left(\frac{b_{bp}}{b_p}\right)^2 \tag{5.61a}$$

$$\Gamma = \Gamma'_0 + \Gamma'_1 \ln\left(\frac{b_{bp}}{b_p}\right) + \Gamma'_2 \ln\left(\frac{b_{bp}}{b_p}\right)^2 + \Gamma'_3 \ln\left(\frac{b_{bp}}{b_p}\right)^3 \tag{5.61b}$$

The particle backscattering to scattering fraction $\frac{b_{bp}}{b_p}$ is a free parameter that is limited to a range of $0.01 - 0.1$. The coefficients, $g_w, G_0, G_1, G_2, \alpha_i, \beta_i, \gamma_i, \delta_i, \zeta'_i$ and Γ'_i are numerically generated from simulated remote sensing reflectance and dependent on the sun-sensor

geometry. A lookup table is used to find the pre-calculated values and is saved with the DalecPPT software[5].

limitations

The lookup table generated for this particular model is very large and has a much greater computer performance requirement than the two other models defined earlier. Furthermore, the inclusion of another free parameter and sun-sensor geometry factors increase the chances of the solution scheme to converge at a local minimum, in solution space, rather than the global minimum.

As with the BRDF-corrected model, the BRUCE-LUT model is only suitable for optically deep water.

5.3.4 SAMBUCA

The Semi-Analytical Model for Bathymetry, Un-mixing, and Concentration Assessment (SAMBUCA) optical model (Brando et al., 2009) is based on HOPE. The difference being that the optical properties of water due to a_{nap} and b_{bnap} are seperated from a_g and b_{bp} respectively. SAMBUCA alters the algorithm described in Lee et al. (1999) to retrieve the optically active constituents; Chlorophyl-a, CDOM and a_{nap}. in the SAMBUCA model Brando et al. (2009) alters equation 5.47 to be:

$$a = a_w + \sum_{j=1}^{N} a_j^* C_j \tag{5.62}$$

and:

$$b = b_{bw} + \sum_{j=1}^{N} b_{bj}^* C_j \tag{5.63}$$

Where a^* and b^* are the Specific Inherent Optical Properties (SIOPs). Furthermore, equation 5.49 is modelled as:

[5] `http://bazaar.launchpad.net/~marrabld/dalecppt/trunk/files/head:/inputs/BRUCE_LUT/`

$$a_{\phi}(\lambda) = C_{chl} a^{*}_{\phi}(\lambda) \tag{5.64}$$

and gelbstoff is devided into its two constituents CDOM and a_{nap}.

$$a_{CDOM} = C_{CDOM} a^{*}_{CDOM}(\lambda_0) \exp[-S_{CDOM}(\lambda - \lambda_0)] \tag{5.65}$$

and:

$$a_{nap}(\lambda) = C_{nap} a^{*}_{nap}(\lambda_0) \exp[-S_{nap}(\lambda - \lambda_0)] \tag{5.66}$$

Furthermore, the particulate scattering term 5.51 is parameterized into:

$$b_{bp} = b_{b\phi} + b_{bnap} \tag{5.67a}$$

$$b_{b\phi} = C_{chl} b^{*}_{b\phi}(\lambda_0)(\frac{\lambda_0}{\lambda})^{Y_{phy}} \tag{5.67b}$$

$$b_{bnap} = C_{nap} b^{*}_{bnap}(\lambda_0)(\frac{\lambda_0}{\lambda})^{Y_{nap}} \tag{5.67c}$$

Where $b^{*}_{b\phi}$ and b^{*}_{bnap} are the specific backscattering of algal particles and NAP respectively.

The advantage that SAMBUCA has over the optical models previously discussed is that the total phytoplankton absorption can be scaled to chlorophyll-a concentration from the absorption coefficient.

limitations

Allthough SAMBUCA can derive chlorophyll-a concentration from remote sensing reflectance, additional knowelege of Specific IOPs is required. Specific IOPs of phytoplankton are highly variable (Braga et al., 2017). For example, the specific absorption coefficient of Chl-a may vary within a single species (Dupouy et al., 2008) depending on growth conditions and light availability (Fujiki and Taguchi, 2002). Natural phytoplankton assemblages vary greatly. It is obvious that if the specific absorption and scattering coefficients of a single species are highly variable then the optical properties of phytoplankton assemblages consisting of many species are even more variable. To certain

extent, this variability can be taken into account in modeling by using variable phytoplankton absorption coefficient like those proposed by Bricaud et al. (1995) or developed for lake waters, e.g., by Ylostalo et al. (2014) and Paavel et al. (2007). However, when the light conditions are low and the measurement uncertainty of IOPs are high, the sensible approach would be to retrieve absorption and scattering coefficients not concentrations of optically active substances (Braga et al., 2017).

As discussed earlier, the range and variability of phytoplankton from site to site along the Swan River can vary greatly in just a single day. If bespoke SIOPs are required for each of the sample locations, and for each day measurements are made, the advantages of using remote sensing techniques are negated. Under these conditions it would be more suitable and accurate to measure the phytoplankton concentration from cell counts and to continue using the laboratory methods currently used by the Swan River Trust.

5.4 Inverting the Model Through Optimisation

As has been discussed in Section 5.2, R_{rs} can be measured by the DALEC but it is usually the magnitude of one or more of the IOPs that is of interest. It is often impractical, expensive and time-consuming to take water samples to characterise the IOPs using in situ samples plus laboratory measurements such as those outlined earlier. The goal of this thesis, to accurately measure phytoplankton absorption, is based on the idea that a reflectance model may be inverted for IOP concentrations and that R_{rs} can be quickly and easily measured with the DALEC.

To achieve this, the IOPs needed to be characterised, using the techniques described in sections 6.5 and 6.5.3. It was then assumed that the IOPs of the water did not change significantly while making a measurement of reflectance.

In order to invert the reflectance model for IOP concentrations, a predictor-corrector algorithm is used. The algorithm works by making an initial prediction of the contributions of each IOP to the reflectance. These are entered into the model, and the R_{rs} is calculated from the reflectance model. The R_{rs} measured by the DALEC is also passed to the algorithm, where it compares the model predicted R_{rs} with the measured one. The magnitude of each IOP is then corrected in order to find the closest match possible between the measured and modelled R_{rs}. The the IOP inputs that produce the closest

R_{rs} match are the quoted results. The process is referred to as optimisation. The optimisation routine is described below in Section 5.4.1.

5.4.1 Optimisation

The specific method of solving the optical model used in this project is the Levenberg–Marquardt method (LM-fit) (Press et al., 2007). Before understanding the LM-fit method it is necessary to define three main functions. They are, the chi-square merit function ($\chi^2(\mathbf{a})$), which is a measure of how accurate the approximation is based on the difference between modelled and measured values; the Hessian matrix ($\mathbf{D}$), which is the second derivative of $\chi^2(\mathbf{a})$; and the steepest descent formulae δa.

The $\chi^2(\mathbf{a})$ merit function (Press et al., 2007) is:

$$\chi^2(\mathbf{a}) = \sum_{i=0}^{N-1} \left[\frac{y_i - y(x_i|\mathbf{a})}{\sigma_i} \right]^2 \tag{5.68}$$

Where:

$y = y(x|\mathbf{a})$ is the function to be solved
$\mathbf{a}$ is a vector of parameters that LM-fit is trying to solve for
σ is the standard deviation.

In our case, $y(x|\mathbf{a})$ is the reflectance model, y is the DALEC measured reflectance and $\mathbf{a}$ is the vector of IOP parameters.

The gradient of $\chi^2(\mathbf{a})$ with respect to parameters $\mathbf{a}$ Press et al. (2007) is:

$$\frac{\partial \chi^2}{\partial a_k} = -2 \sum_{i=0}^{N-1} \frac{[y_i - y(x_i|\mathbf{a})]}{\sigma_i^2} \frac{\partial y(x_i|\mathbf{a})}{\partial a_k} \; k = 0, 1, ...M - 1 \tag{5.69}$$

Which describes the rate at which a change in parameters will converge to a solution.

And the second-order partial derivative that defines the Hessian matrix $\mathbf{D}$:

$$\frac{\partial^2 \chi^2}{\partial a_k \partial a_l} = 2 \sum_{i=0}^{N-1} \frac{1}{\sigma_i^2} \left[\frac{\partial y(x_i|\mathbf{a})}{\partial a_k} \frac{\partial y(x_i|\mathbf{a})}{\partial a_l} - [y_i - y(x_i|\mathbf{a})] \frac{\partial^2 y(x_i|\mathbf{a})}{\partial a_l \partial a_k} \right] \tag{5.70}$$

Which is used to calculate how fast the algorithm is converging to a solution. The Hessian matrix is used to vary the IOP input parameter steps with each iteration.

It is convenient to define:

$$\beta_l \equiv -\frac{1}{2} \frac{\partial \chi^2}{\partial a_k} \qquad \alpha_{kl} \equiv \frac{1}{2} \frac{\partial^2 \chi^2}{\partial a_k \partial a_l} \tag{5.71}$$

The steepest descent function is then defined by:

$$\delta a_l = C \times \beta_l \tag{5.72}$$

Where:

C is a constant

δa_l is the amount estimated to increase or decrease the parameters with each new iteration

This can be represented by a system of linear equations by:

$$\sum_{l=0}^{M-1} a_{kl} \delta a_l = \beta_k \tag{5.73}$$

Which defines the changes needed to be made to the initial estimates to converge to a solution by the fastest descent in solution space. LM-fit attempts to find λ by varying smoothly from the inverse-Hessian method (Press et al., 2007) and the steepest descent method. The steepest descent method is used far from a minimum in solution space and the inverse-Hessian method is used as it gets closer to a solution. LM-fit is considered to have found a solution when the gradient of the $\chi^2(\mathbf{a})$ value is 0.

Looking back at Equation 5.37, which defines the absorption and backscattering terms of the reflectance model (HOPE), and expanding the absorption and backscatter terms, it is possible to parameterise each term that are being solved for, as shown in Equation 5.74.

$$u \approx \frac{b_w(\lambda) + b_p(\lambda, X)}{[a_w(\lambda) + a_y(\lambda, G) + a_\phi(\lambda, P)] + [b_w(\lambda) + b_p(\lambda, X)]} \tag{5.74}$$

P,G and X are now the parameters that make up, **a**, in LM-fit. When LM-fit returns values for these constants, they show relatively how much of each absorption or backscattering term contributes to the total R_{rs}. If the model (HOPE) accurately represents R_{rs}, these values are correlated with concentration levels of the water's IOPs.

The general LM-fit approach is as follows:

1. Predict values for P, G and X, these are used as the starting values.
2. Compute $\chi^2(\mathbf{a})$ for the DALEC measured and HOPE calculate R_{rs}
3. Pick any starting value for C
4. Solve Equation 5.73 for δa and evaluate $\chi^2(\mathbf{a} + \delta\mathbf{a})$
5. If $\chi^2(\mathbf{a} + \delta\mathbf{a}) \geq \chi^2(\mathbf{a})$ increase C by a factor of 10. Repeat previous step.
6. If $\chi^2(\mathbf{a} + \delta\mathbf{a}) < \chi^2(\mathbf{a})$ decrease C by a factor of 10, update the trial solution $\mathbf{a} \leftarrow \mathbf{a} + \delta\mathbf{a}$ and go back to step 3.

There are a number of caveats with this method. If there is more than one possible solution, then it is possible that the algorithm does not find the 'real-world solution' (a solution that does not represent the 'true' values); rather, one of the other possible solutions. By adding more IOP parameters into a reflectance model, the more potential IOP concentrations can be solved for. However, this means that there is potentially also a greater number of possible solutions and increases the chance of finding an incorrect one. The possibility of this happening is reduced by making an accurate prediction about the water property concentrations in step 1. The closer the initial prediction, the less likely the wrong solution will be found. In this study, it was found that the number of IOP parameters had to be restricted to just three (P, G and X) in order to avoid converging on solutions that were not representative of the measured conditions. I.e. the model converged to a local minimum in the solution space rather than the global one. In order to improve the accuracy further, the model was re-run by passing only a single parameter (P) to the algorithm. This is discussed in detail in Section 6.7.14.

The LM-fit algorithm for this project was written in Python, its procedure can be found in (Press et al., 2007, page 803).

LM-fit is not the fastest algorithm capable of finding a solution to this kind of problem; however, it is very robust at finding the correct solution provided the initial estimate is a close approximation of the solution.

5.4.2 Confidence Intervals

The goal of this next section is to find a definitive uncertainty for the IOP measurements. Uncertainty comes from three main sources. The natural variability in the environment is very difficult to account for, the presence of varying cloud cover, water-surface facets due to wind and the natural variability in water constituents over a sample period all contribute the environmental factors of uncertainty. Factors such as electrical noise, variation in instrument temperature and changing measurement angle account for instrumentation uncertainty. The final source of uncertainty comes from how well the radiative transfer model represents the local environment. HOPE was designed for ocean water and tested with data taken from measurements along west Florida shelf (Lee et al., 1999). It is likely the IOPs of the Swan River differ and, therefore, the model may not represent the Swan River conditions.

When solving the HOPE using LM-fit, one of the returned values is the covariance matrix, representing the covariance of IOP parameters, which can be used to calculate the uncertainties of retrieved parameters. However, in order to use the covariance matrix, a few assumptions must be made. First of all, in order to calculate the covariance matrix, LM-fit requires the standard deviation of each measurement of wavelength of reflectance. Because any spectrum produced by the DALEC is only one instantaneous measurement, a distribution of all possible 'realisations' is impossible to produce. It is possible to make educated assumptions in terms of what the standard deviation would be if it were possible to measure all realisations. To do this, it is first assumed that the instantaneous measurement is the mean value of all possible 'true' values and that if it were possible to make many instantaneous measurements the values would produce a normal distribution around that mean value. It is then assumed that the measurement uncertainty represents the standard deviation of the theoretical distribution. Therefore, when defining the chi-square merit function, the standard deviation is assumed to represent as the

uncertainty of that measurement. Because LM-fit is only concerned with minimising the change in χ^2, the absolute value of χ^2 does not affect the parameter retrievals greatly, unless a local minimum is found. However, if the uncertainty value does not accurately predict the standard deviation of the natural variability in the data, the χ^2 value and parameter covariance that LM-fit returns is effectively meaningless as it also will not be a true representation of the natural variability. If the covariance matrix does not represent the covariance of measured IOPs, it cannot be used to calculate the uncertainty.

The measurement and instrument uncertainty of DALEC measurements and predictions of phytoplankton are described in detail in Section 5.5, which describes how the confidence intervals are found from the optimisation method. Section 5.5 describes how these confidence intervals are used to determine the field uncertainty measurements.

Because the covariance is a measure of the natural variability of the 'true' parameters, it was predicted that if the DALEC was pointed at the same patch of water while holding as many variables (such as sensor geometry and environmental conditions) as constant as possible, it should produce a distribution of parameters when inverted that represent the in-water IOPs. In the purely theoretical case, because it was the same patch of water that did not change significantly, LM-fit should retrieve the same parameter values for every spectral measurement. In reality, small perturbations in instrument noise, water surface, water currents, measurement geometry, etc., produce small changes in the measured reflectance. An example of this can be seen in Figure 5.20. Repeated inversion of these reflectance data produce a distribution of possible IOP parameters. This distribution can be used to define the covariance matrix and, therefore, infer the uncertainties of the inverted IOPs. Many examples of this are shown in Section 5.5.

Once the covariance matrix had been defined, the method outlined in Press et al. (2007) was used to find the uncertainties and confidence limits. The technique is summarised here (Press et al., 2007, page 815):

1. Let N be the number of parameters whose joint confidence region is to be displayed.
2. Let p be the pre-defined confidence limit, e.g. 0.95.
3. Find Δ such that the probability of a chi-square variable with N degrees of freedom being less than Δ is p. Useful values are given in (Press et al., 2007, page 815).
4. Take the $M \times M$ covariance matrix of IOPs $\mathbf{C} = \alpha^{-1}$ of the chi-square fit. Copy the

intersection of the N rows and columns corresponding to the inverted IOPs into a $N \times N$ matrix denoted $\mathbf{C}_{proj}$.

5. The equation for the elliptical boundary of the desired confidence region in the N-dimensional subspace of interest is:

$$\Delta = \delta\mathbf{a}\ \mathbf{C}_{proj}^{-1}\ \delta\mathbf{a}' \tag{5.75}$$

The method discussed here was used to define the confidence intervals in Section 5.5.4 and draw the error ellipses in figures 6.30, 6.32, and 6.34. This method was also used in Chapter 6.7 to defind the uncertainty boundaries of the transects in figures 6.90, 6.91, 6.92 and 6.96.

5.5 Coherent Noise Modelling for Uncertainty Estimates of Remote Sensing Data

Estimating uncertainties in remotely sensed environmental parameters presents a challenge, especially as repeated measurements are sometimes difficult to make and noise is produced variously from different environmental and instrument sources. The method, outlined in the previous section, used to calculate the uncertainties of the inverted IOPs, is a useful method for calculating an uncertainty for a single reflectance measurement. It assumes that a single measurement is the mean value of a distribution of all possible realisations. A common estimation method (Press et al., 2007) describes a generic method of estimating uncertainties by generating random synthetic measurements by randomly perturbing model inputs by a small percentage of random noise, then optimising by minimising a cost function and then generating surrogate input parameters. When this process is repeated often enough a distribution of surrogate parameters is generated and the deviation of the distribution is used to infer an uncertainty for the 'true' parameter. When applying this general case to this project, it is unlikely to result in perturbations that reflect the real world, due to the mismatch between modelling, using spectrally random noise, and the effects of natural variability in optical properties being spectrally coherent. It is insufficient to randomly perturb the reflectance and expect this to mimic natural variations found in nature.

In the following section, we build upon the idea of producing surrogate parameters (IOPs in this case) by perturbing the reflectance in a way that is representative of variations in R_{rs} seen in repeat field measurements. The difference between previous Monte-Carlo

methods, and the method we describe in this section is, rather than perturbing the reflectance by random noise, we build a model of coherent noise from a training set of data. The following sections describes a method of perturbing the reflectance that is used to generate synthetic reflectance data that is more representative of natural variations found in field measurements than random perturbations alone. By measuring natural variations in R_{rs}, we produce a power spectrum that can, in turn, be used to generate random synthetic reflectance data. There are a number of reasons this method is useful in this project. Firstly, making repeat measurements at the SCCP locations of R_{rs} makes it possible capture the variations in R_{rs} due to changing environmental conditions and model their effect on the R_{rs}. Secondly, repeat measurements can be made at the SCCP locations while water samples are being collected, but not while making way along the transect. This method allows the coherent noise model, calculated at the sample locations, to be applied to the R_{rs} measurements made between the sample locations, while the boat is making way. Furthermore, the coherent noise model makes it possible to generate many more realisations of reflectance than would be practical to measure. For example, 2400 modelled reflectance, given the symbol in this thesis $\hat{R}_{rs}$, are generated from approximately 50 repeat measurements (50 after filtering erroneous data). If each measurement took one second to make, 2400 R_{rs} samples would take 40 minutes to collect at each SCCP site. This would be far to long and would mean the transect could not be completed in a day. The advantage of generating 2400 $\hat{R}_{rs}$ is that after inverting all spectra, a statistical distribution of IOPs can be generated and the covariance matrix calculated over a range of IOPs. Not only does this method provide more values of IOPs in which to derive statics from, it was found that it reduced the probability of this method finding a local, incorrect, solution. It was found that at some locations a single optimisation was able to converge to a local minimum in solution space, but the majority of the ensemble did not. Because the average inverted IOP parameters are the reported ones, the majority of optimised IOP parameters, which do not converge to the local minimum, prevents the incorrect values (the ones in the local minimum) from being reported. This is discussed more at the end of this section.

5.5.1 Uncertainty calculation methodology

The purpose of this coherent noise method is to estimate the uncertainties on the range of possible IOP parameters for a single measurement of R_{rs}.
The process of generating a set of synthetic R_{rs} would be extremely slow using modelling

packages such has Hydrolight and PlanarRad and it would be impractical to do this for every single measurement. This approach to estimating confidence intervals presented here is, therefore, extended so that a method for generating realisations can be achieved without the need for complex modelling packages.

A naive approach to generating synthetic realisations would be to generate random noise within the uncertainty range of the DALEC measured R_{rs} and multiply the noise with the measurement, repeating for as many iterations required in order to generate statistically valid data set. The problem with this approach is that random perturbations in 'nature' do not happen completely randomly, in respect to one reflective band to another. Naturally occurring variations in CDOM, for example, will affect the blue part of the spectrum more than the red. Furthermore, it is logical to assume that wavelengths that are close together will vary with much higher correlation that wavelengths that are far apart. Or, to be more accurate, certain wavelengths will be highly correlated and others will not. In the case of phytoplankton, there are pigments, such as chlorophyll-a, that absorb more at ∼440 nm and ∼676 nm. Therefore, naturally occurring variances in chlorophyll-a should affect variances in both 440 nm and 676 nm wavelengths. It may be found, therefore, that 440 nm and 676 nm are highly correlated.

It is this correlation that should be adhered to when randomly perturbing values. This is done by finding the power spectrum (also known as the power spectrum density (PSD) function) of a training set of data and the PSD function to generate the random perturbations or 'noise'. The PSD is a measure of the distribution of the variance over the cumulative signals. In fact, the autocovariance can be found by calculating the inverse Fourier transform of the PSD. The autocovariance (Figure 5.25) will describe, in this case, how the components in the Fourier domain vary with each other, including the correlation length. In this case, the cumulative signals are repeat measurements of R_{rs} at a single SCCP location.

Once the PSD function has been modelled, new artificial realisations can be generated very quickly without the need for computationally expensive PlanarRad runs. If a training set is chosen that mimics the natural variability expected in the field, the correlated noise model can be used to accurately generate synthetic realisation of R_{rs} which can be used to estimate the variance of the IOP parameters and infer confidence intervals and measurement uncertainty.

Assumptions:

- The DALEC measured reflectance spectra variance is well characterised. This can be estimated by making repeat measurements at a single location.
- The IOPs in the study area do not vary wildly in spectral shape while repeat measurements are being made.
- IOPs can be modelled accurately using bio-optical models or are known from laboratory measurements.
- Uncertainties in laboratory measured IOPs are small when compared to uncertainties derived from DALEC measurements.

Summary of method: Training Stage

- Choose a phytoplankton spectrum that best represents the absorption spectral shape, this may be obtained from laboratory measurements.
- Define a set of training R_{rs} that captures the natural variance seen in field measurements. In this study this was achieved by making repeat measurements of R_{rs} at the SCCP sample locations while the boat was stationary and water samples were collected. Careful attention was made to keep the sensor pointing at the same point of the water surface.
- Detrend the ensemble average of all the reflectance spectra:

$$\mu_{R_{rs}}(\lambda) = \frac{1}{n}\sum_{i=1}^{n} R_{rs_i}(\lambda) \tag{5.76a}$$

$$\Delta_{Rrs}(\lambda) = \langle R_{rs}(\lambda)\rangle - \mu_{R_{rs}}(\lambda) \tag{5.76b}$$

- Calculate the standard deviation:

$$\sigma_{\Delta_{Rrs}(\lambda)} = \sqrt{\frac{1}{n}\sum_{i=1}^{n}\left(R_{rs_i} - \mu_{R_{rs}}\right)^2} \tag{5.77}$$

- Calculate the normalised difference of the standard deviation:

$$\bar{\Delta}_{Rrs}(\lambda) = \frac{\Delta_{Rrs}(\lambda)}{\sigma_{\Delta_{Rrs}(\lambda)}} \tag{5.78}$$

- Calculate the power spectrum:

$$Y = \mathcal{F}\{\bar{\Delta}_{rs}(\lambda)\} \tag{5.79a}$$

$$S_{\lambda\lambda} = \langle YY^* \rangle \tag{5.79b}$$

Summary of method: Generation Stage

- For each wavelength, generate k random points between -0.05 and 0.5, where k is the number of synthetic measurements to be generated

$$n = rand(k, \lambda)_{-0.5}^{0.5} \tag{5.80}$$

- Calculate the Fourier transform of n

$$N = \mathcal{F}\{n\} \tag{5.81}$$

- Multiply the Fourier transform of the random points by the square root of the power spectrum

$$Y = N\sqrt{S_{YY}} \tag{5.82}$$

- Transform the correlated noise to the real domain by taking the inverse Fourier transform

$$y(\lambda) = \mathcal{F}^{-1}\{Y\} \tag{5.83}$$

- Normalise the correlated noise in the real domain

$$\hat{y}(\lambda) = \frac{y(\lambda)}{\sigma_y} \tag{5.84}$$

- Multiply the standard deviation of the measured R_{rs} by the normalised correlated noise

$$z(\lambda) = \hat{y}(\lambda)\sigma_{\Delta_{rs}}(\lambda) \tag{5.85}$$

- Generate synthetic R_{rs} by adding any measured single R_{rs} with $z(\lambda)$

$$\hat{R}_{rs}(\lambda) = R_{rs} + z(\lambda) \tag{5.86}$$

Summary of method: Solution stage

- For each synthetic $\hat{R}_{rs}$ invert the optical model using the LM-fit algorithm described in Section 5.4.1.
- Follow the steps outlined in Section 5.4.2 to calculate the uncertainty boundaries, except when calculating correlation matrix $\mathbf{C}$, the correlation is calculated from the ensemble $\langle \mathbf{C} \rangle$. This defines the uncertainty boundaries across all of the realisations.

Figure 5.19 shows a flow diagram showing a pictorial description of the coherent noise method.

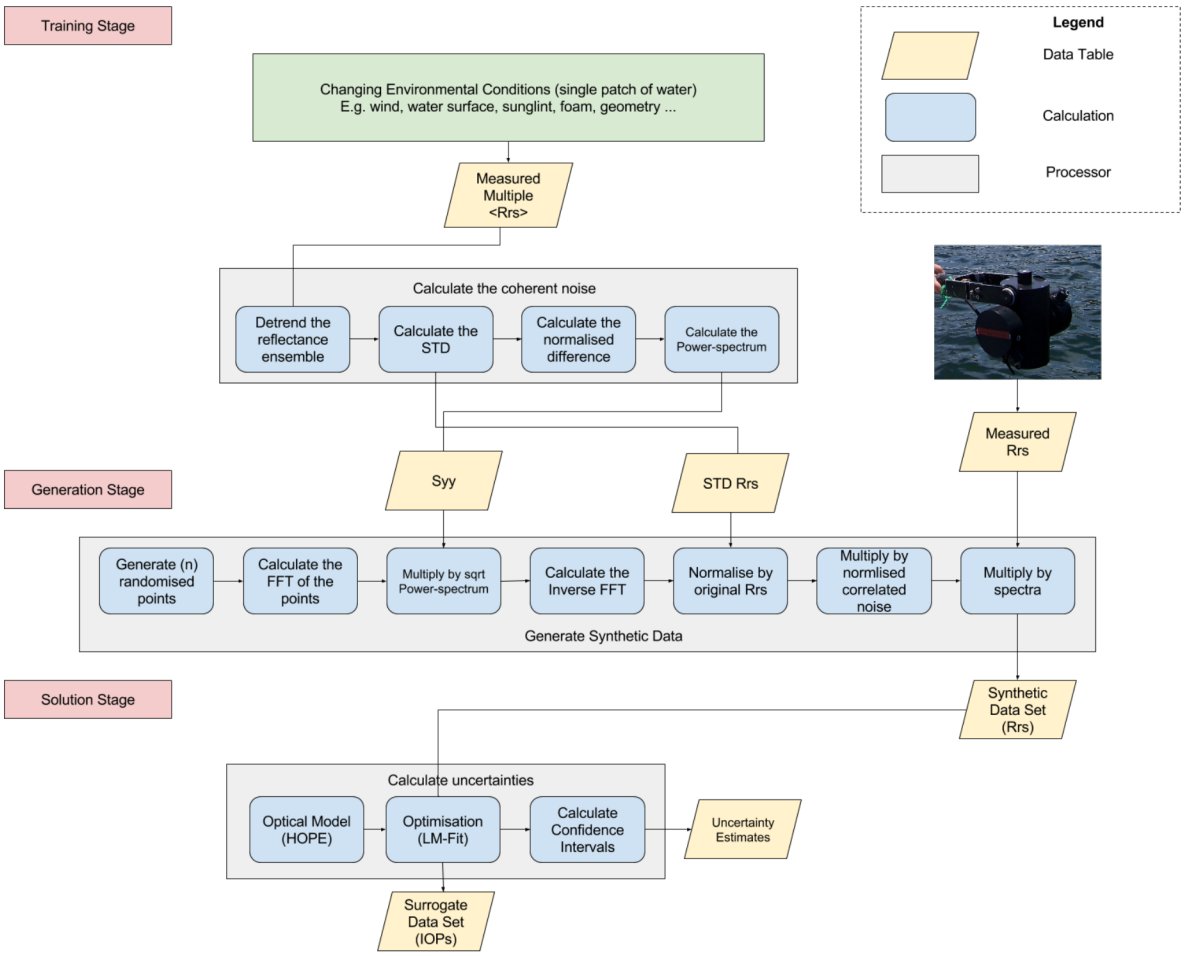

Figure 5.19: Data flow diagram for the coherent noise method.

An example of using the coherent noise method is described in the following section.

5.5.2 Training Stage

In order to capture the naturally varying environmental conditions and their effect on the reflectance spectrum, repeat measurements of R_{rs} at a single location in the river were made. In the ideal scenario, making repeat measurements at the same locations would yield the same spectra. In practice, changes in the water surface, rocking of the boat and reflections of trees on the river bank (to name only a few) mean that the spectra will change independently of the IOPs. It is these variations that are captured by taking repeat measurements. By modelling these changes, through the training stage, these naturally occurring variations can then be propagated through the synthetic data sets and used to infer uncertainties in the retrieved IOPs. The method of modelling these variations is described below. This section uses one SCCP location (ARM) as an exemplar. The process was repeated for all of the SCCP locations on the Swan River. These results are shown in Section 6.7.3.

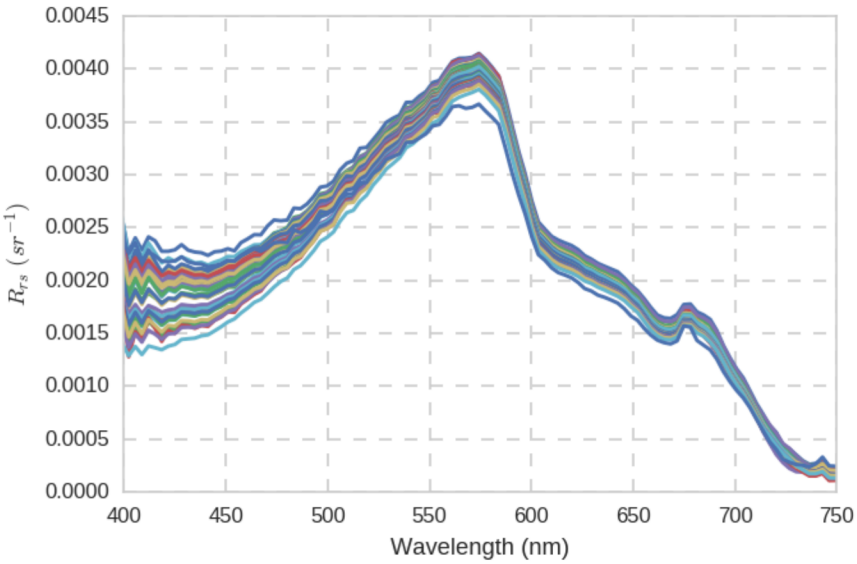

Figure 5.20: Repeat spectral measurements, at at stationary location, taken at the ARM sample location.

Figure 5.20 shows the spectra, measured by the DALEC at ARM, from a stationary boat. Approximately 100 spectra were measured. After filtering for erroneous data (described

in Section 6.7.3), 50 measurements remain. These 50 measurements were used to train the coherent noise model.

Calculate $R_{rs}(\lambda)$ by subtracting the ensemble average:

$$\mu_{R_{rs}}(\lambda) = \frac{1}{n}\sum_{i=1}^{n} R_{rs_i}(\lambda)$$

$$\Delta_{Rrs}(\lambda) = \langle R_{rs}(\lambda)\rangle - \mu_{R_{rs}}(\lambda)$$

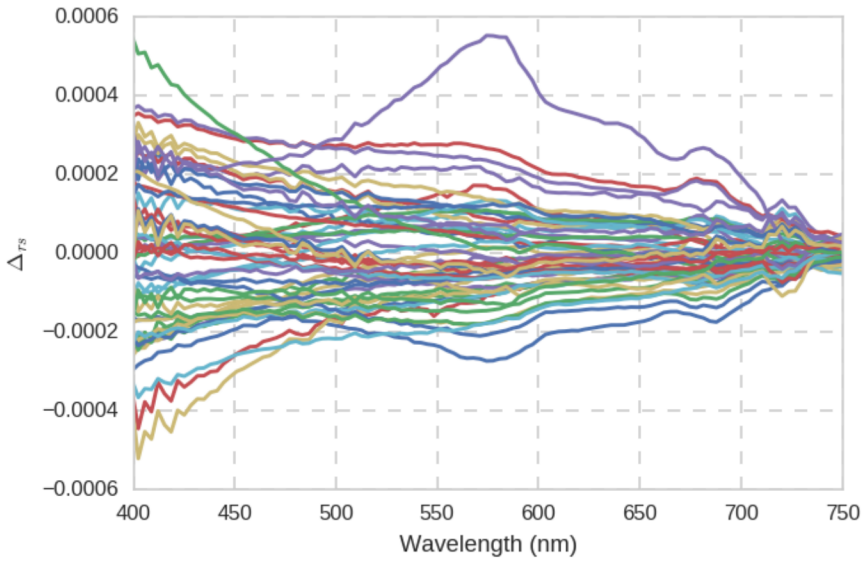

Figure 5.21: The R_{rs} after detrending by subtracting the mean reflectance of the ensemble average.

Figure 5.21 shows the reflectance data after the mean ensemble average, for each wavelength, is subtracted from every spectrum.

Calculate standard deviation of $\Delta_{rs}(\lambda)$:

The standard deviation of each $\Delta_{rs}(\lambda)$ was calculated at each wavelength. The result is shown in Figure 5.22. The figure shows that most of the variability of spectra is in the blue part of the spectrum. There is also an increase in variation around 575 nm, where there is a turning point in all of the spectra.

$$\sigma_{\Delta_{Rrs}(\lambda)} = \sqrt{\frac{1}{n}\sum_{i=1}^{n}(R_{rs_i} - \mu_{R_{rs}})^2}$$

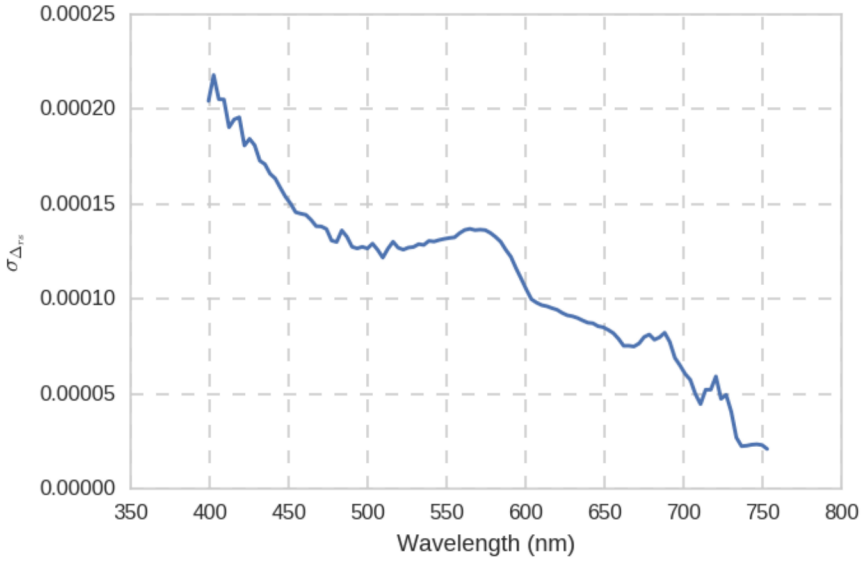

Figure 5.22: The standard deviation of the detrended ensemble average.

Calculate the normalised difference.

The purpose of the next few steps is to calculate the power spectrum of the measured R_{rs} spectra. In order for the statistics of the power spectrum to be correct, the standard deviation at each wavelength must be the same (Press et al., 2007) i.e. the spectrum must be 'stationary'[6]. A convenient method of making sure this remains true is, to divide spectra by the standard deviation at each wavelength.

$$\bar{\Delta}_{rs}(\lambda) = \frac{\Delta_{rs}(\lambda)}{\sigma_{\Delta_{rs}(\lambda)}}$$

This will ensure that the standard deviation of each wavelength is equal to one. The actual standard deviation at each wavelength is temporarily stored and added back at a later stage in the process.

[6]In this case, the term stationary refers to the statistical definition which states that a stationary signal's mean or variance does not change over time.

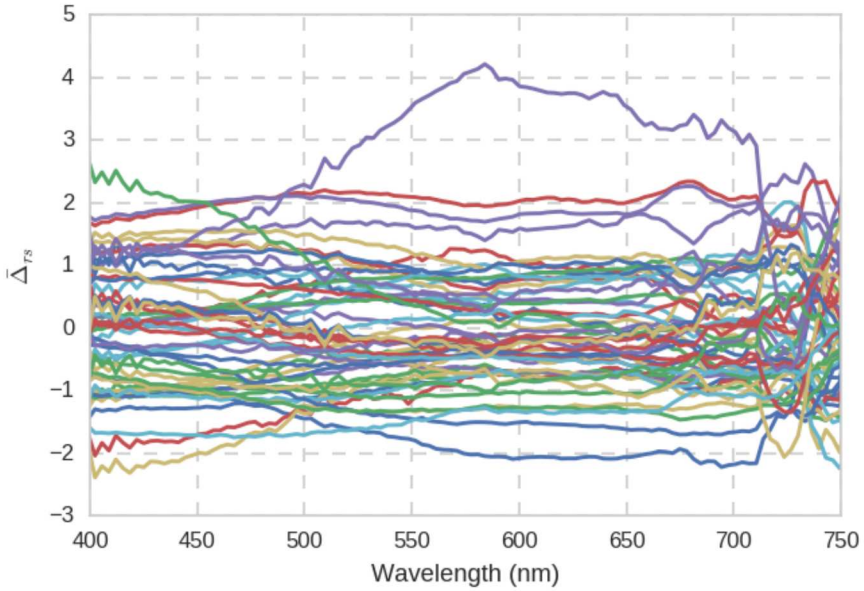

Figure 5.23: The 'stationary' reflectance normalised by dividing each spectra by the standard deviation.

Calculate the power spectrum

The power spectrum is calculated by multiplying the Fourier transform of the normalised difference ($\bar{\Delta}_{rs}$) with the complex conjugate of itself and averaging the results:

$$Y = \mathcal{F}\{\bar{\Delta}_{rs}(\lambda)\}$$

$$S_{\lambda\lambda} = \langle YY^* \rangle$$

The resulting power spectrum is used in later steps to generate a correlated noise model in which synthetic realisation of R_{rs} will be generated.

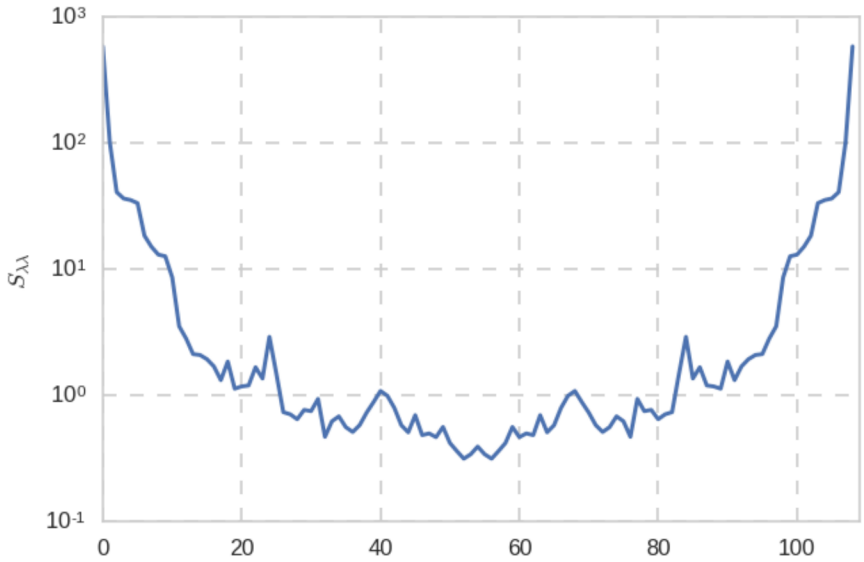

Figure 5.24: The power spectrum of the ensemble.

The power spectrum, shown in Figure 5.24, is a measure of how much relative energy at each wavelength of light is captured by all of the previous measurements. This energy will be convolved with random perturbations at each wavelengths to reproduce spectra analogous to the spectra measured at the sample sites.

The autocovariance function, not used in the algorithm, is shown in Figure 5.25, which shows how the Fourier components contribute to the power spectrum. It can be seen that

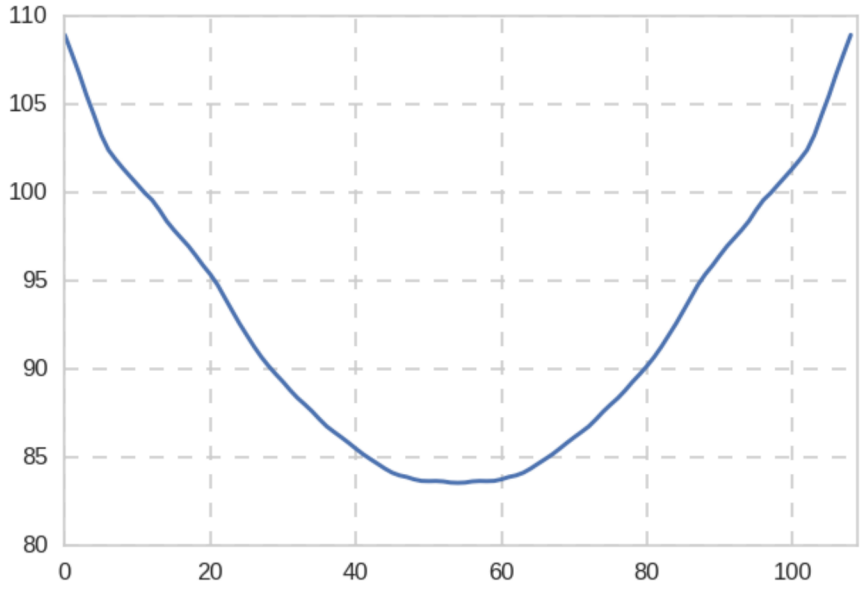

Figure 5.25: The correlation function of the ensemble.

5.5.3 Generation Stage

For each wavelength we wish to randomly generate a value within the defined variance of the reflectance at that wavelength. To do this, first generate random numbers n between -0.5 and 0.5. As a first approximation, a random distribution is used, but the distribution that is used should conform to the distribution that the IOPs conform too. This is usually unknown without numerous repeat measurements, so a random distribution is used as a first guess. The actual distribution is subject to further investigation. These random values will be scaled by the power spectrum in later steps in the process. The power spectrum is a function that models the natural variations seen in the training set. When the randomly generated points are multiplied by by the power spectrum, these statistical natural variations are propagated through the synthetic data. The random points mean that each synthetic $\hat{R}_{rs}$ will be different, but hopefully, will still be within the minimum and maximum R_{rs} bounds seen in the training data. This is the case for nearly all $\hat{R}_{rs}$ and will be shown when comparing figures 5.33 and 5.34 in the following section.

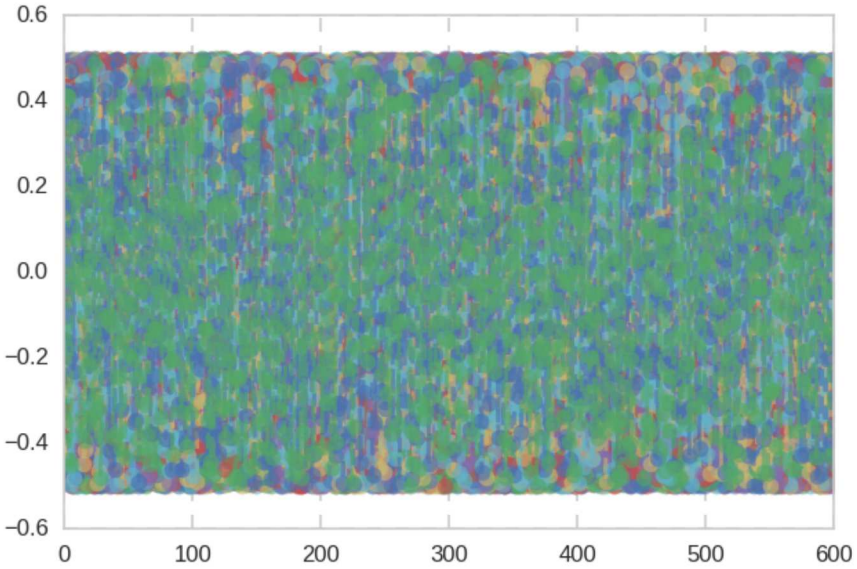

Figure 5.26: Random data points generated for each spectra at each wavelength.

Figure 5.26, shows the randomly generated data points for each wavelength. The number of data points at each wavelength is equal to the number of synthetic spectra generated.

Calculate the Fourier transform of of the random points

Before the random values can be scaled by the power spectrum, they must be transformed into the Fourier domain by taking the Fourier transform of the randomly generated numbers.

$$N = \mathcal{F}\{n\}$$

The number of synthetic data points, shown in the example here, is 600. This number is kept low in order to keep the figures displayed in this section from being too crowded. The results presented in Section 6.7.3, were based on generating 2,400 synthetic data points for each single R_{rs} measurement made.

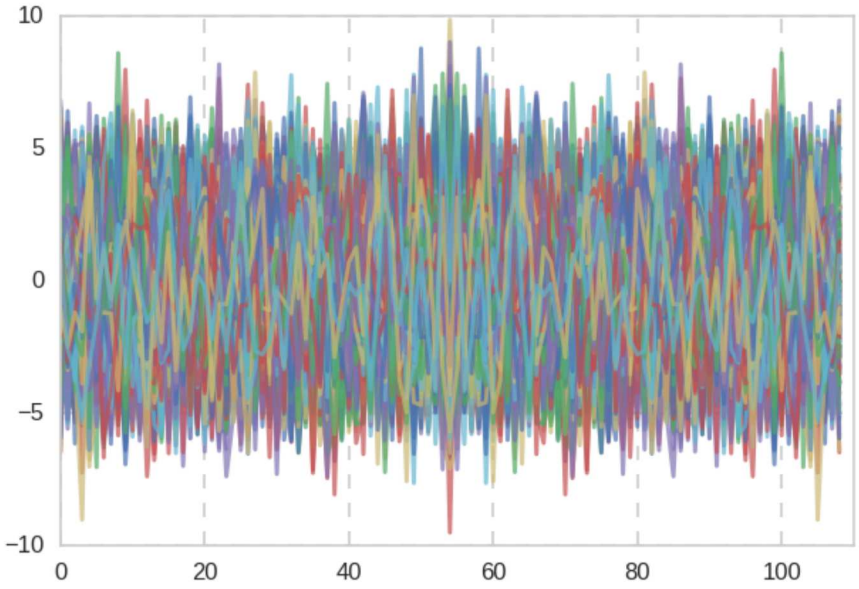

Figure 5.27: The random point transformed to the Fourier domain by taking the FFT of the random points.

Multiply the Fourier transform of n by the square root of the power spectrum

Now that the random numbers, (N), have been transformed to the Fourier domain, they are multiplied by the square root of the power spectrum.

$$Y = N \times \sqrt{S_{\lambda\lambda}}$$

This results in random perturbations of the energy, at each wavelength, proportional to the measured R_{rs} at the river sampling site. The result is, correlated noise in the Fourier domain for each synthetic data point which is shown in Figure 5.27.

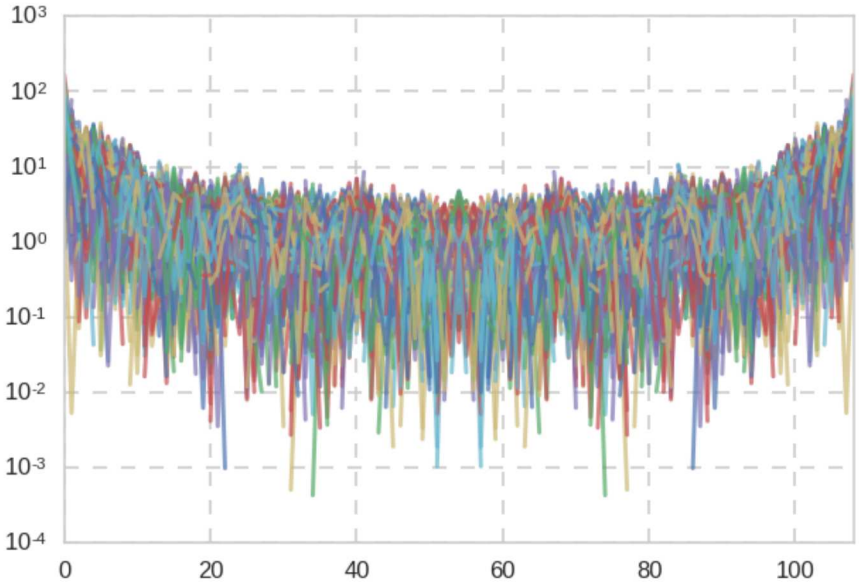

Figure 5.28: The Fourier transform of the randomly generated points multiplied by the power spectrum.

The resulting correlated noise (Y), shown in Figure 5.28, is transformed back to the real domain ($y(\lambda)$) by calculating the inverse Fourier transform shown in Figure 5.29.

$$y(\lambda) = \mathcal{F}^{-1}\{Y\}$$

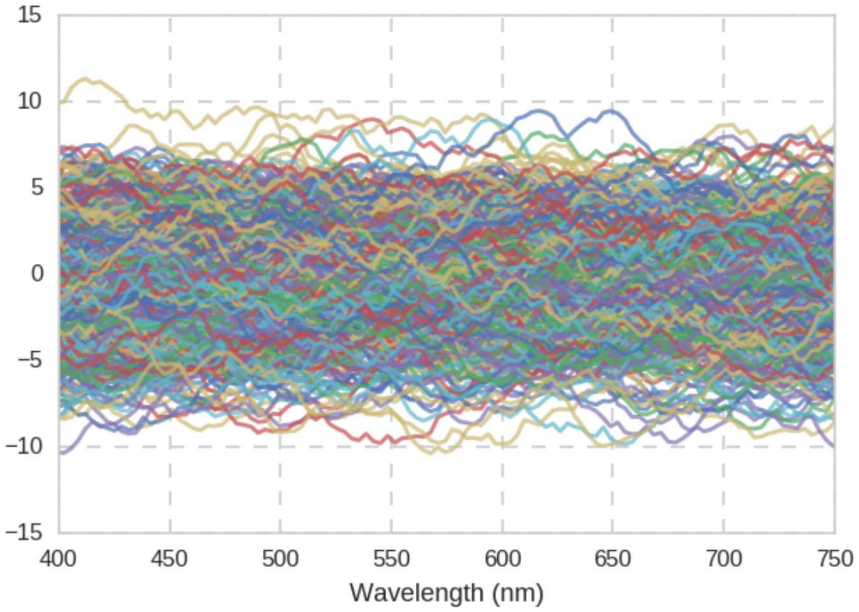

Figure 5.29: The correlated noise transformed back to the real domain by taking the inverse Fourier transform.

Normalise the difference

The R_{rs} at all the wavelengths of the correlated noise in the real domain must have a standard deviation of 1 so that they can be multiplied by the standard deviation of the original training set (Figure 5.20).

$$\bar{y}(\lambda) = \frac{y(\lambda)}{\sigma_y}$$

A standard deviation of one is achieved by dividing $y(\lambda)$ by the standard deviation of itself, producing $\bar{y}(\lambda)$ shown in Figure 5.30.

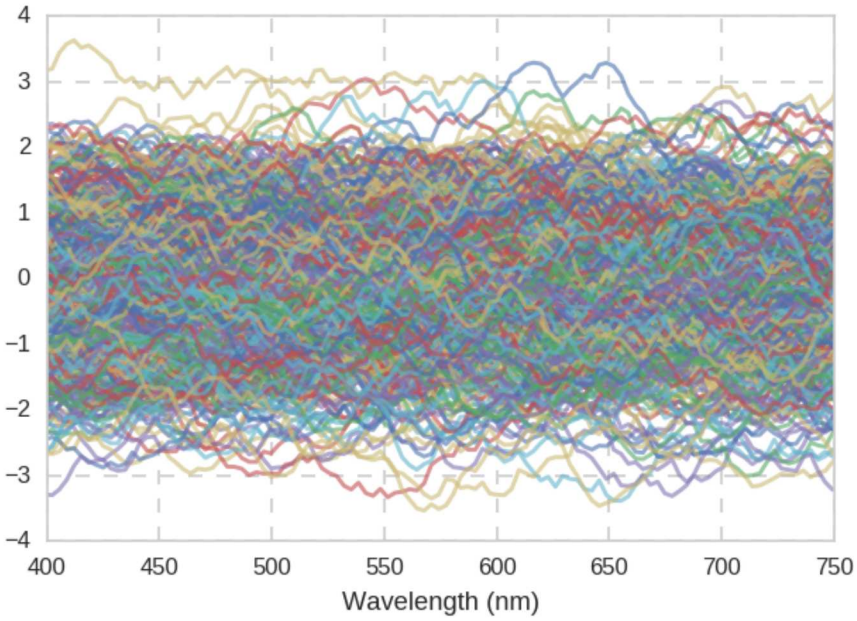

Figure 5.30: Normalised correlated noise calculated by dividing $y(\lambda)$ by the standard deviation of itself.

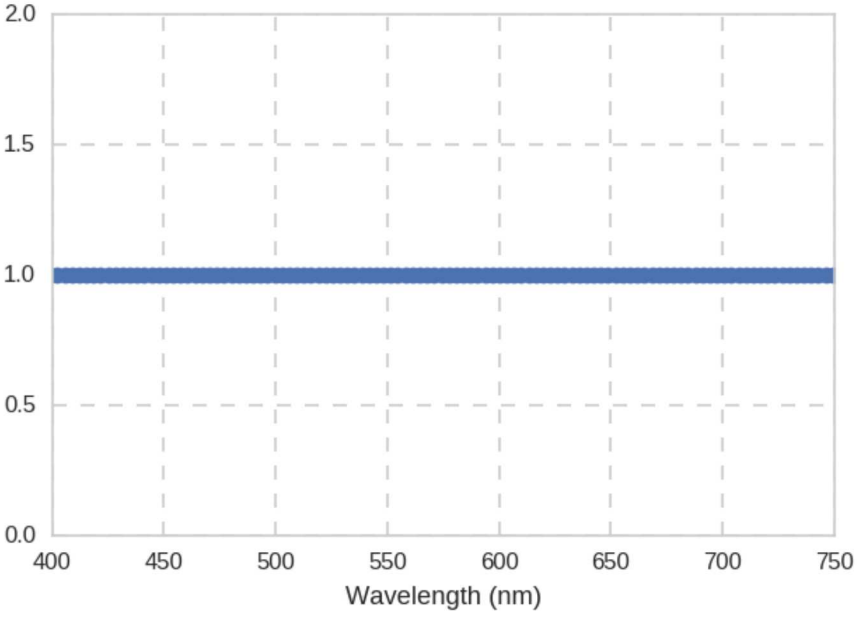

Figure 5.31: The standard deviation of the normalised correlated noise. All wavelengths should be 1. This step is taken to ensure that the process has been followed correctly so far.

The standard deviation is output from the algorithm (Figure 5.31) as a checkpoint. Figure 5.31 shows that the standard deviation of all the synthetic data points is 1 at all wavelengths as expected. The standard deviation of the original training set ($\sigma_{\Delta_{rs}(\lambda)}$) is then multiplied by the normalised correlated noise (Figure 5.32).

$$z(\lambda) = \bar{y}(\lambda)\sigma_{\Delta_{rs}(\lambda)}$$

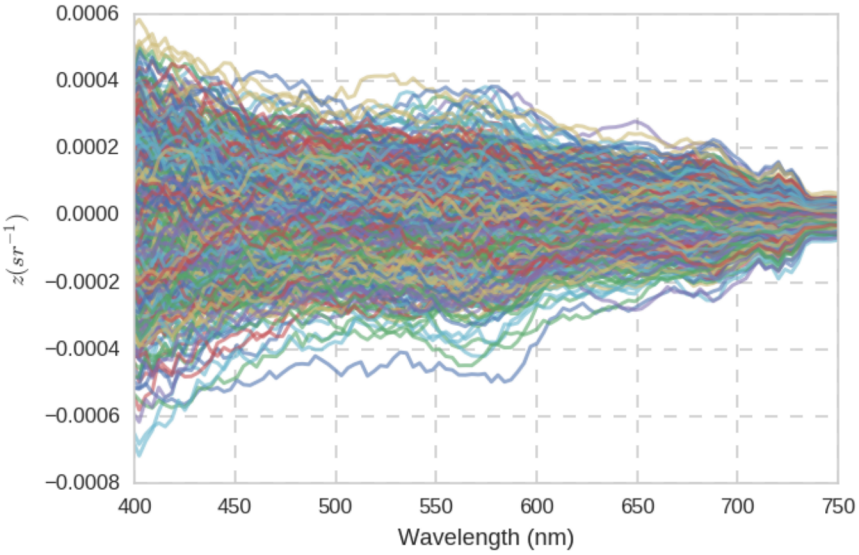

Figure 5.32: The detrended simulated reflectance data created by multiplying the normalised correlated noise by the standard deviation of the simulated R_{rs}.

Generate realisations of R_{rs}

The synthetic $\hat{R}_{rs}$ data are generated by adding back the mean R_{rs} value subtracted in the training stage.

$$\hat{R}_{rs}(\lambda) = \langle R_{rs}(\lambda) \rangle + z(\lambda) \tag{5.89}$$

The result set of $\hat{R}_{rs}$ spectra are shown in Figure 5.33. The R_{rs} from the training stage is shown in Figure 5.34 for easy comparison. When applying this coherent noise model to sites beyond the SCCP water sample locations, where repeat measurements of R_{rs} are not possible, the mean $\langle R_{rs} \rangle$ is replaced by the single DALEC measured R_{rs} that we wish to apply the model to. This is how the model is used to calculate the uncertainties between the SCCP sample locations, while the boat is under way.

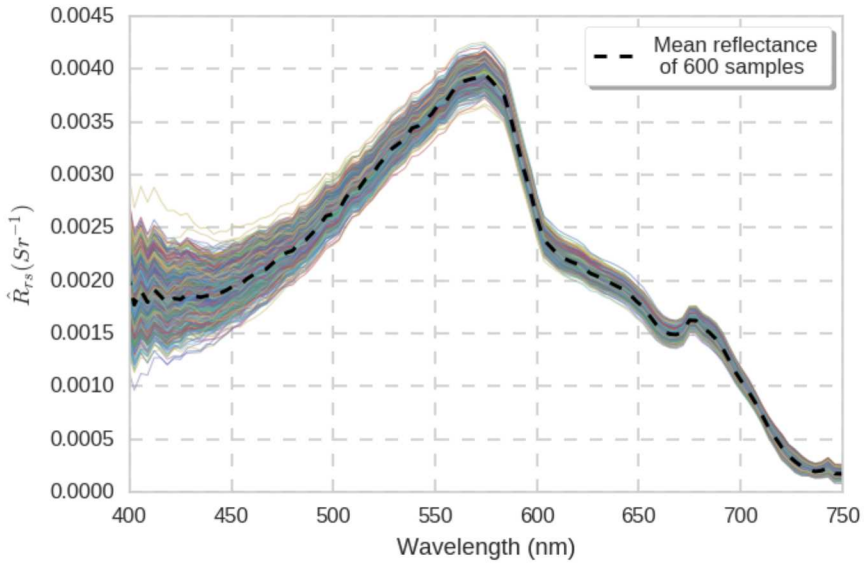

Figure 5.33: Simulated remote sensing reflectance generated by multiplying the detrended simulated reflectance by the reflectance spectra. Compare with 'real' R_{rs} spectra shown in Figure 5.34

.

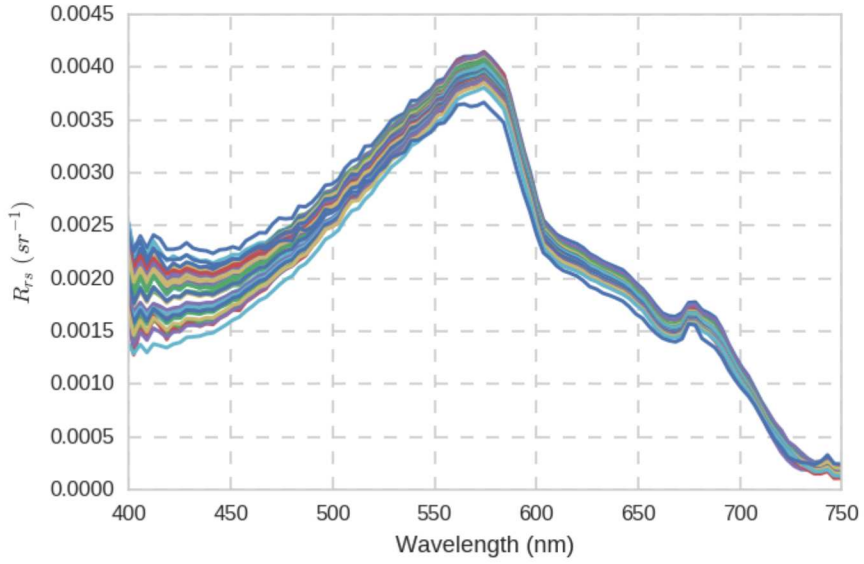

Figure 5.34: The original training R_{rs} data. Compare with synthetic $\hat{R}_{rs}$ shown in Figure 5.33

.

Figure 5.33 shows 600 simulated $\hat{R}_{rs}$ generated from only 50 measured R_{rs}. The simulated data were generated purely from the statistics of the training data and without the use of any radiative transfer modelling. The number of simulated points were restricted to 600 for these figures, as any more points simply crowd the diagrams. The results presented in Chapter 4 used 2400 realisations. The following section uses 2400 simulated $\hat{R}_{rs}$ for one of the Swan River sampling locations in order to produce a distribution of inverted IOP data.

5.5.4 Solution Stage

For the solution stage, 2,400 simulated data are generated from the 50 training R_{rs}. All of the simulated data are inverted to determine a_ϕ, a_g and b_{bp}. The results of using the coherent noise model for the data collected at ARM are presented below. Section 6.7.3 presents the results for the other river sites. For each synthetic $\hat{R}_{rs}$ the optical model is inverted using the LM-fit algorithm described in Section 5.4.1. The uncertainties and error ellipse boundaries are calculated the steps outlined in Section 5.4.2 boundaries. A slight change to the method is, when calculating correlation matrix $\mathbf{C}$, the correlation is calculated from the ensemble $\langle \mathbf{C} \rangle$. This defines the uncertainty boundaries across all of the realisations.

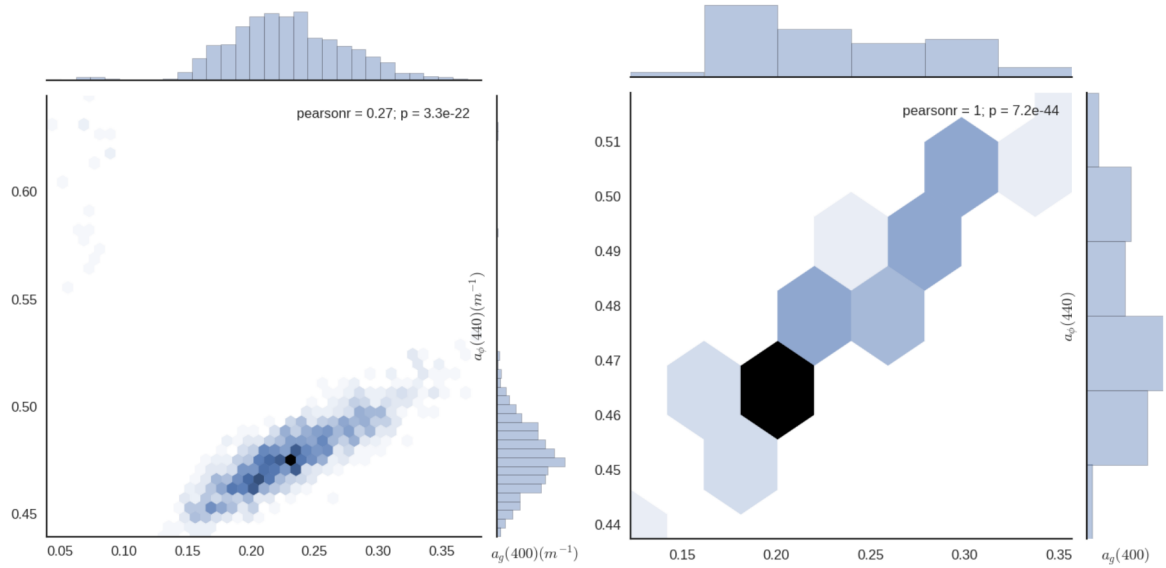

Figure 5.35: (Left) Hex-bin plot of a_ϕ vs a_g derived from the inverted simulated $\hat{R}_{rs}$. (Right) Hex-bin plot of a_ϕ vs a_g derived from the DALEC measured R_{rs} at ARM.

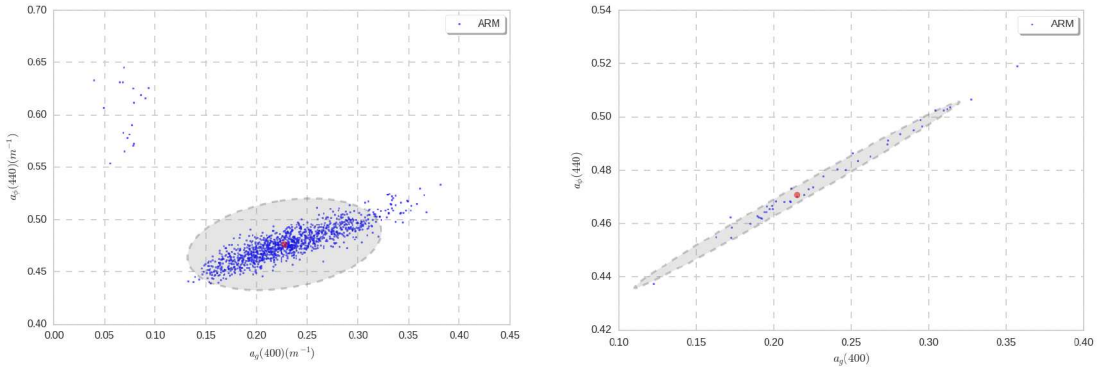

Figure 5.36: (Left) Scatter plot of a_ϕ vs a_g derived from the inverted simulated $\hat{R}_{rs}$. (Right) Scatter plot of a_ϕ vs a_g derived from the DALEC measured R_{rs} at ARM. Both plots show the errors ellipse which defines the 95% confidence boundary. The red point is the average IOP values.

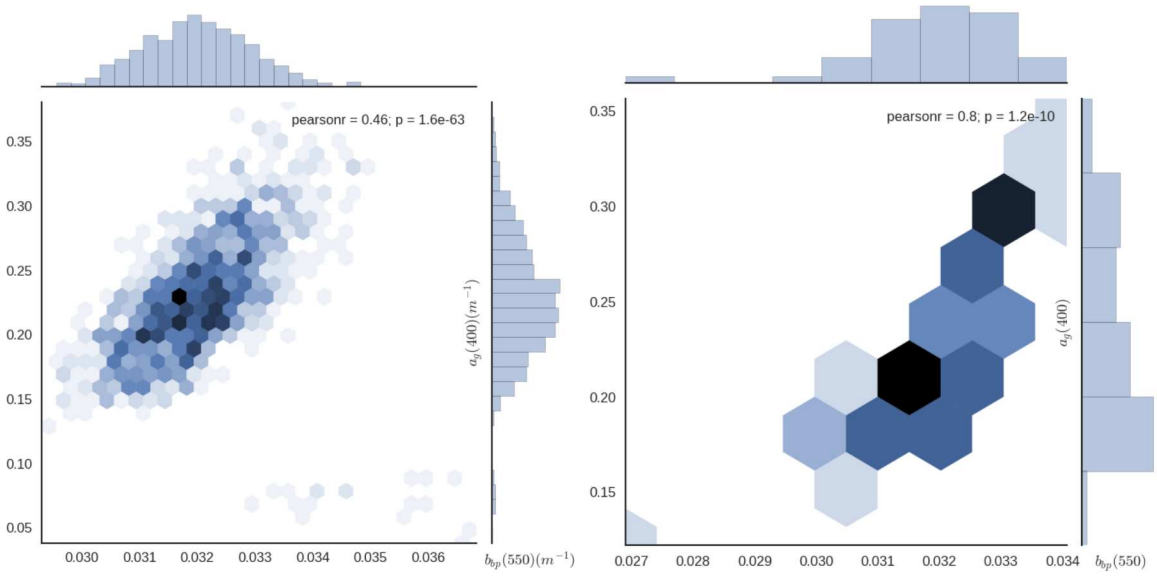

Figure 5.37: (Left) Hex-bin plot of a_g vs b_{bp} derived from the inverted simulated $\hat{R}_{rs}$. (Right) Hex-bin plot of a_g vs b_{bp} derived from the DALEC measured R_{rs} at ARM.

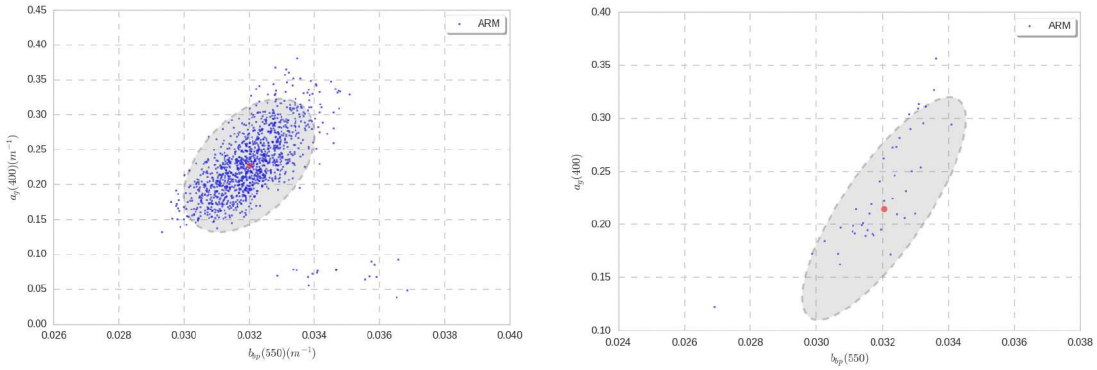

Figure 5.38: (Left) Scatter plot of a_g vs b_{bp} derived from the inverted simulated $\hat{R}_{rs}$. (Right) Scatter plot of a_g vs b_{bp} derived from the DALEC measured R_{rs} at ARM. Both plots show the errors ellipse which defines the 95% confidence boundary. The red point is the average IOP values

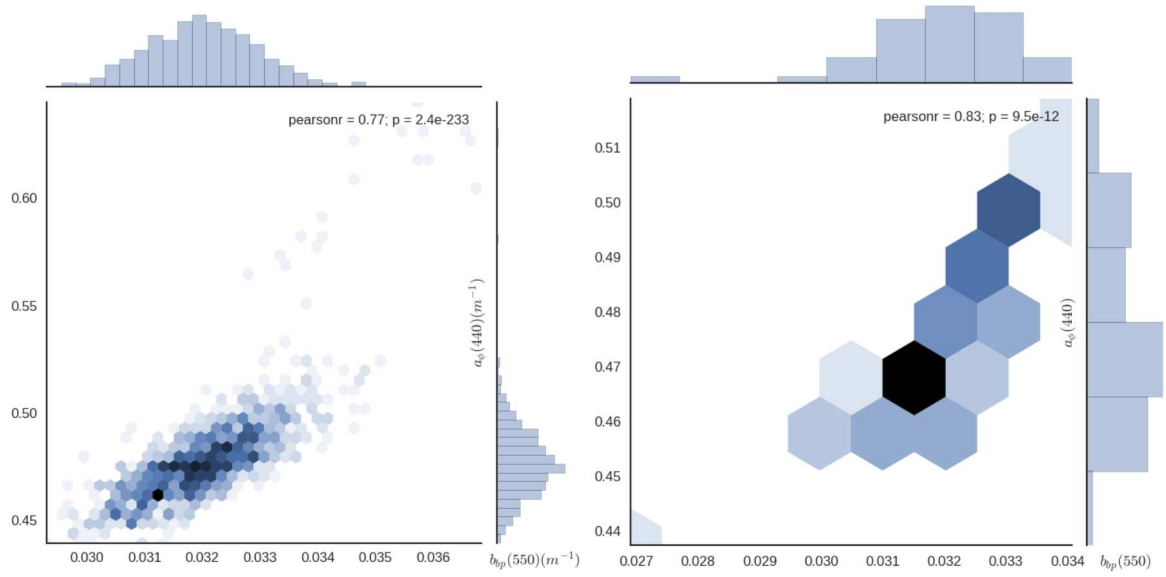

Figure 5.39: (Left) Hex-bin plot of a_ϕ vs b_{bp} derived from the inverted simulated $\hat{R}_{rs}$. (Right) Hex-bin plot of a_ϕ vs b_{bp} derived from the DALEC measured R_{rs} at ARM.

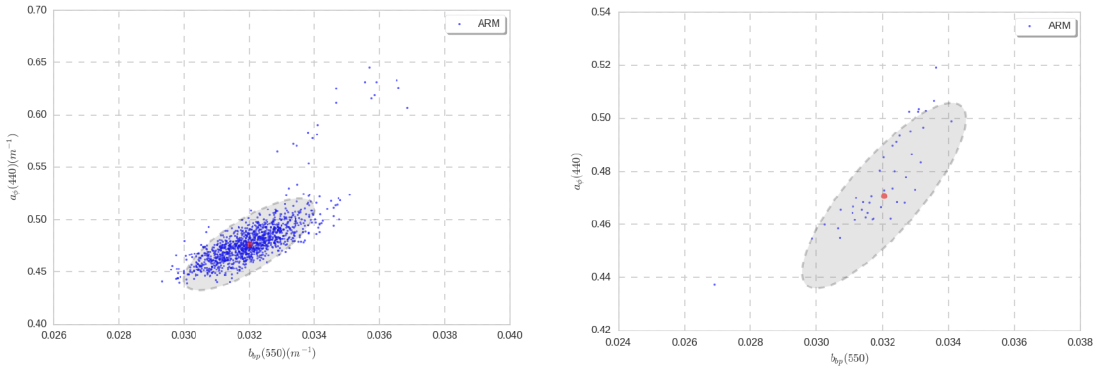

Figure 5.40: (Left) Scatter plot of a_ϕ vs b_{bp} derived from the inverted simulated $\hat{R}_{rs}$. (Right) Scatter plot of a_ϕ vs b_{bp} of the DALEC measured R_{rs} at ARM. Both plots show the errors ellipse which defines the 95% confidence boundary. The red point is the average IOP values

Figures 5.35, 5.36, 5.37, 5.38, 5.39 and 5.40 all show that the distribution of retrieved IOP parameters, $a_\phi(440)$, $a_g(400)$ and $b_{bp}(550)$, for the simulated data, have a much larger sample size in which to calculate statistical parameters. The hex-bin plots show the density and correlation of the parameters as well as the distribution of them along the axis. The scatter plots show distribution of points as well as the confidence interval of 95% defined by the error ellipse. The red points in the center of the ellipse represent the median value, taken as the reported IOP estimate. The major and minor axis of the ellipse are used to quantify the IOP uncertainty, as described in Section 5.4.2.

5.6 Sensitivity Analysis

This section describes the method used to test the sensitivity of the reflectance model around typical IOP values that were observed in the field. Ultimately, it is the sensitivity of the phytoplankton concentration retrieval with natural changes in R_{rs} that is of interest. This is difficult to model and presents many practical challenges and limitations. Using PlanarRad, it is possible to change the IOP parameters and model the change in R_{rs} but it is the inverse of this problem that we are interested in. Furthermore, there are many environmental effects in the field that can affect the reflectance measured by an instrument. Although, PlanarRad can model the effects due to wind speed, sky conditions, and changing sun and sensor geometry, for the sake of keeping the number of simulations sensible and achievable, these were kept constant in the sensitivity analysis.

The sun was set to nadir and the sensor geometry was set to 135° and 40° for viewing azimuth and zenith, respectively, as these are the angles used in field measurements to reduce the effect of sunglint. The wind set to 5 ms^{-1}.

The sensitivity X_{a_g} of the model to a change in $a_\phi(440)$ at a given $a_g(400)$ is defined here as:

$$X_{a_g} = \frac{dR_{rs}}{da_\phi} \tag{5.90}$$

Where:

dR_{rs} is a infinitesimal change in R_{rs}

da_ϕ is a infinitesimal change in a_ϕ

In order to model X_{a_g}, a set of $a_\phi(440)(0.107 - 1.554)$ m^{-1} and $a_g(400)(0.746 - 5.573)$ m^{-1} concentrations that spanned the minimum and maximum values observed on the day of the transect, a set of R_{rs} values were generated using PlanarRad. For each value of $a_g(400)$ a pair of $a_\phi(440)$ values were generated by perturbing each $a_\phi(440)$ value ± 15% which generated a corresponding pair of R_{rs} spectra for every single $a_g(400)$ value. The sensitivity was approximated by descretising Equation 5.90:

$$X_{a_g} \approx \frac{\Delta R_{rs}^{RMS}}{\Delta a_\phi(440)} \tag{5.91}$$

Where:

ΔR_{rs}^{RMS} is the root mean square of the difference in R_{rs}

$\Delta a_\phi(440)$ is the difference in a_ϕ at 440 nm

An example of the R_{rs} pairs generated for a pair of $a_\phi(440)$ values at six different $a_g(400)$ values is shown below in Figure 5.41. The approximated sensitivity for each $a_g(400)$ value for a $\Delta a_\phi(440)$ of ± 15%, for each $a_\phi(440)$ value in the set, is shown below in Figure 5.42.

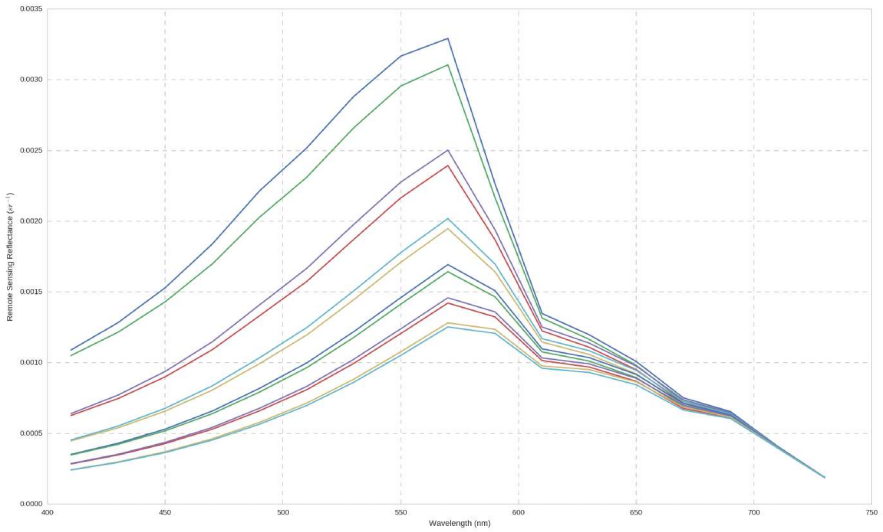

Figure 5.41: A subset of the remote sensing reflectance pairs generated from PlanarRad by altering the phytoplankton concentration by ± 15% for a $a_g(400)$ value of 3.402 m^{-1}.

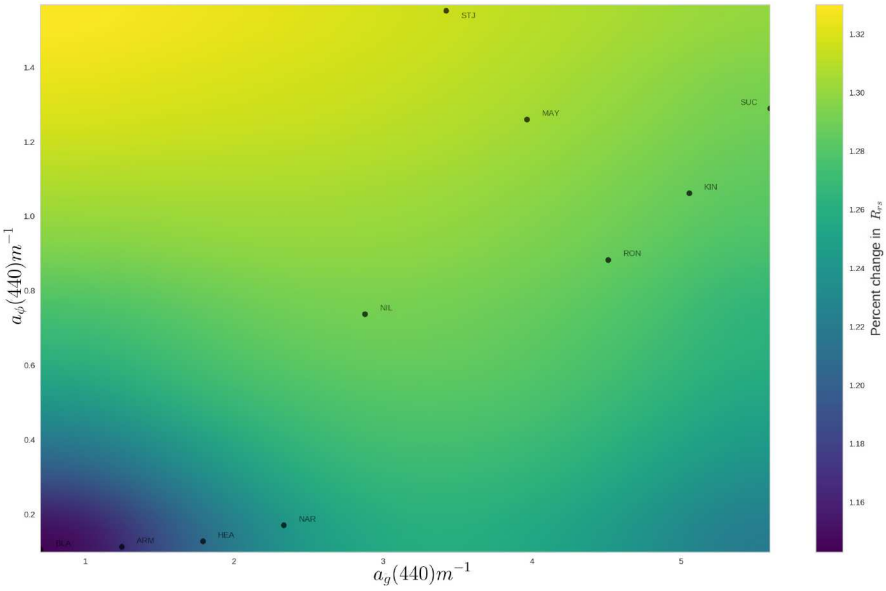

Figure 5.42: Percent change in reflectance that is produced by changing $a_\phi(440)$ by ± 15% over a range of $a_g(400)$ concentrations. The values of $a_\phi(440)$ vs $a_g(400)$ of the in situ measurement at each of the SCCP sample locations on 29/11/2011 are shown for comparison.

As the uncertainty of $a_\phi(440)$ is the parameter of greatest interest, Equation 5.91 was rearranged to give the change in $a_\phi(440)$ that can be expected for a change in R_{rs} by

dividing ΔR_{rs} by the average of the R_{rs} pairs and dividing result by X_{a_g}:

$$\Delta a_\phi(440) \approx \frac{\bar{R}_{rs}^{RMS}}{X_{a_y}} \tag{5.92}$$

Where:

$\bar{R}_{rs}^{RMS}$ is the root mean square of the normalised R_{rs}

X_{a_y} is the sensitivity of the model at a given $a_g(400)$

Consequently, the changes in reflectance were normalised and the corresponding change in $a_\phi(440)$ was calculated. The results of this analysis is shown in Figure 5.43. This figure makes it possible to estimate the uncertainty that can be expected in $a_\phi(440)$ given an RMS change in R_{rs}. For example, if a 1.15% RMS change in measured R_{rs} at $a_g(400) = 1.0m^{-1}$, an uncertainty of $\approx 2\%$ of $a_\phi(440)$ can be expected. A 1.3% RMS change in measured R_{rs} at $a_g(400) = 5.0m^{-1}$ would result in an expected uncertainty of $\approx 15\%$ in $a_\phi(440)$.

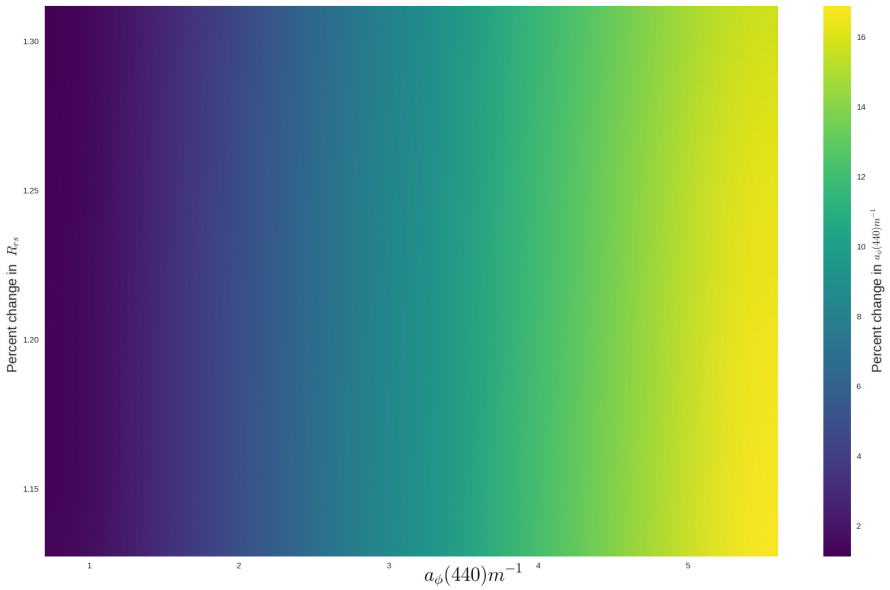

Figure 5.43: Change in $a_\phi(440)$ that can be expected for a percentage change in reflectance.

There are some assumptions made with the method outlined in this section. Because it is not possible to change the reflectance directly by a desired amount, changes in reflectance were, in effect, due to changes in IOP values. Consequently, the changes in

reflectance were rescaled by a 'per cent' change due to IOPs. This implies that there is a linear relationship between the change in reflectance and change in phytoplankton absorption, $a_\phi(440)$. It is assumed that for small changes in reflectance, this assumption is reasonable. For large changes in reflectance, this may not necessarily hold true. The results of this process are shown in Figure 5.43.

As there were some assumptions and estimations made in this simulation, the results from the sensitivity analysis must be used with caution. It does, however, provide a useful table that can be used to estimate approximate error boundaries for particular CDOM and phytoplankton concentrations. The method described here also negates the effect of due to other sources of uncertainty such as wind, perturbations in viewing geometry etc.

5.7 Summary

This chapter has summarised all of the terms, quantities and coordinates required to understand the radiative transfer process, and how RTE can be used to calculate the remote sensing reflectance from IOPs and VSFs. It is not the focus of this thesis to find solutions to the RTE as this problem has already been solved. It is important, however, to understand the inputs, process and outputs of solving the RTE. Without that understanding, it would be impossible to use the computational tools correctly or to correctly interpret the results.

PlanarRad and Hydrolight are 'full', complex models of the radiative transfer process. Due to their complexity, these models are only able to run in the forward sense, i.e. with IOPs, geometry and environmental factors as inputs and remote sensing reflectance (as well as other parameters) as outputs. This study requires the inverse process, i.e. remote sensing reflectance as an input and IOPs as an output. In order to achieve this, this study requires an efficient model that is able to be run thousands of times. In this chapter, three simplified, parametrised, forward models are therefore evaluated. By using a parametrised and more efficient optical model, it is possible to invert the simpler equation hundreds of times in less than a second on a modern desktop computer. Marrable et al. (2009) shows that real-time processing of transects using optical models can be achieved with graphics processing units (GPUs) on relatively cheap laptop computers.

The three optical models evaluated for their ability to reproduce reflectance spectra ob-

served in the river were HOPE, BRDF-corrected HOPE and BRUCE-LUT. It was concluded that HOPE was the most suitable, being capable, in principle, of finding IOPs in both shallow and deep water but with the limitation that IOP inversions are only capable of describing the total absorption and scattering coefficients. Furthermore, high spatial and temporal variability of phytoplankton species and assemblages make it impractical to find sensible SIOP models required to measure chlorophyll-a or cell concentration with the current body of knowledge of the Swan River's optical environment.

The mathematical methodologies used to invert the optical model so that IOPs from remote sensing reflectance are also described. The method used to calculate confidence intervals is shown and a new algorithm (coherent noise model) for calculating measurements uncertainties of the IOPs derived from inverting the optical model is described in detail. This method was used to draw the error ellipses in the figures showing scatter plots of the modelled IOPs. The same method is used to draw the error ellipses of the field derived estimates of IOPs and also used to define the uncertainty of the IOP transects as presented in the next chapter.

A sensitivity analysis of the reflectance model was conducted, to establish the potential IOP uncertainties from field measurements, over a range of CDOM concentrations. These were then compared with the uncertainty estimates derived from using the coherent noise model.

Chapter 6

Application to the Swan River

6.1 Introduction

There are three major parts to this research method: the modelling methods; and the fieldwork and laboratory methods. Fieldwork is required to make measurements of the water spectral reflectance and to collect water samples. The water samples are required to calibrate the results and to provide inputs into the optical models.

As introduced in Section 5.2, the remote sensing reflectance is a function of absorption and scattering and both are required as inputs into the optical model, it is therefore imperative to understand the unique absorption and scattering characteristics for the study area of interest; the Swan River in this case. The two dominant absorption components are: absorption due to pigments found in phytoplankton (primarily green chlorophyll); and absorption due to dissolved organic material (yellow/brown colour). At the beginning of this research project, it was decided that it was important to understand the different absorption characteristics of the main classes of algae found in the Swan River. In a partnership with the Murdoch University Algae R & D Centre, a plan to grow many different species of algae, commonly found in the river, and measure the different absorption characteristics was developed. Before the task of growing specific cultures of the Swan River, three cultures that were immediately available were grown. This decision was made in order to quickly make progress in gaining an understanding of the laboratory techniques required, as well as developing methods and procedures for building a localised spectral library.

It was found, after many weeks of culturing, that the logistics of building a spectral library, within the time budget of the project, was not sustainable. Culturing, subcul-

turing, cell counting and measuring the absorption characteristics, required much more time than was available. Furthermore, obtaining monocultures of the species of interest was also challenging due to price and availability. For these reasons, the plan to build a spectral library through culturing was changed. The research approach was altered to use a spectral library built from the available literature. Finally, after many iterations of refining the optical model inputs and work-flows, it was decided to use the in situ measurements from water samples of bulk phytoplankton absorption as an input into the optical model. This meant that it would not be possible to classify phytoplankton through model inversion but it would be possible to determine the total phytoplankton abundance.

As mentioned earlier, measuring the algal-specific scattering is difficult. It was decided early in the project that an investigation into the scattering of different algal shapes and sizes was required as the naturally occurring phytoplankton in the Swan River varies greatly in size and shape. As this investigation was a substantial amount of work and of scientific interest in its own right, and led to the investigation in Chapter 3.

Before radiometric measurements of the river could be made, the DALEC required careful calibration in a facility with a NIST-traceable[1] light source. The steps required to calibrate the DALEC are described in detail in Section 6.3 before Section 6.4, followed by a description of the field campaign.

Details of the fieldwork are outlined in Section 6.4.1, including describing the transect, water sampling locations and a description of the data that the Swan River Trust collect and have made available.

Following Section 6.4.3, the methods used to process the water samples in the laboratory are described. The methods include filtering the water samples, as well as measuring the absorption properties in a dual-beam spectrophotometer.

Lastly, the results for both the spot measurement and the transect fieldwork are presented.

[1]NIST is the US Department of Commerce National Institute of Standards and Technology.

6.2 Measuring the Above-Water Remote Sensing Reflectance

Before the DALEC was deployed in the field, the spectral response of the instrument needed to be characterised i.e. convert counts to radiometric quantities. This was done by determining the radiometric responsivity calibration coefficients – these define how the radiometers in the DALEC respond to changes in wavelength and sampling 'integration' time. In addition, the spectrum produced by each channel for zero incident light (known as 'dark current') was determined and removed from the signal. The process of calibrating the DALEC and making measurements are outlined as follows.

6.3 Calibrating the DALEC

Finding the radiometric response of the DALEC required some special calibration equipment. One of the crucial pieces of equipment was an extremely stable and very flat optical bench with evenly spaced threaded holes in the table top. It was important to make sure that the calibration equipment could be anchored in such a way that it was unable to move once fastened to the bench.

Another piece of specialist calibrating equipment used was a FEL quartz-halogen lamp. The lamp had been modified, by the manufacturer, specifically to calibrate optical equipment. The spectral irradiance output of the lamp was scanned by the manufacturer with a high-resolution monochromator to make sure the spectrum had very little noise and no unwanted spectral emission features, as well as characterising the irradiance. The lamp was powered with a regulated current source for approximately 24 hours to 'season' it. While it was being seasoned, its terminal voltage was monitored. If the voltage was not stable over the seasoning process the lamp would have been discarded. This ensured the power that the lamp was radiating was highly likely to be constant over its entire lifetime. A highly stable, constant current power supply was used to run the lamp during the DALEC calibration process. The Ocean Optics protocols (Mueller et al., 2003) explain that a well maintained, properly used FEL lamp should maintain an uncertainty level of $< 2\%$ for spectral irradiance and $< 3\%$ for spectral radiance calibrations. FEL-type lamp standards of spectral irradiance are provided by the US National Institute of Standards and Technology (NIST) and secondary standards are usually available through the manufacturer of the lamp.

The irradiance calibration procedure was as follows:

The DALEC irradiance sensor was mounted, in a dark room, on the optical bench and baffled so that no light other than that from the FEL-type lamp could enter the sensor. The baffling was extended to cover the lamp holder so that the light path was not interrupted except by a small closable occult hole used for creating a light window and when making background light measurements. An alignment target window was mounted on the lamp holder to mark the position that the filament was in when the lamp was turned on. To optically align the DALEC with the lamp, a laser was carefully mounted behind and normal to the alignment target and shone through the target crosshair. A mirror was mounted normal to the DALEC irradiance sensor, and its position was altered until the reflected laser light shone back through the target window crosshair, i.e. retro-reflection and its distance from target was made 0.5 m[2].

Next, the FEL-type lamp was turned on with the current ramped slowly so as not to thermally shock the filament. The FEL-lamp was left to warm up for 10 minutes before any measurement was made. The operating current and operation hours were both monitored. Any fluctuations in operating voltages would suggest the lamp was not emitting a stable spectrum and, hence, not suitable for calibration measurements.

The dark current, V_{dark}, for the sensor was found by replacing the caps over the DALEC sensor window and measuring the response. Next, the occult window was closed and a measurement of the background ambient light, V_{amb}, was measured and recorded. The baffling was adjusted and improved if the ambient light was greater than 0.1% of the instruments dark current. The occult window was then opened and the sensors response V_r was measured and recorded in counts per channel. The sensor's irradiance responsivity calibration factors (in air) are determined as:

$$F_E(\lambda) = \frac{E_r(\lambda)}{V_r(\lambda) - V_{amb}(\lambda)}, (\mu W m^{-2} nm^{-1} [digitalcount]^{-1}) \tag{6.1}$$

[2]This is the distance at which the lamps NIST-traceable spectral radiances are calculated. If the DALEC saturates when making measurements and needs to be moved further away from the lamp, the steps required to recalculate the radiances at the new distance are the ones outlined by Mueller et al. (2003).

Where: E_r is the irradiance of the lamp at 0.5 m.

The spectral irradiance responsivity factors are applied to subsequent radiometric measurements by:

$$E(\lambda) = F_E(\lambda)\left[V(\lambda) - V_{dark}(\lambda)\right], (\mu W m^{-2} nm^{-1}) \tag{6.2}$$

Where: $V(\lambda)$ is the field-measured response.

The spectral radiance calibrations procedure is as follows:

To calibrate the radiance response, a Spectralon plaque large enough to fill the view of the DALEC's radiance channels was used. Spectralon is used because it is a Lambertian (spatially uniform) reflector and it has a known bidirectional reflectance distribution function (BRDF), $\rho_{BRDF}(\lambda, \theta_0, \theta)$. $\theta_0 = 0$ is the normal incidence light beam and $\theta = 45°$ is the viewing angle.

The physical setup for spectral radiance calibration was almost identical to the spectral irradiance calibration. The DALEC was replaced with the Spectralon plaque which was set up so that retro-reflection was achieved using a mirror, as before. If the Spectralon plaque was not uniformly illuminated in the field of view of the DALEC, the Spectralon plaque would have been moved further away from the FEL lamp. The DALEC was then placed on the bench so that its field of view was 45° to the normal of the Spectralon plaque. Care was taken to ensure the plaque filled the field of view of the DALEC and that there were no shadows covering the plaque or DALEC. The alignment laser was used to ensure retro-reflectance between the lamp, plaque and DALEC.

The sensor was occulted and the ambient light was measured, followed by the dark current by replacing the covers on the DALEC. The occulter was removed and the responses to radiance reflected from the plaque were measured and recorded. The radiance for the plaque viewed at this angle was found using the following equation:

$$L(\lambda) = \frac{1}{\pi}\rho_{BRDF}(\lambda, 0°, 45°)E_r(\lambda) \tag{6.3}$$

Where $E_r(\lambda)$ is calculated by:

$$E_r(\lambda) = E_{0.5}(\lambda)\left[\frac{0.5 + \Delta f}{r + \Delta f}\right] \tag{6.4}$$

Where: $E_{0.5}(\lambda)$ is the irradiance at 0.5 (m)
r is the distance between the lamp filament and the plaque (m)
Δf is the distance that the centre of the lamp filament is offset behind the front plane of its terminal posts (m).

The radiance responsivity calibration coefficients of the field radiometer were determined as:

$$F_L(\lambda) = \frac{L(\lambda)}{V_r(\lambda)}, (\mu W m^{-2} nm^{-1} [Digitalcount]^{-1}) \tag{6.5}$$

$L(\lambda)$ from field measurements were found by applying the coefficient by:

$$L(\lambda) = F_L(\lambda)\left[V(\lambda) - V_{dark}(\lambda)\right], (\mu W m^{-2} nm^{-1} sr^{-1}) \tag{6.6}$$

Where: $V(\lambda)$ is the field measured response

In both radiance and irradiance calibration cases, at least 10 measurements were made. The average of these measurements was taken and repeated for different integration times. A linear fit of all points was interpolated between points and applied to the calibration coefficients versus integration time. Because the DALEC dynamically changes its integration time with changing light conditions when collecting data, the corresponding coefficient is found by finding the appropriate coefficient from the linear fit, based on the integration time of its measurement.

Other responses that could be characterised and investigated further are temperature response, pressure effects and polarisation sensitivity. Increasing internal temperature can result in increased electronic noise and a changing DC offset, i.e. dark current. The DALEC's internal temperature was logged and could be characterised with further investigation. Pressure effects can deform the DALEC's collectors, resulting in errors, as well

as hysteresis in a time-varying pressure field. Currently, pressure effects have been ignored but may be investigated at a later date. When making above water measurements, the reflected light field is linearly polarised. This can cross-polarise with the upwelling radiance and change the response of the DALEC's sensors. This effect is also ignored at this time and could be investigated further.

6.4 Fieldwork

The research methods presented here are primarily based on the International Ocean Optics Protocols For Satellite Ocean Color, published by NASA (Mueller et al., 2003). These protocols outline best practice for making measurements and calibrating sensors.

Before any radiometric measurements were made, the DALEC was calibrated for its radiometric responsivity and temporal response for varying integration times. The instrument was calibrated with a NIST-traceable light source made available from the Remote Sensing Satellite Research Group (RSSRG). Calibration coefficients were generated using the method outlined in Mueller et al. (2003).

Additional in situ water samples were collected for spectral absorption of CDOM and phytoplankton using a dual-beam spectrophotometer and the methods outlined in Mueller and Fargion (2000). The spectral absorption of phytoplankton was characterised for use in the radiative transfer model.

The remote sensing reflectance was measured using the DALEC and the techniques outlined in Mobley (1999). Calculations of radiometric quantities were made using the equations outlined in Mobley (1999) and were corrected for sunglint due to surface facets caused by capillary waves.

6.4.1 Radiometric Measurements

DALEC was used to make above water measurements of the Swan River starting at approximately -32.019038008:115.783139857 lat:lon at approximately 1050 hours, making continuous measurements up to -31.898440276:115.959250125 lat:lon at approximately

1645 hours[3]. Ten water samples and Secchi depth measurements were taken at the SCCP sample sites along the Swan River[4]. Secchi depth measurements were made by lowering a white and black Secchi disc into the water and measuring the depth at which it could not be seen by the operator.

The DALEC was mounted to the end of a boom by means of a two axis plane pivot gimble to keep the DALEC as upright as possible while the boat lists and squats over waves. The boom was allowed to pivot so its orientation could be controlled by hand. The boat traversed the transect at approximately 5 knots to try and minimise any bow waves and reduce foam. The DALEC simultaneously logged V_{sky}, V_t and V_d[5]. All of the other DALEC's sensors were also continually logged using the DALEConTransect software while the spectral output was monitored for any obvious aberrations or measurement errors. Erroneous measurements were removed with filters described in 6.7.3.

Remote sensing reflectance was derived following Mobley (1999):

$$R_{rs}(\lambda) = \frac{L_t(\lambda) - \rho L_{sky}(\lambda)}{E_d(\lambda)} \tag{6.7}$$

Where ρ is the sky radiance fraction. The viewing angle of the DALEC was set so that the L_u channel was pointing at $\sim 40°$, and at an azimuth angle of $\sim 135°$ relative to the sun. This viewing azimuth is suggested by Mobley (1999) to be the best angle to reduce sunglint from surface facets. All data were logged in a text file containing all the information required to convert the counts measured by the DALEC into a remote sensing reflectance using the calibration formulae discussed in Section 6.3. Other measurements included; UTC time, geographical location (lat:lon), heading. Sky conditions, water state (i.e. foamy, clear, etc.) and dark current for different integration times were logged in field-notebooks.

[3] A transect map is shown in Figure 6.16

[4] The Canning River was inaccessible due to the draft on the boat being too great and the water depth too shallow. Therefore, the Canning river was not included in this study

[5] V_{sky}, V_t and V_d are the sensor's response to sky radiance, reflected skylight and downwelling irradiance, respectively. These quantities are calibrated to L_u, L_{sky} and E_d, respectively, at post-processing using the techniques discussed in Section 6.3. These sensors will be referred to as L_u, L_{sky} and E_d. It should be understood that, technically, these quantities are not directly measured.

6.4.2 Backscattering Coefficients

The spectral particulate backscattering coefficient, $b_{bp}(\lambda)$ was measured in situ using a HOBI Labs HydroScat-6, HS6, backscatter meter. The HS6 was manufacturer-calibrated one month prior to the Swan River survey. At each sampling site, the HS6 measured the fixed-angle volume scattering function at 140°, $\beta(\lambda, 140)$ for six wavelengths (420, 442, 470, 510, 590, and 700 nm). Values of $\beta(\lambda, 140)$ were then processed according to the manufacturer protocols (HOBI Labs, 2011) to derive the $b_{bp}(\lambda)$. A 'sigma' correction (Maffione and Dana, 1997) was applied to the data to correct for attenuation along the illumination and collection pathlength. Values of $b_{bp}(\lambda)$ were subsequently fit using a power law.

$$b_{bp}(\lambda) = b_{bp}(\lambda_0)(\frac{\lambda_0}{\lambda})^{\gamma_{bb}} \tag{6.8}$$

Where λ_0 is a reference wavelength taken as 590 nm and γ_{bb} is the power law exponent of $b_{bp}(\lambda)$.

6.4.3 Water Sample Acquisition

The accuracy of the optical model depends, in part, on the accuracy of the IOP model inputs. It would be best practice to accurately measure all of the IOPs; however, this is not always possible due to limitations in laboratory and field equipment, time and money.

IOPs that are relatively easy to measure are: phytoplankton absorption, non-algal absorption and CDOM absorption. IOPs that are difficult to measure are: absorption and backscatter of pure water (due to the difficulties in water purification as discussed by Pope and Fry, 1997). The absorption and backscatter of pure water doesn't change and is well documented. Therefore, the values published in Smith and Baker (1981) and Pope and Fry (1997) were tabulated and used in the project. The phytoplankton, detritus and CDOM do vary with location and need to be measured for each field-trip.

In order to characterise the IOP absorption spectra, water samples were taken at the same time the R_{rs} was measured. The absorption of the water constituents were measured in a dual-beam spectrophotometer. This was done quickly before the living phytoplankton die, degraded and adds to the detritus and CDOM spectra changing the a_ϕ:CDOM ratio

in a way not representative of the field conditions.

On the dates shown in Table 6.1, field trips were conducted to measure R_{rs} of the Swan River. The purpose of these trips was to collect water samples that were used to find the absorption spectra of a_ϕ and a_g. The absorption spectra were used along with the optical model (HOPE) to produce a phytoplankton concentration estimates. As discussed in earlier sections, taking local samples helps improve the accuracy of the optical model and inversion process.

Triplicate, one-litre water samples were taken at the SCCP sample locations (Figure 6.1) along the river while simultaneously measuring R_{rs} with the DALEC[6]. The sample bottles were cleaned beforehand as well as rinsed with in situ water to remove any contaminants that may have been present in the water used to clean the bottles. After the water samples were collected, they were stored in a dark box, care was taken to keep the samples at a similar temperature to the location where they were collected from, i.e. out of the sun. Samples were filtered within six hours of collection for total total particulates (a_ϕ and a_{nap}). The particulate samples were stored overnight in liquid nitrogen before analysis the following day. The CDOM samples were kept in a cool, dry store before analysis.

[6]See Figure 6.1

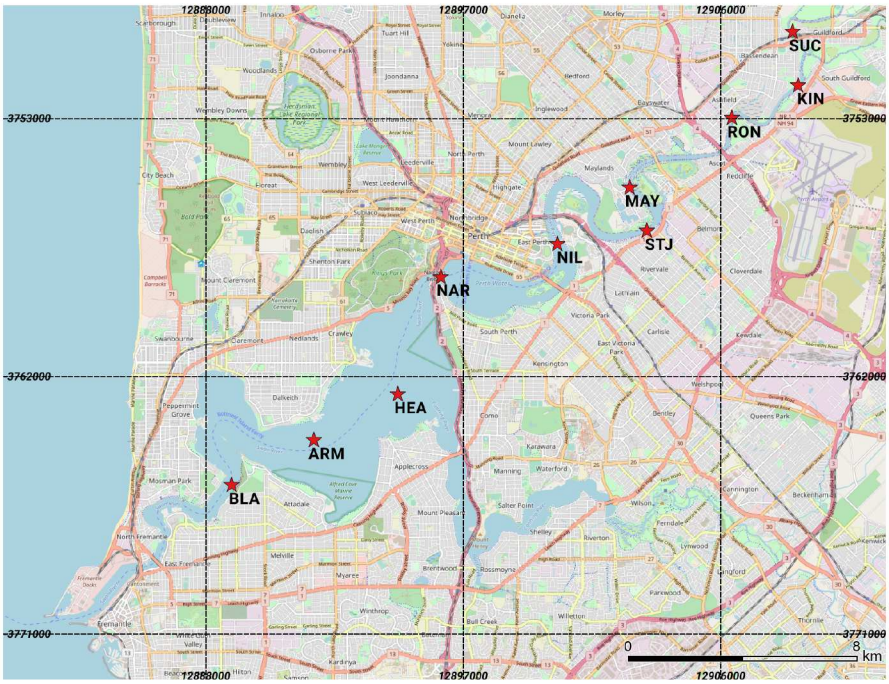

Figure 6.1: SCCP sampling locations where water samples were collected for laboratory analysis.

Table 6.1: SCCP Swan River Sampling dates

Date	Water Samples Collected	DALEC measurements
08/02/2010	✓	✓
20/01/2010	✓	×
22/02/2010	✓	✓
26/10/2010	×	✓
11/01/2011	×	✓
02/03/2011	×	✓
15/03/2011	×	✓
03/05/2011	×	✓
04/05/2011	×	✓
18/07/2011	✓	✓
14/11/2011	✓	✓
15/11/2011	×	✓
29/11/2011	✓	✓– Full Transect

The bold dates in Table 6.1 indicate sample days where both DALEC measurements and water samples were collected at the SCCP sites. These results are shown in Chapter 4.

The other dates indicate days were a limited range of measurements were made, mostly for instrument and methodology testing.

6.5 Laboratory Work

The first laboratory measurement conducted were the spectral absorption of phytoplankton and non-algal particles ($a_\phi + a_{nap}$). Firstly, the phytoplankton needed to be filtered from the water. The problem with the filtering process is that it filters out more than just the phytoplankton: it also filters out any non-algal particles (NAP). This can include silt and minerals, as well as the detritus material from the algal cells. This filtered matter was then placed in a dual-beam spectrophotometer and an absorption spectrum was produced. The method of isolating the phytoplankton absorption spectra from the total absorption spectra was to bleach the pigments out of the biomatter and remeasure the absorption. This left the absorption spectra of all the NAP, a_{nap}, as the bleach only removed the phytoplankton pigments. The phytoplankton absorption, a_ϕ, was found by subtracting a_{nap} from the first total absorption measurement. This process was as follows.

The filters used during the filtering process were Whatman GF/F glass fibre filters. They are binder free and combustible, as well as having a nominal pore size of 0.7 μm. These filters are recommended for particle absorption by Mueller et al. (2003). The GF/Fs were placed onto a filtration ring along with two blank filters that had been soaked in Milli-Q water. The filters were clamped tightly between the filter ring and the collection cup.

The volume of filtrate needed for optimal spectrophotometric absorption signal strength, without clogging the filter, was found through trial and error to be one litre. The protocols in Mueller et al. (2003) recommend that optical densities be in the range of 0.05–0.4 for best performance of measurement. One litre samples were added to the collection cups after agitating to mix particles and then drawn through the filter pads at approximately 5 in Hg in dim light. A vacuum higher than approximately 5 in Hg risks bursting the chloroplasts that hold the pigments in the cells. If this happens, chlorophyll can slip through the fibre pores and will be lost. Dim light was needed to reduce the risk of any living cells adjusting their pigments for the different light field.

6.5.1 Optical Density of $(a_\phi + a_{nap})$

After the filter pads were prepared using the technique discussed above, they were scanned using a dual-beam spectrophotometer which compares the light transmission at different wavelengths between two optical paths. The absorption of a sample was found by comparing a blank sample with a filtered sample. Ideally, this negates the effect the filter pad itself has on transmission. Because filter pads have a very large backscatter attenuation, it was very important that a scan be done over a large dynamic range to achieve the best possible signal-to-noise ratio.

Before the phytoplankton samples were scanned, two reference pads were saturated with filtered river water, placed in the two optical paths and scanned to achieve a 'baseline' scan that was used as the zero reference point and was subsequently subtracted from all the sample scans. The baseline was stored in the spectrophotometer and automatically subtracted from scans by the operating software. The baseline was checked simply by rescanning the blank filters. When the blank scan produced a scan within a deviation of (± 0.005) optical density (OD) for all frequencies, the instrument was considered baseline calibrated.

Before the samples were placed in the optical path, they were rehydrated with river water, filtered through a 0.2 μm filter, and left to soak for approximately 10 minutes. Two thin glass plates were securely attached in front of the instrument's optical windows, perpendicular to the optical path. These glass mounts were rinsed with Milli-Q water and dried with a lint-free tissue. The saturated filters were then placed on the glass mounts and held in place by the surface tension of the water. Any bubbles between the glass and the filter were removed by carefully lifting the pad and rolling it back onto the glass until none were apparent when looking through the plate from the back of the filter.

One of the reference filters was removed and replaced with one of the particulate matter filtered samples and the absorption spectrum was measured. This was repeated for all of the samples making sure the reference filter was rehydrated with filtered river water between samples. The spectra produced were the $(a_\phi + a_{nap})$ absorption. To isolate a_ϕ, the samples were bleached of all their organic pigments and remeasured. The following section describes this process.

6.5.2 Depigmented Absorption (a_{nap})

The sodium hypochlorite oxidation method described in Mueller et al. (2003) was chosen to bleach the pigments in the sample, due to chemical availability. 0.1% active chlorine was mixed with Milli-Q water to make a bleaching solution. The filter pads were placed back on the filtering rings with the filter valves in the closed position and the sample particle side facing up. The bleaching solution was then gently poured down the sides of the filter funnels onto the filter pads until the pads were completely covered by approximately 1 mm of solution. The samples were left to sit for approximately 10 minutes and were periodically topped up to replace any solution lost through the filters. After the filters had been left to sit, they were rinsed with approximately 50 mL of filtered river water. The blank filters were then measured in the dual-beam spectrophotometer in exactly the same way as the sample filters.

The optical density of the bleached sample was found in exactly the same way as the non-bleached samples. If the absorption spectra still showed a peak at 675 nm, this suggested pigments were still present in the sample, as this is the characteristic absorption peak of chlorophyll-*a*. If this was observed, the bleaching process was repeated until the peak disappeared.

6.5.3 Gelbstoff Absorption

To ascertain CDOM absorption, all suspended particles must be removed from the water. The sample water caught after filtering for the combined a_ϕ & a_{nap}, was filtered once more through a 0.2 μm filter to remove any remaining particles, as well as any glass particles from the GF/F filters themselves. The water sample needs to be placed in a longer light path than the phytoplankton (usually 0.1 m). The process of collecting a CDOM absorption is outlined below.

Two 0.1 m path length quartz cuvettes were prepared by rinsing twice with 10% hydrochloric acid (HCl) followed by rinsing twice with pure ethanol and finally rinsing with Milli-Q water. After preparation, the cuvettes were not handled with bare hands to avoid contamination. Two cuvettes were then filled with Milli-Q water and dried with lint-free laboratory tissues. They were inspected to ensure that there were no bubbles, dust or obvious contaminants by looking through the cuvettes against a black background.

To make sure that both cuvettes had matched optical properties, they were both scanned

individually in the spectrophotometer against an air blank (i.e. no sample in the other optical path). If the cuvettes had been handled correctly and were optically matched, they had the same spectral response. If there were anomalies, the preparation procedure was repeated until they were matched.

The matched cuvettes were placed back in the spectrophotometer to collect a baseline scan. A baseline scan was achieved if the deviation was less than (± 0.0007) OD across all wavelengths. When an acceptable baseline was achieved, one of the cuvettes was emptied and rinsed three times with approximately 10 mL of sample water. Once it was fully rinsed, it was filled with the sample water and the outside completely dried and then checked for bubbles, dust and contaminants before being replaced back in the spectrophotometer. A scan was run and saved. This process was repeated for all samples.

6.6 Sample Data Processing

At this point in the procedure, the absorption of both CDOM and particle absorption a_p were expressed as optical density (%). Before they can be used to compare the optical model derived absorption with laboratory measured absorption they need to be converted into units of m^{-1}. The process of deriving a_p is described in Mueller et al. (2003).

$$a_p(\lambda) = \frac{2.303A}{\beta V}\,[OD_f(\lambda)] \tag{6.9}$$

Where: OD_f is the optical density of the filter sample
A is the clearance area of the filter with the concentrated particles (m^2)
V is the volume of water filtered (m^3)
β is the pathlength amplification parameter.

Scattering of light within the GF/F filter increases the absorption pathlength. The pathlength amplification parameter, described by Kiefer and SooHoo (1982), is found through the empirical formula:

Table 6.2: The pathlength amplification factors for various particle types. Reproduced from Mueller et al. (2003)

Quadratic functions	**Particle type**	C_1	C_2
Mitchell (1990)	Mixed cultures	0.392	0.655
Cleveland and Weidemann (1993)	Mixed cultures	0.378	0.523
Moore et al. (1995)	*Prochlorococcus marinus*	0.291	0.051
Moore et al. (1995)	*Thalassiosira weissflogii*	0.299	0.746
Moore et al. (1995)	*Synechococcus WH8103*	0.304	0.450
Tassan and Ferrari (1995)	*Scenedesmus obliqus*	0.406	0.519
Nelson et al. (1998)	*Dunaliella tertiolecta*	0.437	0.022
Nelson et al. (1998)	*Phaeodactylum tricornutum*	0.294	0.587
Nelson et al. (1998)	*Synechococcus WH7803*	0.277	0.000

$$\beta = [C_1 + C_2 (OD_f(\lambda))]^{-1} \tag{6.10}$$

C_1 and C_2 are dependent on the particle type and are usually found by optimisation and published for different particle types. Table 6.2 shows a list of pathlength amplification factors for various particle types.

As the particle type was not yet known for the Swan River samples, the Clevelend and Weidemann (1993) mixed culture values were used to produce the filter absorption. Investigation of particle type and its effect on absorbance is something that needs to be investigated further. The absorption of the detritus (bleached) material, a_{nap}, is found using the same procedure.

After the appropriate pathlength calibrations have been applied to the filter samples, before and after bleaching, the phytoplankton absorption spectrum is simply found by subtracting the bleached absorption from the non-bleached sample, i.e.:

$$a_\phi(\lambda) = a_p(\lambda) - a_{nap}(\lambda) \tag{6.11}$$

This gave the first absorption spectrum used in the optical model. To find the CDOM absorption, a_y, a similar pathlength amplification factor needed to be applied (Clevelend and Weidemann, 1993):

$$a_g(\lambda) = \frac{2.303}{l}\,[OD_s] \tag{6.12}$$

Where: OD_s is the optical density of the soluble sample.
l is the length of the cuvette (m).

This gave the second spectrum that was measured in this project. The other parameters that are more difficult to measure, a_w and b_w were obtained from tabulated data in Pope and Fry (1997) and Smith and Baker (1981) respectively.

6.7 Results

This section presents the major results of the study conducted on the Swan River. This chapter presents the results of the spot measurement, in Section 6.7.2, used to help develop the methods, equipment, software and workflows used conduct the transect in Section 6.7.14. In particular, the spot measurement data was used to develop the coherent noise model which was used to estimate the IOP measurement uncertainties. A full transect of the Swan River was conducted on the 29/11/2011 and the results are shown in Section 6.7.14. The reflectance at each SCCP sample location is first observed and shown in Section 6.7.3. The reflectance measured at the water sample locations were used to train 10 different coherent noise models. An example of these results are shown in Section 6.7.3. In this section the results of inverting 2400 synthetic $\hat{R}_{rs}$ are presented for $a_\phi(440)$, $a_g(440)$ and $b_{bp}(550)$.

6.7.1 Modelling Comparisons

In Section 5.3, a number of models are described and three are investigated in more detail here. These models were chosen as they derive the absorption coefficient due to phytoplankton $a_\phi(440)$. We note here that SAMBUCA, described earlier, is designed to retrieve chlorophyll-a concentration, but would require knowledge of the SIOPs of a_{nap} and b_{nap} in the Swan River. As discussed in great detail in Chapter 2, Literature Review, the variability in phytoplankton, size, species and concentration is highly variable seasonably and from site to site. Deriving chlorophyll-a concentration from an optical model would require knowledge about SIOPs spanning all combinations of this variability. The complexity of such an investigation was outside the scope of the Swan river study and SAMBUCA was excluded from consideration on this basis. Instead, this study limits itself to models that derive total phytoplankton absorption coefficient. At the beginning of the Swan River project, it was not known which optical model would be the most suitable. Three candidate models were implemented in the Python programming language under the GPL 3 open source licence and can be downloaded from Launchpad[7].

In order to investigate which of the models was most suitable for this project, three DALEC measured remote sensing reflectance samples from the beginning middle and end of the river were chosen; BLA, RON and SUC. The three spectra were collected by the DALEC in 'best possible conditions'. At this stage in the study, access to a dual-

[7] `https://launchpad.net/dalecppt`

beam spectrophotometer was not possible. Therefore, the accuracy of the reflectance models was initially considered based on the RMS difference between the modelled and DALEC measured spectra. The colour of the Swan River changes along the length of the river and it was decided that these three sampling locations suitably represented that variability. The R_{rs} spectra were inverted using the three different models in order to choose the 'best' candidate. Figures 6.2, 6.3 and 6.4 show a comparison between the measured spectra and HOPE 'predicted' spectra at BLA, RON and SUC respectively. Figures 6.5, 6.6 and 6.7 show a comparison between the measured spectra and BRUCE-LUT 'predicted' spectra at BLA, RON and SUC respectively. Figures 6.8, 6.9 and 6.10 show a comparison between the measured spectra and the BRDF corrected reflectance model's 'predicted' spectra at BLA, RON and SUC respectively.

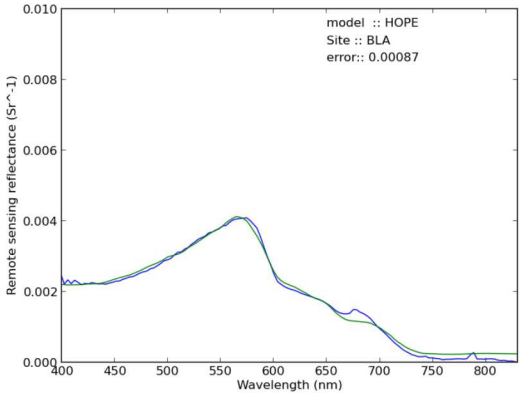

Figure 6.2: Comparison between the model predicted reflectance and the measured reflectance for HOPE at BLA.

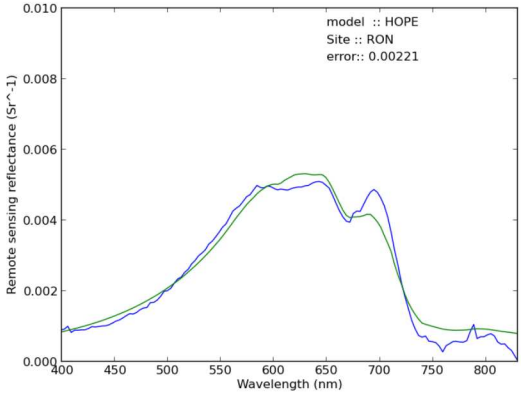

Figure 6.3: Comparison between the model predicted reflectance and the measured reflectance for HOPE at RON.

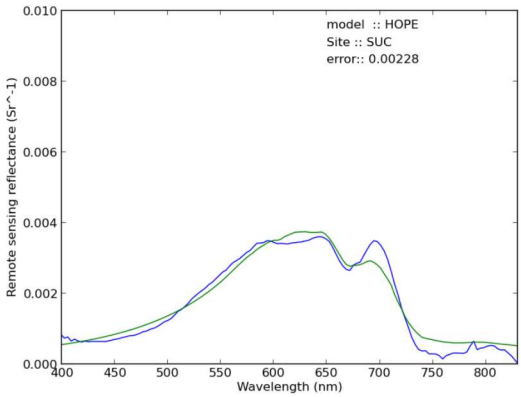

Figure 6.4: Comparison between the model predicted reflectance and the measured reflectance for HOPE at SUC.

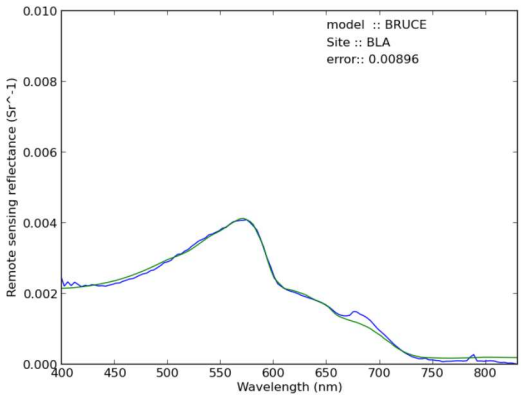

Figure 6.5: Comparison between the model predicted reflectance and the measured reflectance for BRUCE-LUT at BLA.

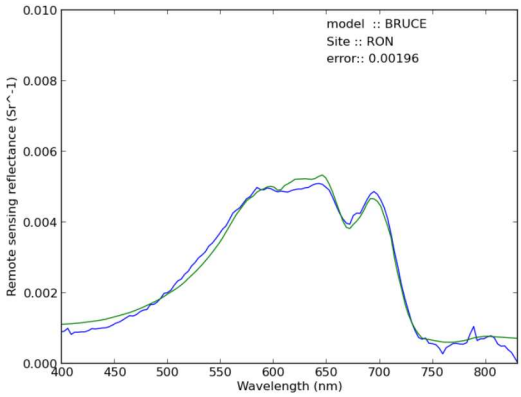

Figure 6.6: Comparison between the model predicted reflectance and the measured reflectance for BRUCE-LUT at RON.

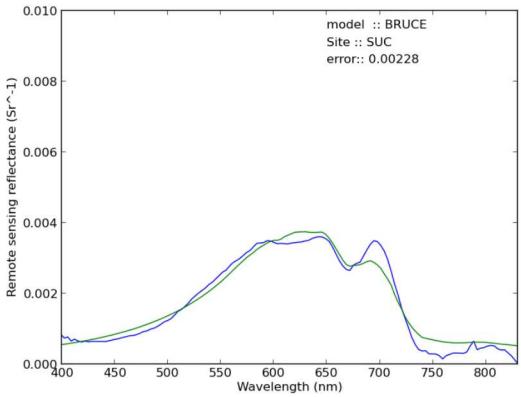

Figure 6.7: Comparison between the model predicted reflectance and the measured reflectance for BRUCE-LUT at SUC.

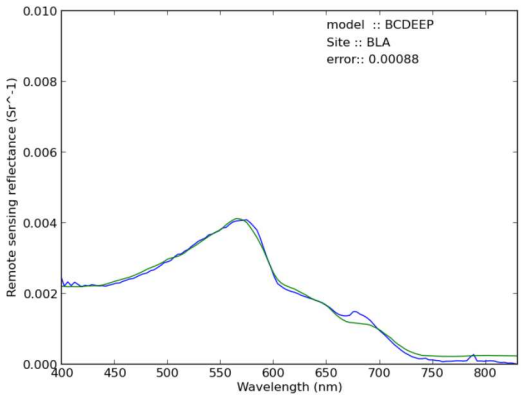

Figure 6.8: Comparison between the model predicted reflectance and the measured reflectance for the BRDF corrected reflectance model at BLA.

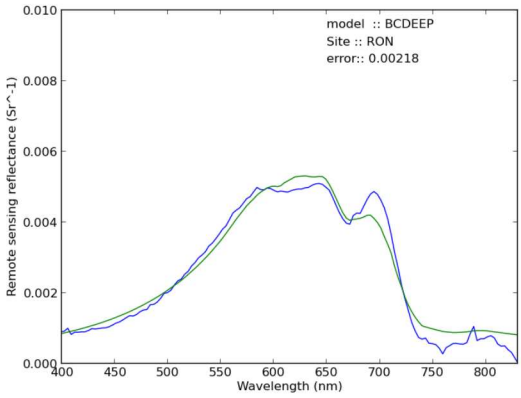

Figure 6.9: Comparison between the model predicted reflectance and the measured reflectance for the BRDF corrected reflectance model at RON.

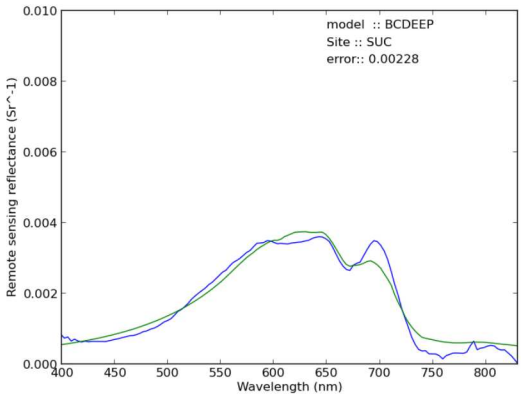

Figure 6.10: Comparison between the model predicted reflectance and the measured reflectance for the BRDF corrected reflectance model at SUC.

The BRUCE-LUT model was able to more accurately reproduce the reflectance shape when compared with the measured reflectance, particularly around the phytoplankton fluorescence peak (around 680 nm) where the other models did not perform very well. However, BRUCE-LUT was produced IOP inverted parameters that were not sensible such as negative IOP values. There were no significant differences between HOPE and BRDF-corrected HOPE. HOPE has the ability to model shallow water where the bottom surface can be seen, as well as deep water. Although the Swan River is very dark and mostly optically shallow, there is a small section of river near BLA where bottom reflectance of sand can be seen. For these reasons it was decided that HOPE would be used for the rest of the project.

The optical models can be reasonably complex and, as such, there are many potential errors, if coded incorrectly, potentially resulting in inaccurate predictions. In order to make sure that the optical model HOPE was coded correctly and the required inputs to the model were also correct, a 'sanity check' was devised using PlanarRad which uses a completely independent radiative transfer method and was coded and published independently. In order to model a range of different water types, shown in Figure 6.11, PlanarRad (Hedley et al., 2009; Hedley, 2012) was used as a point of truth. Furthermore, it produced the same results as the popular proprietary radiative transfer model Hydrolight[8] that was used by Lee et al. (1999) to design HOPE.

The comparison between HOPE and PlanarRad is shown in Figure 6.11 and shows that the two models agree with each other within a small tolerance. It is not expected that the two models be identical, as HOPE is a semi-analytical model that uses some approximations in order to reduce the complexity of the calculations. It was decided that the tolerance between the two models was acceptable, and as such, it was unlikely that any errors had been made when coding up the Python version of HOPE for this project.

[8] `http://www.planarrad.com/images/f/f2/Pr_hl_report.pdf`

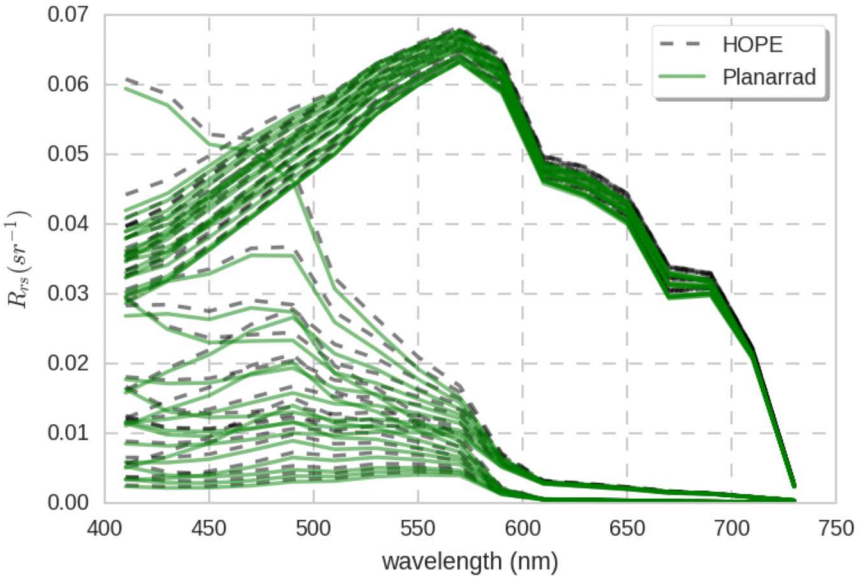

Figure 6.11: A comparison between the Python implementation of HOPE used for this project and the more complex PlanarRad radiative transfer model. The figure shows an acceptable tolerance between the two outputs for the same input parameters.

6.7.2 Spot Measurements

During the development phase of the project, there was the opportunity to make measurements with the Swan River Trust. Although the ultimate goal was to develop a monitoring system that would include a full transect of the Swan River, the opportunity to make measurements at the sampling stations of the SCCP afforded the opportunity to build a spectral library, test processing code, and develop a workflow. A full transect of the Swan River was made on 29/11/2011 the results of which are presented in Section 6.7.3. The sampling locations for the DALEC measurements and water sampling locations are shown in Table 6.3. The Swan River Trust boat did not stop at Heathcote (HEA) on these occasions so samples were not collected.

The following section presents the estimated phytoplankton concentration derived from the DALEC measured remote sensing reflectance and inverted using HOPE. The phytoplankton estimates were made by using the absorption profiles of both phytoplankton and CDOM measured in the laboratory but collected at the sample locations. The HOBI labs HydroScat-6 was not available on these dates, therefore, b_{bp} could not be measured. The following results were limited to inverting for a single $a_\phi(440)$ parameter. It was found that inverting the model for all $a_\phi(440)$, $a_g(440)$ and $b_{bp}(550)$ for these field dates did not yield sensible results. Often retrieved IOP values were negative of many orders of magnitude too high. By using the measured $a_g(440)$ values, and the full measured a_ϕ spectral shape in the inversion routine, values of $a_\phi(440)$ that were close to the measured values were achieved. These results are shown in figures 6.12, 6.13, 6.14 and 6.15 below for the dates, 08/02/2010, 22/02/2010, 18/07/2011 and 14/11/2011 respectively.

The three IOP parameters $a_\phi(440)$, $a_g(440)$ and $b_{bp}(550)$ were inverted for the full transect shown in Section 6.7.14. It will be shown in Section 6.93 that by using this same model restriction, discussed above, the accuracy of the $a_\phi(440)$ parameter is improved. The spot DALEC measurements presented here provided a useful tool for testing equipment, software and algorithms. Table 6.3 shows the coordinates of the sample locations.

Table 6.3: Swan River sampling site locations

Site Name	Station Code	Latitude (°S)	Longitude (°E)
Blackwall Reach	BLA	-32.0190380	115.7831398
Armstrong Spit	ARM	-320070686	115.8089498
Heathcote	HEA	-31.9948919	115.8353485
Narrows Bridge	NAR	-31.9636573	115.8487799
Nile Street	NIL	-31.9548452	115.8853411
Saint John's	STJ	-31.9513718	115.9134004
Maylands Pool	MAY	-31.9398069	115.9081728
Ron Courtney Is	RON	-31.9214037	115.9401324
Kingsley Street	KIN	-31.9125821	115.9610263
Success Hill	SUC	-31.8984402	115.9592501

Table 6.4: In situ measurements of $a_\phi(440)$, $a_g(440)$ and HOPE-derived values of $a_\phi(440)$ for 9 of the SCCP sampling locations on 08/02/2010.

Site	BLA	ARM	HEA	NAR	NIL	STJ	MAY	RON	KIN	SUC
in situ $a_\phi(440)(m^{-1})$	0.003	0.004	-	0.002	0.008	0.016	0.015	0.027	0.019	0.025
HOPE $a_\phi(440)(m^{-1})$	0.003	0.003	-	0.002	0.007	0.014	0.012	0.017	0.011	0.015
in situ $a_g(440)(m^{-1})$	0.600	1.121	-	2.018	3.202	4.000	4.612	5.201	5.517	5.432

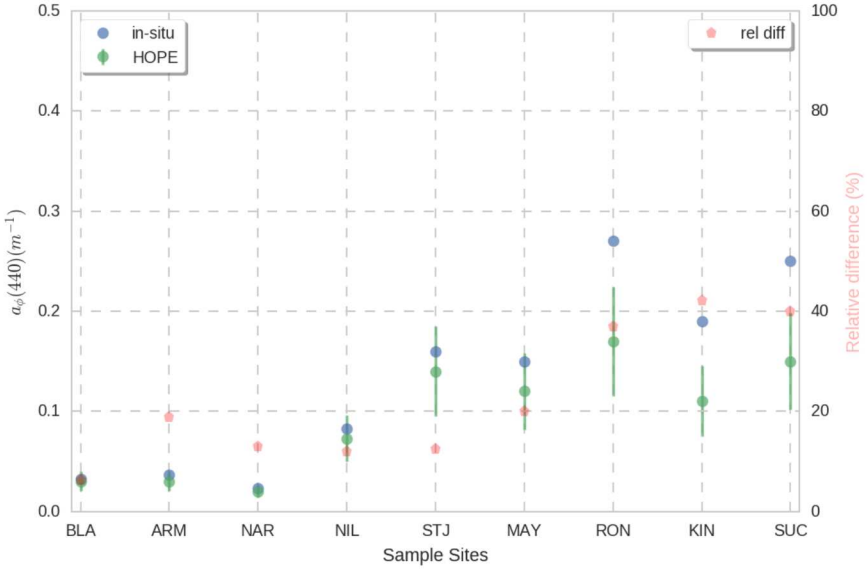

Figure 6.12: DALEC measured, HOPE-derived phytoplankton estimates compared with laboratory processed in situ water measurements

Table 6.5: In situ measurements of $a_\phi(440)$, $a_g(440)$ and HOPE-derived values of $a_\phi(440)$ for 9 of the SCCP sampling locations on 22/02/2010

Site	BLA	ARM	HEA	NAR	NIL	STJ	MAY	RON	KIN	SUC
in situ $a_\phi(440)(m^{-1})$	0.030	0.040	-	0.011	0.061	0.144	0.131	0.782	0.472	0.242
HOPE $a_\phi(440)(m^{-1})$	0.030	0.030	-	0.010	0.073	0.100	0.100	0.60	0.20	0.005
in situ $a_g(440)(m^{-1})$	0.490	1.021	-	1.089	3.011	3.909	4.323	5.007	5.317	5.400

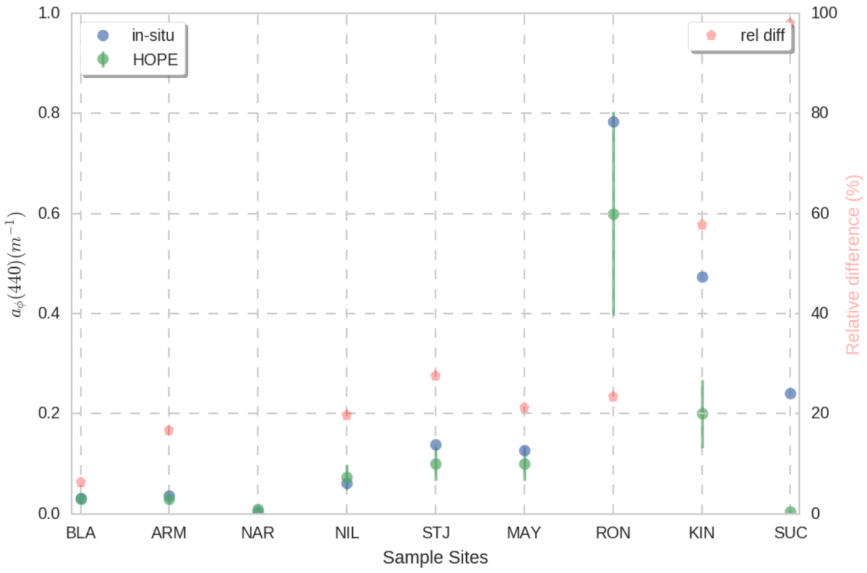

Figure 6.13: DALEC measured HOPE-derived phytoplankton estimates compared with laboratory processed in situ water measurements.

Table 6.6: In situ measurements of $a_\phi(440)$, $a_g(440)$ and HOPE-derived values of $a_\phi(440)$ for 9 of the SCCP sampling locations on 18/07/2011

Site	BLA	ARM	HEA	NAR	NIL	STJ	MAY	RON	KIN	SUC
in situ $a_\phi(440)(m^{-1})$	0.012	0.023	-	0.026	0.120	0.590	0.540	0.420	0.370	0.480
HOPE $a_\phi(44)(m^{-1})$	0.030	0.033	-	0.015	0.075	0.544	0.250	0.301	0.221	0.050
in situ $a_g(440)(m^{-1})$	0.700	0.909	-	1.818	3.449	4.00	4.631	5.060	5.302	5.227

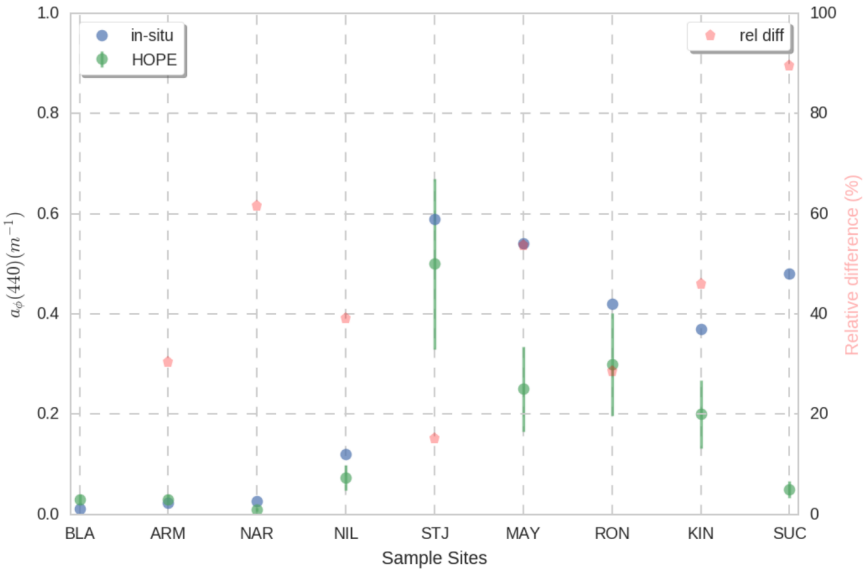

Figure 6.14: DALEC measured, HOPE-derived phytoplankton estimates compared with laboratory processed in situ water measurements.

Table 6.7: In situ measurements of $a_\phi(440)$, $a_g(440)$ and HOPE inverted values of $a_\phi(440)$ for 9 of the SCCP sampling locations on 14/11/2011

Site	BLA	ARM	HEA	NAR	NIL	STJ	MAY	RON	KIN	SUC
in situ $a_\phi(440)(m^{-1})$	0.360	0.0211	-	0.033	0.112	0.110	0.124	0.096	0.088	0.059
HOPE $a_\phi(44)(m^{-1})$	0.333	0.031	-	0.011	0.083	0.115	0.081	0.066	0.063	0.035
in situ $a_g(440)(m^{-1})$	0.916	1.121	-	2.028	3.511	4.515	4.910	5.287	5.509	5.571

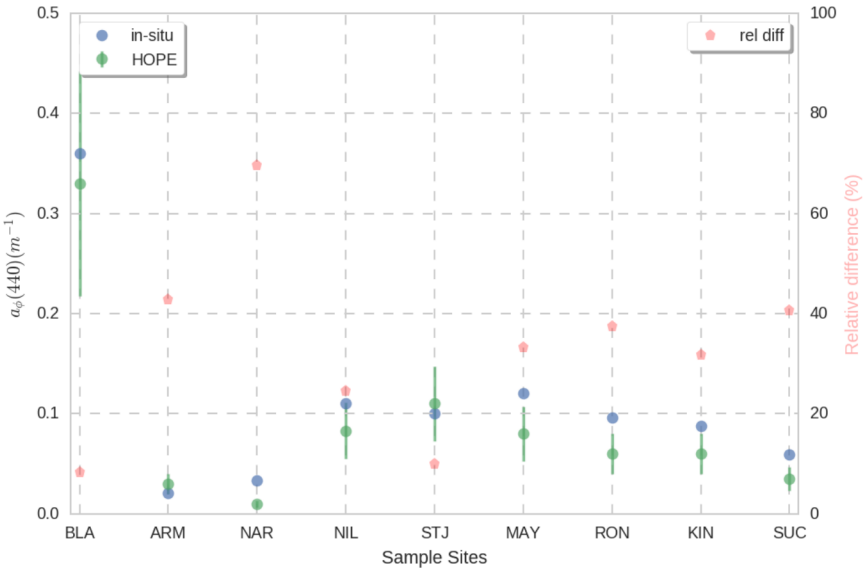

Figure 6.15: DALEC measured phytoplankton estimates compared with laboratory processed in situ water measurements.

The four sampling days with spot measurements presented here did not agree very well between reflectance-derived IOP concentrations and laboratory measurements. Differences between values were often greater that 60%. There were a number of reasons for this. It was expected that it would be possible to show good agreement between the HOPE derived IOPs and the co-located laboratory-measured concentrations. One possible reason for the disagreement was the attenuation of the dark water. This was especially true further up the river, past NAR, where the water became very laden with CDOM. This can be particularly seen in figures 6.12 and 6.13 where the relative error steadily increases up river. The sensitivity analysis in Section 5.6 shows that increased levels of CDOM increases the uncertainty of model retrieved $a_\phi(440)$.

Another possible reason for the disagreement between model derived IOPs and laboratory measurements was the difficulty in keeping the DALEC level, and at a constant viewing geometry of 135° and 40° (relative sun azimuth and viewing zenith, respectively) proved difficult with the available equipment, even on calm days. A viewing geometry of 135° and 40° reduces the effect of sunglint in the R_{rs} measurements (Mobley, 1999), so deviating from these angles likely introduces extra noise. Furthermore, as the DALEC can take up to six seconds to make a measurement (depending on light availability) if the sensor moves while making a measurement this can introduce further errors. Time was spent building a new gimble and mount but it remained a challenge due to boat-drift and the difficulty in keeping the boat on a constant heading.

In fact, much time was spent trying to get reasonable results from the inversion process. It was not known at the time how difficult the heavy amount of CDOM was making the inversion task. This later triggered the sensitivity investigation presented in Chapter 5. In order to get the model to invert, the CDOM and scattering parameters were set constant and only the $a_\phi(440)$ parameter was allowed to be free in the solution scheme. If the CDOM and particle scattering parameter were allowed to be varied in the inversion process, the model would quickly diverge, producing no result at all. This is discussed further in Chapter 7. Improved accuracy was later achieved, on final transect trip (29/11/2011), by paying special attention to keeping the geometry of the sensor constant, in part, due to the extra boat crew on this day. On this occasion, the model was inverted for $a_\phi(440)$, $a_g(440)$ and $b_{bp}(550)$ without the model diverging. It was found, however, the most accurate measure of $a_\phi(440)$ was achieved by enforcing the single parameter inversion restriction. This is shown by comparing figures 6.90 with 6.96 and is discussed in detail in Chapter 7.

6.7.3 Continuous Underway Measurements

One of the aims of this project was to make continuous underway measurements ('transect') of reflectance in order to create a continuous map of the distribution of phytoplankton. The previous section described field trips where reflectance was measured only at the water sampling sites. The next section describes the extra steps required to collect data continuously along an underway transect and the extra steps necessary to process the data.

Transect Preprocessing

While making underway measurements of R_{rs}, the DALEC was prone to collecting erroneous data. Samples could be corrupted for a number of reasons, including foam caused by either the bow of the boat, breaking small waves, or by passing boats. Other sources of corruption included sunglint, and the geometry of the sensor changing mid-sample due to a rocking boat, as well as reflections on the water from trees or houses, particularly in narrow parts of the river.

To deal with these corrupt data points, a preprocessing filter was applied to the data to remove any reflectance spectra that were corrupted before using the data in the model inversion. The filter process comprised three parts. Firstly, the filter would consider the reflectance at 750 nm, where the reflectance was assumed to be zero. If the reflectance at this wavelength was above zero, above a small tolerance 10% of the maximum reflectance vale, the spectrum was discarded. Secondly, the compass data were scanned for sensor geometries that appeared to be erroneous. Wherever the sensor geometry deviated beyond a tolerance of 10% between successive measurements, the R_{rs} spectra was also discarded. Finally, for each reflectance spectrum, the RMS was calculated and any neighbouring R_{rs} that significantly changed above a threshold of 15% were also removed from the suite of R_{rs} spectra. Even after filtering out many of the data points, there still remained over 13 000 R_{rs} spectra for the transect.

Table 6.8: In situ measurements of $a_\phi(440)$, $a_g(440)$ and $b_{bp}(550)$; HOPE inverted values of $a_\phi(440)$, $a_g(440)$ and $b_{bp}(550)$ as well as supplimentary environmental data for all 10 of the SCCP sampling locations on 29/11/2011

Site	BLA	ARM	HEA	NAR	NIL	STJ	MAY	RON	KIN	SUC
in situ $a_\phi(440)(m^{-1})$	0.107	0.114	0.129	0.172	0.739	1.554	1.262	0.885	1.064	1.291
HOPE $a_\phi(440)(m^{-1})$	0.472	0.417	0.709	0.506	0.815	0.269	0.281	0.462	0.404	0.553
in situ $a_{nap}(440)(m^{-1})$	0.089	0.107	0.208	0.286	0.201	0.242	0.211	0.147	0.269	0.187
in situ $a_{cdom}(440)(m^{-1})$	0.746	1.001	1.076	1.918	3.402	4.316	4.832	5.166	5.403	5.573
in situ $a_g(440)(m^{-1})$	0.835	1.107	1.284	2.203	3.603	4.558	5.033	5.312	5.672	5.760
HOPE $a_g(440)(m^{-1})$	0.128	0.209	0.606	1.564	2.778	4.081	5.354	4.997	3.870	4.203
in situ $b_{bp}(590)(m^{-1})$	0.013	0.014	0.016	0.024	0.073	0.084	0.124	0.135	0.140	0.147
HOPE $b_{bp}(590)(m^{-1})$	0.028	0.032	0.057	0.100	0.087	0.119	0.161	0.134	0.135	0.151
$TSS(mgL^{-1})$	29.6	22.1	22.4	21.3	6.2	10.2	10.5	7.6	8.4	12.9
$Secchi\ depth(m)$	4.5	3.5	3.5	3.0	1.5	1.0	1.0	1.0	1.0	1.0
$Salinity(PSU)$	30.12	28.60	28.24	22.37	14.65	10.19	9.36	7.27	6.59	6.78
$Temperature(°C)$	14.51	14.41	13.94	13.33	14.13	13.70	13.55	13.72	13.14	13.22

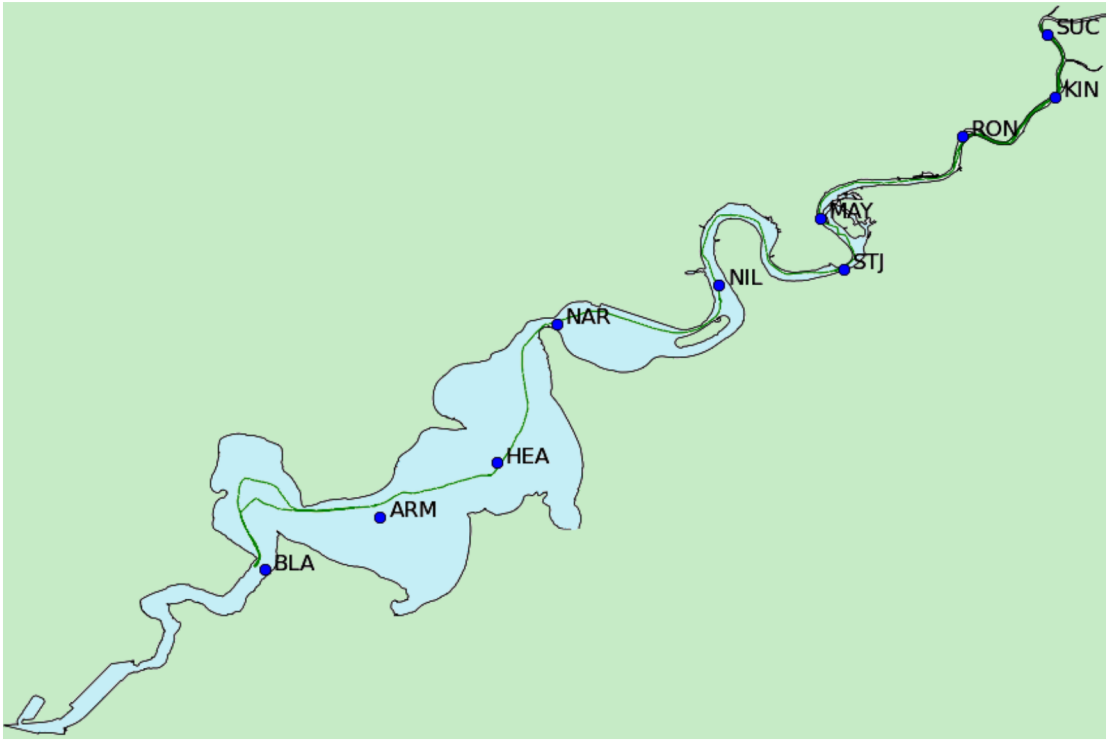

Figure 6.16: The green line represents the transect path along the river that DALEC reflectance measurements were made together with the in situ water sample locations marked in blue.

Transect Processing

After the preprocessing filter was applied to the reflectance data, each R_{rs} spectrum was temporally co-located with the sensor compass and GPS measurements. Because the reflectance measurements are made with a dynamic integration time and the supporting sensors are not, all measurements are interpolated to a common time – the CPU time of the computer logging the measurements.

The DALEC processing software parsed the reflectance data and the sensor geometry to the HOPE model used the LM-fit algorithm to invert the model for IOP estimates. Where the river was not optically deep and the bottom could be seen from the boat, the albedo for sand was used and the depth from the echosounder was used. The HOPE model described by Lee et al. (1999) defines six variables that can be varied through the optimisation routine. It was found, however, that if the routine allowed that many (six) degrees of freedom, the model, in the context of this study, was not able to converge to a solution.

In order for the model to converge on estimates of phytoplankton, which was the ultimate goal of the project, the degrees of freedom had to be restricted. The model was restricted to retrieve only three optical parameters – $a_\phi(440)$, $a_g(440)$ and $b_{bp}(550)$. These results are shown in figures 6.17, 6.18 and 6.19 respectively. These figures show that it is possible to invert the parameters for all three IOPs, however, the accuracy for $a_\phi(440)$ was low when compared to in situ measurements. The difference between the model derived $a_\phi(440)$ parameter and in situ measurements was around 70% for sites up to NIL and many times different past STJ, up to $\approx$ 485% different. In contrast, the model derived $a_g(440)$ parameter agreed more closely than $a_\phi(440)$ in the upper parts of the river. The modelled and measured $a_g(440)$ parameters were many times different for the first three SCCP sites, but were on average $\approx$ 20% different for sites up river from HEA. The model derived $b_{bp}(550)$ parameter was the most accurate. Model derived and measured values agree, on average, within $\approx$ 34% across all sites or $\approx$ 13% for sites up river of NAR.

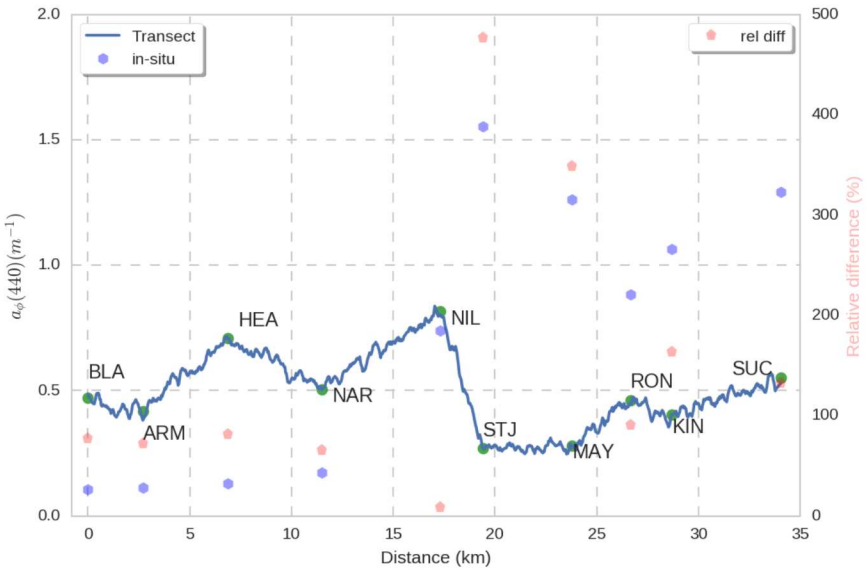

Figure 6.17: The model derived $a_\phi(440)$ measurements over the length of the transect. The phytoplankton in situ measurements are plotted as points on the figure, as well as the relative difference of those points when compared to the inverted parameters at those points.

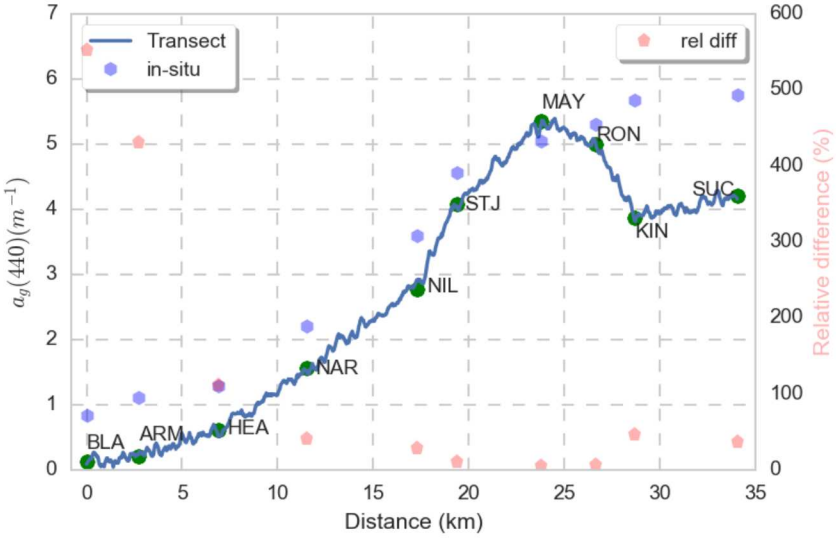

Figure 6.18: The model derived $a_g(440)$ measurements over the length of the transect. The CDOM in situ measurements are plotted as points on the figure, as well as the relative difference of those points when compared to the inverted parameters at those points.

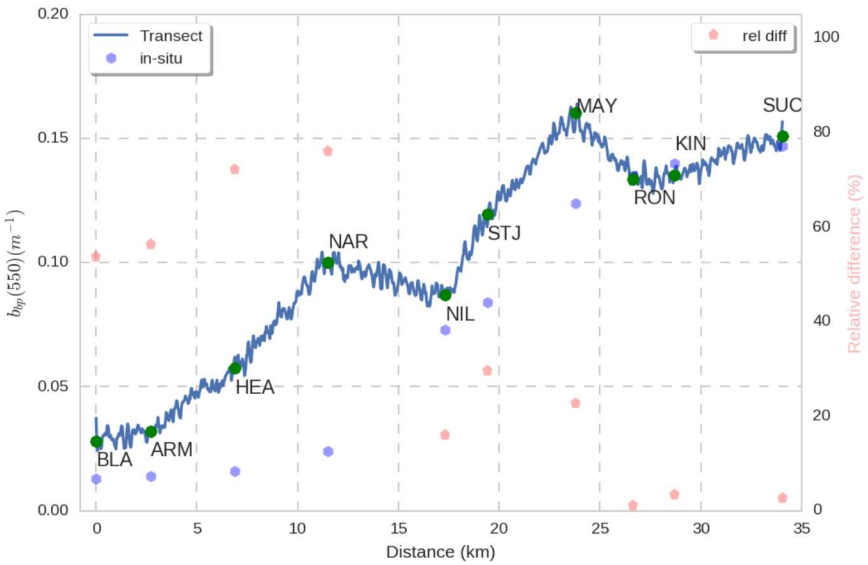

Figure 6.19: The model derived $b_{bp}(550)$ measurements over the length of the transect. The particle scattering in situ measurements are plotted as points on the figure, as well as the relative difference of those points when compared to the inverted parameters at those points.

To further improve the accuracy of the $a_\phi(440)$ parameter, the model was restricted further. As in situ measurements were taken at discrete points along the transect, these values were 'hard-coded' in the inversion routines for the co-located reflectance points (figures 6.84, 6.86 & 6.88). For the many reflectance points between these points, a simple nearest-neighbour interpolated value, proportional to the distance travelled along the transect, was used. Using these techniques and restricting the inversion routine to optimise only for $a_\phi(440)$, the phytoplankton retrieval was greatly improved. The accuracy when comparing model derived with in situ measured $a_\phi(440)$ is $\approx 11\%$ up to NIL. However, the parameter is still quite large, $\approx 121\%$ when considering all 10 SCCP sites.

This is shown by comparing Figure 6.17 with Figure 6.20 and by comparing Figure 6.93 with 6.99 and is particularly true for the smaller values of $a_\phi(440)$. The reason for this is discussed in Chapter 7.

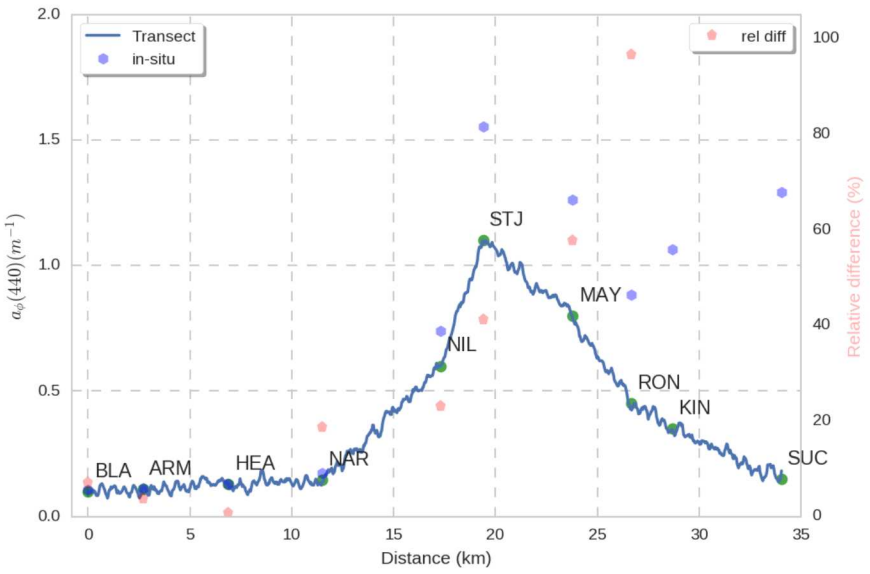

Figure 6.20: The model derived $a_\phi(440)$ measurements over the length of the transect when restricing to a single parameter retrieval. The phytoplankton in situ measurements are plotted as points on the figure, as well as the relative difference of those points when compared to the inverted parameters at those points.

Optimisation of the model required initial estimates of the desired inverted parameters. Lee et al. (1999) suggests ways to calculate initial estimates from the reflectance data. However, in this case, the in situ sampled data were used as the initial estimates for the co-located reflectance points and the result of the previously optimised reflectance measurement was used as the initial estimate of points between the sample locations.

Furthermore, estimates were made for the uncertainty for each model derived parameter using the coherent noise mode described in Section 5.5. Measurements for the training stage of the coherent noise model were conducted for each of the 10 sample locations. At each station, while water samples were being collected and other ancillary measurements (TSS, Secchi depth, Salinity and Temperature) were being undertaken, the reflectance was carefully measured as close to the same point on the water that was sensibly possible. Approximately 200 repeat DALEC R_{rs} measurements were taken at the sample locations which were then used to define ten corresponding coherent noise models. For each reflectance measurement made along the transect, the physically closest coherent noise model to the closest SCCP site was used, together with the method defined earlier in Section 5.5 to produced a synthetic set of $\hat{R}_{rs}$ data and, in turn, a distribution of inverted parameters. The method outlined in Section 5.4.2 was used to calculate the

uncertainty estimates for each model derived IOP measurement of $a_\phi(440)$, $a_g(440)$ and $b_{bp}(550)$.

Lastly, the optimisation routine was also further restricted from diverging, by defining limits that LM-fit was able to invert while using the steepest decent method. Limits of the phytoplankton optimisation were set to zero and twice the initial estimate for the lower and upper boundaries respectively.

Transect Postprocessing

As the preprocessing filter often removed some data points before the optimisation, and some data was interpolated to a new timestamp, the inverted phytoplankton estimate points were not defined at regular points along the transect. Figures 6.90, 6.91, 6.92 and 6.96 were interpolated to a regularly spaced transect by firstly applying a nearest-neighbour interpolation, and secondly, passing both the transect data and uncertainty calculations through a Savitzky-Golay filter (Press et al., 2007, page 766) of length 15 points and a polynomial order of 2 to smooth the transect results.

Water Sampling Sites

This section presents the R_{rs} measurements, as well as the IOP inverted parameters, for each of the SCCP water sampling sites. The ensemble DALEC R_{rs} measurements were used to train the coherent noise model and the mean R_{rs} spectra was subsequently used to produce 2400 synthetic $\hat{R}_{rs}$ measurements. These $\hat{R}_{rs}$ data were inverted using the LM-fit algorithm, and the HOPE optical model, for $a_\phi(440)$, $a_g(440)$ and $b_{bp}(550)$.

In the following section, for each of the 10 sample sites, the range of R_{rs} values are presented, indicated by the light blue envelope. The average reflectance is drawn as a dashed line. Following on, a hex-bin plot and a scatter plot are presented together, for each IOP parameter pair, for all of the inverted $\hat{R}_{rs}$ data. The hex-bin plot shows a histogram, along each axis, presenting the distribution of derived parameters. The density of the parameter distribution is indicated by the intensity of colour of the hexes. The scatter plots show the same data as the hex-bin plots but with 95% confidence interval, indicated by an error ellipse, and the mean values point, indicated by a red dot. The mean values are the values considered the 'solution' for the retrieved IOP values.

6.7.4 IOP Retrievals for the BLA Location

The range of R_{rs} for the BLA sample site are shown in Figure 6.21. The hex-bin plots of the inverted IOP parameter pairs are shown in figures 6.22 $(a_\phi(440), a_g(440))$, 6.24 $(a_g(440), b_{bp}(550))$ and 6.26 $(a_\phi(440), b_{bp}(550))$ and the scatter plots, indicating the confidence intervals, are shown in figures 6.23, 6.25 and 6.27.

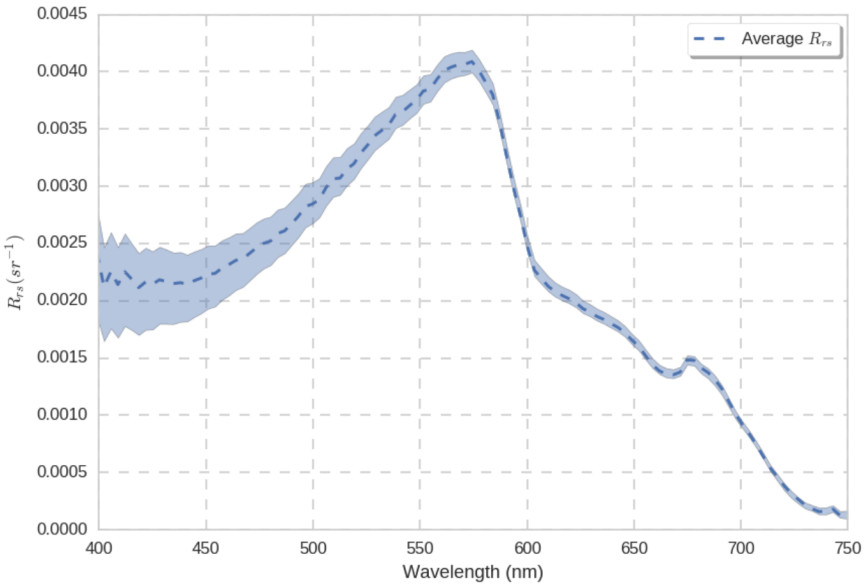

Figure 6.21: R_{rs} measurements taken at BLA with a stationary boat on 29/11/2011. The shaded area shows the maximum and minimum R_{rs} values. The full range of R_{rs} values were used to train the coherent noise model.

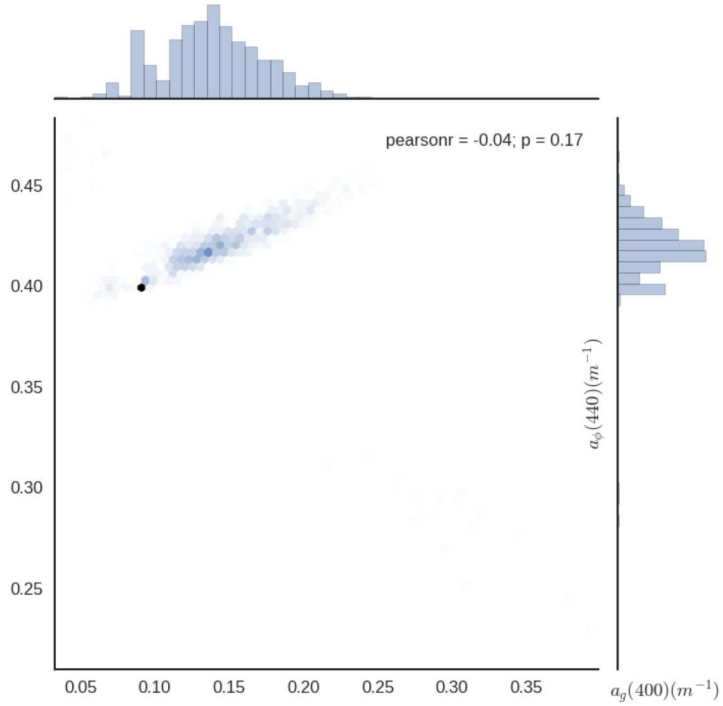

Figure 6.22: Inverted IOP parameters $a_\phi(440)$ versus $a_g(440)$ for the 2400 synthetic R_{rs} data produced using the coherent noise model, trained with measured R_{rs} taken at BLA with a stationary boat on 29/11/2011

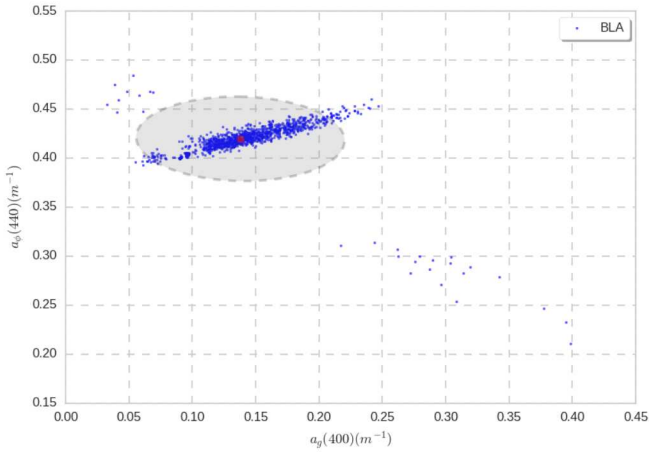

Figure 6.23: Inverted IOP parameters $a_\phi(440)$ versus $a_g(440)$ for the 2400 synthetic R_{rs} data produced using the coherent noise model, trained with measured R_{rs} taken at BLA with a stationary boat on 29/11/2011. The error ellipse represents the 95% confidence interval. The red point represents the average IOP value.

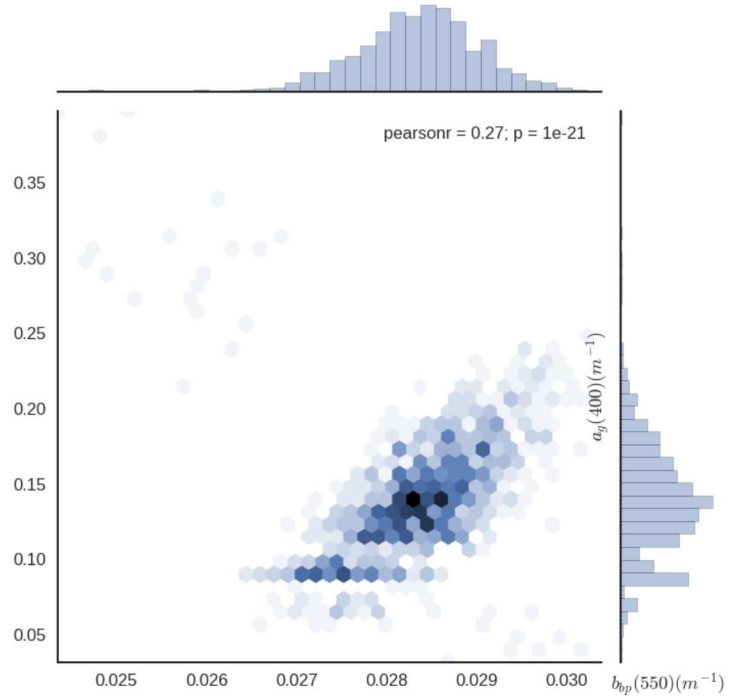

Figure 6.24: Inverted IOP parameters $a_g(440)$ versus $b_{bp}(550)$ for the 2400 synthetic R_{rs} data produced using the coherent noise model, trained with measured R_{rs} taken at BLA with a stationary boat on 29/11/2011

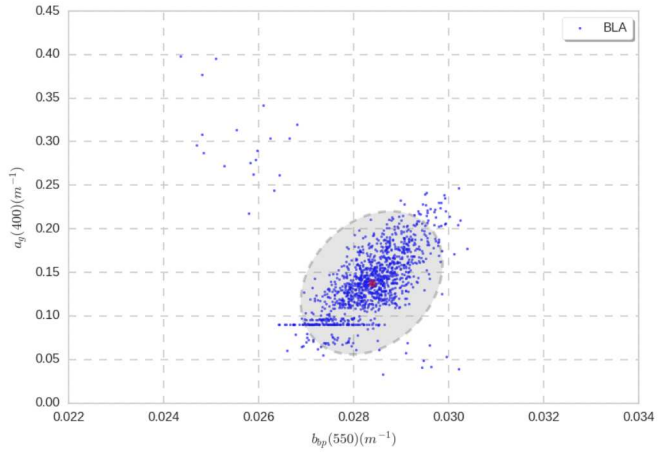

Figure 6.25: Inverted IOP parameters $a_g(440)$ versus $b_{bp}(550)$ for the 2400 synthetic R_{rs} data produced using the coherent noise model, trained with measured R_{rs} taken at BLA with a stationary boat on 29/11/2011. The error ellipse represents the 95% confidence interval. The red point represents the average IOP value.

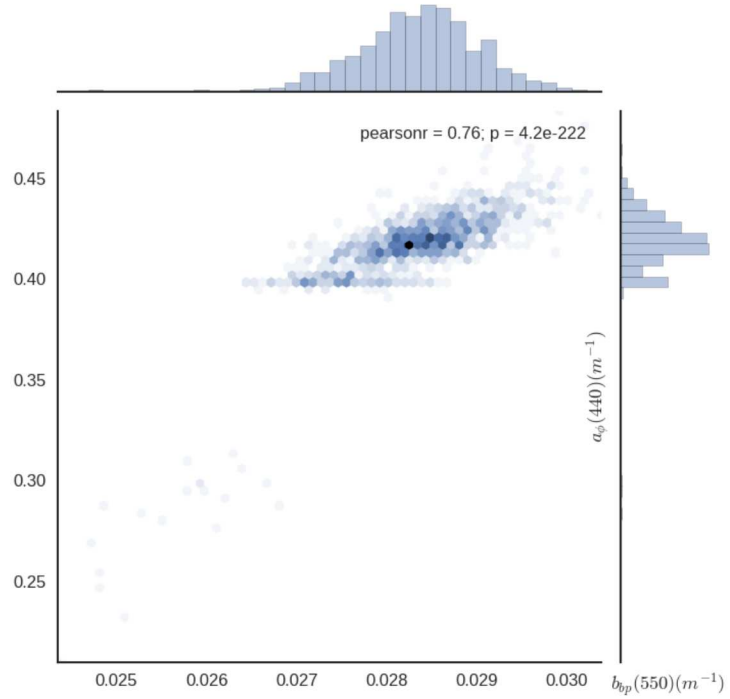

Figure 6.26: Inverted IOP parameters $a_\phi(440)$ versus $b_{bp}(550)$ for the 2400 synthetic R_{rs} data produced using the coherent noise model, trained with measured R_{rs} taken at BLA with a stationary boat on 29/11/2011

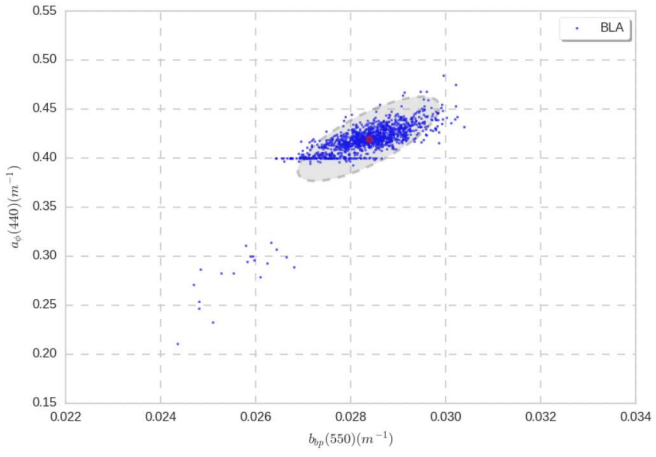

Figure 6.27: Inverted IOP parameters $a_\phi(440)$ versus $b_{bp}(550)$ for the 2400 synthetic R_{rs} data produced using the coherent noise model, trained with measured R_{rs} taken at BLA with a stationary boat on 29/11/2011. The error ellipse represents the 95% confidence interval. The red point represents the average IOP value.

6.7.5 IOP Retrievals for the ARM Location

The range of R_{rs} for the BLA sample site are shown in Figure 6.28. The hex-bin plots of the inverted IOP parameter pairs are shown in figures 6.29 $(a_\phi(440), a_g(440))$, 6.31 $(a_g(440), b_{bp}(550))$ and 6.33 $(a_\phi(440), b_{bp}(550))$ and the scatter plots, indicating the confidence intervals, are shown in figures 6.30, 6.32 and 6.34.

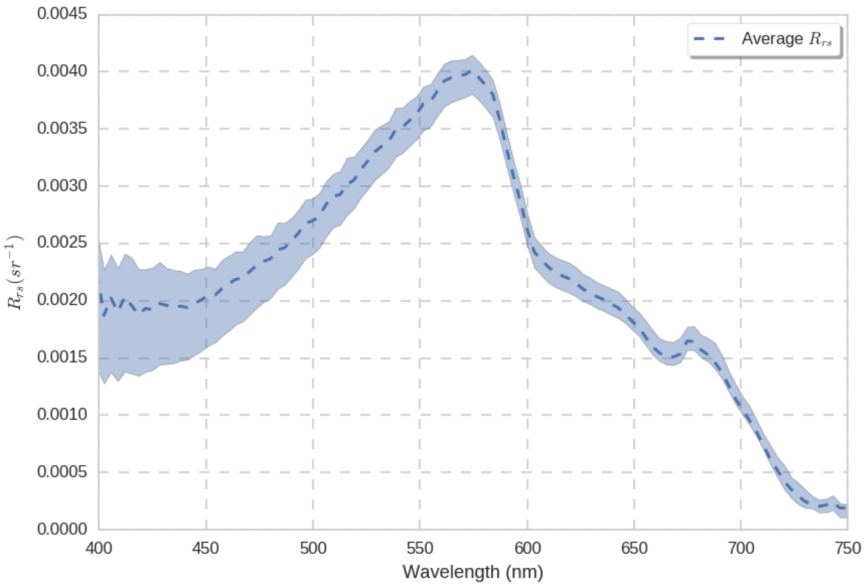

Figure 6.28: R_{rs} measurements taken at ARM with a stationary boat on 29/11/2011. The shaded area shows the maximum and minimum R_{rs} values. The full range of R_{rs} values were used to train the coherent noise model.

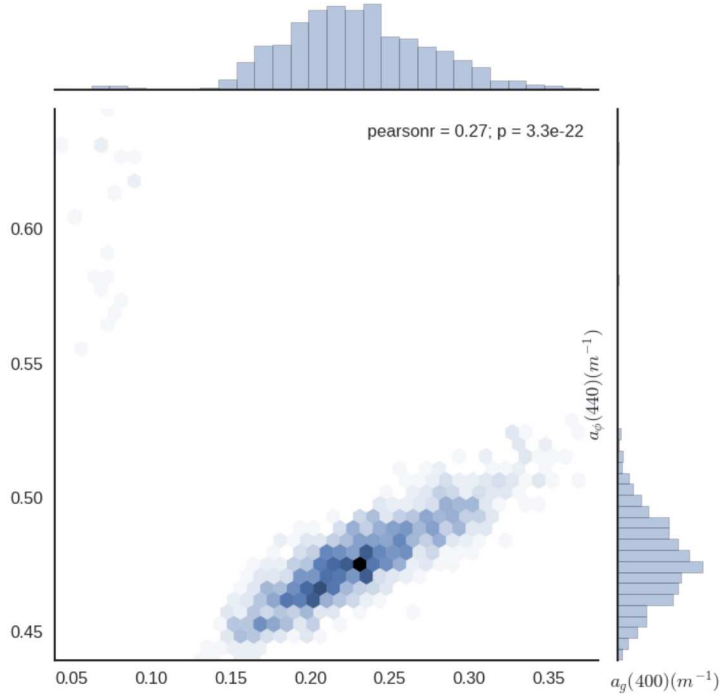

Figure 6.29: Inverted IOP parameters $a_\phi(440)$ versus $a_g(440)$ for the 2400 synthetic R_{rs} data produced using the coherent noise model, trained with measured R_{rs} taken at ARM with a stationary boat on 29/11/2011

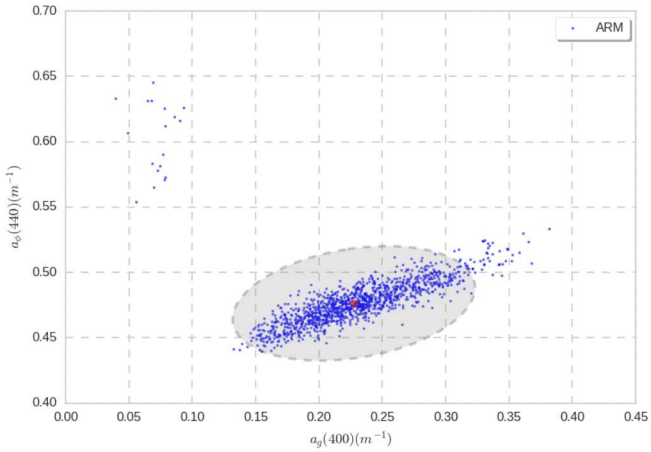

Figure 6.30: Inverted IOP parameters $a_\phi(440)$ versus $a_g(440)$ for the 2400 synthetic R_{rs} data produced using the coherent noise model, trained with measured R_{rs} taken at ARM with a stationary boat on 29/11/2011. The error ellipse represents the 95% confidence interval. The red point represents the average IOP value.

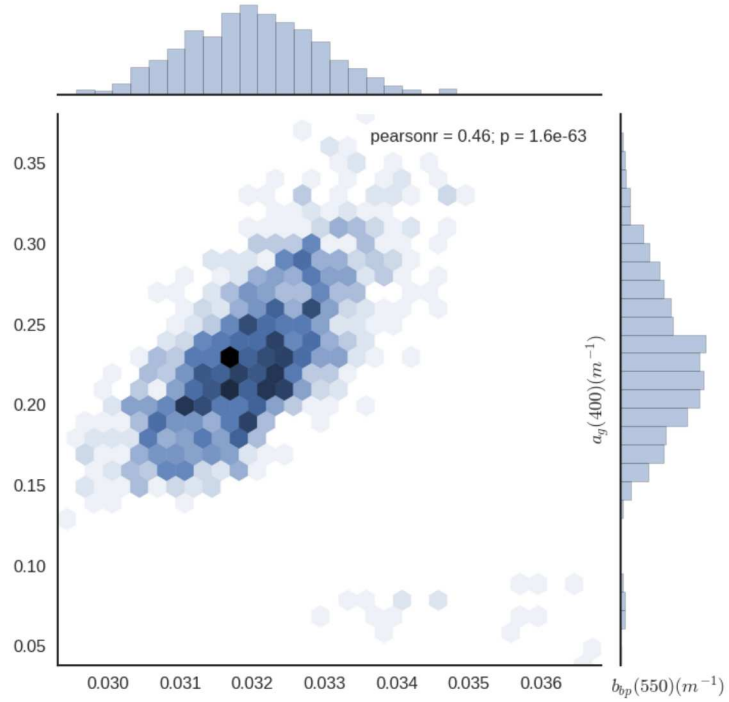

Figure 6.31: Inverted IOP parameters $a_g(440)$ versus $b_{bp}(550)$ for the 2400 synthetic R_{rs} data produced using the coherent noise model, trained with measured R_{rs} taken at ARM with a stationary boat on 29/11/2011

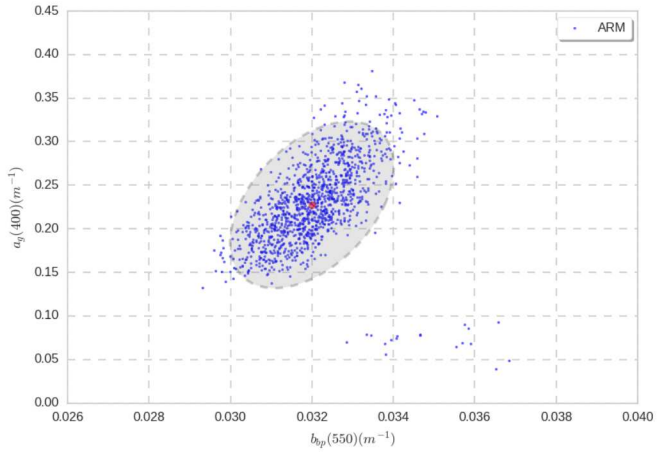

Figure 6.32: Inverted IOP parameters $a_g(440)$ versus $b_{bp}(550)$ for the 2400 synthetic R_{rs} data produced using the coherent noise model, trained with measured R_{rs} taken at ARM with a stationary boat on 29/11/2011. The error ellipse represents the 95% confidence interval. The red point represents the average IOP value.

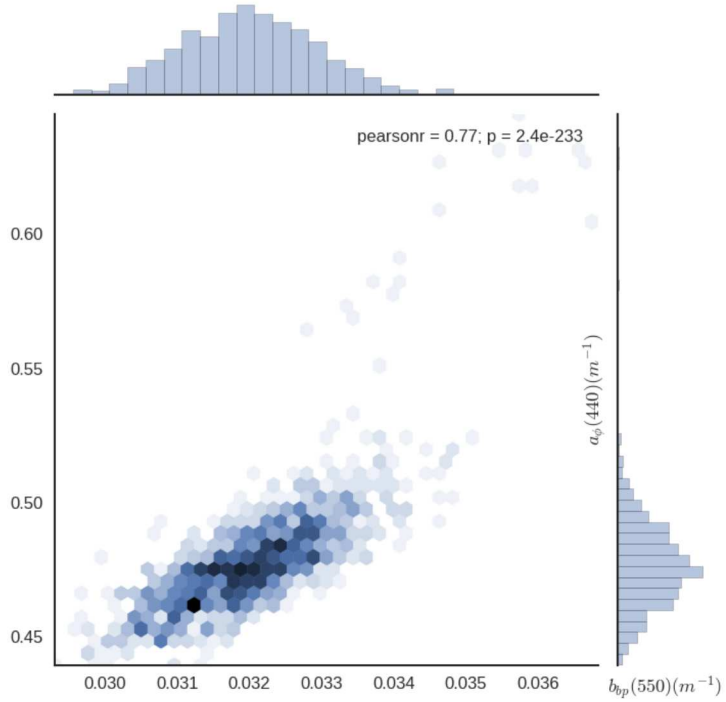

Figure 6.33: Inverted IOP parameters $a_\phi(440)$ versus $b_{bp}(550)$ for the 2400 synthetic R_{rs} data produced using the coherent noise model, trained with measured R_{rs} taken at ARM with a stationary boat on 29/11/2011

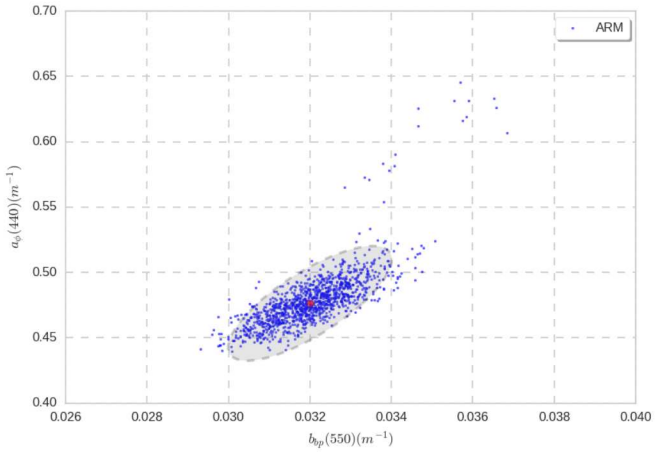

Figure 6.34: Inverted IOP parameters $a_\phi(440)$ versus $b_{bp}(550)$ for the 2400 synthetic R_{rs} data produced using the coherent noise model, trained with measured R_{rs} taken at ARM with a stationary boat on 29/11/2011. The error ellipse represents the 95% confidence interval. The red point represents the average IOP value.

6.7.6 IOP Retrievals for the HEA Location

The range of R_{rs} for the HEA sample site are shown in Figure 6.35. The hex-bin plots of the inverted IOP parameter pairs are shown in figures 6.36 $(a_\phi(440), a_g(440))$, 6.38 $(a_g(440), b_{bp}(550))$ and 6.40 $(a_\phi(440), b_{bp}(550))$ and the scatter plots, indicating the confidence intervals, are shown in figures 6.37, 6.39 and 6.41.

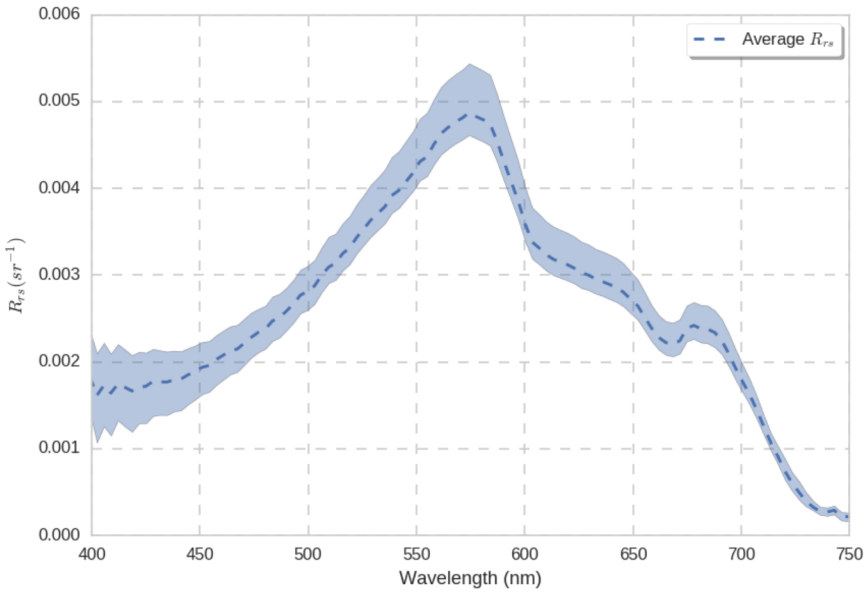

Figure 6.35: R_{rs} measurements taken at HEA with a stationary boat on 29/11/2011. The shaded area shows the maximum and minimum R_{rs} values. The full range of R_{rs} values were used to train the coherent noise model.

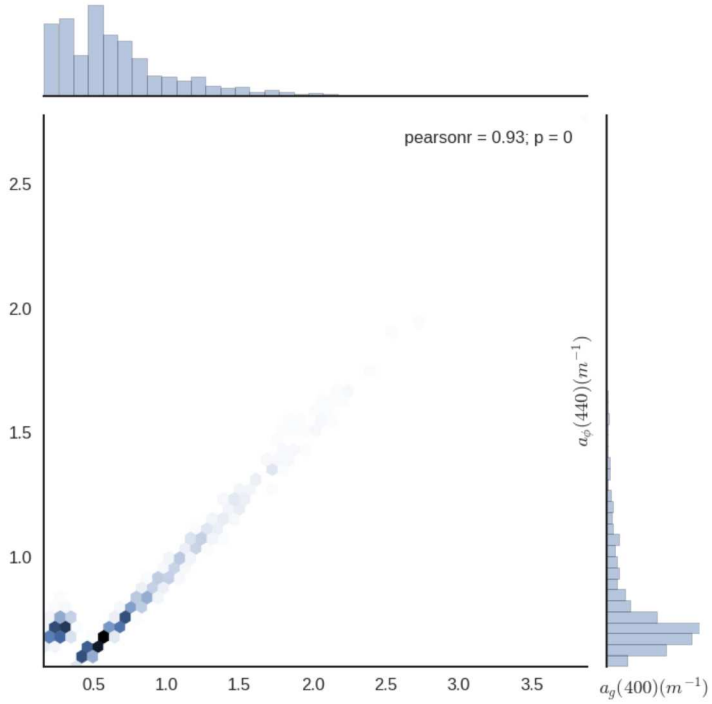

Figure 6.36: Inverted IOP parameters $a_\phi(440)$ versus $a_g(440)$ for the 2400 synthetic R_{rs} data produced using the coherent noise model, trained with measured R_{rs} taken at HEA with a stationary boat on 29/11/2011

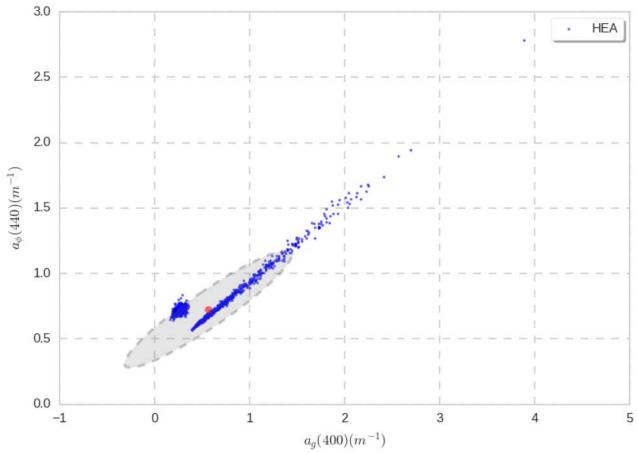

Figure 6.37: Inverted IOP parameters $a_\phi(440)$ versus $a_g(440)$ for the 2400 synthetic R_{rs} data produced using the coherent noise model, trained with measured R_{rs} taken at HEA with a stationary boat on 29/11/2011. The error ellipse represents the 95% confidence interval. The red point represents the average IOP value.

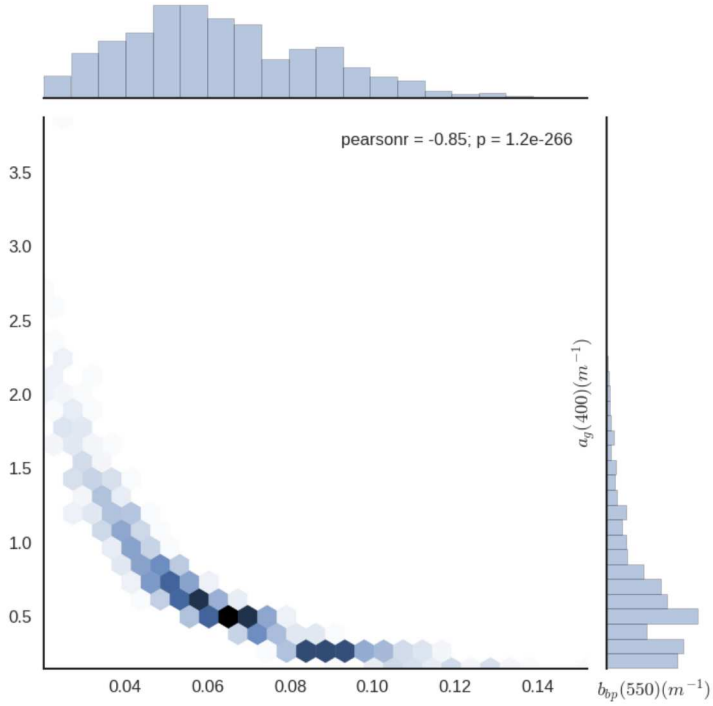

Figure 6.38: Inverted IOP parameters $a_g(440)$ versus $b_{bp}(550)$ for the 2400 synthetic R_{rs} data produced using the coherent noise model, trained with measured R_{rs} taken at HEA with a stationary boat on 29/11/2011

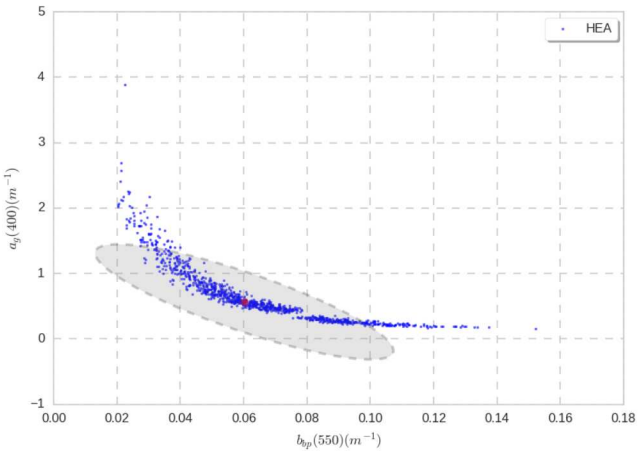

Figure 6.39: Inverted IOP parameters $a_g(440)$ versus $b_{bp}(550)$ for the 2400 synthetic R_{rs} data produced using the coherent noise model, trained with measured R_{rs} taken at HEA with a stationary boat on 29/11/2011. The error ellipse represents the 95% confidence interval. The red point represents the average IOP value.

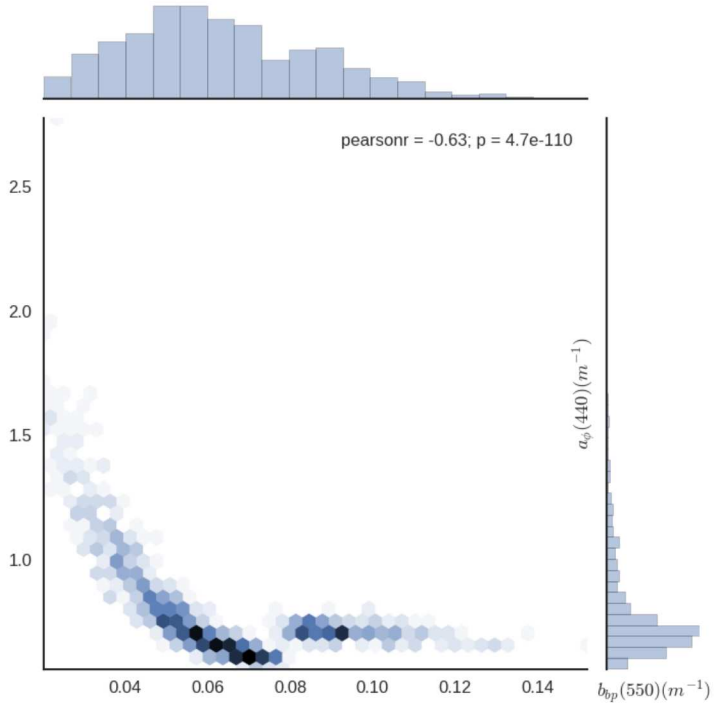

Figure 6.40: Inverted IOP parameters $a_\phi(440)$ versus $b_{bp}(550)$ for the 2400 synthetic R_{rs} data produced using the coherent noise model, trained with measured R_{rs} taken at HEA with a stationary boat on 29/11/2011

6.7.7 IOP Retrievals for the NAR Location

The range of R_{rs} for the NAR sample site are shown in Figure 6.42. The hex-bin plots of the inverted IOP parameter pairs are shown in figures 6.43 $(a_\phi(440), a_g(440))$, 6.45 $(a_g(440), b_{bp}(550))$ and 6.47 $(a_\phi(440), b_{bp}(550))$ and the scatter plots, indicating the confidence intervals, are shown in figures 6.44, 6.46 and 6.41.

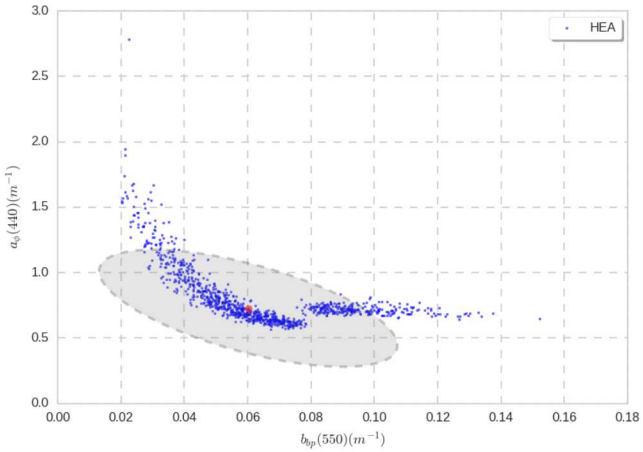

Figure 6.41: Inverted IOP parameters $a_\phi(440)$ versus $b_{bp}(550)$ for the 2400 synthetic R_{rs} data produced using the coherent noise model, trained with measured R_{rs} taken at HEA with a stationary boat on 29/11/2011. The error ellipse represents the 95% confidence interval. The red point represents the average IOP value.

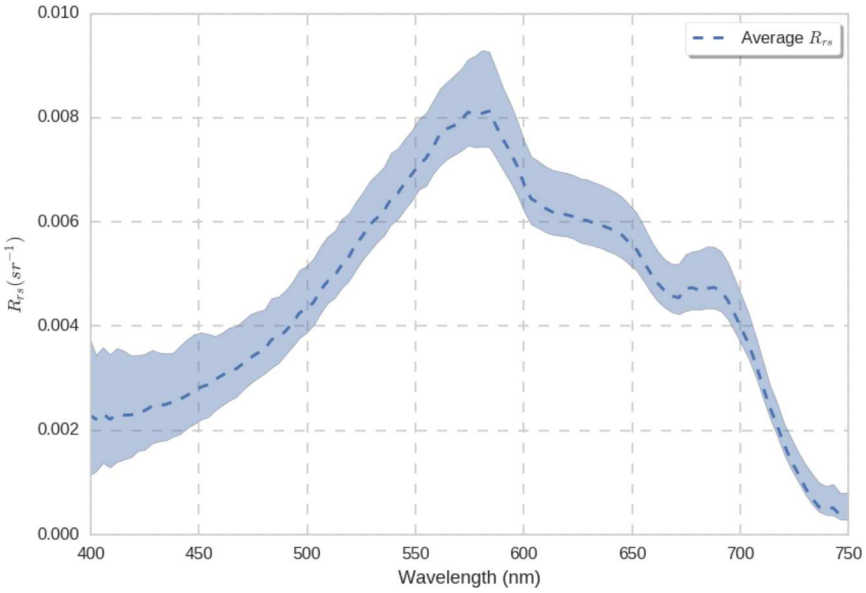

Figure 6.42: R_{rs} measurements taken at NAR with a stationary boat on 29/11/2011. The shaded area shows the maximum and minimum R_{rs} values. The full range of R_{rs} values were used to train the coherent noise model.

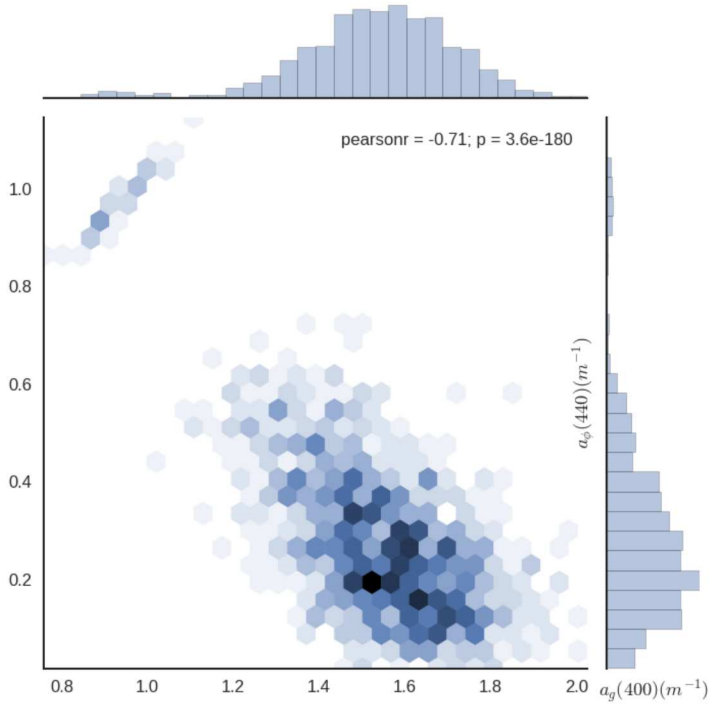

Figure 6.43: Inverted IOP parameters $a_\phi(440)$ versus $a_g(440)$ for the 2400 synthetic R_{rs} data produced using the coherent noise model, trained with measured R_{rs} taken at NAR with a stationary boat on 29/11/2011

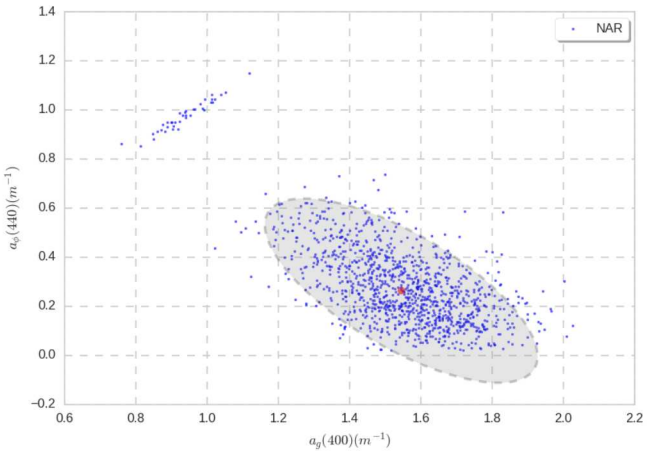

Figure 6.44: Inverted IOP parameters $a_\phi(440)$ versus $a_g(440)$ for the 2400 synthetic R_{rs} data produced using the coherent noise model, trained with measured R_{rs} taken at NAR with a stationary boat on 29/11/2011. The error ellipse represents the 95% confidence interval. The red point represents the average IOP value.

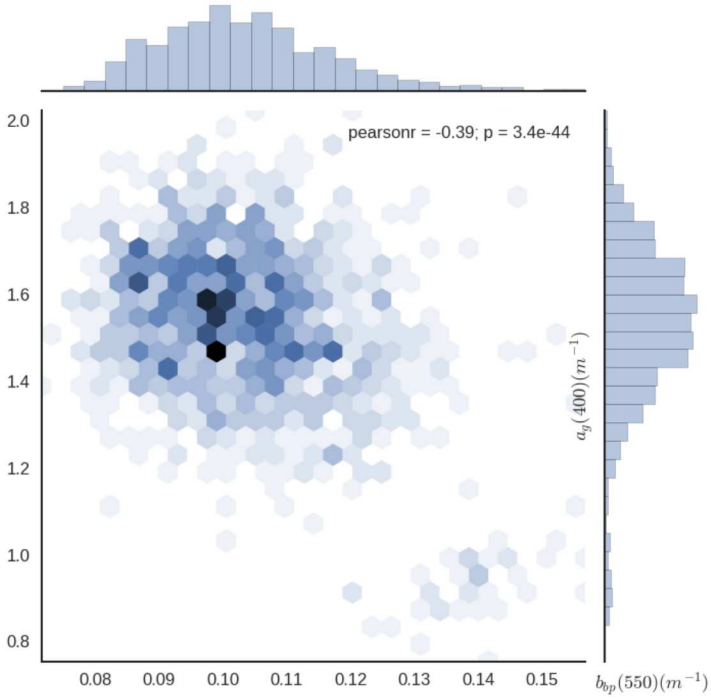

Figure 6.45: Inverted IOP parameters $a_g(440)$ versus $b_{bp}(550)$ for the 2400 synthetic R_{rs} data produced using the coherent noise model, trained with measured R_{rs} taken at NAR with a stationary boat on 29/11/2011

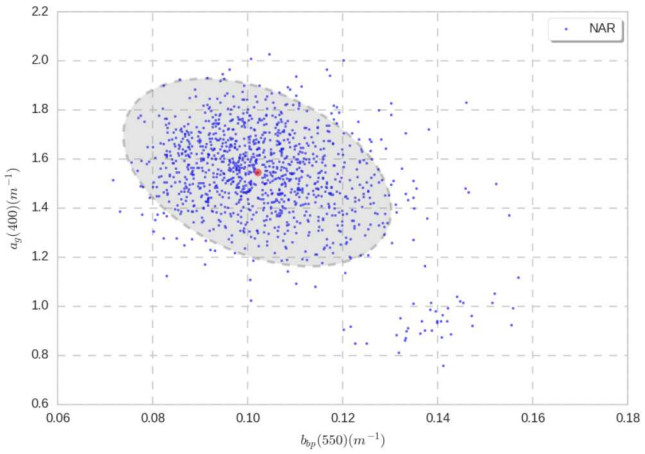

Figure 6.46: Inverted IOP parameters $a_g(440)$ versus $b_{bp}(550)$ for the 2400 synthetic R_{rs} data produced using the coherent noise model, trained with measured R_{rs} taken at NAR with a stationary boat on 29/11/2011. The error ellipse represents the 95% confidence interval. The red point represents the average IOP value.

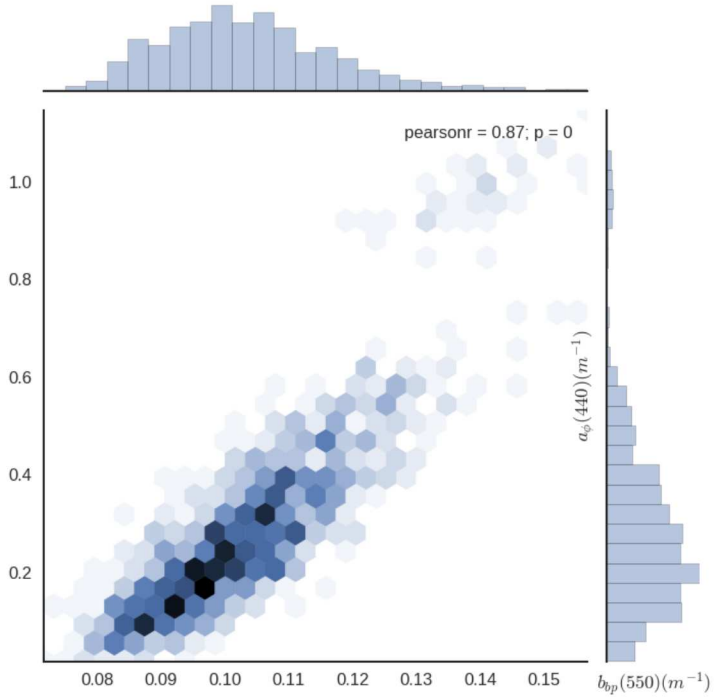

Figure 6.47: Inverted IOP parameters $a_\phi(440)$ versus $b_{bp}(550)$ for the 2400 synthetic R_{rs} data produced using the coherent noise model, trained with measured R_{rs} taken at NAR with a stationary boat on 29/11/2011

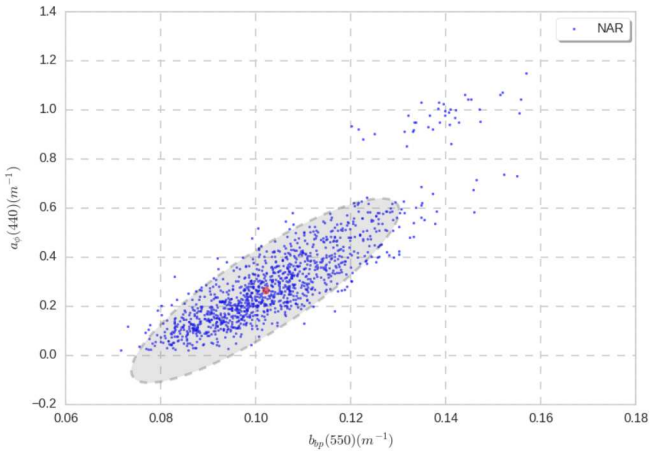

Figure 6.48: Inverted IOP parameters $a_\phi(440)$ versus $b_{bp}(550)$ for the 2400 synthetic R_{rs} data produced using the coherent noise model, trained with measured R_{rs} taken at NAR with a stationary boat on 29/11/2011. The error ellipse represents the 95% confidence interval. The red point represents the average IOP value.

6.7.8 IOP Retrievals for the NIL Location

The range of R_{rs} for the NIL sample site are shown in Figure 6.49. The hex-bin plots of the inverted IOP parameter pairs are shown in figures 6.50 $(a_\phi(440), a_g(440))$, 6.52 $(a_g(440), b_{bp}(550))$ and 6.54 $(a_\phi(440), b_{bp}(550))$ and the scatter plots, indicating the confidence intervals, are shown in figures 6.51, 6.53 and 6.55.

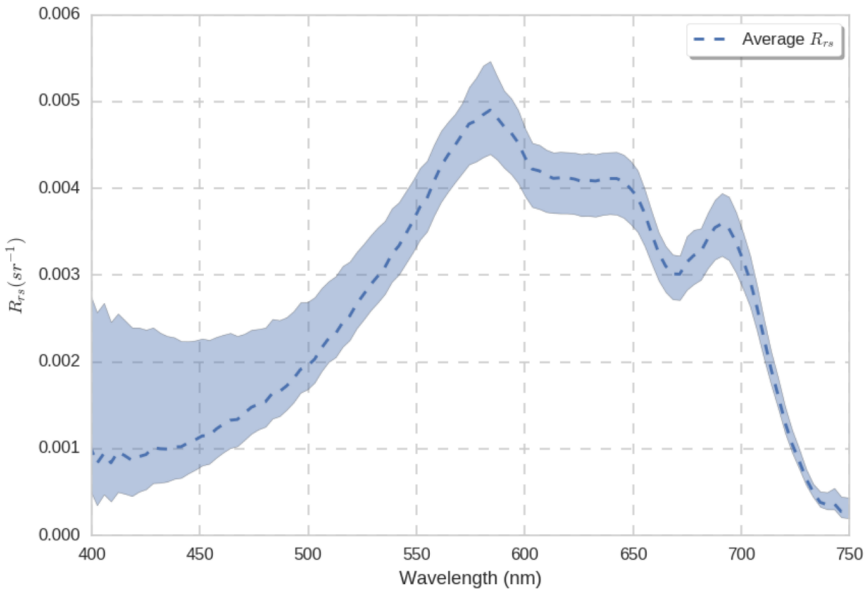

Figure 6.49: R_{rs} measurements taken at NIL with a stationary boat on 29/11/2011. The shaded area shows the maximum and minimum R_{rs} values. The full range of R_{rs} values were used to train the coherent noise model.

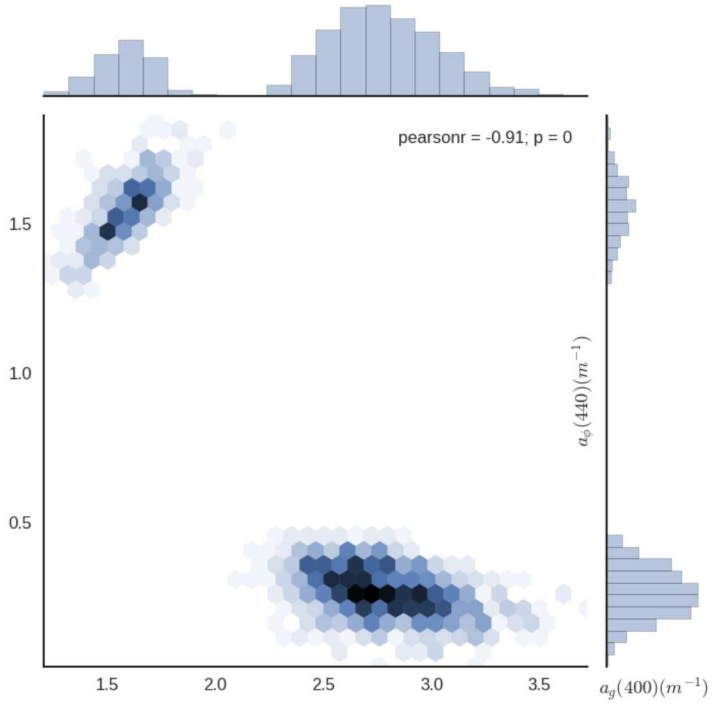

Figure 6.50: Inverted IOP parameters $a_\phi(440)$ versus $a_g(440)$ for the 2400 synthetic R_{rs} data produced using the coherent noise model, trained with measured R_{rs} taken at NIL with a stationary boat on 29/11/2011

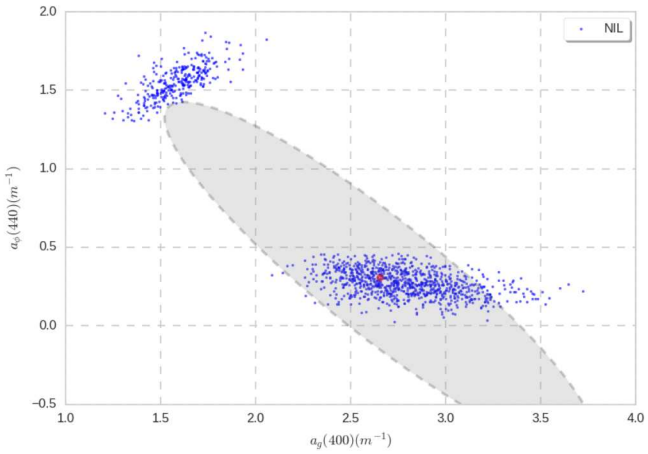

Figure 6.51: Inverted IOP parameters $a_\phi(440)$ versus $a_g(440)$ for the 2400 synthetic R_{rs} data produced using the coherent noise model, trained with measured R_{rs} taken at NIL with a stationary boat on 29/11/2011. The error ellipse represents the 95% confidence interval. The red point represents the average IOP value.

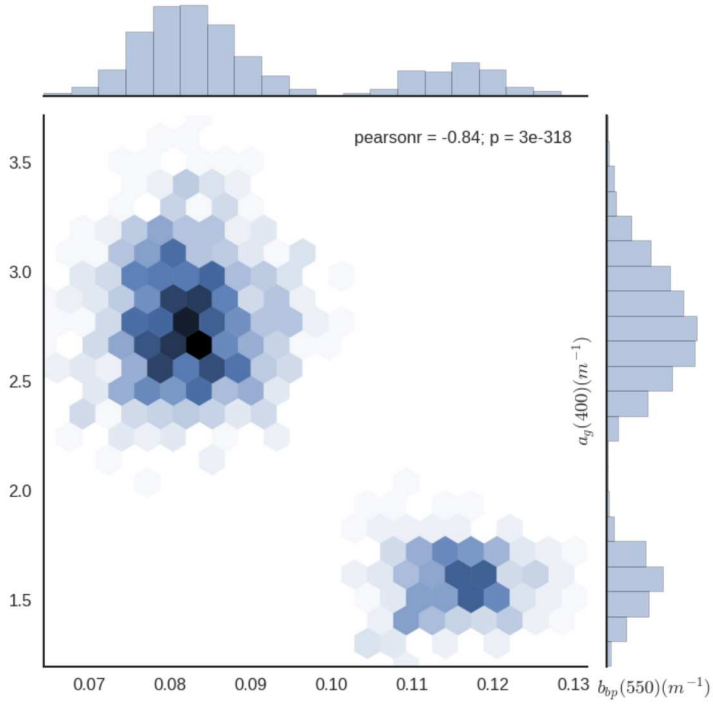

Figure 6.52: Inverted IOP parameters $a_g(440)$ versus $b_{bp}(550)$ for the 2400 synthetic R_{rs} data produced using the coherent noise model, trained with measured R_{rs} taken at NIL with a stationary boat on 29/11/2011

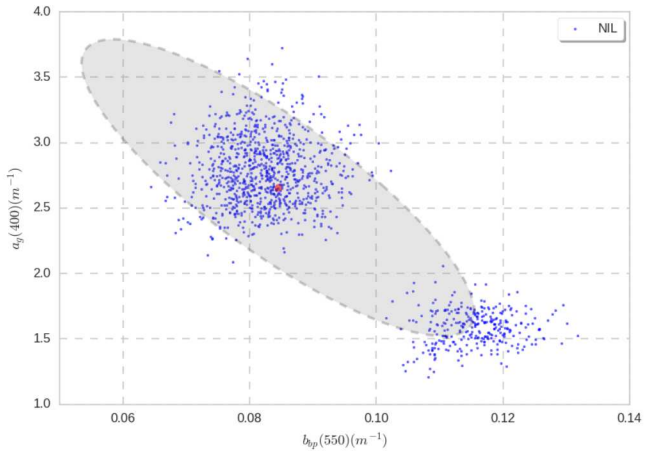

Figure 6.53: Inverted IOP parameters $a_g(440)$ versus $b_{bp}(550)$ for the 2400 synthetic R_{rs} data produced using the coherent noise model, trained with measured R_{rs} taken at NIL with a stationary boat on 29/11/2011. The error ellipse represents the 95% confidence interval. The red point represents the average IOP value.

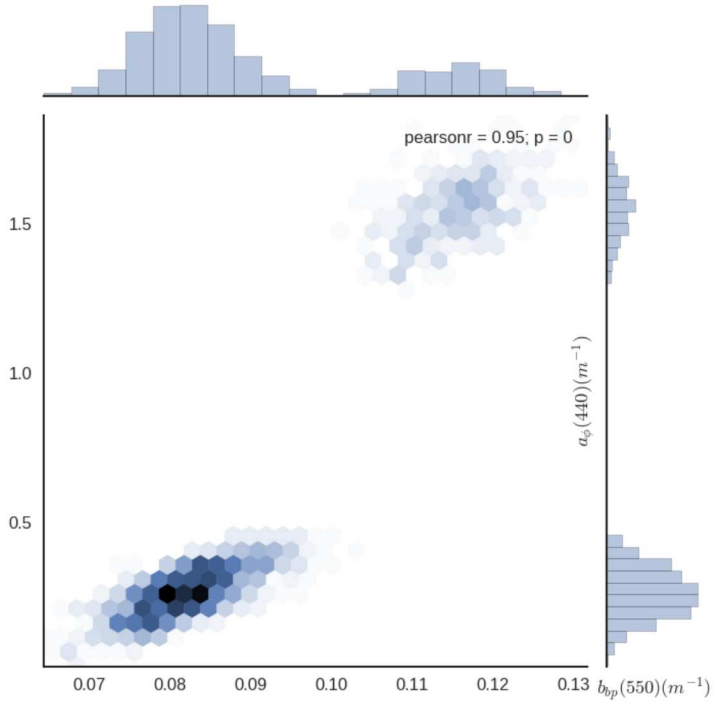

Figure 6.54: Inverted IOP parameters $a_\phi(440)$ versus $b_{bp}(550)$ for the 2400 synthetic R_{rs} data produced using the coherent noise model, trained with measured R_{rs} taken at NIL with a stationary boat on 29/11/2011

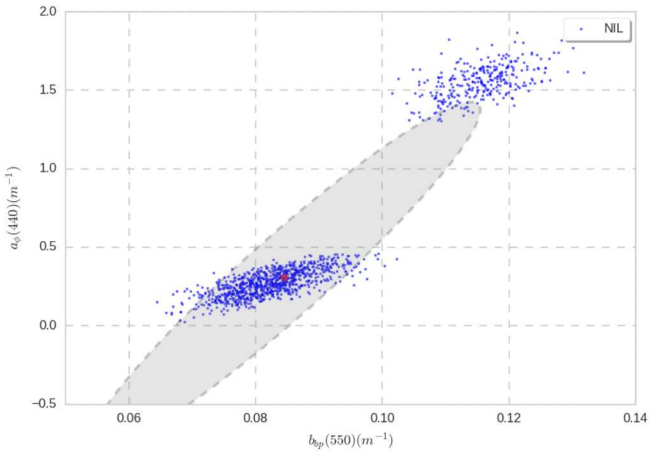

Figure 6.55: Inverted IOP parameters $a_\phi(440)$ versus $b_{bp}(550)$ for the 2400 synthetic R_{rs} data produced using the coherent noise model, trained with measured R_{rs} taken at NIL with a stationary boat on 29/11/2011. The error ellipse represents the 95% confidence interval. The red point represents the average IOP value.

6.7.9 IOP Retrievals for the STJ Location

The range of R_{rs} for the STJ sample site are shown in Figure 6.56. The hex-bin plots of the inverted IOP parameter pairs are shown in figures 6.57 $(a_\phi(440), a_g(440))$, 6.59 $(a_g(440), b_{bp}(550))$ and 6.61 $(a_\phi(440), b_{bp}(550))$ and the scatter plots, indicating the confidence intervals, are shown in figures 6.58, 6.60 and 6.62.

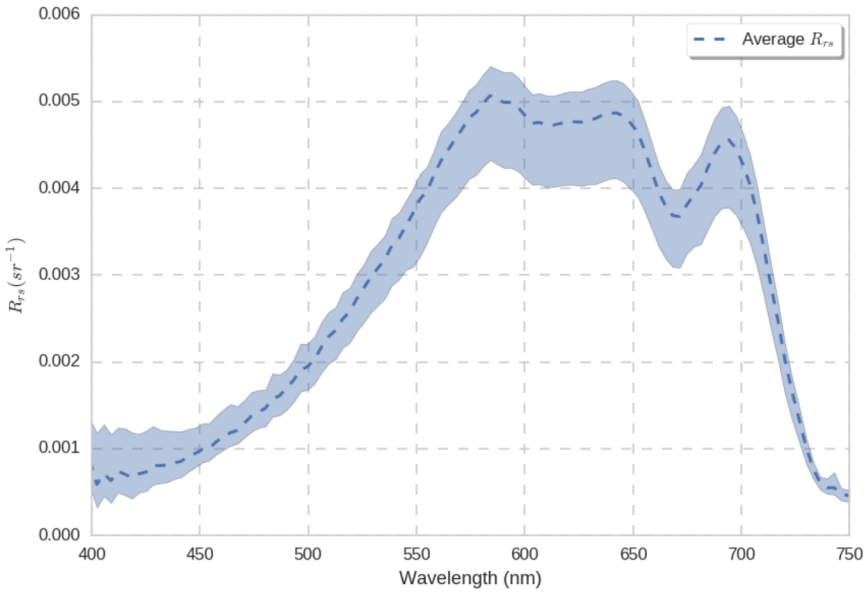

Figure 6.56: R_{rs} measurements taken at STJ with a stationary boat on 29/11/2011. The shaded area shows the maximum and minimum R_{rs} values. The full range of R_{rs} values were used to train the coherent noise model.

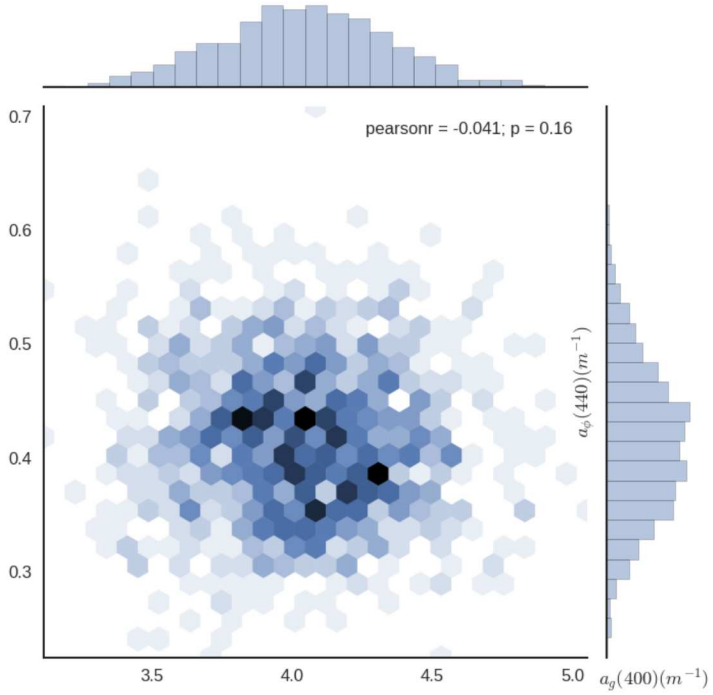

Figure 6.57: Inverted IOP parameters $a_\phi(440)$ versus $a_g(440)$ for the 2400 synthetic R_{rs} data produced using the coherent noise model, trained with measured R_{rs} taken at STJ with a stationary boat on 29/11/2011

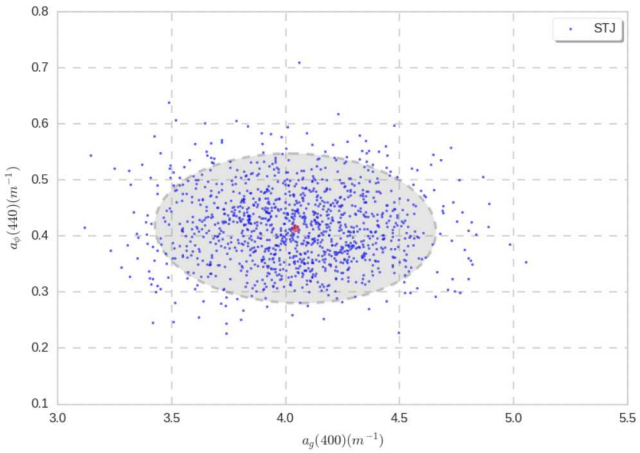

Figure 6.58: Inverted IOP parameters $a_\phi(440)$ versus $a_g(440)$ for the 2400 synthetic R_{rs} data produced using the coherent noise model, trained with measured R_{rs} taken at STJ with a stationary boat on 29/11/2011. The error ellipse represents the 95% confidence interval. The red point represents the average IOP value.

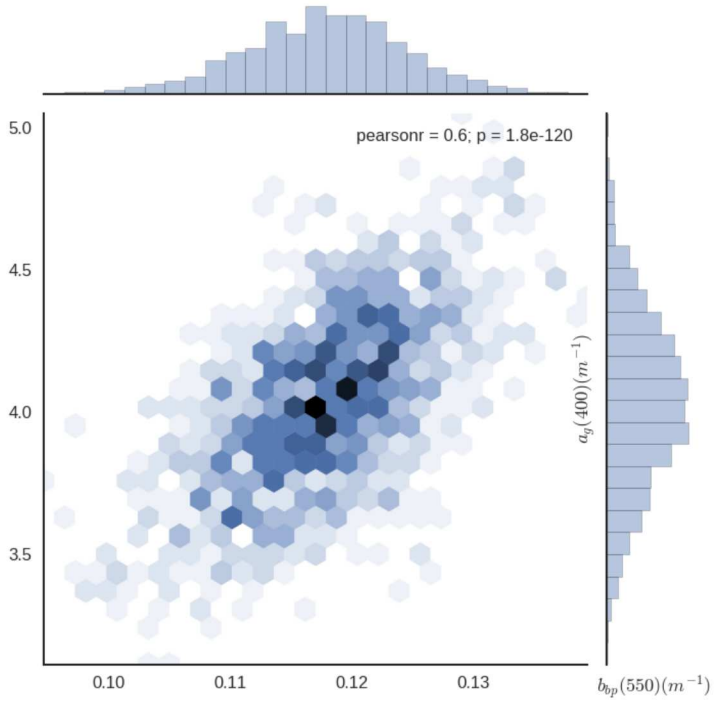

Figure 6.59: Inverted IOP parameters $a_g(440)$ versus $b_{bp}(550)$ for the 2400 synthetic R_{rs} data produced using the coherent noise model, trained with measured R_{rs} taken at STJ with a stationary boat on 29/11/2011

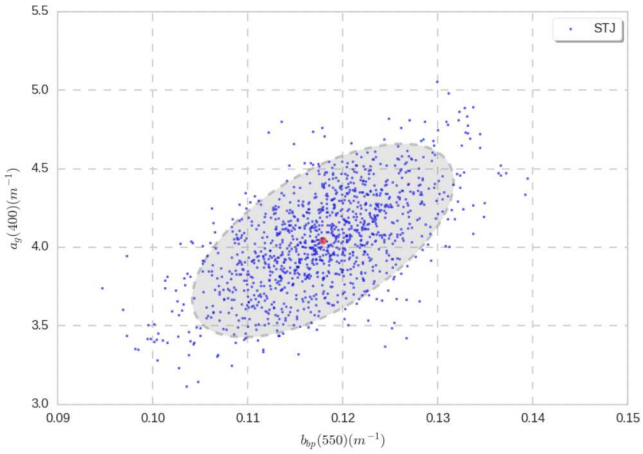

Figure 6.60: Inverted IOP parameters $a_g(440)$ versus $b_{bp}(550)$ for the 2400 synthetic R_{rs} data produced using the coherent noise model, trained with measured R_{rs} taken at STJ with a stationary boat on 29/11/2011. The error ellipse represents the 95% confidence interval. The red point represents the average IOP value.

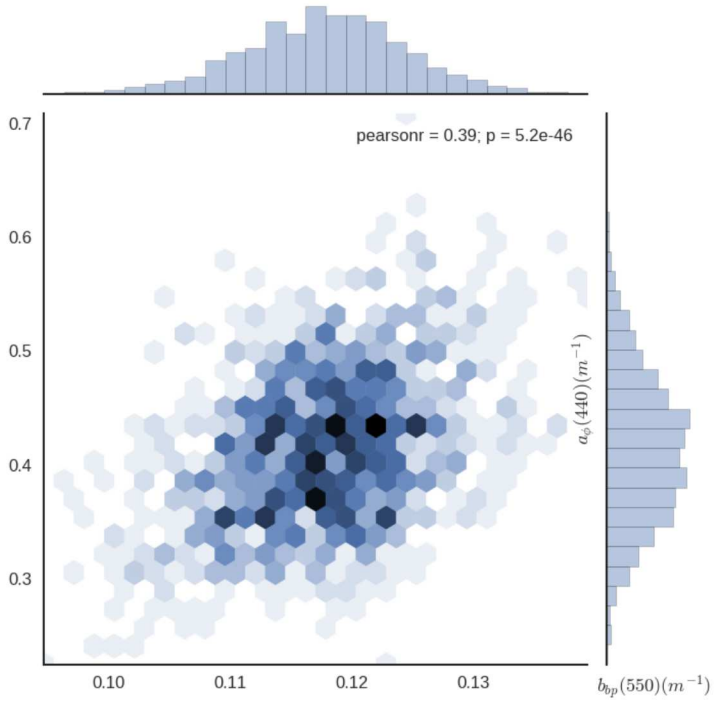

Figure 6.61: Inverted IOP parameters $a_\phi(440)$ versus $b_{bp}(550)$ for the 2400 synthetic R_{rs} data produced using the coherent noise model, trained with measured R_{rs} taken at STJ with a stationary boat on 29/11/2011

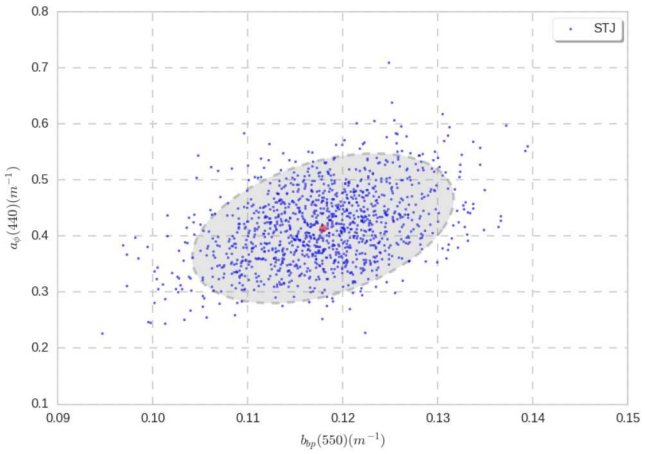

Figure 6.62: Inverted IOP parameters $a_\phi(440)$ versus $b_{bp}(550)$ for the 2400 synthetic R_{rs} data produced using the coherent noise model, trained with measured R_{rs} taken at STJ with a stationary boat on 29/11/2011. The error ellipse represents the 95% confidence interval. The red point represents the average IOP value.

6.7.10 IOP Retrievals for the RON Location

The range of R_{rs} for the RON sample site are shown in Figure 6.63. The hex-bin plots of the inverted IOP parameter pairs are shown in figures 6.64 $(a_\phi(440), a_g(440))$, 6.66 $(a_g(440), b_{bp}(550))$ and 6.68 $(a_\phi(440), b_{bp}(550))$ and the scatter plots, indicating the confidence intervals, are shown in figures 6.65, 6.67 and 6.62.

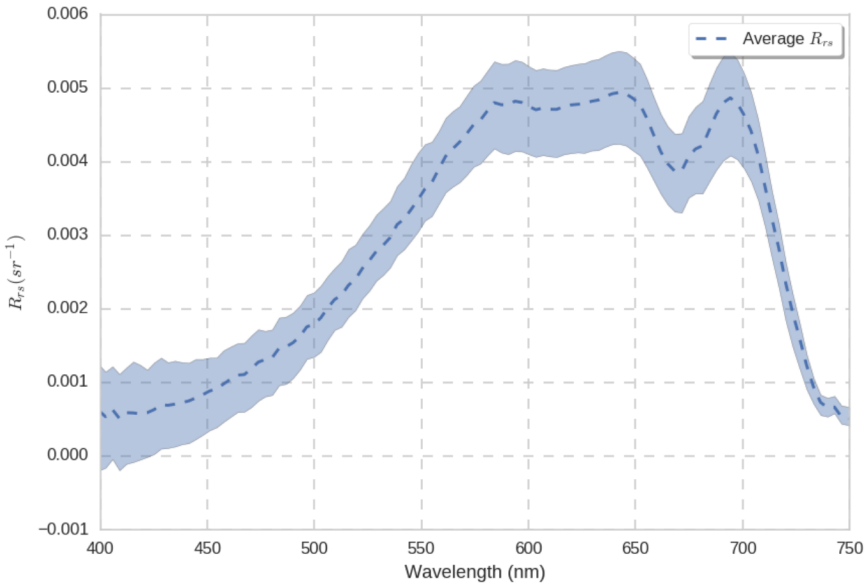

Figure 6.63: R_{rs} measurements taken at RON with a stationary boat on 29/11/2011. The shaded area shows the maximum and minimum R_{rs} values. The full range of R_{rs} values were used to train the coherent noise model.

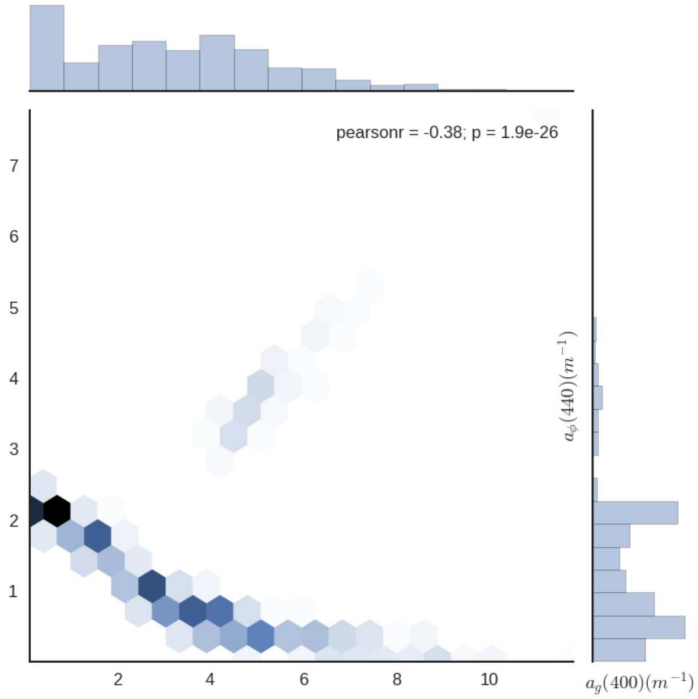

Figure 6.64: Inverted IOP parameters $a_\phi(440)$ versus $a_g(440)$ for the 2400 synthetic R_{rs} data produced using the coherent noise model, trained with measured R_{rs} taken at RON with a stationary boat on 29/11/2011

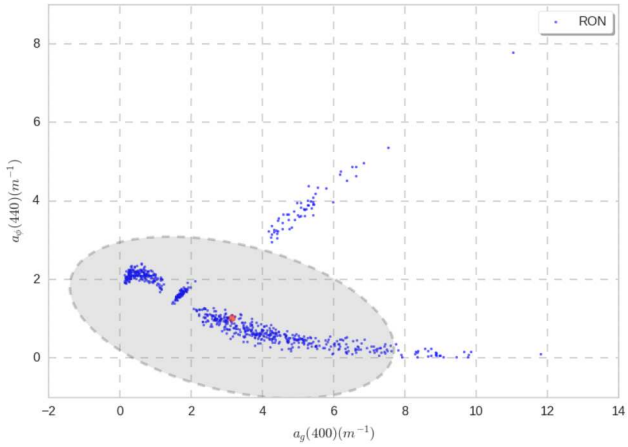

Figure 6.65: Inverted IOP parameters $a_\phi(440)$ versus $a_g(440)$ for the 2400 synthetic R_{rs} data produced using the coherent noise model, trained with measured R_{rs} taken at RON with a stationary boat on 29/11/2011. The error ellipse represents the 95% confidence interval. The red point represents the average IOP value.

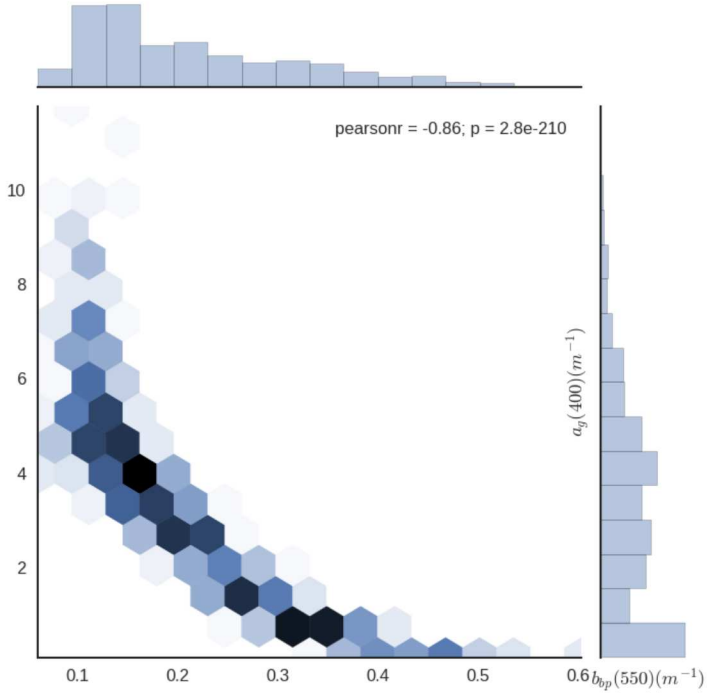

Figure 6.66: Inverted IOP parameters $a_g(440)$ versus $b_{bp}(550)$ for the 2400 synthetic R_{rs} data produced using the coherent noise model, trained with measured R_{rs} taken at RON with a stationary boat on 29/11/2011

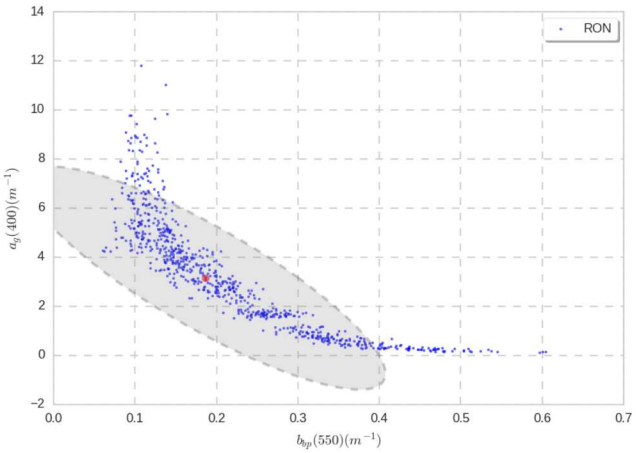

Figure 6.67: Inverted IOP parameters $a_g(440)$ versus $b_{bp}(550)$ for the 2400 synthetic R_{rs} data produced using the coherent noise model, trained with measured R_{rs} taken at RON with a stationary boat on 29/11/2011. The error ellipse represents the 95% confidence interval. The red point represents the average IOP value.

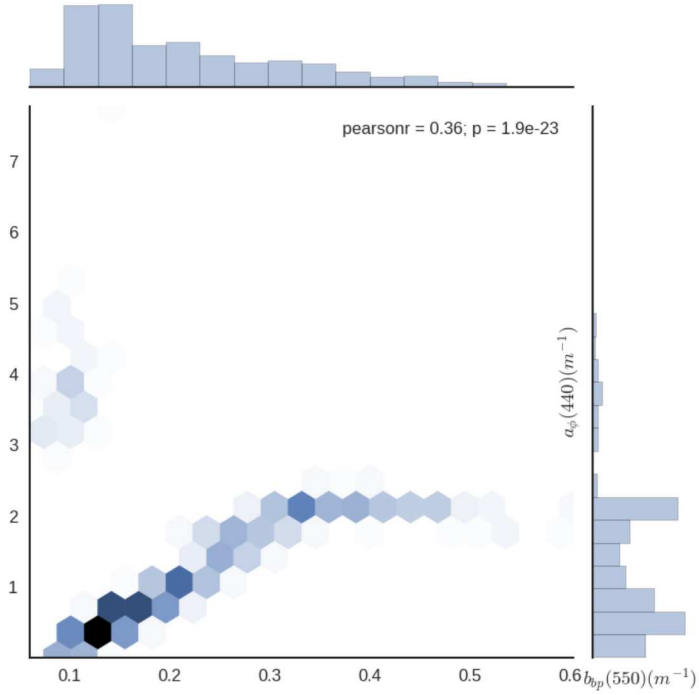

Figure 6.68: Inverted IOP parameters $a_\phi(440)$ versus $b_{bp}(550)$ for the 2400 synthetic R_{rs} data produced using the coherent noise model, trained with measured R_{rs} taken at RON with a stationary boat on 29/11/2011

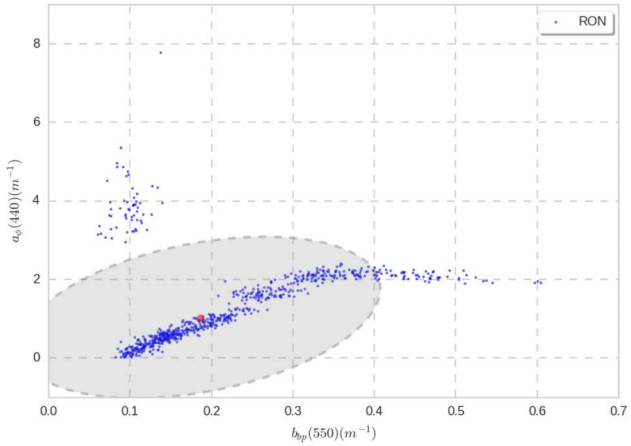

Figure 6.69: Inverted IOP parameters $a_\phi(440)$ versus $b_{bp}(550)$ for the 2400 synthetic R_{rs} data produced using the coherent noise model, trained with measured R_{rs} taken at RON with a stationary boat on 29/11/2011. The error ellipse represents the 95% confidence interval. The red point represents the average IOP value.

6.7.11 IOP Retrievals for the KIN Location

The range of R_{rs} for the KIN sample site are shown in Figure 6.70. The hex-bin plots of the inverted IOP parameter pairs are shown in figures 6.71 $(a_\phi(440), a_g(440))$, 6.73 $(a_g(440), b_{bp}(550))$ and 6.75 $(a_\phi(440), b_{bp}(550))$ and the scatter plots, indicating the confidence intervals, are shown in figures 6.72, 6.74 and 6.76.

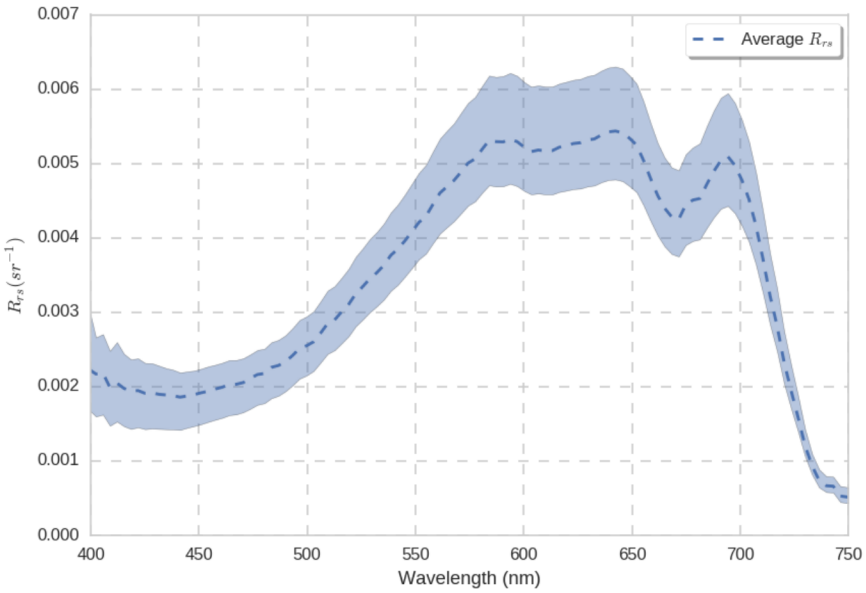

Figure 6.70: R_{rs} measurements taken at KIN with a stationary boat on 29/11/2011. The shaded area shows the maximum and minimum R_{rs} values. The full range of R_{rs} values were used to train the coherent noise model.

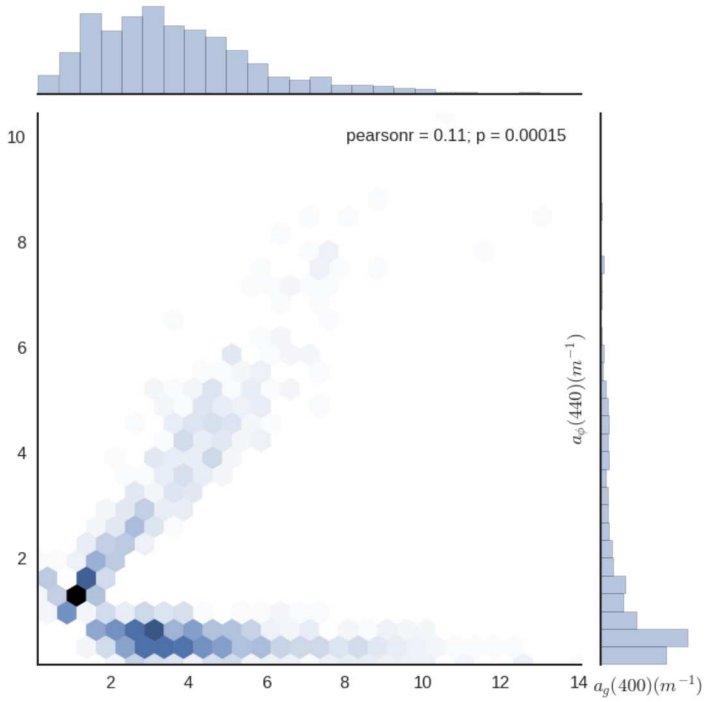

Figure 6.71: Inverted IOP parameters $a_\phi(440)$ versus $a_g(440)$ for the 2400 synthetic R_{rs} data produced using the coherent noise model, trained with measured R_{rs} taken at KIN with a stationary boat on 29/11/2011

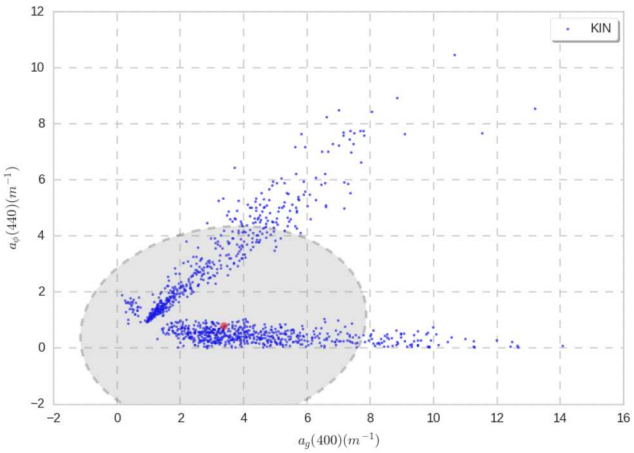

Figure 6.72: Inverted IOP parameters $a_\phi(440)$ versus $a_g(440)$ for the 2400 synthetic R_{rs} data produced using the coherent noise model, trained with measured R_{rs} taken at KIN with a stationary boat on 29/11/2011. The error ellipse represents the 95% confidence interval. The red point represents the average IOP value.

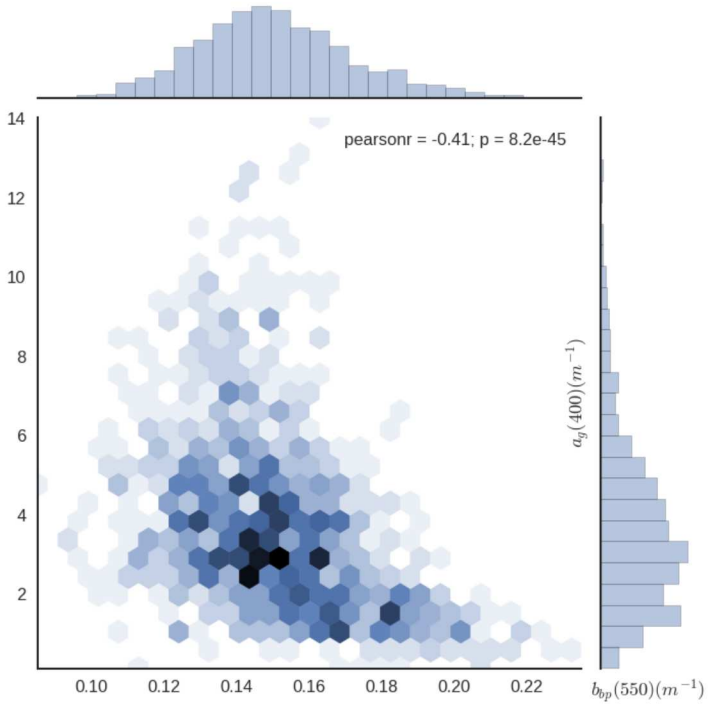

Figure 6.73: Inverted IOP parameters $a_g(440)$ versus $b_{bp}(550)$ for the 2400 synthetic R_{rs} data produced using the coherent noise model, trained with measured R_{rs} taken at KIN with a stationary boat on 29/11/2011

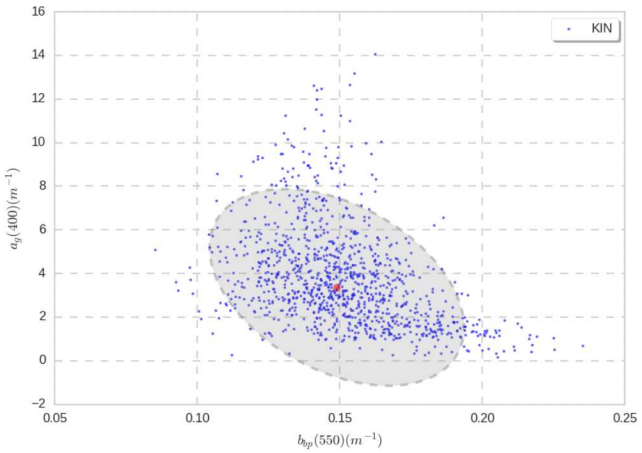

Figure 6.74: Inverted IOP parameters $a_g(440)$ versus $b_{bp}(550)$ for the 2400 synthetic R_{rs} data produced using the coherent noise model, trained with measured R_{rs} taken at KIN with a stationary boat on 29/11/2011. The error ellipse represents the 95% confidence interval. The red point represents the average IOP value.

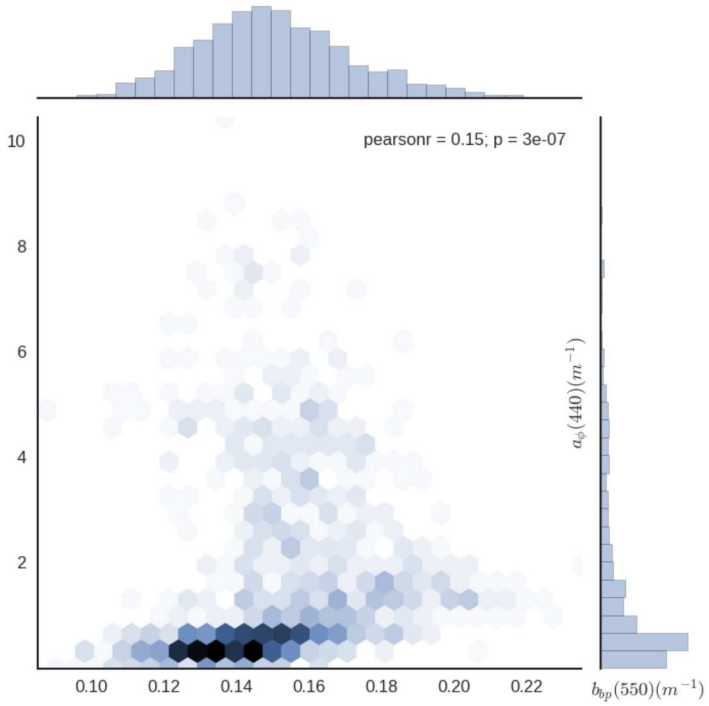

Figure 6.75: Inverted IOP parameters $a_\phi(440)$ versus $b_{bp}(550)$ for the 2400 synthetic R_{rs} data produced using the coherent noise model, trained with measured R_{rs} taken at KIN with a stationary boat on 29/11/2011

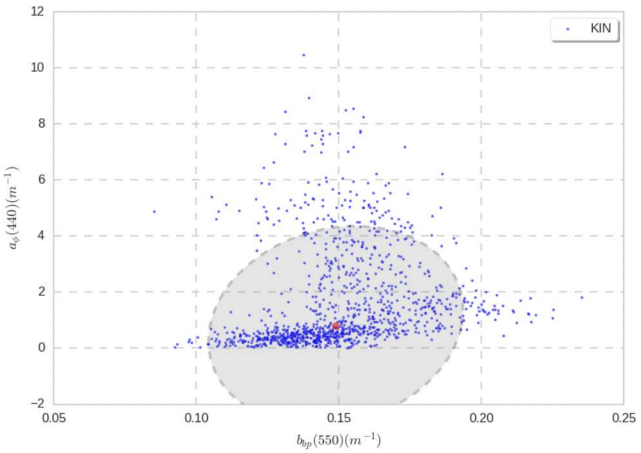

Figure 6.76: Inverted IOP parameters $a_\phi(440)$ versus $b_{bp}(550)$ for the 2400 synthetic R_{rs} data produced using the coherent noise model, trained with measured R_{rs} taken at KIN with a stationary boat on 29/11/2011. The error ellipse represents the 95% confidence interval. The red point represents the average IOP value.

6.7.12 IOP Retrievals for the SUC Location

The range of R_{rs} for the SUC sample site are shown in Figure 6.77. The hex-bin plots of the inverted IOP parameter pairs are shown in figures 6.78 $(a_\phi(440), a_g(440))$, 6.80 $(a_g(440), b_{bp}(550))$ and 6.82 $(a_\phi(440), b_{bp}(550))$ and the scatter plots, indicating the confidence intervals, are shown in figures 6.79, 6.81 and 6.83.

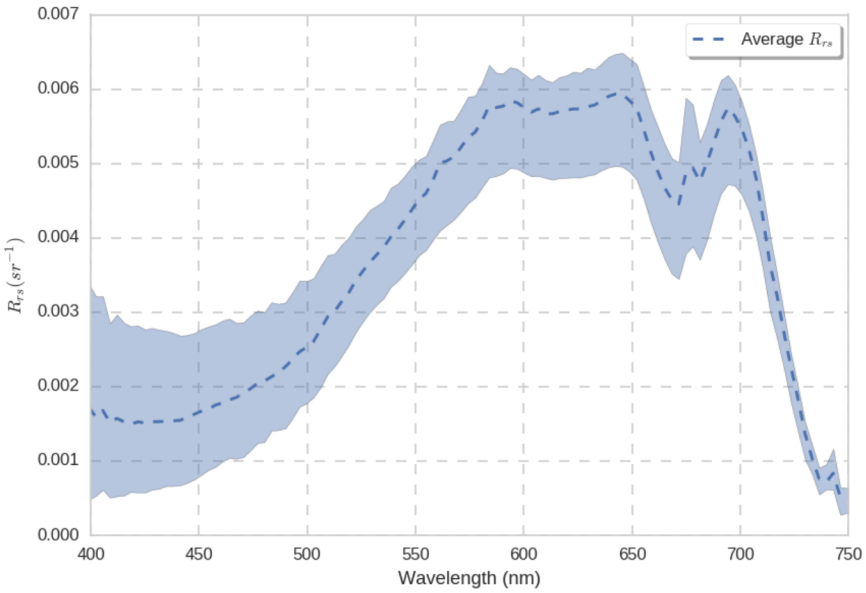

Figure 6.77: R_{rs} measurements taken at SUC with a stationary boat on 29/11/2011. The shaded area shows the maximum and minimum R_{rs} values. The full range of R_{rs} values were used to train the coherent noise model.

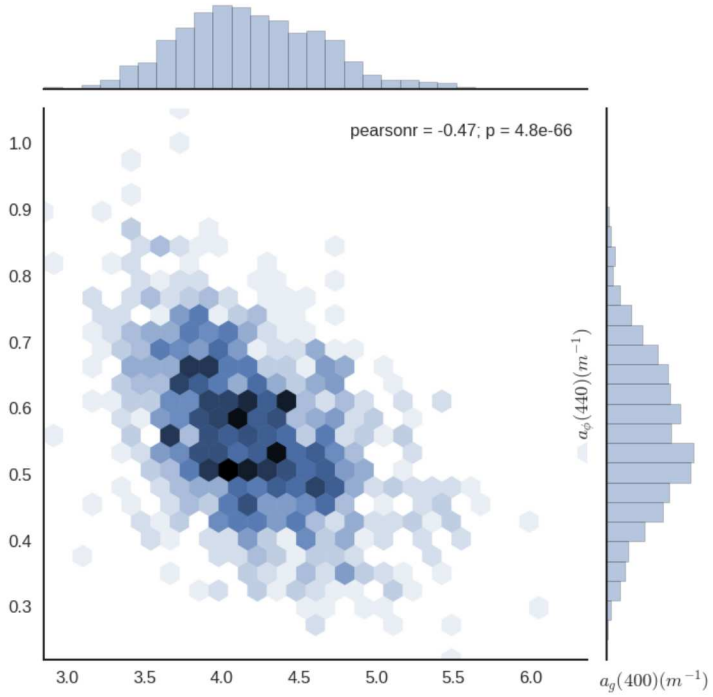

Figure 6.78: Inverted IOP parameters $a_\phi(440)$ versus $a_g(440)$ for the 2400 synthetic R_{rs} data produced using the coherent noise model, trained with measured R_{rs} taken at SUC with a stationary boat on 29/11/2011

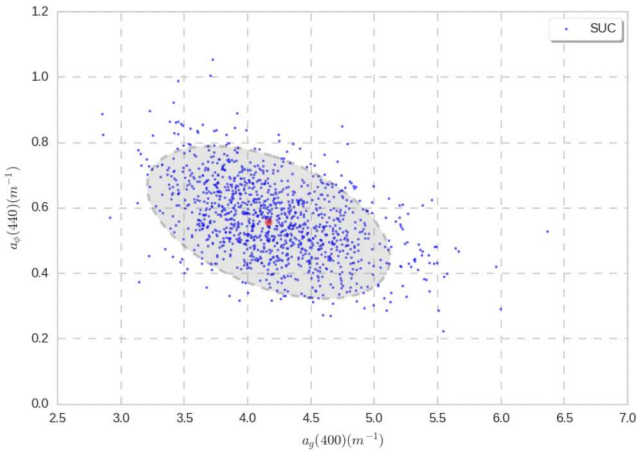

Figure 6.79: Inverted IOP parameters $a_\phi(440)$ versus $a_g(440)$ for the 2400 synthetic R_{rs} data produced using the coherent noise model, trained with measured R_{rs} taken at SUC with a stationary boat on 29/11/2011. The error ellipse represents the 95% confidence interval. The red point represents the average IOP value.

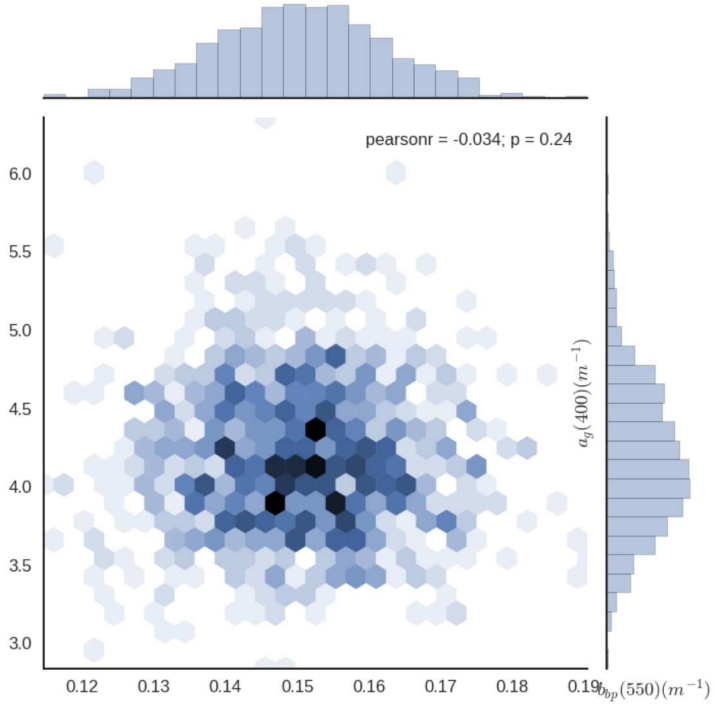

Figure 6.80: Inverted IOP parameters $a_g(440)$ versus $b_{bp}(550)$ for the 2400 synthetic R_{rs} data produced using the coherent noise model, trained with measured R_{rs} taken at SUC with a stationary boat on 29/11/2011

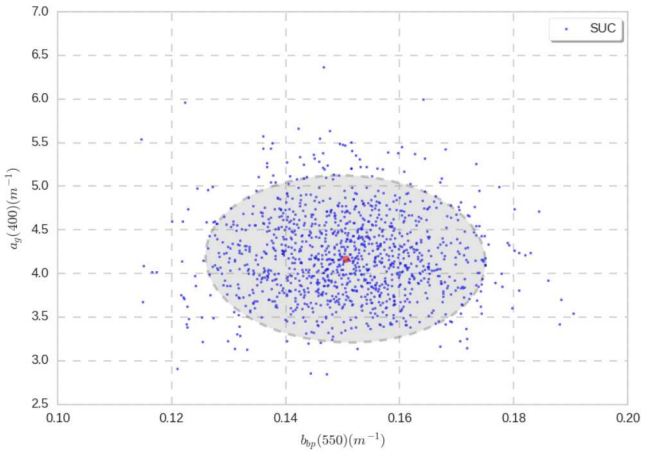

Figure 6.81: Inverted IOP parameters $a_g(440)$ versus $b_{bp}(550)$ for the 2400 synthetic R_{rs} data produced using the coherent noise model, trained with measured R_{rs} taken at SUC with a stationary boat on 29/11/2011. The error ellipse represents the 95% confidence interval. The red point represents the average IOP value.

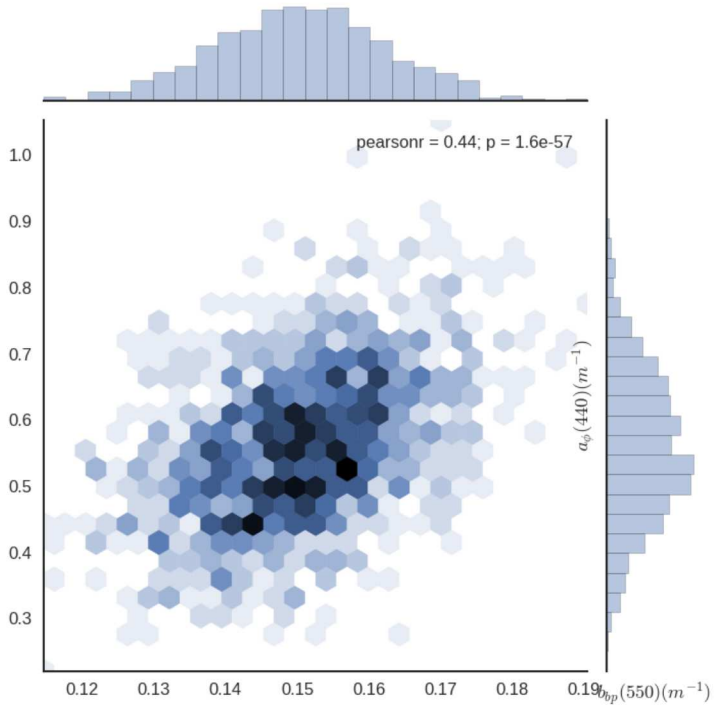

Figure 6.82: Inverted IOP parameters $a_\phi(440)$ versus $b_{bp}(550)$ for the 2400 synthetic R_{rs} data produced using the coherent noise model, trained with measured R_{rs} taken at SUC with a stationary boat on 29/11/2011

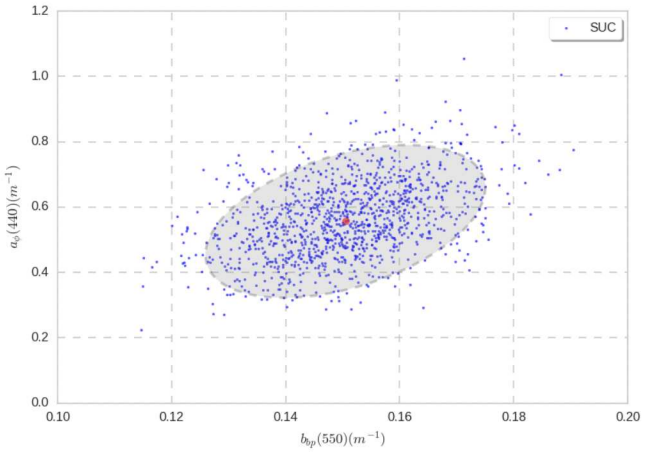

Figure 6.83: Inverted IOP parameters $a_\phi(440)$ versus $b_{bp}(550)$ for the 2400 synthetic R_{rs} data produced using the coherent noise model, trained with measured R_{rs} taken at SUC with a stationary boat on 29/11/2011. The error ellipse represents the 95% confidence interval. The red point represents the average IOP value.

6.7.13 In situ Measurements at the 10 SCCP Locations

This section presents the data measured from the in situ water samples collected at the SCCP sample locations on 29/11/2011. Figure 6.84 shows the spectral absorption due to phytoplankton pigments at each location. The absorption spectra was measured in a dual-beam spectrophotometer using the techniques described in Section 6.5. The CDOM absorption, shown in Figure 6.86, was also measured in a dual-beam spectrophotometer using the techniques described in Section 6.5.3. The backscattering coefficients, shown in Figure 6.88, were measured using using a Hobi Labs HydroScat-6 using the methods described in Section 6.4.2.

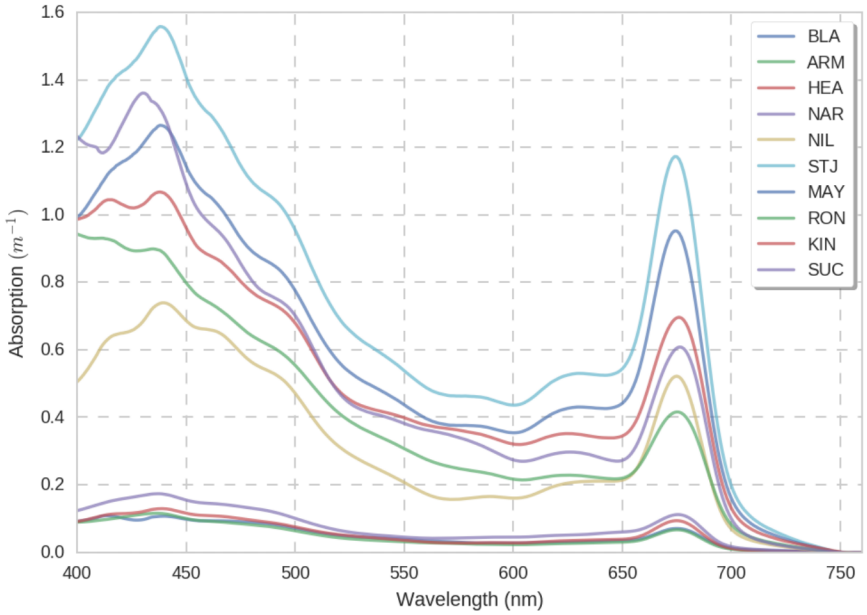

Figure 6.84: The total phytoplankton pigment absorption spectra measured at each of the sample locations on 29/11/2011.

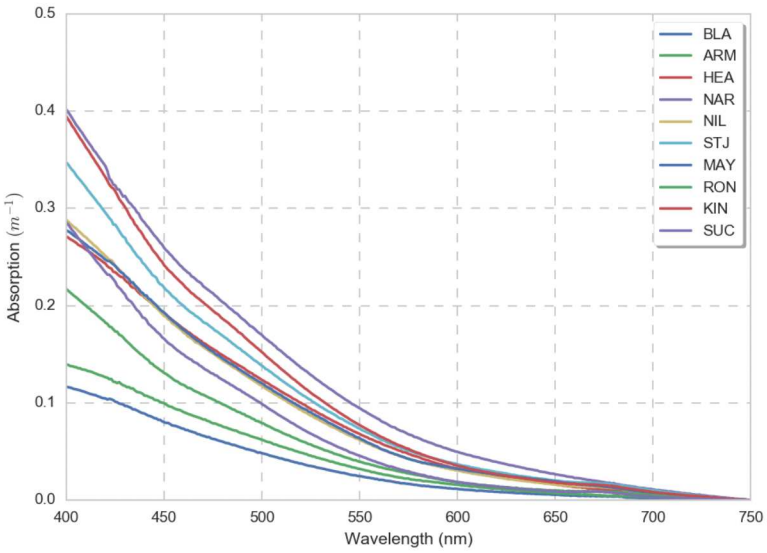

Figure 6.85: The total non-algal particulate absorption spectra measured at each of the sample locations on 29/11/2011.

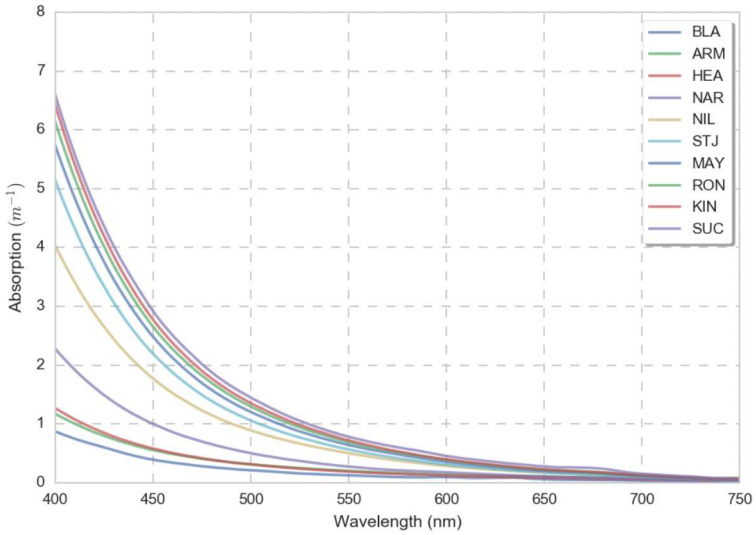

Figure 6.86: The CDOM absorption spectra measured at each of the sample locations on 29/11/2011.

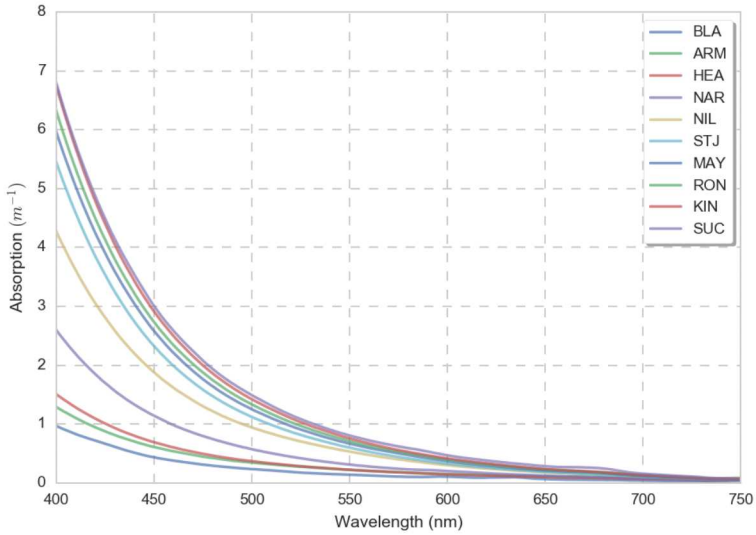

Figure 6.87: The total gelbstoff absorption spectra measured at each of the sample locations on 29/11/2011.

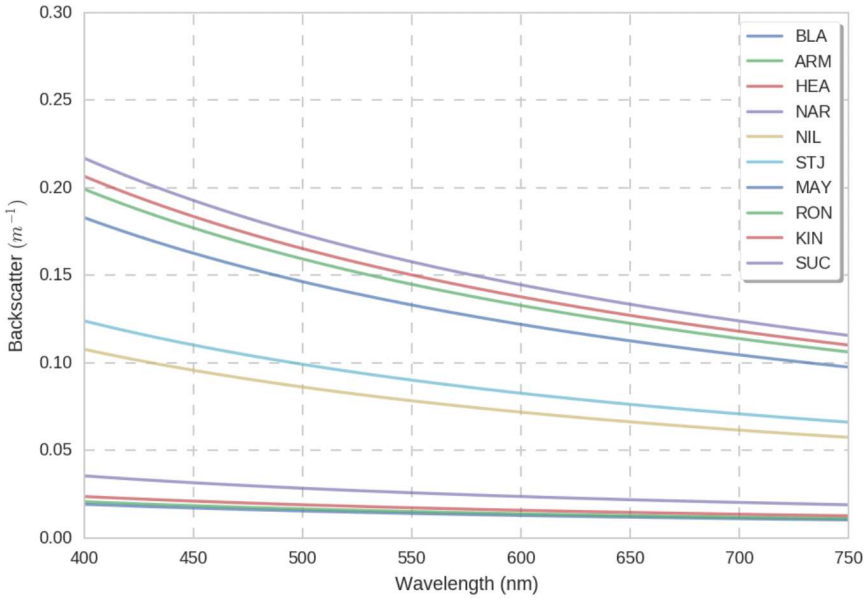

Figure 6.88: The total particulate backscatter of b_{bp} measured by HOBI Labs HydroScat-6 for each of the sample locations on 29/11/2011.

6.7.14 Swan River Profiling

The following section presents the results of the underway measurements. Beginning with Figure 6.89 which shows the relationship between the DALEC sample number and the distance along the transect. Figures 6.90, 6.91 and 6.92 show the inverted IOP parameters along the length of the transect, when the reflectance model HOPE is inverted for three IOP parameters, $a_\phi(440)$, $a_g(440)$ and $b_{bp}(550)$. The light blue envelope shows the uncertainty limits, calculated using the coherent noise method, for each DALEC sample. For every DALEC R_{rs} spectrum along the transect, 2400 synthetic $\hat{R}_{rs}$ data were generated for the uncertainty calculation.

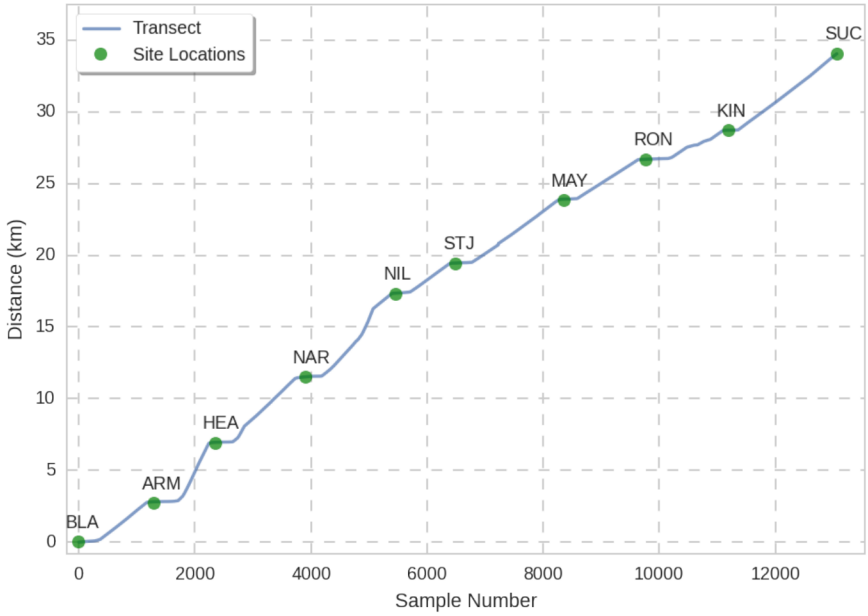

Figure 6.89: The cumulative distance for each DALEC R_{rs} measurement along the transect for each sample number. The flat points on the transect show the locations where the boat was stationary to collect water samples and repeat DALEC measurements of R_{rs} were made for the training stage of the coherent noise model and uncertainty estimates.

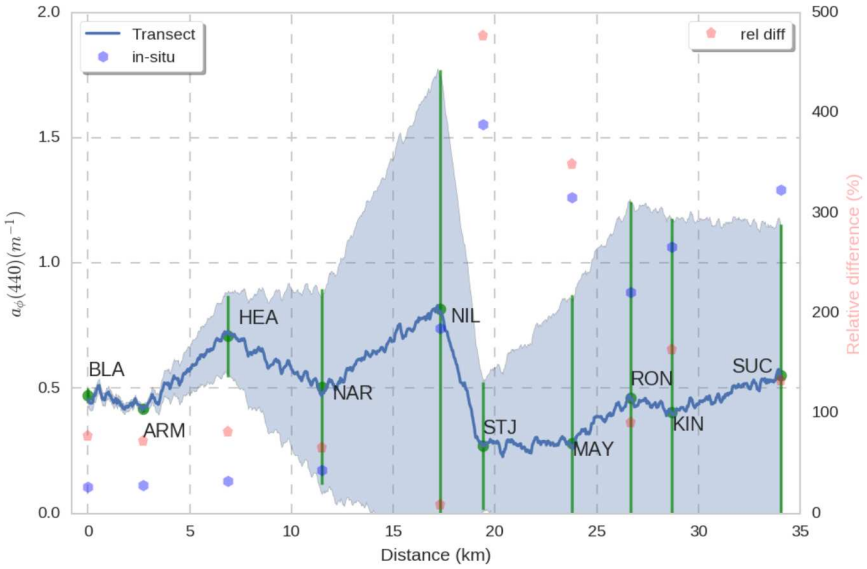

Figure 6.90: The model-derived $a_\phi(440)$ measurements over the length of the transect. The outer envelope shows the uncertainty estimates from the coherent noise modelling. The phytoplankton in situ measurements are plotted as points on the figure, as well as the relative difference of those points when compared to the model-derived parameters at those points.

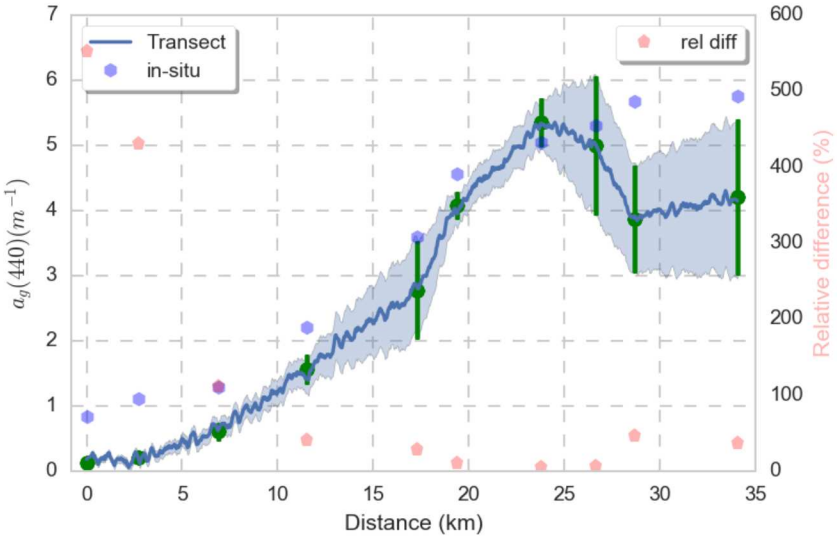

Figure 6.91: The model-derived $a_g(440)$ measurements over the length of the transect. The outer envelope shows the uncertainty estimates from the coherent noise modelling. The phytoplankton in situ measurements are plotted as points on the figure, as well as the relative difference of those points when compared to the model-derived parameters at those points.

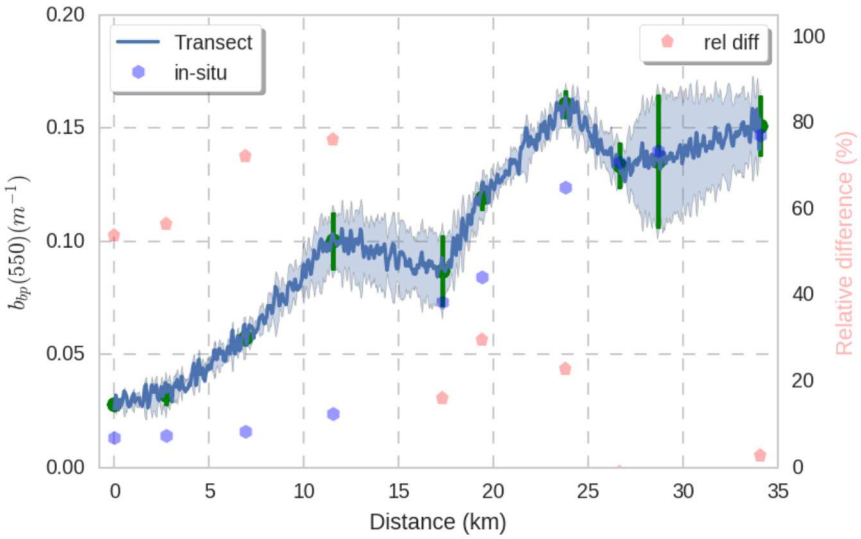

Figure 6.92: The model-derived $b_{bp}(550)$ measurements over the length of the transect. The outer envelope shows the uncertainty estimates from the coherent noise modelling. The phytoplankton in situ measurements are plotted as points on the figure, as well as the relative difference of those points when compared to the model-derived parameters at those points.

The following figures, 6.93, 6.94 and 6.95, compare the model-derived IOP parameters (from DALEC measurements) with the in situ measured IOPs. The figures show the results of using the DALEC data from 29/11/2011, solving from $a_\phi(440)$, $a_g(440)$ and b_{bp} respectively. Points lying on the 1:1 line would indicate that the modelled and measured are in perfect agreement.

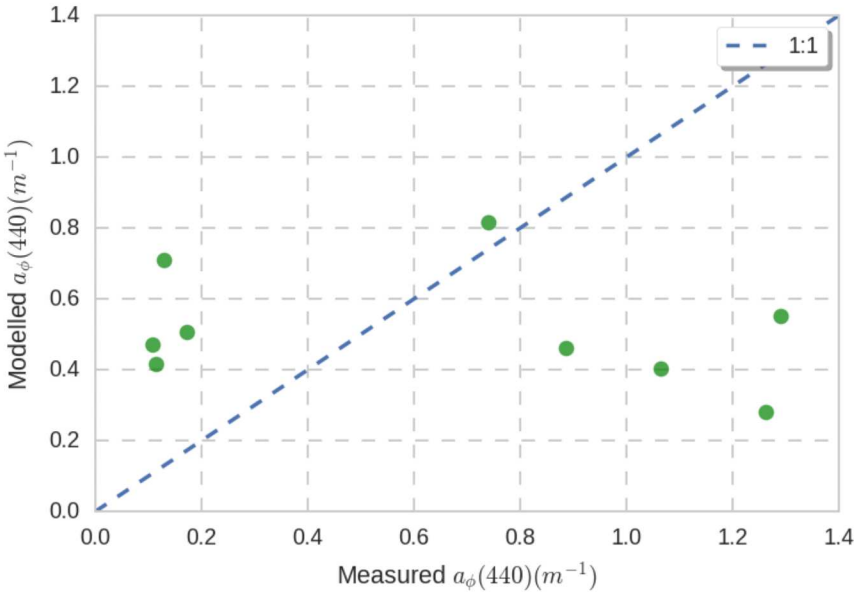

Figure 6.93: The DALEC retrieved $a_\phi(440)$ compared to in situ measured values for the transect on 29/11/2011.

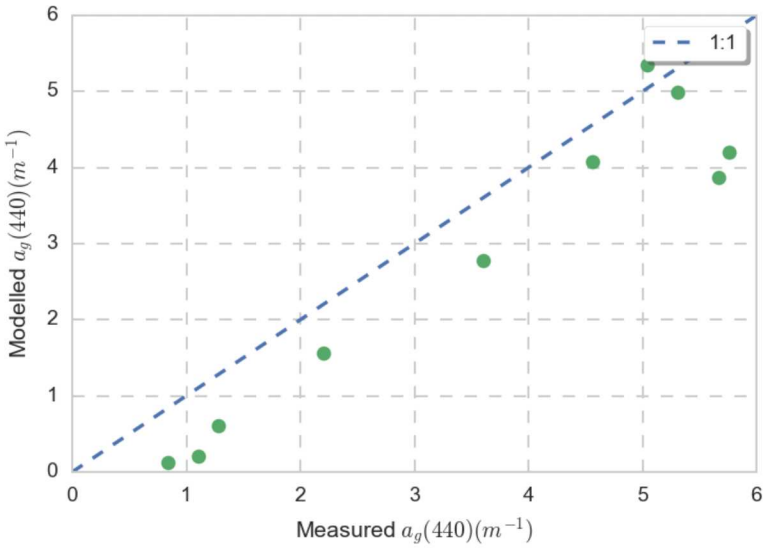

Figure 6.94: The DALEC retrieved $a_g(440)$ compared to in situ measured values for the transect on 29/11/2011.

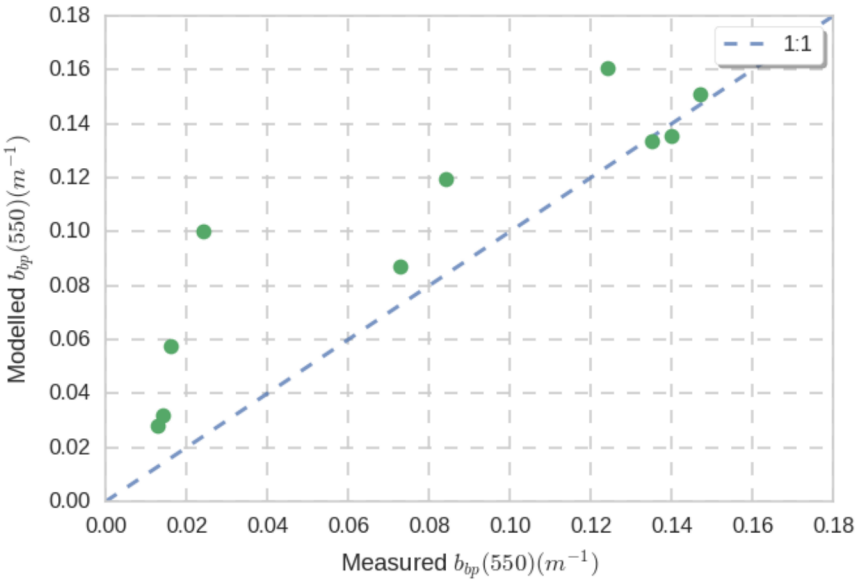

Figure 6.95: The DALEC retrieved $b_{bp}(550)$ compared to in situ measured values for the transect on 29/11/2011.

The transects results shown in figures 6.90, 6.91 and 6.92 show that there are differences between the in situ samples and DALEC-derived values of IOPs at each in situ collection site. In particular, there are large relative differences for the $a_\phi(440)$ transect (Figure 6.90) particularly for stations in the upper river (STJ to SUC).

We repeated the process by restricting the degrees of freedom in which the model was optimised for, by only inverting for $a_\phi(440)$ (Figure 6.96). In order to improve the accuracy of the $a_\phi(440)$ retrieval, the values of $a_g(440)$ and $b_{bp}(550)$ were set to the measured values at the sample locations and linearly interpolated values were used for locations in between. By restricting the model to retrieve only $a_\phi(440)$, the transect accuracy was improved, particularly for points along the transect up to NIL. These results can be seen in Figure 6.96.

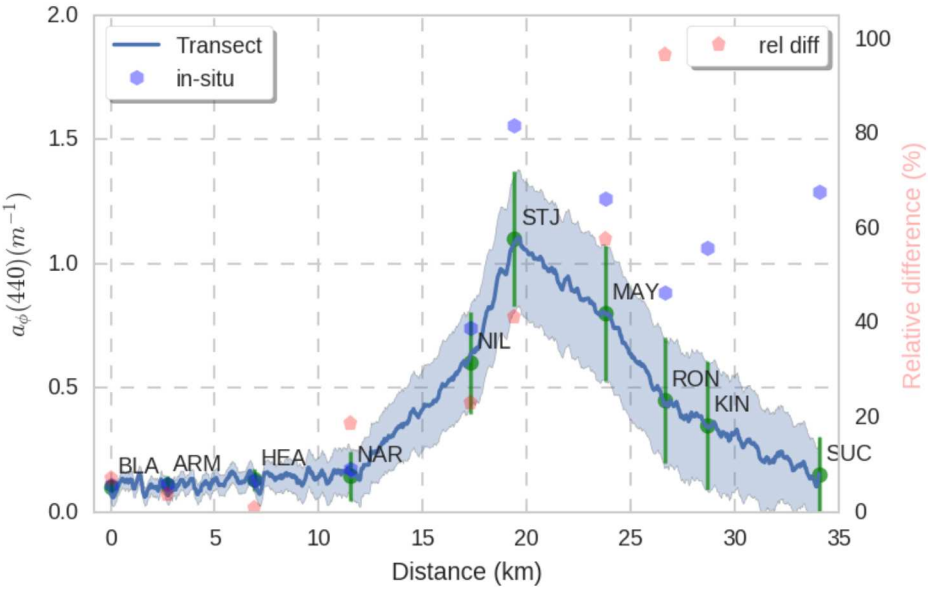

Figure 6.96: DALEC-derived $a_\phi(440)$ compared to the in situ measured values for all of the sample sites. The model was restricted to retrieve the $a_\phi(440)$ parameter only.

The following figures compares the DALEC-derived $a_\phi(440)$ parameter with the measured $a_\phi(440)$ parameter for the case where the model was restricted to a single variable, $a_\phi(440)$. Figure 6.97 shows the DALEC-retrieved and 10 in situ points collected along the transect for 29/11/2011. Figures 6.98 and 6.99, show the modelled and measured $a_\phi(440)$ values for all of the field trips using the same, single parameter, restriction.

Figure 6.100 shows that there is a high correlation between the CDOM concentration and the error between the model inverted values and the in situ measurements. It is due to this relationship that it was thought that concentration of CDOM was the main contribution to model error. To gain a better understanding of the sources of error, the sensitivity analysis presented in Section 5.6 was conducted. This analysis supports the conclusion that the model is not sensitive enough in high CDOM concentrations to accurately predict the phytoplankton concentration.

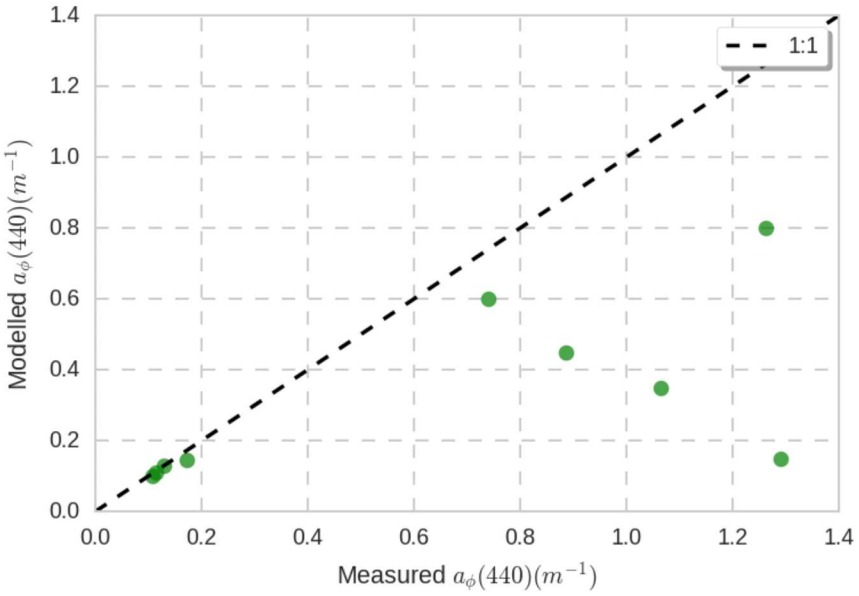

Figure 6.97: DALEC-derived $a_\phi(440)$ compared to in situ measured values collected along the transect for 29/11/2011 when restricted to a single $a_\phi(440)$ retrieval parameter.

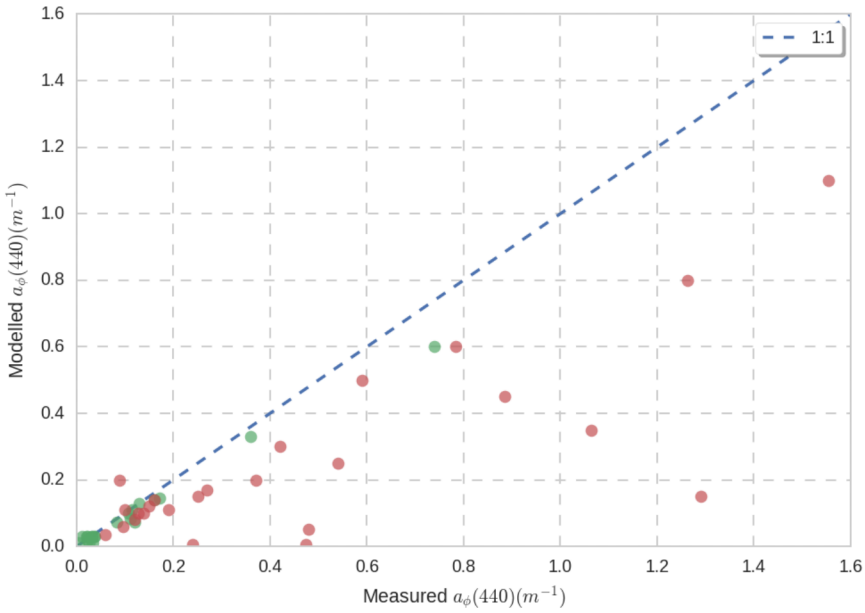

Figure 6.98: DALEC-derived $a_\phi(440)$ and in situ measured values for all of the sample sites for all five field trips. The green markers represent the data points where CDOM is relatively low, which corresponds to the sites before NIL. The red markers represent the points further up river from NIL, where the CDOM is high and the model produces less accurate results.

Figure 6.99 compares values, for all field trips (dates shown in Table 6.1), only for sites up to NIL. The red points represent the points that are up river from NIL. Figure 6.100 shows there is a correlation between the $a_\phi(440)$ retrieval error and the CDOM concentration, possibly highlighting why the $a_\phi(440)$ error increases up river, where the CDOM is high.

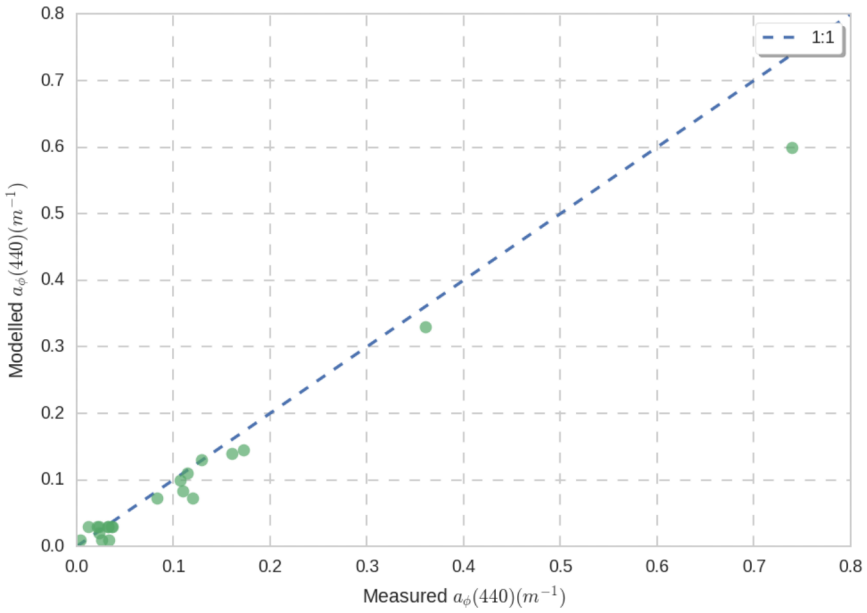

Figure 6.99: DALEC-derived $a_\phi(440)$ compared to the in situ measured values for all of the sample sites for all five field trips. Here, only the first five sampling sites (up to NIL) are shown, where CDOM values are considered relatively low.

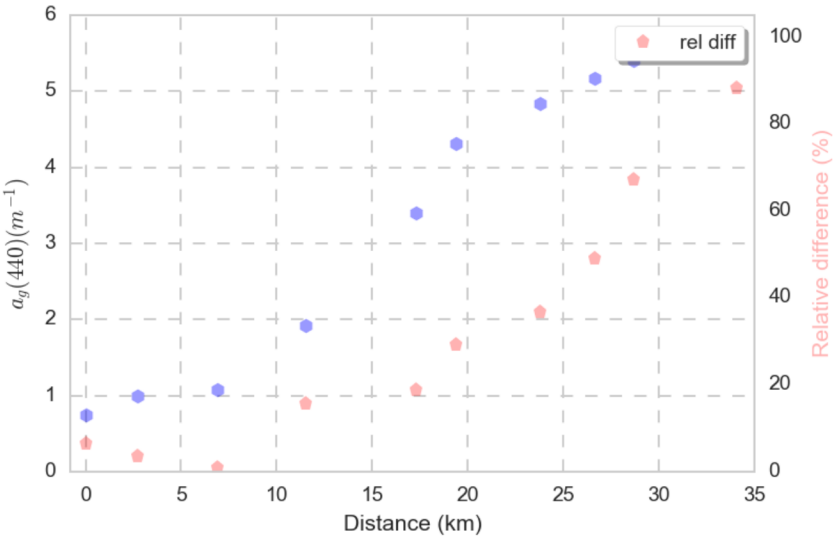

Figure 6.100: In situ measured absorption due to glebstoff at 440 nm for the transect, and relative differences between measured and modelled $a_\phi(440)$. The figure shows that there is a high correlation between the level of CDOM and the uncertainty of the DALEC retrieved $a_\phi(440)$ values.

Figure 6.96 shows that the model is able to accurately predict the phytoplankton absorption within ∼18% at sampling sites BLA, ARM, HEA, NAR and NIL when the optimisation routine is restricted to retrieving the single $a_\phi(440)$ IOP parameter. The uncertainty for all of the $a_\phi(440)$ retrievals, as estimated by the coherent noise model is ∼34%. For the upper river sites, STJ, MAY, RON, KIN, and SUC, the model regularly underestimates the amount of phytoplankton, when compared to the in situ samples. This mismatch is generally seen on the four spot-sampling field days as well (Figure 6.98). It is at these sites that in situ measurements do not fall within the uncertainty estimates as predicted by the coherent noise model. It is encouraging that the accuracy of the DALEC-derived results (for all sites) lies will within the 34% uncertainties predicted by the coherent noise model.

Figure 6.98 shows the model versus measured results across all of the field trips presented in this thesis. The figure shows that phytoplankton concentration is generally underestimated by the model, particularly for the higher values of $a_\phi(440)$. The sites STJ, MAY, RON, KIN and SUC are marked in red and represent the sites where the model does not agree with the water sample results and the CDOM is too high. If the data is restricted to the sites BLA, ARM, HEA, NAR and NIL, (Figure 6.99) the model results show good agreement with the phytoplankton concentration, albeit slightly underestimating for most of the data points.

These data show that the results presented here suggest there is a clear limit to where the model and methods described in this study can be used to estimate the phytoplankton concentration with confidence, even with the single parameter restriction.

6.8 Summary

Over the course of the study, the Swan River Trust (SRT) made a place available on their boat so that the DALEC and associated equipment could be tested. It was not possible at that stage to make underway measurements due to safety rules, imposed by the SRT, and the speed that the boat travelled between sample sites. There was quite a large learning curve, and time to make measurements at each site, while the Swan River Trust collected their samples, was short. For this reason, and due to equipment failure or by sample contamination and other errors on many days reflectance spectra were not collected. Of the many occasions in which field trips were undertaken, only four were

able to produce acceptable results (tables 6.4, 6.5, 6.6 and 6.7). These days provided invaluable opportunities to improve equipment and workflows. There were many lessons learned on how to collect this data accurately, which ultimately lead to the best results possible when the transect data was eventually captured.

This chapter presented the transect results, as well as the IOP data that were used in the optimisation process. The transect started at Blackwall Reach (BLA) and ended at Success Hill (SUC). Continuous measurements of reflectance were made with the DALEC following the methods described earlier in Section 6.7.14. Discrete water samples were collected at ten sample locations along the length of the transect for both inputs into the optical model and for model truthing. The transect results (Figure 6.96) shows that when compared to in situ measurements, the phytoplankton abundance, described here by $a_\phi(440)$, can be estimated within a 18% accuracy for approximately the first half of the river; that is, between BLA and NIL. To achieve this accuracy, however, the optimisation routine must be restricted to retrieve just the single $a_\phi(440)$ parameter. After NIL, for the upper reaches of the transect, the accuracy quickly becomes very low (with above 80% error at SUC) when compared to the in situ samples regardless of any model restrictions. It is at this point that the model has a lot of difficulty in accurately estimating the phytoplankton absorption and the differences in modelled and measured results are not captured by the uncertainty estimates. It is at points, close to NIL, where the uncertainties are not accurate predictions of model uncertainty due to the model's inability to accurately model the conditions of the Swan River.

The main reason the model fails in the upper reaches of the river is, the CDOM load in the river at these points makes the water too dark to retrieve accurate results of phytoplankton. At these high CDOM concentrtions, changes in a_ϕ have little to no affect on the R_{rs}. It is shown in Figure 6.100 that there is a very high correlation between the CDOM load and the percentage difference between the measured and modelled values of phytoplankton absorption. This suggests that it is likely to be the CDOM causing the difference between the measurements.

After the transect on 29/11/2011 was completed, the in situ measurements were used to generate reflectance spectra using PlanarRad that spanned the CDOM and phytoplankton absorption observed during the experiment. These sensitivity results are presented in Section 5.6. In this section Figure 5.43 shows that, as the CDOM increases, the model uncertainty increases.

The procedure used to invert the model, to achieve the higher accuracy results, was much more restrictive than originally intended. With Lee et al. (1999) outlining six parameters that can be used to optimise the model, it was originally planned to have a workflow that enabled the reflectance data to be used to predict the phytoplankton abundance, CDOM concentration and particulate scattering. It was planned that in situ measurements would be used to independently verify the results and not in the optimisation process itself. Any attempt to optimise for all six parameters resulted in parameter values that were orders of magnitude from the expected values, or the optimisation routine would not be able to converge on a solution. It was only by restricting the model to three IOP parameters, $a_\phi(440)$, $a_g(440)$ and $b_{bp}(550)$, that the optimisation routine could converge to a solution. Furthermore, in order to achieve the most accurate measures of phytoplankton, the model and optimisation routine had to be further restricted to retrieve only a single parameter, $a_\phi(440)$. Restricting the optimisation to a single parameter $a_\phi(440)$, was the only way that the model was able to reliably converge on sensible phytoplankton results. Nonetheless, this is only true for those parts of the river where the CDOM concentration is relatively low. Where the CDOM levels exceed those seen past NIL, ($\approx 3.402m^{-1}$), the model quickly starts underestimating the phytoplankton absorption.

This chapter has shown that, where the water is relatively low in CDOM, a restricted version of the optimisation routine and optical model can accurately estimate the phytoplankton concentration, expressed as $a_\phi(440)$. These high CDOM conditions are reported at the first five sample locations accounting for approximately half of Swan River's length. Attempting to apply the inversion routine passed NIL, exceeded the upper limit of the optical model and inversion routine. The section of the transect where the model is unable to retrieve accurate estimates of the phytoplankton are the narrow sections of the river, high in CDOM, shown in Figure 6.101 below.

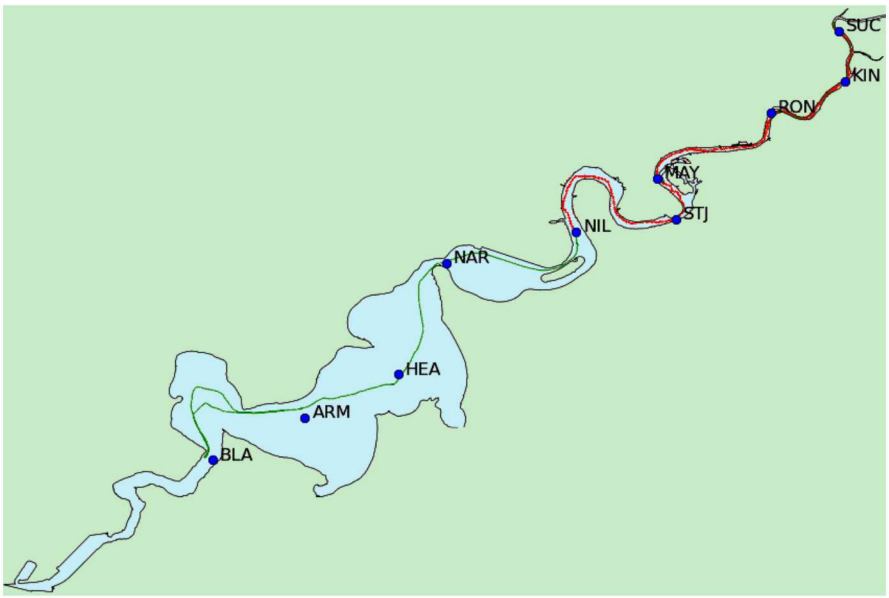

Figure 6.101: The transect path undertaken on the 29/11/11. The green section of the transect represents the section of the river where the $a_\phi(440)$ measurements, predicted with the single parameter restricted model, agree with the in situ measurements. The red section represents the section of the river where the model is unable to agree with in situ measurements of $a_\phi(440)$ within the uncertainty boundaries.

Chapter 7

Discussion

7.1 Introduction

The principle research aim of this study was to establish whether continuous underway measurements of remote sensing reflectance using a boat-mounted instrument (e.g. the DALEC) could be used to improve and support river monitoring programs such as the Swan-Canning Cleanup Programme (SCCP), and more recently the Swan Canning River Protection Strategy (SCRPS), by deriving accurate estimates of phytoplankton concentrations at locations in between the discrete sample locations along the Swan River.

A number of key issues were identified in the literature review and addressed throughout the study, principly that satellite data and airborne-based data are not feasible for monitoring the Swan River because of spectral and spatial resolution limitations, or the cost associated with acquisition of commercial data. As explained, due to the high range of individual components and variability in concentrations, the in-water light environment is extremely complex, and specialised remote sensing algorithms are necessary to derive the inherent optical properties from remote sensing reflectance (e.g. Morel and Prieur, 1977; IOCCG, 2000).

A range of approaches were taken to address this aim, from field sampling to optical modelling, and this discussion will consider and examine the results and novel methodology developments in relation to the research objectives.

7.2 Swan River Results and Validation

The following sections span a number of the research objectives focused on fieldwork and optical modelling. In this section, the IOP results from the field work conducted along the Swan River are first discussed, followed by the measurement uncertainties, including the range of uncertainties observed in different sections of the river. The field measurement uncertainties are then compared to the sensitivity analysis results in order to assess the validity of the field uncertainties. Lastly, this section looks at the suitability of HOPE for this particular application.

7.2.1 DALEC and Field Measurements

Huang et al. (2017) present a clear daily modeled chlorophyll-a variation that is currently not captured by the Swan River weekly sampling campaigns, and conclude that weekly sampling may not be sufficient for understanding some key water quality variables such as chlorophyll-a concentration, among others. Moreover, field sampling can only take place when weather conditions are favourable, thus resulting in too sparse data to capture the required information. From a modeling perspective therefore, Huang et al. (2017) recommend that higher-frequency data are required in order to capture variation and provide more information for models and their validation. The results in Chapter 6, particularly figures 6.16 and 6.96, showed that it was possible to make continuous underway measurements of DALEC-derived phytoplankton absorption between the discrete SCCP sample locations with varying accuracy depending on how the model was restricted. The accuracy of the results improved by restricting the model to a single $a_\phi(440)$ parameter. As a result, an accuracy within 18% was achieved at the sampling sites BLA, ARM, HEA, NAR and NIL and an accuracy of within 34% for the upper river sites, STJ, MAY, RON and SUC. Addressing the modelling requirements raised by Huang et al. (2017) underway data is shown here to increase spatial coverage, and offers potential for greater temporal coverage also; a DALEC (or DALEC style) instrument, can be cost effective for a monitoring program as it offers the opportunity to make continuous autonomous measurements, and more than one could be deployed at once. While the potential for collecting more optical data than currently exists, and augmenting sampling campaigns with autonomous optical instruments is demonstrated here, more work to improve accuracy of retrieval would need to be done.

There are hundreds of different species of phytoplankton commonly present in the Swan River (Hipsey et al., 2016b; Hipsey et al., 2016a and Huang et al., 2017). SIOPs of these

different species can be used, in principle, to relate the spectral absorption and scattering to chlorophyll-a specific concentration. SIOPs vary greatly between species and can even vary greatly within a single species (Fujiki and Taguchi, 2002). As discussed in Chapter 2, the chlorophyll-a concentration can double between the mouth of the river and the upper parts of the estuary; therefore, the limitation of using HOPE and the methodology outlined in 6 is, the accuracy of the reported phytoplankton abundance is restricted to total phytoplankton absorption. The concentration of chlorophyll-a cannot be inferred, nor species specific information can be drawn from the results, until accurate measurements of the SIOPs are known. However, the advantage to limiting the model to total phytoplankton absorption is, monitoring can be carried out using instruments such as the DALEC rapidly, and simple laboratory measurements can be carried out to validate the results. An empirical model relating average SIOPs to total phytoplankton absorption maybe developed in the future, but currently there is insufficient data available (Huang et al., 2017).

In the Swan River, and for many inland waterways, the high CDOM concentration compounds the difficulty of accurate phytoplankton concentration retrieval and increases the measurement uncertainty. In the models by Kutser (1997) and Kutser et al. (2001) changing chlorophyll by 0.1 mg/m^3 when the concentrations are in tens to hundreds or changing CDOM with the step of 0.1 m^{-1} when the values approach tens is not feasible as such small changes in concentrations have negligible effect on reflectance spectra that no remote sensing instrument can detect. The results presented in this thesis are consistent with the findings of Kutser (1997) and Kutser et al. (2001), and are confirmed with the sensitivity study conducted in Section 5.6.

Furthermore, separating the dissolved and particulate fraction from each other based on water reflectance spectra is very difficult and sometimes nearly impossible (Del Castillo, 2005; Siegel et al., 2013; Wei and Lee, 2015). The issue with solving the inverse problem is non-uniqueness of the results. In the case of water remote sensing it means that many different combinations of chlorophyll-a, CDOM and TSS may give perfectly identical reflectance spectra. Creating more IOPs for the inverse of the model only creates more combinations of these IOPs that give identical reflectance spectra. As we saw in figures 6.85, 6.86 and 6.87, the total contribution of a_{nap} to the gelbstoff compared to CDOM is negligible. For this reason and due to the complexity in defining the requisite SIOPs, in this study of the Swan River, the absorption due to CDOM and a_{nap} are not separated in the optical model.

7.2.2 Measurement Uncertainties

As discussed by IOCCG (2006) a systematic approach to calculating uncertainties in IOPs derived from remote sensing optical models is lacking. Measurements are generally reported without uncertainties and are instead, simply compared with in situ measurements. Furthermore as noted by the IOCCG, this common approach is insufficient for documenting the variations in uncertainty in both time and space. One of the research objectives of this thesis was to address this in the Swan River by developing a uncertainty methodology capable of reporting uncertainties for the sites encompassed by the Swan River Trust sampling programme. In particular, this new approach does not require in situ measurements. Moreover, this methodology has the advantage that is applicable to any remote sensing application where IOPs are derived from remote reflectance. Another research objective was to develop a new methodology of estimating measurement uncertainties of IOPs calculated from remote sensing reflectance.

This new approach to estimating uncertainties of model optimised-parameters was presented in Section 5.5. The method simulates the uncertainty in the model parameters by including the natural variation of the remote sensing reflectance spectrum due to changes in the environment. Unlike the approach presented in the IOCCG report (IOCCG, 2006), the method developed in this thesis does not require synthetic data or in situ measurements; rather, the method requirements are taken completely from field measurements of remote sensing reflectance. The coherent noise model was used to estimate the uncertainties of the DALEC-derived $a_\phi(440)$, $a_g(440)$ and $b_{bp}(550)$. Using the coherent noise method to generate 2400 $\hat{R}_{rs}$ spectra revealed that on some occasions, the solutions to each $\hat{R}_{rs}$ resulted in clusters of solutions. An example of this can clearly be seen at NIL in figures 6.50–6.55. In these figures two distinct clusters of solutions can be seen for all pairs of $a_\phi(440)$, $a_g(440)$ and $b_{bp}(550)$. This is due to the fact that the reflectance model HOPE is highly non-linear and more than one combination of $a_\phi(440)$, $a_g(440)$ and $b_{bp}(550)$ can result in a minimum in solution space. The LM-fit optimisation method can often converge on a local minimum, particularly when the initial guess is close to one.

These clusters can be seen, most clearly, in the results shown in sections 6.7.8 and 6.7.11 at the NIL and KIN sites. It is quite possible that these local minima are very common in the solution space, particularly when the number of parameters LM-fit is trying to solve for is large. It may be the case, in this study, that the solution space has a large number of these local minima and is what prevented the model to converging to sensible solutions when all six model parameters were optimised for. It is likely that, in the case of the

Swan River, by reducing the number of parameters in HOPE from six to three ($a_\phi(440)$, $a_g(440)$ and $b_{bp}(550)$) the optimisation method was able to converge on a solution by reducing the number of local minima, hence avoiding them and reducing the number of false positive solutions. For this reason, it is likely that by further restricting the model to a single $a_\phi(440)$ parameter, as shown in Figure 6.96, the model was able to give the most accurate results for $a_\phi(440)$.

Even when the number of model parameters are restricted to three parameters ($a_\phi(440)$, $a_g(440)$ and $b_{bp}(550)$), there are local minima present in the solution space. This can be seen as multiple clusters in figures 6.50–6.55. An example of this is shown in Figure 6.55, where it can be seen that the solution of HOPE, for each $\hat{R}_{rs}$ converged in two different clusters. One at ∼0.25 and ∼0.85 for $a_\phi(440)$ and $b_{bp}(550)$ respectively and one at ∼1.5 and ∼0.12 for $a_\phi(440)$ and $b_{bp}(550)$ respectively. The median value of all the $\hat{R}_{rs}$ points, indicated by a red dot in the figure, is the value reported for a single DALEC measurement. Using the median value of all the $\hat{R}_{rs}$ weights the result heavily toward the cluster with the majority of points. Using the coherent noise method, in this case, avoids the local minimum. If the coherent noise model were not used, and only a single R_{rs} was inverted, that data point may have corresponded to any one of the points on the scatter plot and not weighted towards the median point. And as such, more likely to report a value corresponding to a local minimum or extreme point.

The uncertainty of each measurement is indicated by the error ellipse. The existence of these clusters skews and elongates the error ellipses. An example of this can be seen in Figure 6.55. It can be seen that the error ellipse is skewed by the cluster of higher values in the top right corner and the ellipse passes through the zero axis because it is stretched. Uncertainty ranges that go below 0 are not possible in real world measurements as negative values of $a_\phi(440)$, $a_g(440)$ and $b_{bp}(550)$ are not possible. This overestimate in uncertainty can be seen in 6.90 where the error bars and error envelope are both very large and go below zero and is likely due to the existence of multiple clusters in solution space which skew the error estimates.

The coherent noise method was used to define ten different coherent noise models (one at each SCCP site) that were used in the inversion process for reflectance data closest to the corresponding sampling site. This method should capture all of the variation that is expected to be seen, due to fluctuations in environmental parameters, many of which cannot be captured by modelling alone, or would be too complex to model individually.

For each measurement made by the DALEC, 2400 pseudo $\hat{R}_{rs}$ measurements were generated by the coherent noise models. All pseudo-measurements were inverted for $a_\phi(440)$, and the distribution of the parameter was used to define the uncertainty of the derived $a_\phi(440)$ for each DALEC measurement of R_{rs}. For the length of the transect between BLA and NIL, the in situ measurements of $a_\phi(440)$ agreed within the uncertainty measurements of $a_\phi(440)$ at the sample locations. Up river from the NIL sample location, the in situ measurements did not lie within the uncertainty estimate.

The section of the transect from NIL to SUC was where the CDOM absorption was the greatest. It appears from the results in Figure 6.16 that the uncertainty estimates are too low. These estimates are smaller than the difference between the measured and derived values. The reason that the uncertainties are small is that the model itself is not able to accurately model the environment for many of the reasons already presented here. For the coherent noise model to accurately estimate the uncertainty, it assumes that the model is able to accurately reproduce the measured IOPs when inverted. If the model is unable to invert accurately then the uncertainty estimates will also be inaccurate. It can be seen in Figure 6.16 that upstream from NIL the relative difference between DALEC-derived $a_\phi(440)$ and in situ measurements are larger than accounted for by the blue error envelope. It is at this point in the transect that the reflectance model is unable to accurately predict $a_\phi(440)$ through inversion and, as a result, the coherent noise model is also unable to accurately estimate the uncertainty in the DALEC-derived $a_\phi(440)$.

When comparing the relative errors, it can be seen that for sites up river from NIL, the model consistently underestimates the phytoplankton concentration and underestimates the uncertainty. This is consistent with comments made by Lee et al. (1999) in the discussion section of the paper which states that $a_\phi(440)$ and $a_g(440)$ were generally underestimated, and that in order to identify the cause of the underestimation, further measurements would need to be made (Lee et al., 1999). The sensitivity analysis shown in Figure 5.42, shows that when CDOM concentration is very high the model is not very sensitive to change in $a_\phi(440)$. Therefore, under these high CDOM conditions, it is believed that the optimisation routine (LM-fit) is able to converge to a solution faster by altering the $a_g(440)$ parameter than the $a_\phi(440)$. The model is not sensitive enough to changes in phytoplankton absorption when the CDOM concentration is high and therefore LM-fit preferences changing $a_g(440)$.

A major contribution to the error budget is that there are non-unique solutions to the

optical model. That is to say, there are many different combinations of IOPs that will results in the same remote sensing reflectance. This problem is amplified in low light conditions where the signal to noise ratio is low and furthermore, in estuarine environments where number of different IOPs range greatly compared to the ocean.

The coherent noise method, discussed in this thesis, was originally designed to calculate uncertainties in IOP, particularly in low light conditions where environmental noise such as shadows, sunglint and debris make a high contribution to the overall remote sensing signal . As an unintended consequence, the coherent noise method reduced the number of times the inverse method to solving the optical model was unable to converge to a sensible solution. Furthermore, by making many permutations of reflectance, much of the error space was mapped and local minima were self evident. Examples of this can be seen in Sections 6.7.8 and 6.7.11. By taking the median value of all these permutations, the confidence that the final IOP value used had not converged to a local minima, or a physically impossible results was improved. One of the consequences of using this uncertainty method, is there was a very high computational demand for all permutations of the pseudo $\hat{R}_{rs}$ measurements; this may present a limitation if attempting to do a real-time inversion (Marrable et al., 2009), particularly if using low-powered instruments.

The methodologies and results discussed in this section address two of the research objectives of this thesis: to improve IOPs retrieval confidence in highly non-linear and low light conditions, and further, to estimate measurement uncertainties of these results.

7.2.3 Model Sensitivity

The results presented in Figure 6.100 show that there is a correlation between the phytoplankton retrieval error and the magnitude of CDOM present in the river. This is particularly evident in the upper parts of the river past NIL. To investigate this phenomenon further and address one of the research objectives, the sensitivity analysis in Chapter 5 was subsequently carried out. The sensitivity analysis also assists in better understanding the limitations of the model and its impact on monitoring the Swan River. Many reflectance spectra were generated using PlanarRad for values of $a_\phi(440)$ and $a_g(440)$ that spanned the values measured at the sample locations on the day of the full transect, shown in Table 6.8. The plots of reflectance shown in Figure 5.41 show that for a high CDOM concentration value of 5.0 m^{-1}, changing $a_\phi(440)$ by 15% only results in an approximate change of 1% RMS reflectance. What this shows is that the

model is not very sensitive to change in phytoplankton absorption when the CDOM concentration is high. The full sensitivity analysis for all values is presented in Figure 5.42 and shows that the model is most sensitive to changes in $a_\phi(440)$ at low CDOM values. The figure shows the model is relatively sensitive for sites BLA, ARM, HEA and NAR and moderately sensitive at NIL; however, beyond this location, where $a_g(440)$ are high, the model is the least sensitive to change in $a_\phi(440)$ even though $a_\phi(440)$ is high. This finding is consistent with the results seen after making the transect upriver. Figure 6.100 shows that along the transect, as $a_g(440)$ increases so does the relative error between DALEC-derived $a_\phi(440)$ and in situ measurements of $a_\phi(440)$. It is because of the low sensitivity to a change in $a_\phi(440)$ that the model is unable to converge without applying the restrictions described in previous sections.

Furthermore, when the sensitivity was used to estimate the order of magnitude of uncertainties expected to be seen in the uncertainty models shown in Figure 5.43, it was shown that for a 1% change in RMS reflectance, magnitudes of 16% uncertainty could be expected, depending on conditions. If this behaviour extrapolates linearly, typical changes of a few percent of R_{rs} would result in $30\% - 45\%$ uncertainty under modelled conditions. It is expected that it would be even higher in practice, due to the added effects of environmental noise, that are not captured by the sensitivity analysis. This level of uncertainty is observed in the field measurements. When the CDOM is high, the model is so insensitive to changes in phytoplankton concentration that it is unable to converge to an accurate solution. In order to increase the accuracy of the DALEC-derived $a_\phi(440)$ parameter, the model has to be restricted to retrieving a single $a_\phi(440)$ parameter in order to get a result reflective of the river conditions; however even under these restrictions it is unable to make accurate or precise predictions of phytoplankton concentration upriver from NIL, as the CDOM concentration is too high. Furthermore, the estimates of the DALEC-derived $a_\phi(440)$ uncertainty reach approximately 40%, after which they are unable to account for the difference between the inverted and measured results.

As noted earlier uncertainties are often not quoted in literature (e.g. IOCCG, 2006), so a direct comparison of the published uncertainties and those presented in this thesis becomes problematic. The literature does show however, that high phytoplankton uncertainty in the presence of high CDOM is not unexpected due to both the a_ϕ maximum near 440 nm and the high absorption of gelbstoff at this wavelength. The compounding effect of the absorption properties of tripton being so similar to the exponential function

of CDOM (e.g. Babin et al., 2003; Binding et al., 2008; Matthews and Bernard, 2013), causes much uncertainty when solving for the additive total absorption coefficient, and significant ambiguity in solutions given the nonuniqueness of the solution (Defoin-Platel and Chami, 2007). Therefore, high uncertainties as seen in the Swan River are consistent with the literature, and an uncertainty range $30\% - 45\%$ is consistent with those shown by the sensitivity analysis.

7.2.4 Optical Model Assessment

As specified in the research objectives, preliminary studies were conducted to assess the suitability of different remote sensing reflectance models; HOPE, BRUCE-LUT and BRDF-corrected. SAMBUCA was considered for use, but with no SIOP models specific to the Swan River available, it was not possible to be used for field trials. Three R_{rs} measurements at different points in the river, that best represented the different water quality parameters were used to test the three different models. The results of this study, shown in Figures 6.2–6.10, compare the ability of the models to reproduce the DALEC measured R_{rs}. The BRUCE-LUT model was able to reproduce the DALEC-measured R_{rs} the most accurately when comparing the difference between the spectra (see figures in Section 6.7.1. However, the inverted IOP values were not as accurate as HOPE or BRDF-corrected HOPE when compared to in situ measurements. The reasoning for choosing HOPE over other models for the remainder of the project is explained in more detail in Section 5.3.

HOPE was originally designed using IOP values much lower than those observed in the Swan River and therefore one research objective was to assess its performance in the Swan River, in particular under high CDOM conditions. Of the field data presented in Lee et al. (1999) the $a_g(440)$ values ranged between $(0.023 - 0.240)$ m^{-1} and $a_\phi(440)$ values ranged between $(0.010 - 0.07)$ m^{-1}. In contrast the values presented in this study of $a_g(440)$ ranged between $(0.746 - 5.573)$ m^{-1} and $a_\phi(440)$ values ranged between $(0.107 - 1.554)$ m^{-1}, respectively, on the day of the full transect on the 29/11/2011. These values are much higher, 20-30 times larger, than simulated in Lee et al. (1999).

HOPE parameterises the full radiative transfer model down to a function of six variables that uniquely influence the remote sensing reflectance. These variables are; P, G, X, B, H and Δ, which parameterise phytoplankton, CDOM, particle scattering, bottom albedo, depth, and a spectrally constant offset of R_{rs}, respectively. These variables are

derived through mathematical optimisation of the model and are used to infer the total contribution of each parameter to the remote sensing reflectance. HOPE was originally designed for deriving bottom depths for shallow water coastal environments. Although it is a simplified version of the full radiative transfer model, when applied to the Swan River it was demonstrated that the six retrievable parameters still resulted in too many degrees of freedom; this resulted in high ambiguity due to the environment being more optically complex to that which the model is optimised for in the original publication. Therefore, the number of degrees of freedom was reduced by restricting the number of parameters firstly from six to three and later down to one; the consequence of doing this was an improvement in accuracy and precision which can be seen by comparing Figure 6.90 (three) with Figure 6.96 (one). It is worth emphasising that with six degrees of freedom, the model was not able to converge on a realistic solution; furthermore, with six degrees of freedom, the inversion method resulted in IOP combinations that do not represent 'real world' values such as negative, infinity or unrealistically large values of IOPs. Attempts to restrict the model from diverging from unrealistic values (less than zero and greater than 30% of the maximum measured value) by applying minimum and maximum thresholds cause IOP values to get stuck at those thresholds suggesting that the error space is divergent from the global minima at these thresholds. As discussed previously (Section 7.2.2, it is conjectured that these unrealistic values are a consequence of the nonunique nature of the problem due to having so many degrees of freedom in the presence of a highly variable number SIOPs and sources of SIOPs (Defoin-Platel and Chami, 2007) as occurring in many inland waterways, e.g. many phytoplankton species, combinations of mineral types and non-algal particles). In this case, there is a direct correlation between the number of degrees of freedom and the number of nonunique solutions.

The findings of this study are consistent with the study conducted by Mouw et al. (2013), which concludes that they were unable to retrieve chlorophyll concentration using an inversion algorithm approach, due to the very large contribution of absorption due to CDOM and the error in the derived CDOM being greater than the phytoplankton values. Furthermore, Mouw et al. (2015), based on the studies of (Dong, Shang, & Lee, 2013; Le & Hu, 2013; Zhu, Yu, Tian, Chen, & Gardner, 2011) state that in order to retrieve many OACs simultaneously, improved separation of a_ϕ and a_{dg} and a_{nap} are required. That a_{nap} is not separated from a_g nor b_{nap} from b_{bp} in this study may be an additional source of uncertainty. When comparing 6.85, 6.86 and 6.87, the contribution of a_{nap} to a_g is low compared a_{cdom} to a_g. It is not known what contribution this makes to

the total error budget and is therefore left as future work, if and when, more SIOP data becomes available for the Swan River. Furthermore, it is recommended that a further uncertainty analysis be conducted by measuring site specific SIOPs along the Swan River at the monitoring sampling sites and analysing the error contribution as a result of not separating a_{nap} and b_{nap} from the other IOPs.

The values of error cited in Lee et al. (1999) (7% - 8%) are much lower than the results presented in this study (30% - 45%), which is almost certainly due to the reasons discussed above. However, another source of error may well be due to the model hyper-parameters and application to an optical environment it was not designed for. The general form of HOPE is shown in Equation 5.39. Based on quasi-single-scattering theory, this equation defines nine spectrally constant model hyper-parameters; g_0, g_1, g_2, α_0, α_1, D_0, D_1, D'_0 and D'_1. Hydrolight was used to solve the model for these hyper-parameters giving the specific form of the model shown in Equation 5.43. These hyper-parameters were solved for by making multiple forward runs with Hydrolight for three different viewing angles and a number of changes in optical properties and water depth. It was these published model hyper-parameter values that were used in this study. It is assumed that because the Swan River light environment is different to the original designed application, that the model hyper-parameters that best fit our environment may well be different than those published in Lee et al. (1999). It remains unknown at this time what the effect of not having site-specific hyper-parameters have had on the accuracy and precision of the results presented in this thesis, and finding more site specific hyper-parameters would be recommended as further work.

Following an assessment of remote sensing optical models and their suitability for the Swan River, this study adapts a methodology outlined by Lee et al. (1999) and uses localised in situ measurements as inputs into the bio-optical models. There are other bio-optical models (e.g. Twardowski et al., 2004, Allen et al., 2015), that may be more suited to the Swan River, and it remains as further work to investigate and assess how these models could affect the accuracy and precision of the results in this thesis, as alternatives to the ones defined in Lee et al. (1999).

7.3 Optical Scattering Comparison and Assessment

To address the Mie Theory and Finite Difference Time Domain algorithms research objective, a comparative assessment of both methods in regards to modelling the scattering

of different phytoplankton was presented in Chapter 3. This assessment found that, even though there was a large difference in scattering between Mie and FDTD for any one particular scattering simulation, when the scattering was run multiple times and the results averaged, the results between Mie and FDTD converged quite closely for most of the simulations, with exception to the sickle cell *Selenastrum capricornutum* where the results agreed more closely with the experimental results in Volten et al. (1998).

It was also found that the scattering fraction of $\frac{b_b}{b}$ was very low in comparison to the Petzold measurements (Figure 5.12) of phase functions and measurements published in Ladner et al. (2002). The scattering fractions in 3 were many orders of magnitude lower. Figures 3.17–3.26 show that when considering the scattering fractions of spherical particles with the same refractive indices of the particles in Table 3.4, the size of the particle is the dominant scattering feature. That is to say that smaller particles scatter orders of magnitude more light than the cells modelled in this study. It is for this reason that the scattering fractions measure by Petzold (1972) were dominated by smaller algal particles and mineral sediment.

A preliminary study of the FDTD algorithm and its ability to model the spectral scattering of non-spherical particles shown in Section 3.1.5; this provided evidence that this approach yields a more accurate scattering model than the traditionally used Mie theory. Constructed 3D models of homogeneous spheres gave results that very closely agreed with Mie theory, as expected (shown in Figure 3.3), the small differences being due to the finite discretisation of the volume. Further investigation of non-spherical homogeneous solids (figures 3.4 and 3.5) showed that there were differences between the scattering of the solids and the Mie-predicted equivalent volume sphere.

These results led to the idea that this technique could be used to model the scattering of algal cells more accurately than using Mie theory. A number of multilayered 3D algal cells were built using Gmsh[1] and Blender[2] modelling packages, and exported to RTCode. The models were simple representations of real algal cells and used as a test bed to see if it was possible to calculate the scattering of a multilayered model of a cell with different refractive indices describing different parts of the cell structure. Figure 3.6 shows that it is possible, in principle, to build analogical phytoplankton cells and model the light scattering using the FDTD method and RTCode software.

[1] `http://gmsh.info/`
[2] `https://www.blender.org/`

The RTCode software enables the scattering of light to be modelled using GPUs. GPUs are highly parallel processors compared to CPUs and speed up the processing time of these particular simulations by at least an order of magnitude. RTCode makes it possible to run the FDTD calculations on a standard gaming PC with a high–end graphics card. For the simulation of realistic algae cells however, nearly all commodity GPUs lack the onboard video RAM needed to build phytoplankton cells that are sufficiently large enough. An algal cell of a few micrometres requires approximately $4 - 6$ Gb of video RAM to fit the Yee cell in memory. Furthermore, in order to model the total scattering of algae, as seen by a sensor in the field, it is insufficient to simply complete a single scattering event as cells found in nature vary in shape, size, rotation and structure. To model this as accurately as possible with RTCode, many repeat simulations were run where the cell's rotation and size was varied randomly within measured cell size variances measured by Volten et al. (1998) for each species.

This high computational workload meant that the standard desktop GPU was not sufficiently powerful enough to model the number and size of the simulations presented in Chapter 3. To address this problem, a proposal was submitted to the Pawsey Supercomputing Centre[3] (iVEC at the time) to get access to the Fornax supercomputer. The Fornax supercomputer system comprises 96 nodes, each containing two 6-core Intel Xeon X5650 CPUs, an NVIDIA Tesla C2050 GPU and 48 GB of RAM. This results in a system containing 1152 cores and 96 GPUs. It was this access to Fornax that made it possible to produce the scattering results in 3. Even with this increased computing resource, only 10 out of 17 (Table 5.1) of the cells presented in Volten et al. (1998) were able to be simulated, due to the cell size and time restraints.

Ultimately, these scattering results were not used in the radiative transfer modelling by either PlanarRad or by the inputs into HOPE not to develop bio-optical models of phytoplankton scattering. This chapter showed that there were differences in the scattering predicted by Mie theory and the FDTD method. In particular for highly aspherical particles such as *Selenastrum capricornutum*. Further investigations into the cause of these differences and if they can be explained using FDTD is required, particularly when more data on the refractive indices of difference algal cells and cell structures are published.

[3] www.pawsey.org.au

7.4 Phytoplankton Culturing and Absorption

The Swan River, unless under bloom conditions, contains a mixture of different phytoplankton species. As the Murdoch University cultures were mono-cultures and not necessarily representative of the species found in the river, it was decided to use the in situ measurements of phytoplankton absorption as inputs into the reflectance model as these measurements would capture all of the contributing absorption features due to the mix of species found in the water. For transect points between the sampling locations, the spatially closest in situ measurement was used as the algae absorption input. Furthermore, as the CDOM was the dominant spectral absorption feature, it was believed that small differences in pigment absorption would unlikely affect the inversion results. In order to confirm this assumption, the Swan River reflectance transect was reprocessed using the cultures grown at Murdoch University and compared with the mixed-culture in situ results, shown in Figure 7.1.

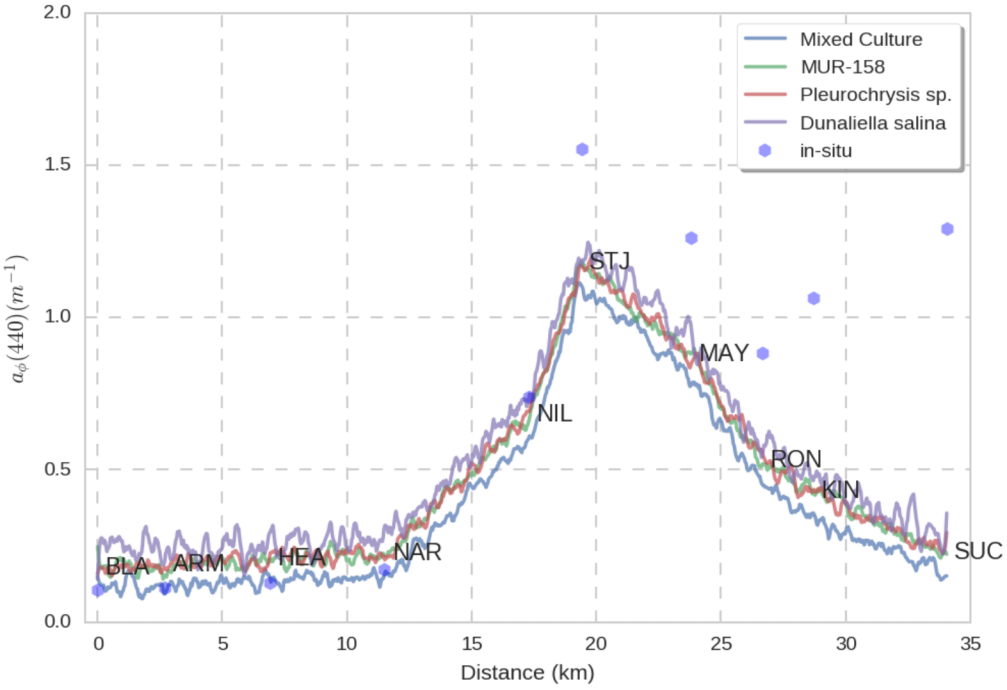

Figure 7.1: The transect 29/11/2011 reprocessed using the Murdoch University phytoplankton culture absorption as inputs into HOPE. The mixed culture transect was processed using the normalised absorption profile measured at the in situ sampling locations. The in situ points on the plot show the $a_\phi(440)$ measurement results at the sampling sites.

Figure 7.1 shows that there is little difference between the results using the three labora-

tory grown cultures. The largest difference between results was *Dunaliella salina* and the other two laboratory grown cultures. This was also the culture that showed the largest difference in spectral absorption (Figure 4.1). This suggests that the accessory pigments may in fact affect the inversion results. However, these results are small when compared to the larger uncertainties in the inversion results. It may be the case, in much clearer water types, where the algae pigments contribute much more to the R_{rs} signal, the differences between species may have a larger effect on the inversion results. This remains as future work at this point in time.

Although spectra from the Murdoch University cultures were not used to produce the results in 4, the time spent was still a useful and worthwhile part because the lessons learned helped set up the radiometry laboratory at Curtin University and provided the cultures used to test and calibrate the dual-beam spectrophotometer before field trips were undertaken. The experience also provided a beneficial experience that helped to set up the wet laboratory, used for filtering and analysis of the in situ measurements that were ultimately used to produce the final results.

7.5 Software and Open Source Community Tools

There was a considerable amount of software written and used for this study. Wherever possible, open source tools were used in preference of proprietary ones, such as PlanarRad over Hydrolight. Wherever software was written to support the study, the source code was published under a GPL licence and hosted in publicly accessible code repositories. This was done in order to improve the reproducibility of the results through open access to most of the tools, and is increasingly recognised as a standard in software development (Jimenez et al., 2017), for adhering to FAIR data principles (Wilkinson et al., 2016). This has resulted in a small community of researchers who actively use the tools and report bugs in the software, contribute to the source code and make improvements (see Appendices for descriptions of the software tools as well as instructions on how to access them and their community pages).

Section 5.1 of the literature review introduces the radiative transfer process and equations. Even though software packages like PlanarRad and Hydrolight exist to solve the RTE, the results they produce are only as good as the inputs they are given. These tools will always produce a result of some sort. Whether or not those results accurately

represent the environment they are trying to model is dependent on the inputs. If bad parameters are passed to the tool, the outputs will be incorrect and it is up to the operator to check and identify errors in the results.

PlanarRad can take over 100 different input parameters, including sun and sensor viewing geometries; absorption and scattering properties; different phase functions; the sky and water surface state; and the type of integration method, including the number of integration steps. These are just a few of the exhaustive parameters that need to be defined in order for the tool to work correctly. Combining the different combinations of parameters required to develop the coherent noise mode in Section 5.5 or for the sensitivity analysis in Section 5.6, required special scripts and access to supercomputing facilities to run them.

PlanarRad is essentially an integration tool that integrates through plane–parallel slabs of water. The software comes with a graphical user interface (GUI) that can be used to run the tool and visualise the outputs. This is useful for single simulations; but in practice, the tool needs to run for many (often hundreds of) runs for many different input parameters. This has been particularly true for this project; specifically, for the sensitivity analysis, presented in Chapter 5; as well as the uncertainty method, also presented in Chapter 5. In order to run these many simulations, software was developed as part of this project (Planarradpy) to batch run PlanarRad for the many different inputs required[4]. Users can define a range of parameters that they wish to simulate, such as many different phytoplankton concentrations or different environmental conditions. Planarradpy will generate the many run scripts that PlanarRad requires which define the conditions in which to simulate. Planarradpy also acts as job a job scheduler that distributes multiple instances of PlanarRad across the available CPUs on the simulation computer. When jobs are complete, the results are saved in unique directories for post-processing and reporting, and new jobs are spawned.

As many different parameters are defined in a particular PlanarRad analysis, the total number of combinations can quickly hit hundreds, or thousands of runs. The time that a single run can take is up to an hour at a time, depending on a few different conditions. In particular, PlanarRad lacks the ability to directly model optically deep water. A water depth and bottom albedo must be defined. In the case of this project, the Swan River is considered optically deep. In order to accurately approximate this water type using PlanarRad, a sensitivity analysis was conducted to see how deep that PlanarRad simula-

[4]See Appendix for community page and download instructions

tion needed to be, in order for it to approximate optically deep water. A bottom albedo of all zeros (black) was used and the depth was set to incrementally increase while all other conditions were kept constant. The depth in which no change in reflectance was detected between simulations was considered to be optically deep. This does change with different IOP concentrations. To be on the safe side, a depth greater than all of the tested conditions was used – 50 m. Such a great depth for optically deep water means that there are many more plane-parallel slabs to integrate over, and increases the simulation time significantly, when compared to a shallow-water coastal simulation, for example.

Nearly all of the simulations required for this project met these long-running criteria and it was quickly realised that more computational time was needed than could be reasonably handled by a standard desktop computer. In order to conduct the sensitivity analysis, and the uncertainty method, presented in 5, many thousands of simulations were run. Access to the supercomputer Magnus at the Pawsey Supercomputing Centre[5] was required, in order to complete these simulations, and in excess of 10 000 CPU hours were used running many simulations at once, using the Planarradpy software. These simulations produced many gigabytes of data that included reports from PlanarRad which included full-radiance distributions. Planarradpy includes tools for collating data in a sensibly sized report, as well as tools for making the necessary calculations and interpolations needed to produce the surface reflectance at the viewing geometries that represented the DALEC-measured reflectance of the Swan River.

As a result of this project, open-sourcing the Planarradpy software and publishing in the public domain, a small user community has formed, and contributions and bug reports have been made by many other researchers who have started using the software to make batch simulations using PlanarRad. There are more features that exceed the scope of this project that will be added in the future, and it is hoped that the community will continue to grow.

PlanarRad is a reliable model that can be used to make calculations to accurately predict R_{rs} for the wide range of conditions encountered in the Swan River. This tool has been used extensively in this project to understand how the environmental factors are related to the R_{rs} and develop the model inversion tools.

[5] www.pawsey.org.au

7.6 Project Challenges and Limitations - Lessons Learned

7.6.1 Fieldwork

One of the major challenges of this project was getting access to a boat that was suitable for making remote sensing reflectance measurements with the DALEC. In retrospect, committing to a project that required access to a boat without first securing access to one was not the best approach. The Swan River Trust (SRT) gave access to its boat on a number of occasions, but with some limitations. Firstly, any activities undertaken by this project could not interfere with any of the activities undertaken by the SRT. This meant that loading equipment onto the boat for early departure was quite a challenge, as mounting the DALEC to a non-permanent fixture was difficult in its own right. Custom-made brackets were made in the Curtin University Physics Department workshop with the help of workshop staff. Furthermore, the DALEC is quite cumbersome and requires many cables to operate it, as well as heavy battery power supplies and a laptop computer. Stowing all of this equipment, and the equipment required for collection of water samples without contamination on a small boat without impeding on the work of other scientists aboard was a tremendous challenge. On more than one occasion, data was incorrectly recorded, equipment failed or water samples were contaminated or lost as a result of these complications.

Furthermore, as the SRT had strict deadlines, any activities had to adhere to its schedule. Early boat departures (no later than 7.30 am) meant that light conditions were usually too low in the early part of the trip, especially in winter when it was often still very dark. The SRT boat crew were only interested in collecting their own data at the discrete sampling locations (shown in Figure 6.1). As such, the speed at which the boat travelled between the locations was too fast and unstable for making any underway measurements.

Despite these challenges, four of the trips yielded data that were instrumental in testing and refining the processing methodologies, which included all of the steps, from making the reflectance measurements, processing the water samples, and testing the optical model. Many software bugs, fieldwork and laboratory equipment issues were improved as a result of these preliminary field trips.

As mentioned above, the equipment required to make the measurements, namely the DALEC, is bulky and cumbersome. This is, in part, due to the DALEC being actively developed over the duration of the project. There is scope for the DALEC to be reduced

in size and complexity in the future but this was not possible during the developmental stages of the project[6]. In particular, having equipment, such as the laptop computer and DALEC with large power requirements and sensitive electronics, is often difficult to manage around a wet boat and while collecting water samples. Power and cable management was difficult in its own right, even without introducing a wet working environment. Moreover, the noise that most boat motors produce interferes with the electronic equipment and produces noise in the reflectance signal. This meant that the boat's power supply could not be used, so large, portable lead–acid batteries had to be used instead. The draw on the batteries, especially when powering water pumps and laptops with 240V, was particularly high.

The length of time that it took to load the boat and mount the DALEC, as well as make the measurements on the river, was quite a burden. Especially when coupled with the time it took to filter water samples before they degraded. This needed to be carried out on the same day, as soon as possible, before the samples could be stored in liquid nitrogen for processing the following day. Field days often ran well over 12 hours which meant that repeat field trips were logistically difficult to plan for, especially when it came to booking time on a boat. The majority of the fieldwork described in this study was carried out by one person (the author), who also drove the boat on many occasions[7]. The exception being, the day on which the last transect was carried out where a team of four people (a coxswain and three researchers)[8] were able to share the field and laboratory work. This meant that measurements could be made with much more attention and due diligence and this was reflected in the quality of the results.

7.6.2 Laboratory work

The original vision of this study included an analysis of phytoplankton pigments and a method of unmixing signals in reflectance due to accessory pigments with a view to identifying major classes of algae in the river. This fuelled a further investigation into growing different species in a laboratory. However, it was quickly concluded that this was too ambitious and would not be possible until the inversion of the optical model was

[6]A commercial version of the DALEC has since been developed by In-situ Marine Optics (`http://insitumarineoptics.com/`).

[7]This was not true of the field trips conducted with the SRT; they had their own coxswain. There were many development days in the early part of the study where access to a boat was donated by Graham Thompson.

[8]Special thanks to Lachlan McKinna, Rodrigo Garcia and Graham Thompson for volunteering their time for this field trip.

able to produce much more accurate results.

The Murdoch Algae R & D Centre agreed to donate time and laboratory space for culturing and growing phytoplankton for this project. Although the original plan to build a spectral library using these facilities was abandoned due to time and resources constraints, it provided a valuable experience for gaining an understanding of the phytoplankton and provided many samples that were used when developing the workflows for spectrometry in the laboratory.

Culturing and growing algae required a specialist laboratory and trained technicians, something that this project did not have access to at the beginning. As mentioned before, the Murdoch Algae R & D centre kindly agreed to donate both time and laboratory access for this project. However, there was not the resource for staff to donate time to the task itself. Nevertheless, substantial training was donated and much time was spent by both technicians and researchers toward this project in order to provide expertise and training in safely culturing algae.

The time it took to learn the laboratory techniques and safe use of chemicals and equipment were substantial. Combined with the time taken to grow algae in the media, culture, daily subculture, cleaning the equipment, as well as counting cells, quickly exceeded the time and scope of the project. It was soon realised that the time it was taking to complete this work was subtracting from time required in other areas of the project, such as building equipment, designing data-processing tools and conducting fieldwork. A compromise was made between building an algae-absorption library that would represent local conditions, and a more generic approach of using either published absorption profiles or by using in situ profiles of algae absorption. It was originally believed that growing monocultures in the laboratory would provide very useful inputs for identifying different algal species at a later point in the algorithm development. It was found however that getting the model to converge to an accurate estimate of $a_\phi(440)$ was more difficult than originally expected. Therefore, it was decided that using in situ measurements of phytoplankton absorption taken at the time of DALEC measurement would likely yield the most accurate results in total DALEC-derived measurements of phytoplankton.

Three species of algae were successfully grown in the laboratory and the spectral absorption of each are presented in Figure 4.1. Shortly after growing the algae at Murdoch University, a dual-beam spectrophotometer had just been acquired by the Curtin Uni-

versity Physics Department and was made available for use in this project. The algae grown at Murdoch University was used to test the spectrophotometer, and laboratory techniques to correctly operate the machine in accordance with the methods described in Chapter 6. Python scripts were written to process the outputs, including subtracting the calibration slides and applying the path-length amplification factors, as described in Section 3.5. The algae grown at Murdoch University was used in the development process of the laboratory measurements and workflows.

As well as making the spectrophotometric measurements, in situ water samples needed to be correctly filtered and bleached. Before this part of the project was carried out, a wet laboratory was created with space made available in the Curtin University John de Laeter building by the Curtin University Physics Department and new equipment was purchased through funding provided by the Swan River Trust. It took time to set up the laboratory with the correct equipment, safety equipment and procedures. The algae grown at Murdoch University was used to help develop the laboratory and procedures in a controlled manner.

Chapter 8

Conclusions

The work presented in this thesis was focused on the viability for water quality monitoring programmes such as the SCCP to include remotely-sensed optical measurements in sampling campaigns, to determine chlorophyll-a concentration, a key indicator of water quality in the Swan River.

In the course of reviewing relevant literature, and assessing and investigating optical models for the potential for adapting them for localised application, novel methodologies were developed and open source coding practises employed to support potential application in monitoring campaigns. In particular:

- A new method for modeling the optical scattering of non-spherical particles using the FTDT algorithm;
- A new data-driven approach for estimating uncertainties - the coherent noise method;
- A mathematical inversion methodology for improving IOP retrieval reliability in low light environments;
- All the code is available on Github for researchers, managers, government etc to access, use again and develop further for mutual community benefit and potential improvement to monitoring programmes.

Overall, the study presented in this thesis has shown that it is possible to estimate the phytoplankton concentration derived from DALEC measurements of R_{rs} using a remote sensing optical model (HOPE) using inputs of $a_g(400)$ and $b_{bp}(550)$ from in situ measurements. It was found that it was possible to derive phytoplankton concentration where CDOM values of $a_g(400)$ were between 0.00 m^{-1} and 3.402 m^{-1}, and phytoplankton

concentration of $a_\phi(440)$ were between 0.00 m^{-1} and 0.739 m^{-1}, with an error less than ∼23% when compared to in situ measurements. The model inversion uncertainty was ∼34% for the corresponding concentrations. For larger CDOM concentrations of $a_g(400)$ between 3.402 m^{-1} and 5.573 m^{-1}, it was found that the model could not accurately determine the phytoplankton absorption. At these high values of CDOM absorption, the model consistently underestimated the phytoplankton concentration.

The SCCP sampling methodology was limited to 10 discrete measurements. This thesis has demonstrated that continuous underway transect measurements of hyperspectral remote sensing reflectance can be processed to give continuous measurements of phytoplankton absorption. This means that it is possible to use the methods described in this thesis to supplement the data collected at the discrete sampling sites up to and including NIL by estimating the phytoplankton concentration in between the SCCP sampling sites between BLA and NIL. Using these methods and DALEC measurements, the coverage of phytoplankton can be significantly increased between these sites. Furthermore, algal mats and blooms could be potentially missed by only sampling at the 10 discrete SCCP locations, where the methods here would identify them.

Specific conclusions are drawn next, in reference to the original research objectives as laid out in Section 1.4, and the key findings and developments are highlighted.

Conducting a comparative research assessment of Mie Theory and the Finite Difference Time Domain algorithms. Assessing whether modelling light scattering, with a high degree of variability in shape and size of different phytoplankton species, benefits from using the more advanced FDTD algorithm in order to improve results with optical inversion of remote sensing models.

A novel approach to modeling the scattering of individual phytoplankton species was developed that makes use of the FDTD algorithm, and demonstrated to be capable of i) modeling the spectral scattering of spheres as well as non-spherical particles and ii) modelling the scattering of multilayered volumes. Although limited to a small number of species in this study, this model is applicable to any species with enough available data.

While Mie theory provides a good method for calculating the b/bb ratio, it was shown that with highly non-spherical particles the FDTD is more accurate for modeling the total scattering of particles. The method described in this thesis is recommended for further in-

vestigation as complex refractive index data become available for more individual species.

Assessing existing remote sensing optical models, and determine their applicability and limitations for use with the optically complex Swan River. Further, develop the inputs and computational tools needed to accurately model the Swan River's water colour, as required. Note that these optical models include radiative transfer models, as well as bio-optical models, required for modelling the spectral inputs to the radiative transfer equation.

Three different optical models which were able to approximate the radiative transfer equations (RTE) with parameterised inputs, were assessed and compared. Of these, HOPE was determined to have the most applicability to the Swan River and was used to produced estimates of phytoplankton absorption. Using in situ measurements of a_g and b_{bp}, the model converged to a solution using the coherent noise model and Levenberg–Marquardt optimisation method; this demonstrated that it is possible to estimate phytoplankton concentration from a DALEC (and potentially, other boat-mounted instruments) using a remote sensing optical model (HOPE).

A Swan River water quality monitoring programme may therefore consider employing this as an additional monitoring method up to NIL, but be aware that HOPE generally underestimated the phytoplankton concentration, particularly in high CDOM concentrations. Upriver after NIL this method is not reliable.

All the computational tools and source code that were developed for this thesis are made openly available on Github for anyone (managers, government, researchers) to access, use and contribute to.

Developing new mathematical inversion methods that improve the IOPs retrieval reliability in low light environments where the relationship between remote sensing reflectance and IOPs have a highly non-linear relationship.

Due to the non-linearity of HOPE, there are local minima in which the model has a propensity to converge to, particularly when the initial estimates of the inputs are inaccurate. Under very high CDOM conditions, the six solvable parameters of HOPE provide too many degrees of freedom when applied to the Swan River, and the optimisation rou-

tine is not able to converge to a solution.

It was shown here that HOPE can be constrained in order to converge to an accurate solution of phytoplankton concentration in the Swan River by limiting the degrees of freedom to a single parameter, $a_\phi(440)$. Furthermore, it was found that the coherent noise method, developed in this study to define the uncertanties, was also required for the model to converge to realistic solutions and produce accurate results up to NIL.

Applying the developed models and tools to investigate the sensitivity of remote sensing reflectance with regard to a range of IOPs using synthetic data sets.

The results of both a sensitivity analysis and field results show that due to the very high CDOM absorption in the Swan River compared to ocean waters, the model is not very sensitive to changes in phytoplankton absorption. When CDOM is high, a 1% RMS change in measured reflectance can correspond to up to 16% uncertainty value of the measured phytoplankton absorption. This presents a significant challenge when attempting to make accurate estimates of phytoplankton absorption using the optical model, HOPE, in particular upriver from NIL.

These high levels of CDOM make it difficult to detect small changes in phytoplankton absorption; the difference in absorption spectra between species of phytoplankton are even smaller and therefore, difficult to measure. As a result, it is infeasible to detect different species of phytoplankton under these optical conditions.

Developing a method for calculating uncertainties of IOPs derived from remote sensing reflectance.

As highlighted by Bracher et al. (2017) and the IOCCG (2006), the lack of quantitative uncertainty estimates provided with satellite and in situ data, remain a major gap in remote sensing of IOPs. As such, using traditional uncertainty methods, these uncertainties cannot be propagated through to IOP inversions.

As an outcome of this research a purely data driven approach that is model and sensor agnostic, and which does require in situ data, has been developed; this has the advantage of circumventing the above highlighted issues, and has major potential for many appli-

cations, including ocean colour and quantifying uncertainties.

The coherent noise model developed for calculating the uncertainties of derived IOPs is a completely data driven model that can be applied to any remote sensing reflectance model and does not require, any knowledge of the model, or in situ measurements. Furthermore, the method is not limited to remote sensing and can be applied to many disciplines of science where parameters are derived from any number of signal sources, for example; acoustic, electrical or radio.

Developing an inversion algorithm and workflow capable of retrieving algal absorption concentration using the chosen optical model with inputs specific to the Swan River. Moreover, develop a confidence interval and uncertainty range within which estimates are deemed valid.

The coherent noise model developed in this study for calculating uncertainties had an added advantage; the model design also helped the optimisation method avoid converging to local minima in solution space which would result in false positive inversion results. As a result, this allowed HOPE to converge to a realistic solution when the parameters (degrees of freedom) were restricted to one ($a_\phi 440$).

Assessing the accuracy of measuring phytoplankton abundance in the Swan River using the research methods developed in this thesis.

There is a high correlation between the model accuracy and the CDOM concentration, in that HOPE generally underestimated the phytoplankton concentration, particularly in high CDOM concentrations. It is possible to measure the phytoplankton concentration ranging between $0.00m^{-1}$ and $0.739m^{-1}$ within an accuracy of $\sim 23\%$ when the CDOM concentration of $a_g(400)m^{-1}$ is less than $3.402m^{-1}$.

The sampling sites where CDOM concentrations are low enough to confidently estimate the phytoplankton concentrations are BLA, ARM, HEA, NAR and NIL which covers approximately 15 km of the river and about half of the SCCP sampling Sites.

Developing an approach for using the DALEC, a boat-mounted radiometer, in the field while using concurrent water samples to truth the results.

The fieldwork component of the study required several developments in order to meet this objective of taking continuous underway radiometric measurements and truthing them with water samples. The transects along the river were presented following this approach. Significantly, software was written for the DALEC for this specific application (available on Github), inversion techniques were developed and field trials designed to acquire local inputs for the optical models.

Developing quality control algorithms to filter out erroneous data, such as sunglint effects, measurements taken with the incorrect viewing geometry, and inversion results that could not converge to a solution.

The coherent noise model developed for optimising the optical model had the largest influence on the ability of the model to converge to a solution. Without it, and in particular if the degrees of freedom were not restricted, HOPE was not able to converge to a solution under high CDOM conditions.

The transect data were also quality controlled using both pre- and post-processing filters develop- specifically for this study and application.

Validating the accuracy of the phytoplankton-retrieval scheme by comparing remote sensing reflectance derived measurements of phytoplankton with in situ water sampled laboratory measurements.

The results of the underway transect were compared to in situ measurements of a_ϕ, a_g and b_{bp} at the 10 SCCP sampling locations. These comparisons show that up to and including NIL, the in situ measurements agree with the inverted IOP estimates. Up stream from NIL, the model derived IOPs do not agree with the in situ measurements, supporting the recommendations that a monitoring programme in the Swan River up to NIL may benefit from the work presented in this thesis.

8.1 Recommendations and Future Work

It was originally planned that the algae commonly found in the Swan River would be grown in the laboratory in partnership with Murdoch University and those algae absorption spectra would be used as inputs into the optical model. It was also planned that he scattering of those algae would be modelled using the methods presented in Chapter 3 and could be used to define SIOPs for specific phytoplankton found in the Swan River. This was overly ambitious for the length and scope of this study and the question of how this could be used to improve the results in this thesis remains unanswered. This remains as the focus of future work of optical modelling in the Swan River and other inland waterways.

The software tools developed for this project were designed to address specific needs. There is a lot of scope for these tools to be developed, making them more generic and adaptable to other environments. It is recommended that time be spent increasing the scope of the software tools, and increasing their uses, making them more generic. In fact, this is already happening due to the project software being open source, with a small international group of users contributing to the development of the tools. As the tools become more user-friendly and more useful to a greater audience, there will be greater participation in their development.

It was posited in the original project plan that the different accessory pigments in the phytoplankton absorption spectra could be used to help identify different classes of algae. In particular, the pigment phycocyanin could be used to identify the toxic species of blue-green algae. The Swan River is dominated by CDOM absorption and the relatively small changes in reflectance due to these pigments are likely to be too small to use in classification under such conditions. A small study done by Marrable et al. (2010) and presented at Ocean Optics XX, 2010, Anchorage, USA, showed that it was possible to separate and quantify blue-green algae from other species of algae in Hydrolight-simulated data. Further work could include the clearer parts of the Swan River or in other Case 1 ocean waters. Moreover, it is feasible with further refinements to the accuracy of the model, a station with a sensor similar to the DALEC may be deployed at fixed stations along the river, potentially providing a real-time data stream that could be used to monitor for HABs.

For sections of the river where CDOM is low, and reasonable estimates of the phyto-

plankton concentration can be made, the onboard GPU of the laptop used to run DalecOnTransect, could be used to do real-time inversions of the model. A proof of concept of this is shown in Marrable et al. (2009). The CUDA GPU libraries could be leveraged to develop a real-time detection system. This would be particularly useful if a harmful bloom is suspected and the DALEC could be used to quickly identify the location of the bloom and respond appropriately. Health warnings could be issued much faster than the current method of in situ sampling and cell counting allows, and risk control plans could be executed immediately.

In this thesis, the coherent noise model was used to estimate the uncertainties of the DALEC-derived $a_\phi(440)$, $a_g(400)$ and $b_{bp}(550)$. Furthermore, The coherent noise model provided a method that was less likely to converge to a non-global minimum. An example of this is shown in Figure 6.55, where it can be seen that the solution of HOPE, for each $\hat{R}_{rs}$ converged in two different clusters. One at $\sim$0.25 and $\sim$0.85 for $a_\phi(440)$ and $b_{bp}(550)$ respectively and one at $\sim$1.5 and $\sim$0.12 for $a_\phi(440)$ and $b_{bp}(550)$ respectively. The coherent noise model weights the reported result close to the larger cluster corresponding to lower IOP values. The corresponding uncertainty of the measurement is indicated by the error ellipse. It can be seen in the figure that the error ellipse is skewed by the cluster of higher values and the ellipse passes through the zero axis. Assuming that the cluster with less data points represents a local minimum in the solution space, which we would like to avoid, a method could be devised that ignores these points when calculating the error ellipse. A clustering algorithm such as the k-means method could be used to identify discrete clusters of solutions. Once identified, the cluster with the majority of points could be considered as the global minimum and all other points excluded. The mean value of the points could be reported as the DALEC-derived results and the error ellipse defined over only these points. In the case shown in Figure 6.55 this would likely result in an error ellipse defined over a much smaller range and would not pass through zero on the x-axis. Therefore, uncertainty ranges would be less likely to report values of $a_\phi(440)$, $a_g(440)$ and $b_{bp}(550)$ that are less than zero, as is the case in real-world measurements. Such a clustering method is left as future work and investigation.

As noted in Chapter 7 a potential source of error may well be due to the choice of model hyper-parameters when using HOPE. In this study, the published values from Lee et al. (1999) of g_0, g_1, g_2, α_0, α_1, D_0, D_1, D'_0 and D'_1 were used for the Swan River. These values may not be the most suitable hyper-parameters for the river as the light environment is different to the originally designed application. Therefore, it is recommended

that the hyper-parameters be recalculated, for a light environment more representative of the Swan River, using the method outlined in Lee et al. (1999) and the impact of the new site specific hyper-parameters be investigated. The mismatch between modelled and measured results may be used to improve the model hyper-parameters (Baird et al., 2016).

It is also recommended that a further uncertainty analysis be conducted by measuring site specific SIOPs along the Swan River at the monitoring sampling sites and analysing the error contribution as a result of not separating a_{nap} and b_{nap} from the other IOPs.

The particle scattering results in Chapter 3 showed that there were some differences between Mie theory and the FDTD method. The most aspherical particle *Selenastrum capricornutum* (Figure 3.14) showed the greatest difference in scattering between Mie and FDTD and the FDTD predicted scattering agreed more closely with Volten et al. (1998) than Mie. Because there is not a lot of documented data on the complex refractive index of phytoplankton, this study was limited to simulations of only 10 different species. Furthermore, the scattering of 7 out of the 17 phytoplankton studied in Volten et al. (1998) were unable to be simulated due to the phytoplankton cell size. The larger cell radii meant that they could not fit in the available GPU memory. As the technology of GPUs are advancing at a very fast rate, accelerated by the personal gaming industry, hardware with much larger memory is likely to be available on the market soon. As hardware with larger memory becomes available and data regarding the refractive index of phytoplankton is published, the FDTD method could be used for further investigation into the scattering of complex shaped hydrosols.

The environmental modeling work of Hipsey et al. (2016b), Hipsey et al. (2016a) and Huang et al. (2017) could potentially incorporate more sophisticated optical modeling than currently included, accounting more than CDOM absorption (Kostoglidis et al., 2005).

Appendices

Appendix A

Dominant Phytoplankton Species by Cell Count

	Summer	Autumn	Winter	Spring
BLA	Thalassiosira (MDIAT) 16.92%	Skeletonema costatum (MDIAT) 61.81%	Skeletonema costatum (MDIAT) 85.38%	Skeletonema costatum (MDIAT) 57.58%)
	Chlamydomonas (GRN) 11.10%	Chaetoceros (chains) (MDIAT) 13.62%	Cyclotella (MDIAT) 4.38%	Chaetoceros (chains) (MDIAT) 15.58%)
	Cylindrotheca closterium (MDIAT) 9.10%	Chaetoceros curvateus (MDIAT) 7.14%	Plagioselmis (DINO) 3.22%	Cyclotella / Thalassiosira (MDIAT) 8.10%)
	Gymnodinium (small) (DINO) 8.69%	Cylindrotheca closterium (MDIAT) 4.78%	Cyclotella / Thalassiosira (MDIAT) 1.40%	Gymnodinium (small) (DINO) 6.11%)
	Chaetoceros (single) (MDIAT) 7.01%	Plagioselmis (DINO) 2.61%	small cryptophytes (DINO) 1.20%	Cyclotella (MDIAT) 2.78%)
	Skeletonema costatum (MDIAT) 6.73%	Gymnodinium (small) (DINO) 1.82%	Gymnodinium (small) (DINO) 1.01%	small cryptophytes (DINO) 2.11%)
	Heterocapsa (<10um) (DINO) 4.34%	Cyclotella / Thalassiosira (MDIAT) 1.18%	Heterocapsa (<10um) (DINO) 0.51%	Plagioselmis (DINO) 1.65%)
	Cyclotella / Thalassiosira (MDIAT) 3.94%	passive chlorophyte (<3um) (GRN) 1.04%	Pyramimonas (GRN) 0.37%	Chaetoceros (single) (MDIAT) 1.33%)
	Thalassionema (MDIAT) 3.67%	Naviculoid (>10um) (FDIAT) 0.79%	Heterocapsa (>10um) (DINO) 0.32%	Gymnodinium (Medium) (DINO) 0.96%)
	Katodinium (small) (DINO) 3.41%	small cryptophytes (DINO) 0.69%	Apedinella spinifera (DINO) 0.31%	Ankistrodesmus (GRN) 0.83%)
ARM	Thalassionema (MDIAT) 17.54%	Skeletonema costatum (MDIAT) 64.62%	Skeletonema costatum (MDIAT) 71.95%	Skeletonema costatum (MDIAT) 48.99%)
	Gymnodinium (small) (DINO) 11.97%	Chaetoceros (chains) (MDIAT) 11.11%	Cyclotella (MDIAT) 7.78%	Chaetoceros (chains) (MDIAT) 17.77%)
	Chlamydomonas (GRN) 9.82%	Gymnodinium (small) (DINO) 2.69%	Plagioselmis (DINO) 5.75%	others (Hetero/Gymno - shrunk) (DINO) 9.54%)
	Skeletonema costatum (MDIAT) 8.52%	Prorocentrum dentatum (DINO) 2.50%	Pyramimonas (GRN) 2.62%	Gymnodinium (small) (DINO) 5.46%)
	Cylindrotheca closterium (MDIAT) 6.96%	Chaetoceros curvateus (MDIAT) 2.46%	Heterocapsa (<10um) (DINO) 2.60%	Cyclotella (MDIAT) 5.14%)
	Chaetoceros (single) (MDIAT) 6.05%	Cylindrotheca closterium (MDIAT) 2.22%	Cyclotella / Thalassiosira (MDIAT) 1.96%	Cyclotella / Thalassiosira (MDIAT) 2.73%)
	Thalassiosira (MDIAT) 5.60%	others (Hetero/Gymno - shrunk) (DINO) 2.14%	Gymnodinium (small) (DINO) 1.77%	Plagioselmis (DINO) 2.25%)
	Prorocentrum dentatum (DINO) 5.19%	Plagioselmis (DINO) 1.96%	small cryptophytes (DINO) 0.89%	small cryptophytes (DINO) 2.00%)
	Cyclotella / Thalassiosira (MDIAT) 4.28%	Cyclotella / Thalassiosira (MDIAT) 1.45%	Scrippsiella trochoidea (DINO) 0.61%	Ankistrodesmus (GRN) 1.09%)
	Ceratium furca (DINO) 2.56%	Heterocapsa (<10um) (DINO) 1.10%	Apedinella spinifera (DINO) 0.59%	Gymnodinium (Medium) (DINO) 0.65%)
NAR	Skeletonema costatum (MDIAT) 84.90%	Prorocentrum dentatum (DINO) 59.56%	Skeletonema costatum (MDIAT) 33.61%	Gymnodinium (small) (DINO) 35.12%)
	Gymnodinium (small) (DINO) 2.48%	Gymnodinium (small) (DINO) 7.56%	small cryptophytes (DINO) 17.91%	Skeletonema costatum (MDIAT) 28.81%)
	Chlamydomonas (GRN) 1.80%	Gymnodinium (Medium) (DINO) 4.53%	Gymnodinium (small) (DINO) 16.22%	Gymnodinium (Medium) (DINO) 5.42%)
	passive chlorophyte (<3um) (GRN) 1.71%	Skeletonema costatum (MDIAT) 4.37%	Cyclotella (MDIAT) 14.73%	Scrippsiella trochoidea (DINO) 4.90%)
	Cylindrotheca closterium (MDIAT) 1.62%	GKC (DINO) 3.92%	Cyclotella / Thalassiosira (MDIAT) 7.49%	small cryptophytes (DINO) 3.70%)
	Cyclotella / Thalassiosira (MDIAT) 1.39%	Plagioselmis (DINO) 3.17%	Cylindrotheca closterium (MDIAT) 1.50%	Heterocapsa (<10um) (DINO) 3.43%)
	Scrippsiella trochoidea (DINO) 0.84%	Cyclotella / Thalassiosira (MDIAT) 1.94%	Gymnodinium (Medium) (DINO) 1.43%	Cyclotella / Thalassiosira (MDIAT) 3.21%)
	Gymnodinium (Medium) (DINO) 0.73%	others (Hetero/Gymno - shrunk) (DINO) 1.88%	Naviculoid (>10um) (FDIAT) 1.09%	others (Hetero/Gymno - shrunk) (DINO) 2.44%)
	Thalassionema (MDIAT) 0.71%	Scrippsiella trochoidea (DINO) 1.74%	Plagioselmis (DINO) 1.01%	Cyclotella (MDIAT) 2.34%)
	Chaetoceros (single) (MDIAT) 0.51%	Cylindrotheca closterium (MDIAT) 1.59%	Oscillatoria (BGA) 0.97%	Plagioselmis (DINO) 1.86%)
STJ	Skeletonema costatum (MDIAT) 66.51%	Prorocentrum dentatum (DINO) 52.59%	Gymnodinium (small) (DINO) 42.41%	Skeletonema costatum (MDIAT) 47.98%)
	Chlamydomonas (GRN) 17.07%	Skeletonema costatum (MDIAT) 17.05%	small cryptophytes (DINO) 23.93%	Plagioselmis (DINO) 13.58%)
	Gymnodinium (small) (DINO) 3.97%	Cyclotella / Thalassiosira (MDIAT) 6.57%	Cyclotella (MDIAT) 9.90%	Cyclotella (MDIAT) 11.17%)
	Euglena (DINO) 3.01%	Plagioselmis (DINO) 4.02%	Cyclotella / Thalassiosira (MDIAT) 7.61%	Gymnodinium (small) (DINO) 11.12%)
	Thalassiosira (MDIAT) 1.75%	Gymnodinium (small) (DINO) 3.32%	Naviculoid (>10um) (FDIAT) 4.31%	Gymnodinium (Medium) (DINO) 2.78%)
	Scrippsiella trochoidea (DINO) 1.61%	Prorocentrum micans (DINO) 2.55%	Cylindrotheca closterium (MDIAT) 2.29%	Cryptomonas (DINO) 2.03%)
	Peridinium (DINO) 0.62%	Gymnodinium (Medium) (DINO) 1.85%	Gymnodinium (Medium) (DINO) 2.16%	Entomoneis (MDIAT) 1.67%)
	Gyrodinium (>10um) (DINO) 0.58%	Scrippsiella trochoidea (DINO) 1.52%	Plagioselmis (DINO) 1.06%	Cyclotella / Thalassiosira (MDIAT) 1.27%)
	Oscillatoria (BGA) 0.58%	Teleaulax (DINO) 1.15%	Navicula sp. (<10um) (FDIAT) 0.98%	Pyramimonas (GRN) 1.10%)
	Naviculoid (>10um) (FDIAT) 0.57%	Euglena (DINO) 1.01%	Skeletonema costatum (MDIAT) 0.87%	Chaetoceros (chains) (MDIAT) 1.07%)
KIN	Chlamydomonas (GRN) 90.75%	Cyclotella / Thalassiosira (MDIAT) 16.80%	Gymnodinium (small) (DINO) 38.09%	Gymnodinium (small) (DINO) 27.03%)
	Euglena (DINO) 2.88%	Gymnodinium (small) (DINO) 13.82%	small cryptophytes (DINO) 26.20%	Cryptomonas (DINO) 13.31%)
	Scrippsiella trochoidea (DINO) 1.91%	Plagioselmis (DINO) 12.69%	Cyclotella (MDIAT) 10.41%	small cryptophytes (DINO) 10.25%)
	Gymnodinium (Medium) (DINO) 1.14%	Pyramimonas (GRN) 10.91%	Cyclotella / Thalassiosira (MDIAT) 7.08%	Gymnodinium (Medium) (DINO) 9.86%)
	Thalassiosira (MDIAT) 1.07%	Prorocentrum dentatum (DINO) 9.21%	Cylindrotheca closterium (MDIAT) 5.15%	Scrippsiella trochoidea (DINO) 9.33%)
	Skeletonema costatum (MDIAT) 0.94%	Euglena (DINO) 4.33%	Plagioselmis (DINO) 4.67%	Naviculoid (>10um) (FDIAT) 6.18%)
	Gymnodinium (small) (DINO) 0.28%	Akashiwo sanguineum (DINO) 3.99%	Naviculoid (>10um) (FDIAT) 3.16%	passive chlorophyte (<3um) (GRN) 5.98%)
	Gyrodinium (>10um) (DINO) 0.13%	Gymnodinium (Medium) (DINO) 3.28%	Navicula sp. (<10um) (FDIAT) 1.33%	Pyramimonas (GRN) 5.39%)
	Heterocapsa (<10um) (DINO) 0.11%	Gyrodinium (>10um) (DINO) 3.05%	Gymnodinium (Medium) (DINO) 0.74%	Plagioselmis (DINO) 2.09%)
	Cyclotella / Thalassiosira (MDIAT) 0.11%	Skeletonema costatum (MDIAT) 2.91%	Pyramimonas (GRN) 0.62%	Cyclotella / Thalassiosira (MDIAT) 1.97%)
SUC	Chlamydomonas (GRN) 89.72%	Cyclotella / Thalassiosira (MDIAT) 43.82%	Gymnodinium (small) (DINO) 44.04%	Cryptomonas (DINO) 31.84%)
	Euglena (DINO) 6.16%	Plagioselmis (DINO) 13.64%	small cryptophytes (DINO) 25.21%	Gymnodinium (small) (DINO) 20.55%)
	Scrippsiella trochoidea (DINO) 2.31%	Teleaulax (DINO) 5.33%	Cyclotella (MDIAT) 9.43%	passive chlorophyte (<3um) (GRN) 10.71%)
	Thalassiosira (MDIAT) 0.73%	Gymnodinium (small) (DINO) 5.32%	Cyclotella / Thalassiosira (MDIAT) 7.10%	Naviculoid (>10um) (FDIAT) 6.43%)
	Skeletonema costatum (MDIAT) 0.21%	Gymnodinium (Medium) (DINO) 4.40%	Cylindrotheca closterium (MDIAT) 6.03%	Gymnodinium (Medium) (DINO) 5.73%)
	Gymnodinium (small) (DINO) 0.20%	Skeletonema costatum (MDIAT) 3.05%	Naviculoid (>10um) (FDIAT) 3.10%	small cryptophytes (DINO) 4.90%)
	Peridinium (DINO) 0.10%	Prorocentrum dentatum (DINO) 2.99%	Navicula sp. (<10um) (FDIAT) 0.84%	Pyramimonas (GRN) 3.36%)
	Cylindrotheca closterium (MDIAT) 0.09%	passive chlorophyte (<3um) (GRN) 2.78%	Synedra (MDIAT) 0.79%	Skeletonema costatum (MDIAT) 2.70%)
	Cyclotella / Thalassiosira (MDIAT) 0.08%	Gyrodinium (>10um) (DINO) 2.32%	Pyramimonas (GRN) 0.60%	Navicula sp. (<10um) (FDIAT) 2.08%)
	Gyrodinium (>10um) (DINO) 0.06%	Navicula sp. (<10um) (FDIAT) 1.91%	Plagioselmis (DINO) 0.57%	Cyclotella (MDIAT) 1.91%)

Figure A.1: From Hipsey et al. (2016b) Summary of the dominant phytoplankton species by cell count, identified and quantified for each season and sampling site.

	Summer	Autumn	Winter	Spring
BLA	Ceratium furca (DINO) 59.63%	Skeletonema costatum (MDIAT) 65.50%	Cyclotella (MDIAT) 67.53%	Skeletonema costatum (MDIAT) 52.43%)
	Cyclotella (MDIAT) 12.12%	Gyrodinium (>10um) (DINO) 4.73%	Skeletonema costatum (MDIAT) 28.55%	Cyclotella (MDIAT) 32.30%)
	Coscinodiscus (MDIAT) 4.12%	Ceratium furca (DINO) 3.18%	Plagioselmis (DINO) 0.56%	GKC (DINO) 4.12%)
	Prorocentrum micans (DINO) 2.97%	Chaetoceros curvateus (MDIAT) 3.17%	GKC (DINO) 0.53%	Polykrikos (DINO) 1.79%)
	Prorocentrum dentatum (DINO) 2.39%	GKC (DINO) 3.01%	Cyclotella / Thalassiosira (MDIAT) 0.36%	Scrippsiella trochoidea (DINO) 1.65%)
	Katodinium (small) (DINO) 1.88%	passive chlorophyte (<3um) (GRN) 2.61%	Heterocapsa (>10um) (DINO) 0.31%	Cyclotella / Thalassiosira (MDIAT) 1.51%)
	Thalassiosira (MDIAT) 1.86%	Protoperidium pentagonum (DINO) 2.59%	Gyrodinium (>10um) (DINO) 0.27%	Chaetoceros (chains) (MDIAT) 1.15%)
	Peridinium (DINO) 1.68%	Naviculoid (>10um) (FDIAT) 2.15%	Coscinodiscus (MDIAT) 0.24%	Gymnodinium (small) (DINO) 1.04%)
	Naviculoid (>10um) (FDIAT) 1.60%	Peridinium (DINO) 1.74%	Teleaulax (DINO) 0.18%	Peridinium (DINO) 0.71%)
	Chlamydomonas (GRN) 1.48%	Teleaulax (DINO) 1.33%	Naviculoid (>10um) (FDIAT) 0.17%	Naviculoid (>10um) (FDIAT) 0.50%)
ARM	Ceratium furca (DINO) 41.88%	Skeletonema costatum (MDIAT) 48.23%	Cyclotella (MDIAT) 76.14%	Cyclotella (MDIAT) 56.41%)
	Cyclotella (MDIAT) 34.01%	Ceratium furca (DINO) 11.79%	Skeletonema costatum (MDIAT) 15.28%	Polykrikos (DINO) 16.69%)
	Coscinodiscus (MDIAT) 3.95%	Gyrodinium (>10um) (DINO) 9.70%	Polykrikos (DINO) 2.16%	Skeletonema costatum (MDIAT) 13.03%)
	Gyrodinium (>10um) (DINO) 3.17%	Coscinodiscus (MDIAT) 7.77%	Protoperidium pentagonum (DINO) 1.51%	GKC (DINO) 3.55%)
	Peridinium (DINO) 2.60%	Prorocentrum micans (DINO) 4.27%	Gyrodinium (>10um) (DINO) 0.68%	Gyrodinium (>10um) (DINO) 2.25%)
	Prorocentrum micans (DINO) 2.30%	Prorocentrum dentatum (DINO) 4.00%	Plagioselmis (DINO) 0.63%	Coscinodiscus (MDIAT) 1.80%)
	Prorocentrum dentatum (DINO) 1.47%	GKC (DINO) 2.65%	GKC (DINO) 0.58%	Chaetoceros (chains) (MDIAT) 1.06%)
	Thalassionema (MDIAT) 1.11%	Chaetoceros curvateus (MDIAT) 0.98%	Scrippsiella trochoidea (DINO) 0.45%	Scrippsiella trochoidea (DINO) 0.72%)
	Naviculoid (>10um) (FDIAT) 1.08%	Protoperidium pentagonum (DINO) 0.93%	Cyclotella / Thalassiosira (MDIAT) 0.31%	Teleaulax (DINO) 0.59%)
	GKC (DINO) 1.02%	Cyclotella / Thalassiosira (MDIAT) 0.80%	Teleaulax (DINO) 0.30%	others (Hetero/Gymno - shrunk) (DINO) 0.57%)
NAR	Cyclotella (MDIAT) 57.13%	Prorocentrum dentatum (DINO) 33.41%	Cyclotella (MDIAT) 88.68%	Cyclotella (MDIAT) 41.59%)
	Skeletonema costatum (MDIAT) 23.32%	GKC (DINO) 21.81%	Skeletonema costatum (MDIAT) 4.53%	Scrippsiella trochoidea (DINO) 11.83%)
	GKC (DINO) 2.00%	Skeletonema costatum (MDIAT) 19.88%	Plagioselmis (DINO) 0.98%	Skeletonema costatum (MDIAT) 9.56%)
	Rhizosolenia (MDIAT) 1.96%	Akashiwo sanguineum (DINO) 8.16%	Gymnodinium (small) (DINO) 0.73%	Polykrikos (DINO) 8.58%)
	Gyrodinium (>10um) (DINO) 1.80%	Gyrodinium (>10um) (DINO) 6.73%	Naviculoid (>10um) (FDIAT) 0.70%	Protoperidium pentagonum (DINO) 7.19%)
	Peridinium (DINO) 1.58%	Prorocentrum micans (DINO) 2.38%	Cyclotella / Thalassiosira (MDIAT) 0.69%	GKC (DINO) 6.17%)
	Protoperidium pentagonum (DINO) 1.43%	Protoperidium pentagonum (DINO) 1.12%	Prorocentrum micans (DINO) 0.65%	Gymnodinium (small) (DINO) 3.20%)
	Gonyaulax (DINO) 1.33%	Scrippsiella trochoidea (DINO) 0.97%	Gyrodinium (>10um) (DINO) 0.59%	Gymnodinium (Medium) (DINO) 1.78%)
	Scrippsiella trochoidea (DINO) 0.97%	Cyclotella / Thalassiosira (MDIAT) 0.74%	Protoperidium pentagonum (DINO) 0.49%	Entomoneis (MDIAT) 1.08%)
	Naviculoid (>10um) (FDIAT) 0.82%	Gymnodinium (Medium) (DINO) 0.69%	Cryptomonas (DINO) 0.29%	Gyrodinium (>10um) (DINO) 1.02%)
STJ	Skeletonema costatum (MDIAT) 22.00%	Skeletonema costatum (MDIAT) 38.72%	Cyclotella (MDIAT) 83.22%	Cyclotella (MDIAT) 79.95%)
	Cyclotella (MDIAT) 19.96%	Prorocentrum dentatum (DINO) 29.72%	Prorocentrum micans (DINO) 2.24%	Skeletonema costatum (MDIAT) 7.31%)
	Peridinium (DINO) 18.58%	Prorocentrum micans (DINO) 6.88%	Naviculoid (>10um) (FDIAT) 1.92%	Peridinium (DINO) 3.38%)
	Gyrodinium (>10um) (DINO) 8.85%	Gyrodinium (>10um) (DINO) 4.10%	Heterocapsa (>10um) (DINO) 1.88%	GKC (DINO) 2.23%)
	Alexandrium (DINO) 5.38%	GKC (DINO) 3.98%	Gymnodinium (small) (DINO) 1.55%	Entomoneis (MDIAT) 1.31%)
	Chlamydomonas (GRN) 4.81%	Akashiwo sanguineum (DINO) 3.50%	Gyrodinium (>10um) (DINO) 1.23%	Cryptomonas (DINO) 0.93%)
	Heterocapsa (<10um) (DINO) 3.08%	Scrippsiella trochoidea (DINO) 2.34%	Tetraselmis (GRN) 0.86%	Plagioselmis (DINO) 0.93%)
	Scrippsiella trochoidea (DINO) 2.89%	Protoperidium pentagonum (DINO) 1.90%	Protoperidium pentagonum (DINO) 0.84%	Gyrodinium (>10um) (DINO) 0.77%)
	Gymnodinium (small) (DINO) 2.75%	Cyclotella / Thalassiosira (MDIAT) 1.75%	GKC (DINO) 0.82%	Gymnodinium (small) (DINO) 0.73%)
	Naviculoid (>10um) (FDIAT) 2.09%	Coscinodiscus (MDIAT) 1.23%	Polykrikos (DINO) 0.80%	Naviculoid (>10um) (FDIAT) 0.53%)
KIN	Chlamydomonas (GRN) 36.05%	Polykrikos (DINO) 24.68%	Cyclotella (MDIAT) 89.41%	Cyclotella (MDIAT) 31.16%)
	Scrippsiella trochoidea (DINO) 30.27%	Gyrodinium (>10um) (DINO) 14.10%	GKC (DINO) 2.22%	Cryptomonas (DINO) 16.99%)
	Cyclotella (MDIAT) 16.16%	Skeletonema costatum (MDIAT) 14.04%	Naviculoid (>10um) (FDIAT) 2.11%	Scrippsiella trochoidea (DINO) 13.99%)
	Cryptomonas (DINO) 3.65%	Scrippsiella trochoidea (DINO) 7.80%	Gymnodinium (small) (DINO) 1.44%	Naviculoid (>10um) (FDIAT) 13.95%)
	Euglena (DINO) 2.62%	Akashiwo sanguineum (DINO) 7.10%	Cyclotella / Thalassiosira (MDIAT) 0.70%	Gymnodinium (Medium) (DINO) 4.77%)
	Prorocentrum cordatum (DINO) 2.17%	Cyclotella (MDIAT) 4.90%	Gyrodinium (>10um) (DINO) 0.69%	Gymnodinium (small) (DINO) 4.04%)
	Gyrodinium (>10um) (DINO) 1.55%	Gymnodinium (small) (DINO) 4.17%	Plagioselmis (DINO) 0.66%	GKC (DINO) 3.87%)
	Peridinium (DINO) 1.28%	Prorocentrum cordatum (DINO) 3.20%	Cylindrotheca closterium (MDIAT) 0.28%	passive chlorophyte (<3um) (GRN) 1.66%)
	Skeletonema costatum (MDIAT) 1.16%	Cyclotella / Thalassiosira (MDIAT) 2.86%	Navicula sp. (<10um) (FDIAT) 0.27%	Navicula sp. (<10um) (FDIAT) 1.49%)
	Gymnodinium (Medium) (DINO) 0.82%	Prorocentrum micans (DINO) 2.83%	Oxyrrhis marina (DINO) 0.26%	Entomoneis (MDIAT) 1.27%)
SUC	Chlamydomonas (GRN) 50.90%	Prorocentrum cordatum (DINO) 25.31%	Cyclotella (MDIAT) 92.86%	Cyclotella (MDIAT) 33.57%)
	Cyclotella (MDIAT) 18.21%	Gyrodinium (>10um) (DINO) 23.00%	Cylindrotheca closterium (MDIAT) 1.71%	Cryptomonas (DINO) 32.91%)
	Scrippsiella trochoidea (DINO) 9.66%	Cyclotella / Thalassiosira (MDIAT) 9.17%	Naviculoid (>10um) (FDIAT) 1.34%	Naviculoid (>10um) (FDIAT) 11.14%)
	Peridinium (DINO) 8.16%	Skeletonema costatum (MDIAT) 8.97%	Gymnodinium (small) (DINO) 1.21%	GKC (DINO) 4.19%)
	Euglena (DINO) 4.09%	Rhizosolenia (MDIAT) 8.09%	GKC (DINO) 0.68%	Gymnodinium (small) (DINO) 2.61%)
	Skeletonema costatum (MDIAT) 3.85%	GKC (DINO) 4.29%	Cyclotella / Thalassiosira (MDIAT) 0.51%	passive chlorophyte (<3um) (GRN) 2.40%)
	Gyrodinium (>10um) (DINO) 1.10%	Polykrikos (DINO) 3.61%	Gyrodinium (>10um) (DINO) 0.29%	Gymnodinium (Medium) (DINO) 2.33%)
	Naviculoid (>10um) (FDIAT) 1.05%	Prorocentrum micans (DINO) 3.34%	Synedra (MDIAT) 0.20%	Peridinium (DINO) 1.80%)
	Entomoneis (MDIAT) 0.69%	Gyrodinium (<10um) (DINO) 2.75%	Plagioselmis (DINO) 0.16%	Navicula sp. (<10um) (FDIAT) 1.64%)
	GKC (DINO) 0.47%	Scrippsiella trochoidea (DINO) 1.55%	Oxyrrhis marina (DINO) 0.16%	Heterocapsa (>10um) (DINO) 1.35%)

Figure A.2: From Hipsey et al. (2016b) Summary of the dominant phytoplankton species by cell count, identified and quantified for each season and sampling site.

Appendix B

Software and Data Processing Scripts

B.1 DalecOnTransect

DalecOnTransect was written in C# and used to operate the DALEC. The software logged all of the data the DALEC and ancillary instruments (GPS & compass) produced, as well as, sending driver instructions to the DALEC radiometer.

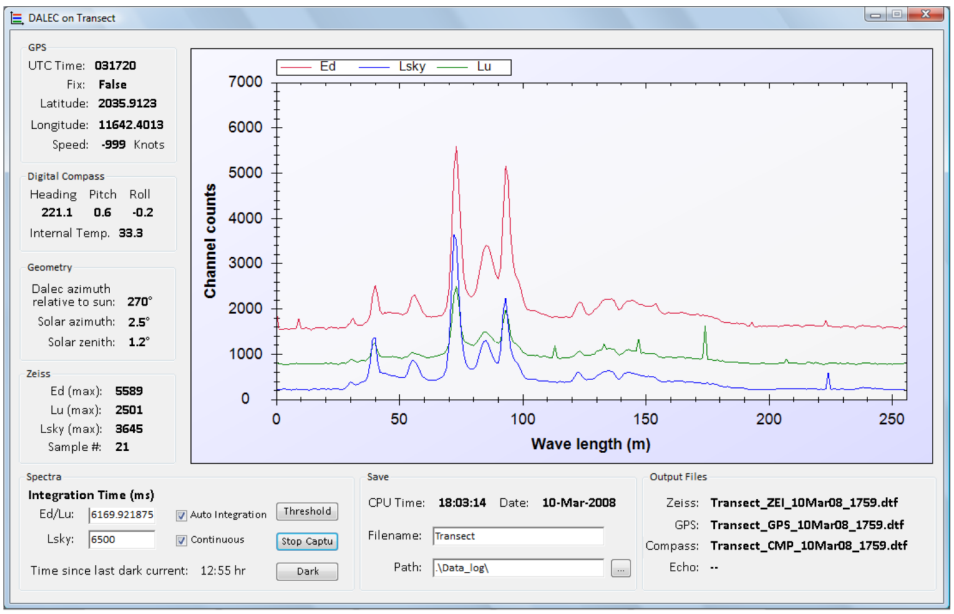

Figure B.1: The user interface for the software written to operate the DALEC. All of the plots and telemetry are updated in real time.

B.2 DalecPPT

DalecPPT was developed in Python and contains the tools for: calibrating the DAELC; Inverting the remote sensing reflectance; mapping the results and, compiling the reports. The software includes a simpl GUI that allows users to visualise the data. The source code is hosted at `https://launchpad.net/dalecppt` and is free to download and use.

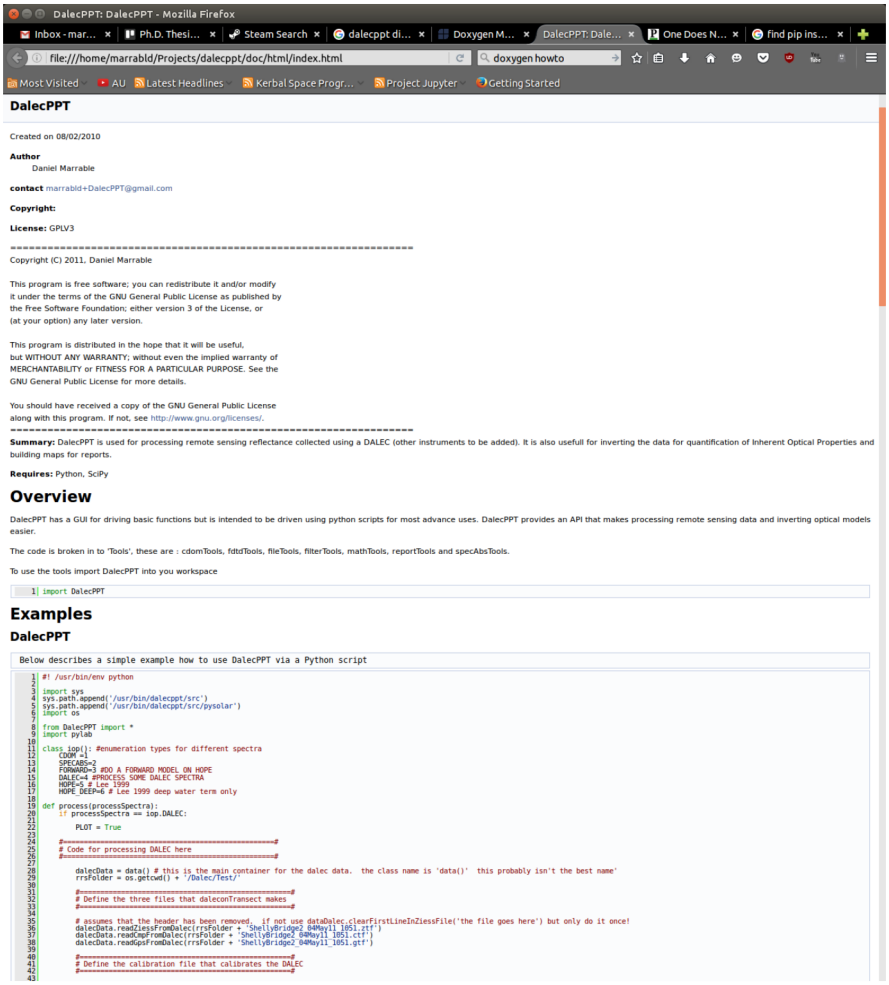

Figure B.2: The community web page with instructions on how to download and use the software.

DalectPPT also includes tools for batch running RTCode for and processing the outputs from its simulations.

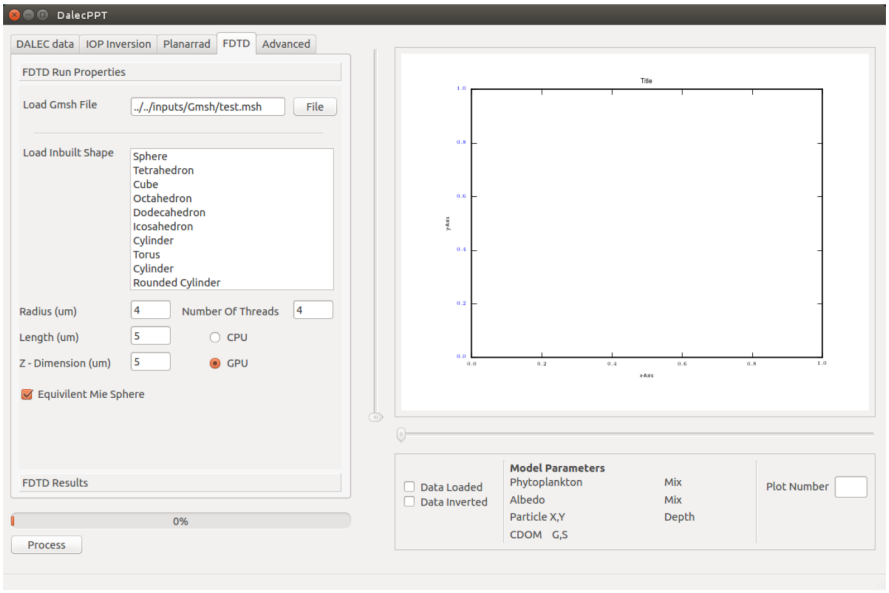

Figure B.3: The user interface for the software written to parse the inputs and outputs to FDTD. The tool is most often driven by scripting. The GUI is useful for visualising outputs and debugging.

B.3 Planarradpy

Planarradpy was written in Python in order to batch run and batch process the outputs from PlanarRad. The tool can be driven by parsing batch scripts or via the GUI. The reports can also be visualised in the GUI. PlanarRad has a small community of users that have made a number of meaningful contributions to the project. The community page with instructions on how to download and use the tool can be found at `https://marrabld.github.io/planarradpy/`

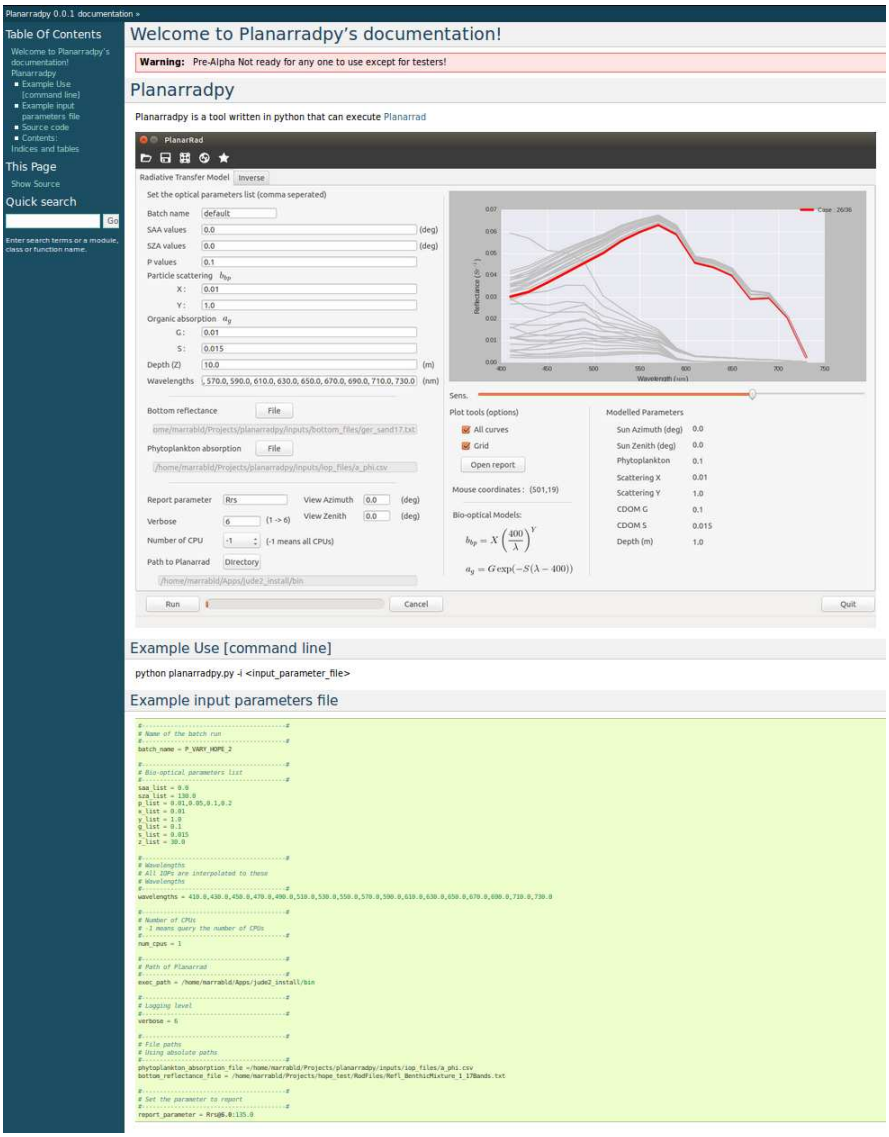

Figure B.4: Community web for Planarradpy. The page includes instructions for use as well as links to the source code hosted on github.

B.4 Bootstrappy

The code for using the coherent noise model can be found at `https://github.com/marrabld/bootstrappy`, and a Jupyter notebook with an example and instructions on how to use the tools at `http://goo.gl/Qht2zh`

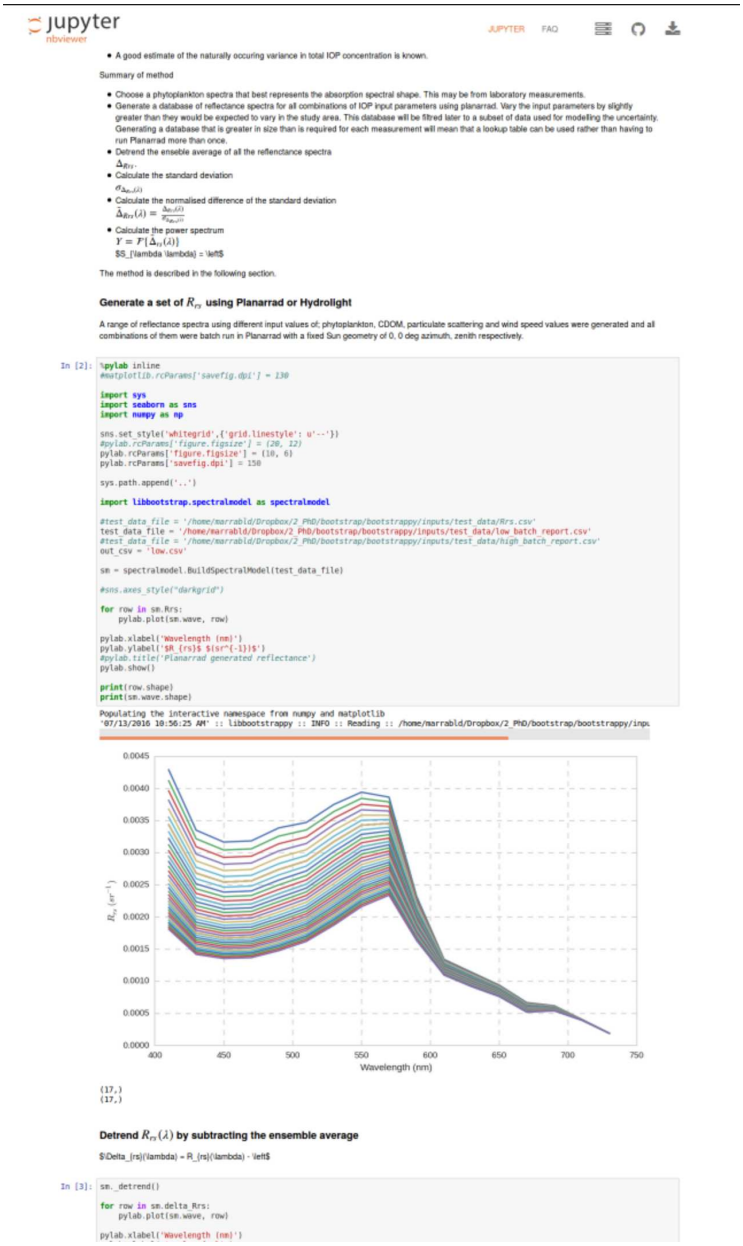

Figure B.5: Jupyter notebook with examples of how to use the coherent noise model of uncertainty estimates.

B.5 DALEC and Boat Mount

The DALEC in used in this thesis shows the instrument and boat–mount.

Figure B.6: DALEC mount.

Appendix C

Coherent Noise Model

The method of using Planarrad to train the coherent noise model, when multiple field measurements are unavailable, is described in the following section.

C.1 Training Stage

A range of reflectance spectra using different input values of phytoplankton, CDOM, particulate scattering and wind speed values were generated and all combinations of them were batch run in PlanarRad with a fixed sun geometry of 0, 0 degrees azimuth, zenith, respectively.

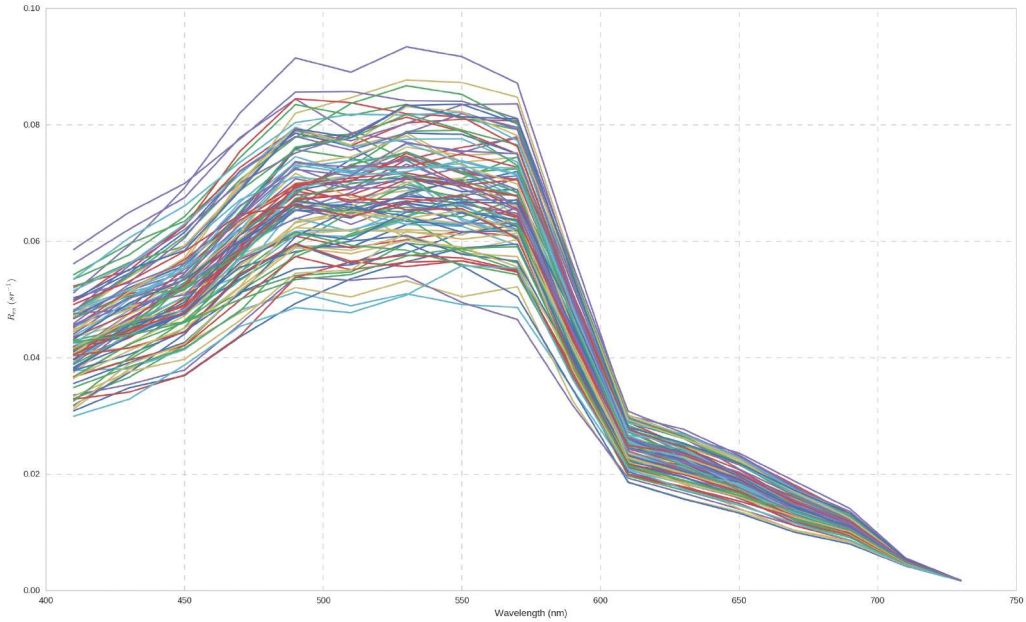

Figure C.1: Spectra generated by running PlanarRad many times and changing the $a_\phi(440)$ and $a_g(400)$ concentrations.

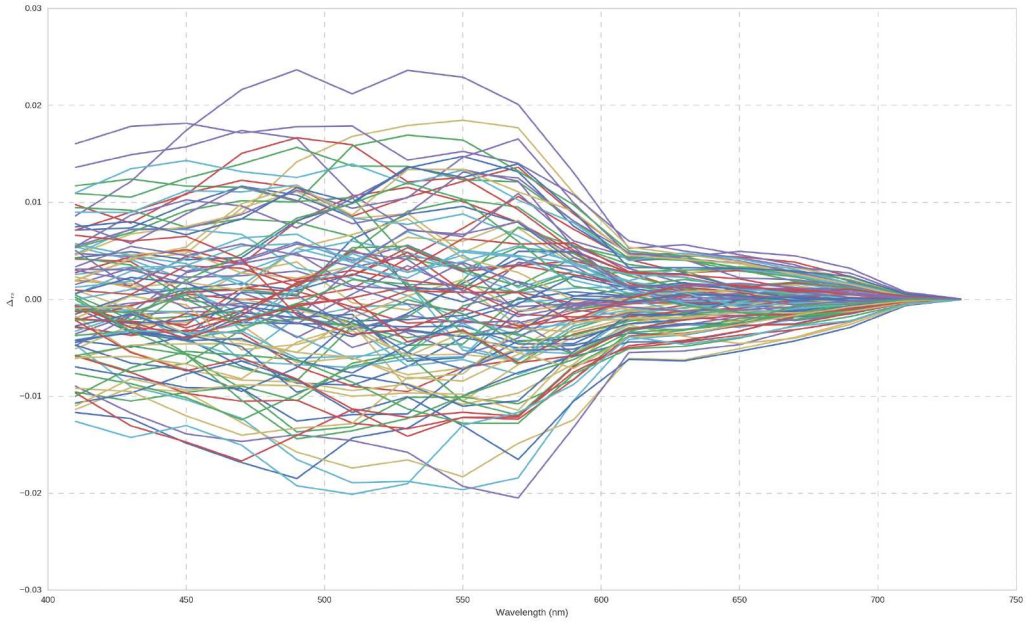

Figure C.2: The R_{rs} after detrending by subtracting the mean reflectance of the ensemble average.

Detrend $R_{rs}(\lambda)$ by subtracting the ensemble average:

$$\Delta_{rs}(\lambda) = R_{rs}(\lambda) - \langle R_{rs}(\lambda) \rangle \tag{C.1}$$

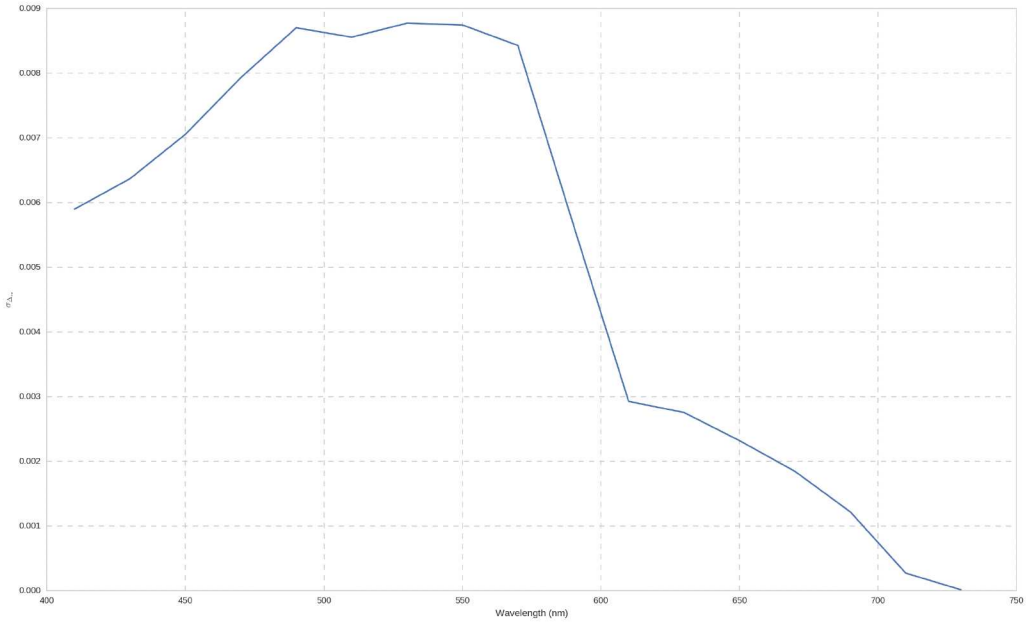

Figure C.3: The standard deviation of the detrended ensemble average.

Calculate standard deviation of $\Delta_{rs}(\lambda)$:

$$\sigma_{\Delta_{rs}(\lambda)} \tag{C.2}$$

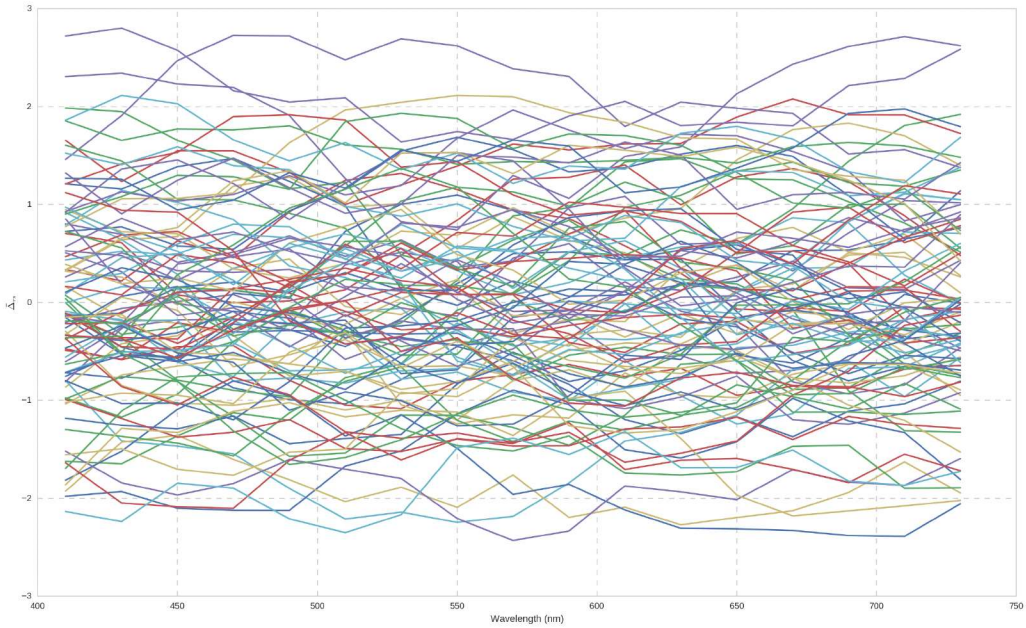

Figure C.4: The stationary reflectance normalised by dividing each spectra by the standard deviation.

Calculate the normalised difference.

This step is to make sure the data is 'stationary':

$$\bar{\Delta}_{rs}(\lambda) = \frac{\Delta_{rs}(\lambda)}{\sigma_{\Delta_{rs}(\lambda)}} \tag{C.3}$$

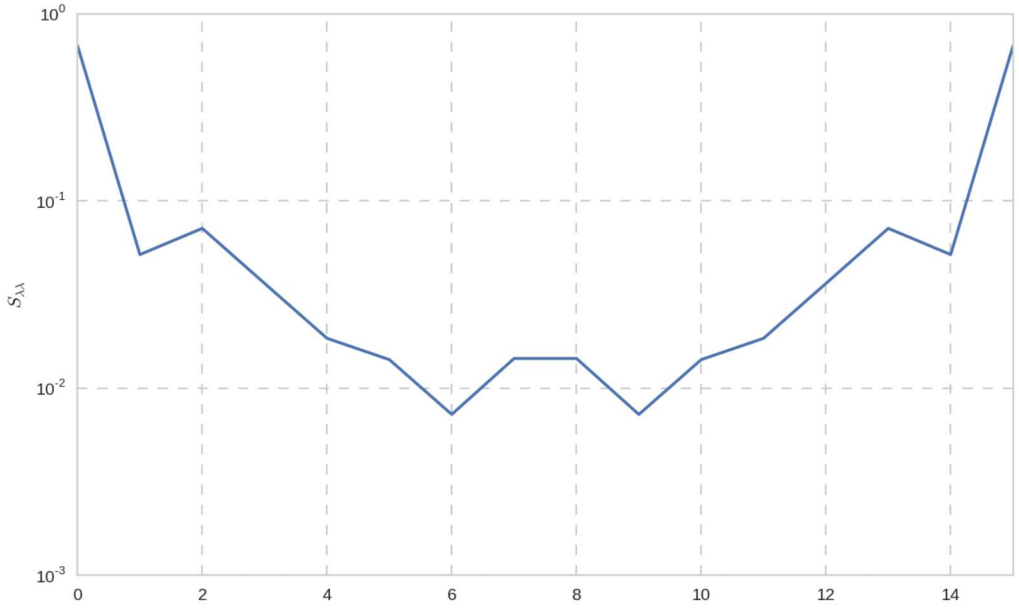

Figure C.5: The power spectrum of the ensemble.

Calculate the power spectrum

The power spectrum is calculated by multiplying the Fourier transform of normalised difference ($\bar{\Delta}_{rs}$) with the complex conjugate of itself and averaging the results:

$$Y = \mathcal{F}\{\bar{\Delta}_{rs}(\lambda)\} \tag{C.4}$$

$$S_{\lambda\lambda} = \langle YY^* \rangle \tag{C.5}$$

The resulting power spectrum is used in later steps to generate a correlated noise model in which realisation of R_{rs} will be generated.

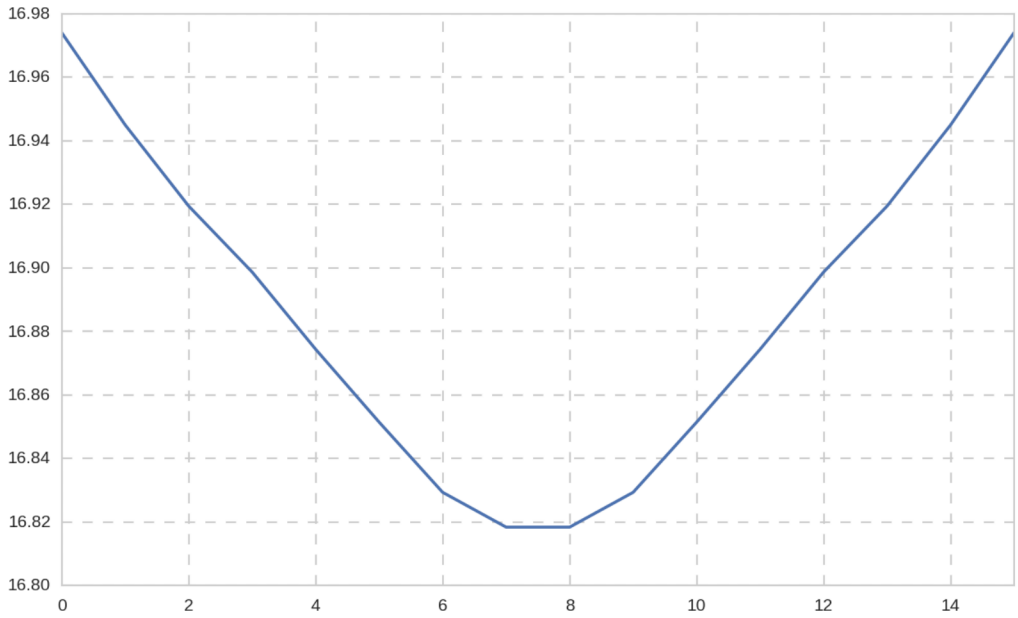

Figure C.6: The correlation function of the ensemble.

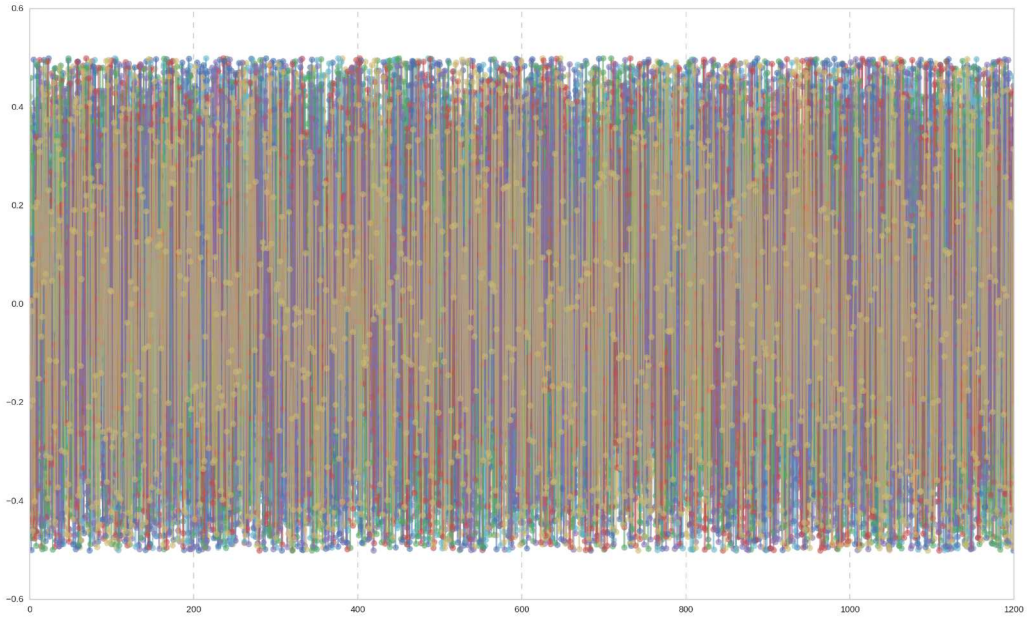

Figure C.7: Random data points generated for each spectra at each wavelength.

C.2 Generation Stage

For each wavelength we wish to randomly generate a value within the defined variance of that wavelength. To do this, first generate random numbers n between -0.5 and 0.5. As a first approximation, a Gaussian distribution can be used but the distribution that is used should conform to the distribution that the IOPs conform too. This is usually unknown without lots of repeat measurements, so a normal distribution is used as a first guess. These random values will later be scaled by the power spectrum.

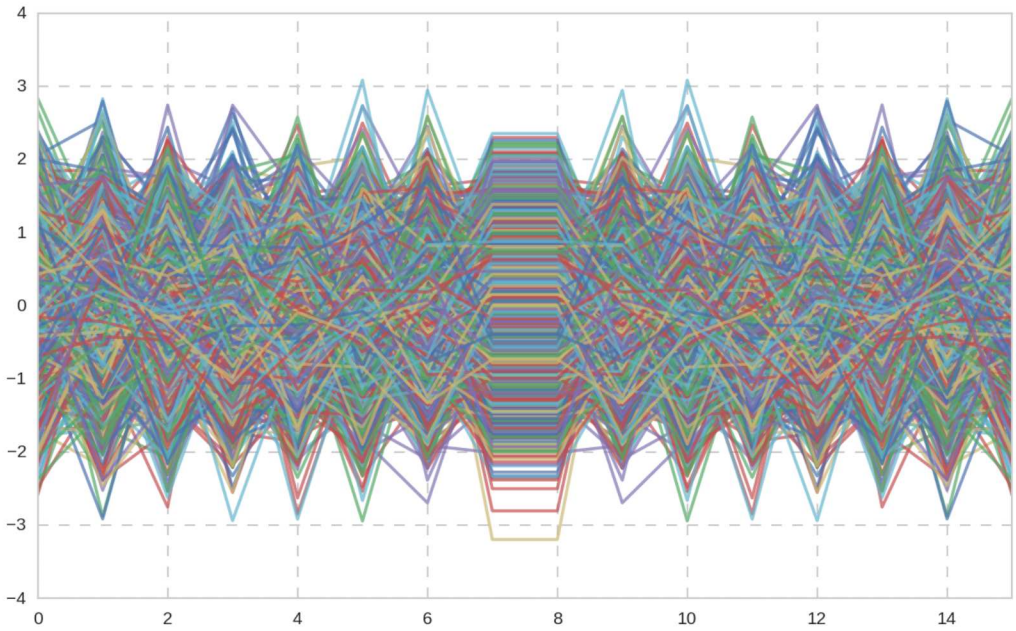

Figure C.8: The random point transformed to the Fourier domain by taking the FFT of the random points.

Calculate the FFT of n

Before the random values can be scaled by the power spectrum they must first be transformed into the Fourier domain by taking the fast Fourier transform of the randomly generated numbers.

$$N = \mathcal{F}\{n\} \tag{C.6}$$

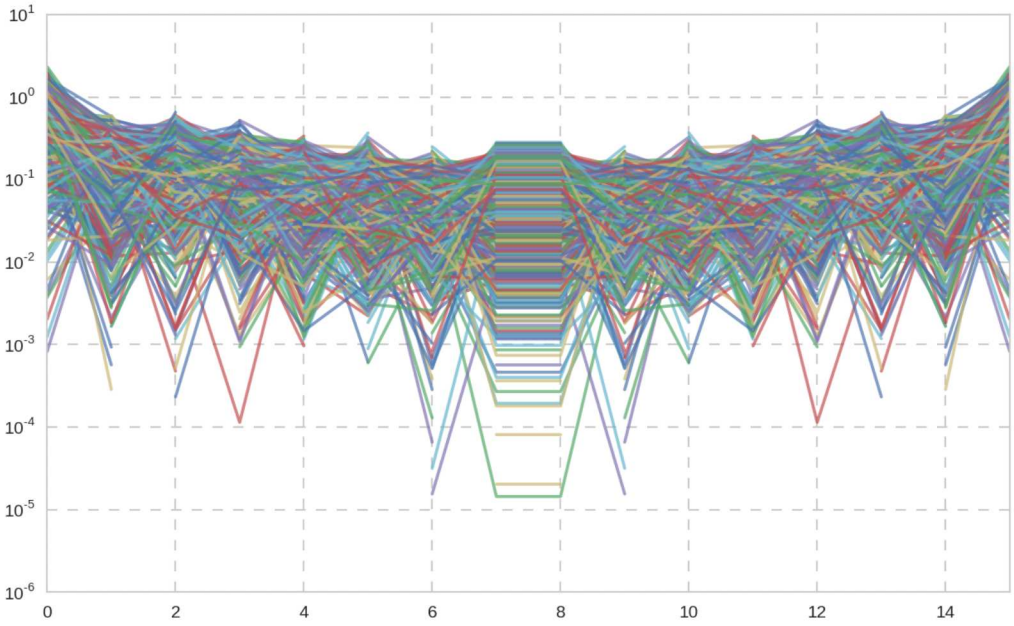

Figure C.9: The Fourier transform of the randomly generated points multiplied by the power spectrum.

Multiply the FFT of n by the square root of the power spectrum

Now that the random numbers are in the Fourier domain they are multiplied by the square of the power spectrum in order to scale them. The result is correlated noise in the Fourier domain:

$$Y = N \times \sqrt{S_{\lambda\lambda}} \tag{C.7}$$

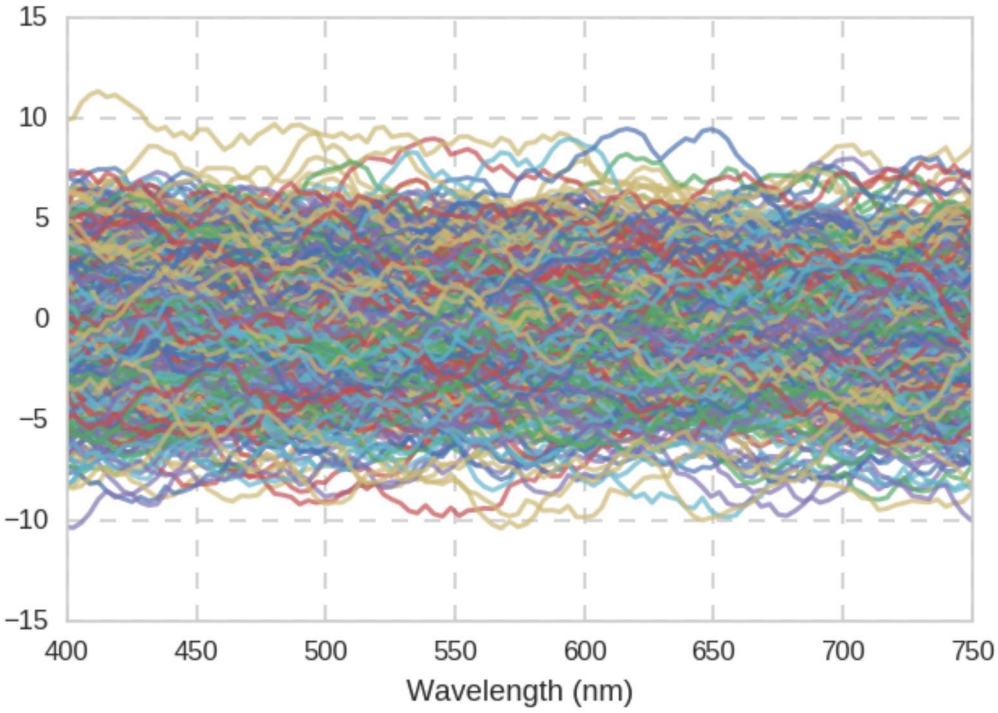

Figure C.10: The correlated noise transformed back to the real domain by taking the inverse Fourier transform.

The resulting correlated noise (Y) is transformed back to the real domain ($y(\lambda)$) by calculating the inverse Fourier transform:

$$y(\lambda) = \mathcal{F}^{-1}\{Y\} \tag{C.8}$$

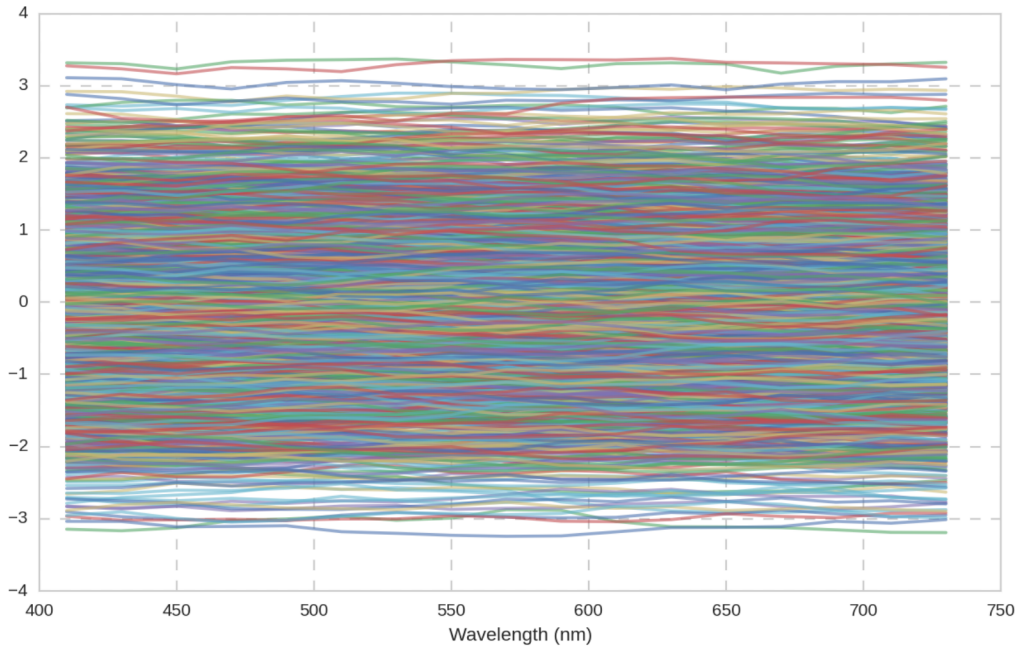

Figure C.11: Normalised correlated noise calculated by dividing by the standard deviation.

Normalise the difference

All the wavelengths of the correlated noise in the real domain must have a standard deviation of 1 so that they can be multiplied by the standard deviation of the original R_{rs}. This is done by dividing $y(\lambda)$ by the standard deviation of itself:

$$\bar{y}(\lambda) = \frac{y(\lambda)}{\sigma_y} \tag{C.9}$$

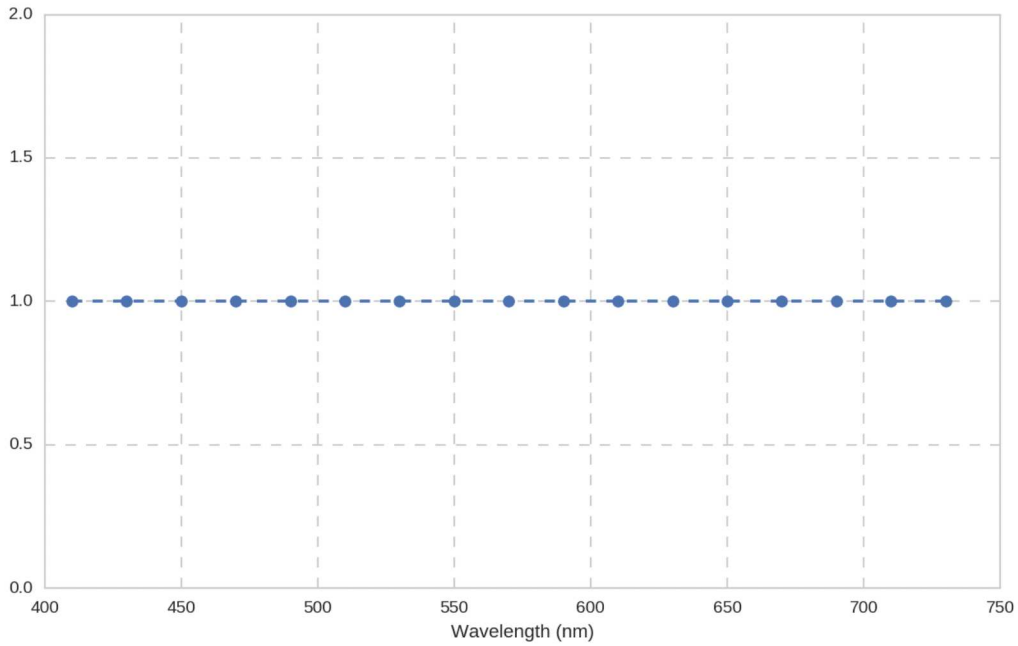

Figure C.12: The standard deviation of the normalised correlated noise. All wavelengths should be 1. This step is taken to ensure that the process has been followed correctly so far.

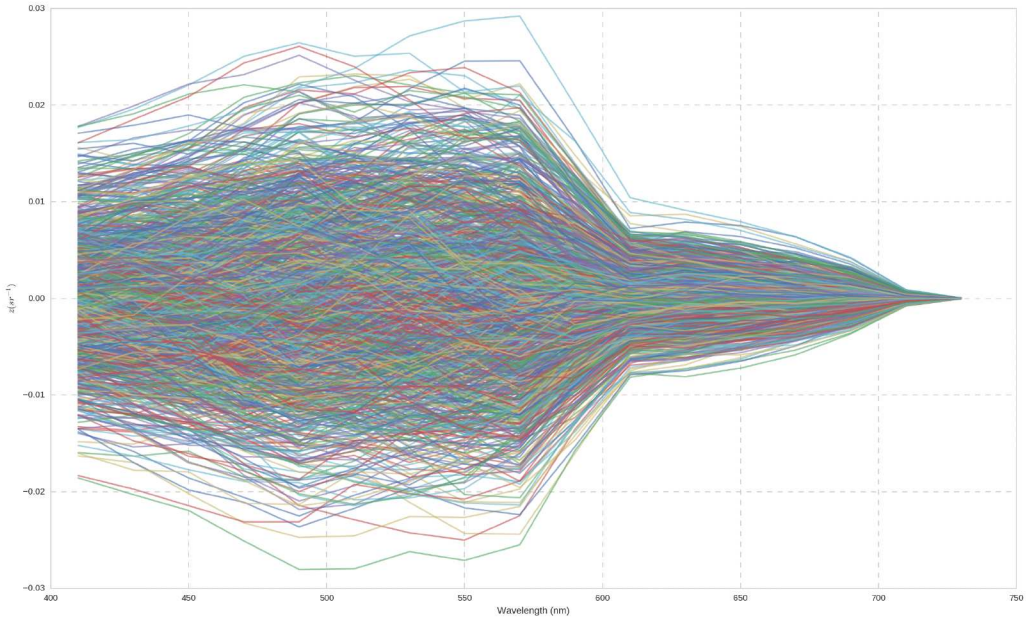

Figure C.13: The detrended simulated reflectance data created by multiplying the normalised correlated noise by the standard deviation of the simulated R_{rs}.

The standard deviation of the modelled R_{rs} is multiplied by the normalised correlated noise:

$$z(\lambda) = \bar{y}(\lambda)\sigma_{\Delta_{rs}(\lambda)} \tag{C.10}$$

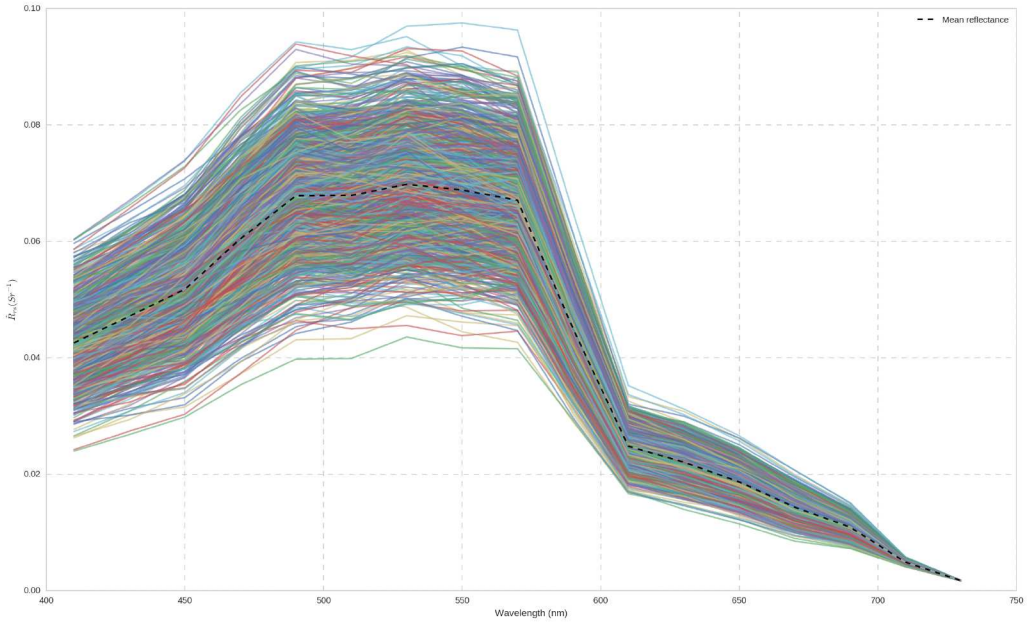

Figure C.14: Simulated remote sensing reflectance generated by multiplying the detrended simulated reflectance by the reflectance spectra.

Generate a realisation of R_{rs} by adding back the mean value subtracted in step 2 of defining the noise model:

$$\hat{R}_{rs}(\lambda) = \langle R_{rs}(\lambda) \rangle + z(\lambda) \tag{C.11}$$

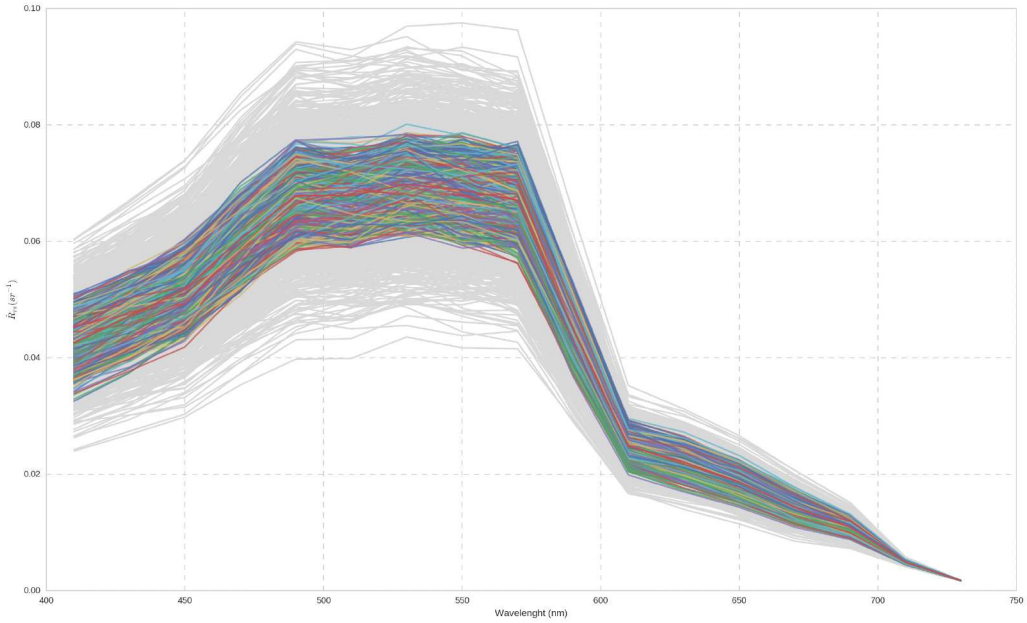

Figure C.15: Optionally, the simulated reflectance data is filtered to further reduce the simulated data to fall within expected field measurements of reflectance data.

Filter the reflectances

This is more variance in our reflectance than expected from a single measurement. This data is useful as a sensitivity analysis only. A typical reflectance variance for a single sample site is approximately 1.5%. Reflectances are identified in the ensemble that are within those bounds and only those are inverted using a deepwater analytical model.

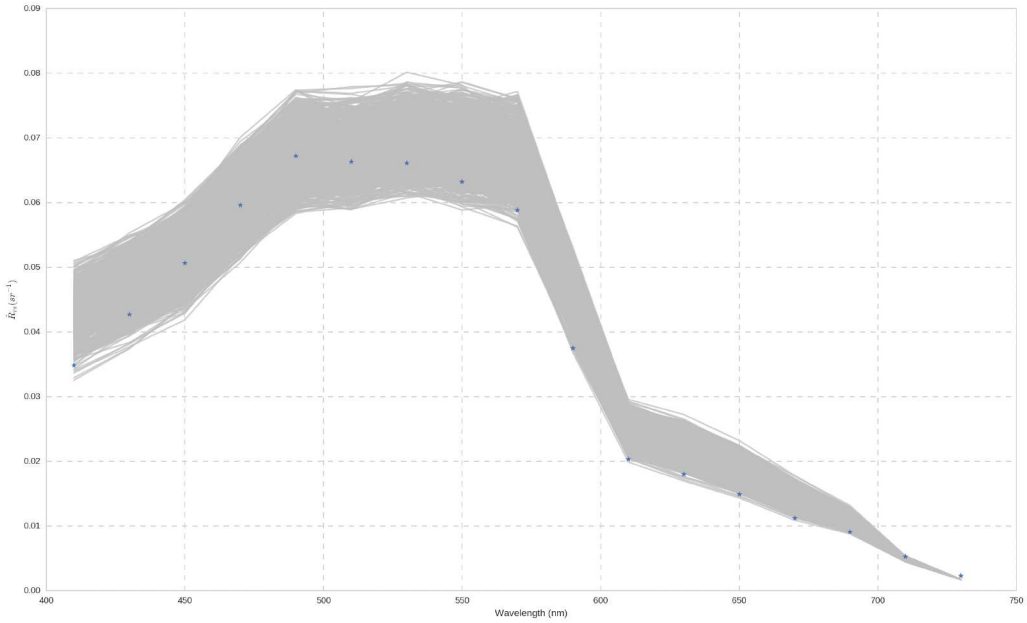

Figure C.16: The mean inverted IOP values calculated from the ensemble synthetic data used to forward model the remote sensing reflectance, shown in blue dots. The mean reflectance plotted over the top of the ensemble synthetic data.

C.3 Solution Stage

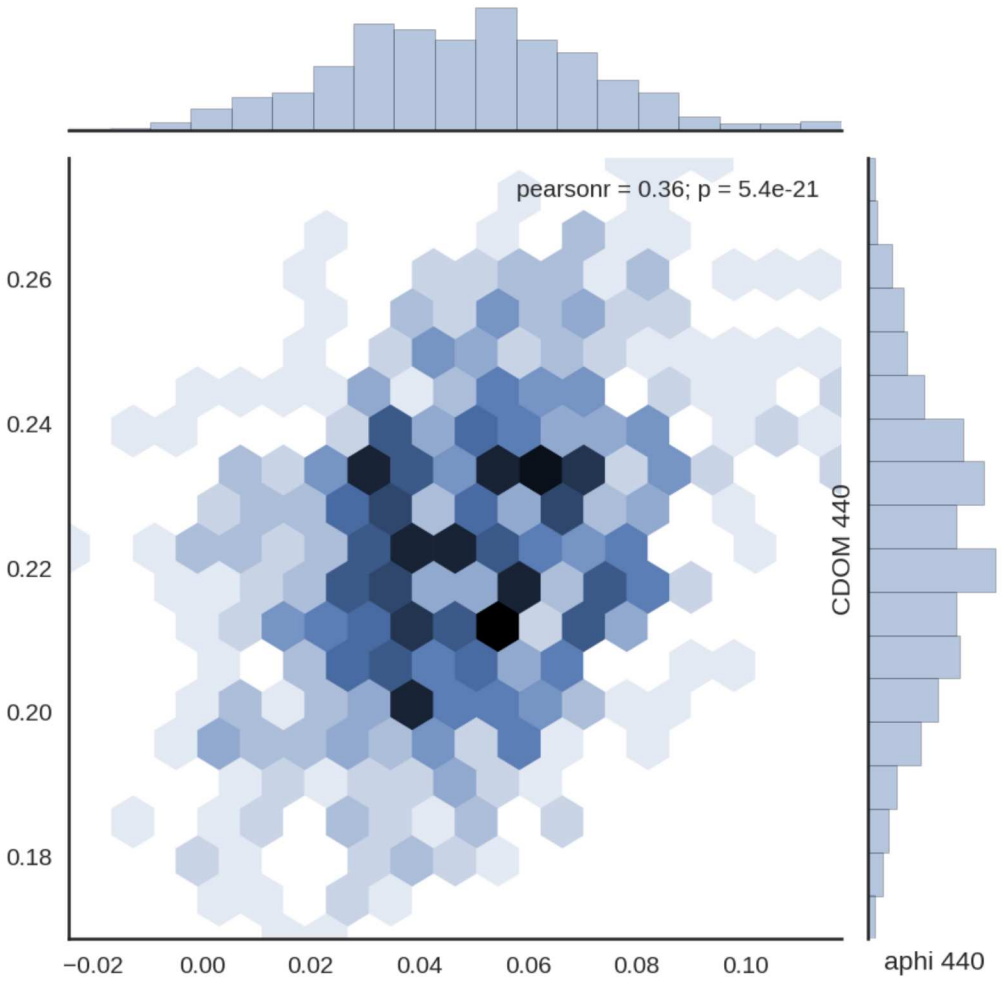

Figure C.17: Scatter 'Hex' plot of $a_\phi(440)$ versus $a_g(400)$ on the x and y axis. The distribution of each IOP is shown top and right.

References

Aarup, T., S. Groom, and P. Holligan (1989). CZCS imagery of the North Sea. Remote sensing of atmosphere and oceans. *Advances in Space Research 9*, 443–451.

Aden, A. L. and M. Kerker (1951). Scattering of Electromagnetic Wave from Two Concentric Spheres. *Journal of Applied Physics*.

Adeney, J. A. (2001). Cyanobacterial Issues in the Lake Powell / Torbay Inlet Drainage System. *CSIRO Land and Water*. Technical Report, prepared for the Water and Rivers Commission, Western Australia. CSIRO Land and Water. Perth, Western Australia.

Aiken, J., G. Moore, and P. Holligan (1992). Remote sensing of oceanic biology in relation to global climate change. *Journal of Phycology 28*, 579–590.

Allan, M. G., D. P. Hamilton, B. Hicks, and L. Brabyn (2015). Empirical and semi-analytical chlorophyll a models for multi-temporal monitoring of New Zealand lakes using Landsat. *Environmental Monitoring and Assessment 187*, 364.

Andersen, R. A. (2005). *Algal Culturing Techniques*. Academic Press. Boston MA.

Anderson, D. M., P. Gilbert, and J. M. Burkholder (2002). Harmful algal blooms and eutrophication: nutrients sources, composition, and consequences. *Estuaries 25(4)*, 704–726.

Antoine, D., D. A. Siegel, T. Kostadinov, S. Maritorena, N. B. Nelson, B. Gentili, V. Vellucci, and N. Guillocheau (2011). Variability in optical particle backscattering in contrasting bio-optical oceanic regimes. *Limnology and Oceanography 56*, 955–973.

Aurin, D. A. and H. M. Dierssen (2012). Advantages and limitations of ocean color remote sensing in CDOM-dominated, mineral-rich coastal and estuarine waters. *Remote Sensing of Environment 125*, 181–197.

Bader, H. (1970). The hyperbolic distribution of particle sizes. *Journal of Geophysical Research 75*, 2822–2830.

Baird, M. E., N. Cherukuru, E. Jones, N. Margvelashvili, M. Mongin, K. Oubelkheir, P. J. Ralph, F. Rizwi, B. J. Robson, T. Schroeder, J. Skerratt, A. D. Steven, and K. A. Wild-Allen (2016). Remote-sensing reflectance and true colour produced by a coupled hydrodynamic, optical, sediment, biogeochemical model of the Great Barrier Reef, Australia: Comparison with satellite data. *Environmental Modelling & Software 78*, 79 – 96.

Barker, K. (Ed.) (2013a). *In-situ Measurement Protocols. Part A: Apparent Optical Properties*, Volume CO-SCI-ARG-TN-008. ARGANS Ltd, UK, and ACRI-ST, France.

Barker, K. (Ed.) (2013b). *In-situ Measurement Protocols. Part B: Inherent Optical Properties and in-water constituents*, Volume CO-SCI-ARG-TN-008. ARGANS Ltd, UK and ACRI-ST, France.

Barsanti, L. and P. Guarltieri (2006). *Algae: Anatomy, Biochemistry and Biotechnology*. CRC Press, Taylor and Francis Group. Boca Raton, FL.

Bastviken, D., L. Tranvik, J. Downing, P. Crill, and A. Anrich-Prast (2011). Freshwater methane emissions offset the continental carbon sink. *Science 331*, 50.

Billy, G. (1986). *Rationale for sampling and interpretation of ecological data in the assessment of freshwater ecosystems: a symposium sponsored by ASTM Committee D-19 on Water*. ASTM International.

Bohren, C. F. and D. R. Huffman (1983). *Absorption and Scattering of Light by Small Particles*. John Wiley & Sons, Inc. New York.

Bracher, A., H. A. Bouman, R. J. W. Brewin, A. Bricaud, V. Brotas, A. M. Ciotti, L. Clementson, E. Devred, A. D. Cicco, S. Dutkiewicz, N. J. Hardman-Mountford, A. E. Hickman, M. Hieronymi, T. Hirata, S. N. Losa, C. B. Mouw, E. Organelli, D. E. Raitsos, J. Uitz, M. Vogt, and A. Wolanin (2017). Obtaining Phytoplankton Diversity from Ocean Color: A Scientific Roadmap for Future Development. *Frontiers in Marine Science 3*.

Braga, F., V. E.Brando, M. Bresciani, I. Cazzaniga, L. D. Keukelaere, T. Fincke, P. Gege, C. Giardino, A. A. Gilerson, A. A. Gitelson, Y. Huot, K. Y. Kallio, E. Knaeps, S. Koponen, T. Kutser, L. Li, T. J. Malthus, M. W. Matthews, D. R. Mishra, M. J. Montes, W. J. Moses, I. Ogashawara, B. Paavel, K. Song, and S. Sterckx (2017). *Bio-optical Modeling and Remote Sensing of Inland Waters*.

Brando, V. and A. Dekker (2003). Satellite Hyperspectral Remote Sensing for Estimating Estuarine and Coastal Water Quality. *IEEE Transactions on Geoscience and Remote Sensing 41*, 1378–1387.

Brando, V. E., J. L. Lovell, E. A. King, D. Boadle, R. Scott, and T. Schroeder (2016). The Potential of Autonomous Ship-Borne Hyperspectral Radiometers for the Validation of Ocean Color Radiometry Data. *Remote Sensing 8*, 150.

Brando, V. E., J. M. A. M. Wettle, A. G. Dekker, and S. R. P. C. Roelfsema (2009). A physics based retrieval and quality assessment of bathymetry from suboptimal hyperspectral data. *Remote Sensing of Environment*.

Brearley, A. and E. Hodgkin (2005). *Ernest Hodgkin's Swanland: Estuaries and Coastal Lagoons of South-western Australia*. Univiersity of Western Australia Press.

Brewin, B., E. Devred, S. Sathyendranath, S. Lavender, and N. J. Hardman-Mountford (2011). Model of phytoplankton absorption based on three size classes. *Applied Optics 50*, 4535–4549.

Bricaud, A., M. Babin, A. Morel, and H. Claustre (1995). Variability in the chlorophyll-specific absorption coefficient of natural phytoplankton : analysis and parametrization. *Journal of Geophysical Research 100*, 13321–13332.

Bricaud, A., A.-L. Bedhomme, and A. Morel (1988). Optical properties of diverse phytoplankton species: experimental results and theoretical interpretation. *Journal of Plankton Research 10*(5), 85–873.

Bricaud, A., E. Bosc, and D. Antoine (2001). Algal biomass and sea surface temperature in the Mediterranean Basin Intercomparison of data from various satellite sensors, and implications for primary production estimates. *Remote Sensing of Environment 81*, 163 – 178.

Bricaud, A., A. Morel, and L. Prieur (1981). Absorption by dissolved organic matter of the sea (yellow substance) in the UV and visible domains. *Limnology and Oceanography 26*(1), 43–53.

Campbell, G., S. R. Phinn, A. G. Dekker, and V. E. Brando (2011). Remote sensing of water quality in an Australian tropical freshwater impoundment using matrix inversion and MERIS images. *Remote Sensing of Environment 115*(9), 2402 – 2414.

Carder, K. L., F. R. Chen, Z. P. Lee, S. K. Hawks, and D. Kamykowski (1999). Semianalytic Moderate-Resolution Imaging Spectrometer algorithms for chlorophyll a and absorption with bio-optical domains based on nitrate-depletion temperatures. *Journal of Geophysical Research 104*.

Chami, M., E. B. Shybanov, T. Y. Churilova, G. A. Khomenko, M. E.-G. Lee, O. V. Martynov, G. A. Berseneva, and G. K. Korotaev (2005). Optical properties of the particles in the Crimea coastal waters (Black Sea). *Journal of Geophysical Research 110*, C11020.

Chan, T., H. D.P., B. Robson, B. Hodges, and C. Dallimore (2002). Impacts of hydrological changes on phytoplankton succession in the Swan River, Western Australia. *Estuaries 25*, 1406–1415.

Chan, T. and D. P. Hamilton (2001). Effect of freshwater flow on the succession and biomass of phytoplankton in a seasonal estuary. *Marine and Freshwater Research 52*.

Chase, A. P., E. Boss, I. Cetinic, and W. Slade (2017). Estimation of Phytoplankton Accessory Pigments From Hyperspectral Reflectance Spectra: Toward a Global Algorithm. *Journal of Geophysical Research: Oceans 122(12)*.

Cheng, D. K. (1992). *Field and Wave Electromagnetics* (Second ed.). Addison-Wesley Publishing Company, Inc.

Cherukuru, N., T. J. Malthus, B. S. Sherman, E. L. Hestir, and R. A. Devilla (2017). Optical response associated with changing summer biogeochemical conditions in a turbid lake. *Limnologica 63*, 83 – 96.

Chester, R. (2003). *Marine geochemistry*. Wiley-Blackwell.

Clark, M. B. A., J. A.Darling, E. A.Urquhart, J. M.Johnston, A. R.Ignatius, M. H.Myer, K. A.Loftin, P. J. Werdell, and R. P.Stumpfe (2017). Satellite monitoring of cyanobacterial harmful algal bloom frequency in recreational waters and drinking water sources. *Ecological Indicators 80*, 84–95.

Clevelend, J. S. and A. D. Weidemann (1993). Quantifying absorption by aquatic particles: A multiple scattering correction for glass-fiber filters. *Limnology and Oceanography*.

Cox, C. and W. Munk (1954). Measurement of the Roughness of the Sea Surface from Photographs of the Sun's Glitter. *Journal of the Optical Society of America 44*(11), 838–850.

Cox, G. (1993). *Ultrastructure of microalgae*. CRC Press.

Craig, S. E., S. E. Lohrenz, Z. Lee, K. L. Mahoney, G. J. Kirkpatrick, O. M. Schofield, and R. G. Steward (2006). Use of hyperspectral remote sensing reflectance for detection and assessment of the harmful alga, Karenia brevis. *Applied Optics 45*(21), 5414–5425.

Defoin-Platel, M. and M. Chami (2007). How ambiguous is the inverse problem of ocean color in coastal waters? *Journal of Geophysical Research: Oceans 112*.

Dekker, A., S. R. Phinn, J. Anstee, P. Bissett, V. E. Brando, B. Casey, P. Fearns, J. Hedley, W. Klonowski, Z. P. Lee, M. Lynch, M. Lyons, C. Mobley, and C. Roelfsema (2011). Intercomparison of shallow water bathymetry, hydro-optics, and benthos mapping techniques in Australian and Caribbean coastal environments. *Limnology and Oceanography: Methods 9*, 396–425.

Department Of Parks And Wildlife (2015). Swan Canning River Protection Strategy.

Department Of Water (2016). Swan Canning Estuarine Data Report, June 2015 to May 2016. Technical report, Department of Water for the Department of Parks and Wildlife.

Dornhofer, K. and N. Oppelt (2016). Remote sensing for lake research and monitoring - Recent advances. *Ecological Indicators 64*, 105–122.

Duan, H., R. Ma, Y. Xu. J., Zhang, and B. Zhang (2010). Comparison of different semi-empirical models to estimate chlorophyll-a concentration in inland lake water. *Environmental Monitoring and Assessment 170*, 231–244.

Dupouy, C., N. Jacques, G. Dirberg, R. Rottgers, M. Tenorio, and S. Ouillon (2008). Bio-optical properties of marine cyanobacteria Trichodesmium spp. *Journal of Applied Remote Sensing 2*.

Evans, S. J. (2009). A baseline study of contaminants in groundwater at disused waste disposal sites in the Swan Canning catchment. *Water Science Technical Series Report, Department of Water, Western Australia.* (4).

Fearns, P., W. Klonowski, R. Babcock, P. England, and J. Phillips (2011). Shallow water substrate mapping using hyperspectral remote sensing. *Continental Shelf Research 32*, 1249–1259.

Fellman, J., K. Petrone, and P. Grierson (2011). Source, biogeochemical cycling, and fluorescence characteristics of dissolved organic matter in an agro-urban estuary. *Limnology and Oceanography 56*, 243–256.

Feng, L., C. Hu, X. Chen, L. Tian, and L. Chen (2012). Human induced turbidity changes in Poyang Lake between 2000 and 2010: Observations from MODIS. *Journal of Geophysical Research 117*, p. C07006.

Fisher, S. (2013). Investigations of polychlorinated biphenyls and other organic contaminants in the waters of the Swan Canning estuary using passive sampling technology. *Department of Water Technical Report prepared for the Swan River Trust, Western Australia.*.

Foulsham, G., H. Nice, S. Fisher, M. J, M. Bartkow, and Komorova (2009). A baseline study of organic contaminants in the Swan and Canning catchment drainage system using passive sampling devices. *Water Science Technical Series Report Department of Water, Western Australia.* (5).

Fournier, G. and J. L. Forand (1994). Analytic phase function for ocean water. *Ocean Optics XII 2258*, 194–201. J.S.Jaffe (ed.).

Fournier, G. and M. Jonasz (1999). Computer-based underwater imaging analysis. *Airborne and In-water Underwater Imaging 3761*, 62–77.

Fujiki, T. and S. Taguchi (2002). Variability in chlorophyll a specific absorption coefficient in marine phytoplankton as a function of cell size and irradiance. *Journal of Plankton Research*.

Garcia, R. A., P. R. Fearns, and L. I. McKinna (2014). Detecting trend and seasonal changes in bathymetry derived from HICO imagery: A case study of Shark Bay, Western Australia. *Remote Sensing of Environment 147*, 186 – 205.

Giardino, C., M. Bresciani, E. Valentini, L. Gasperini, R. Bolpagni, and V. E. Brando (2015). Airborne hyperspectral data to assess suspended particulate matter and aquatic vegetation in a shallow and turbid lake. *Remote Sensing of Environment 157*, 48 – 57. Special Issue: Remote Sensing of Inland Waters.

Gitelson, A. A., J. F. Schalles, and C. M. Hladik (2007). Remote chlorophyll-a retrieval in turbid, productive estuaries: Chesapeake Bay case study. *Remote Sensing of Environment 109(4)*, 464–472.

Gons, H. J., M. T. Auer, and S. Effler (2008). MERIS satellite chlorophyll mapping of oligotrophic and eutrophic waters in the Laurentian Great Lakes. *Remote Sensing of the Environment 112*, 4098–4106.

Gordon, H. R., O. B. Brown, and M. M. Jacobs (1975). Computed Relationships Between the Inherent and Apparent Optical Properties of a Flat Homogeneous Ocean. *Applied Optics 14*(2), 417–427.

Gordon, H. R., K. Clark, J. Brown, O. Brown, R. Evans, and W. W. Broenkow (1983). Phytoplankton pigment concentrations in the Middle Atlantic Bight: Comparison of ship determinations and CZCS estimations. *Applied optics 22*, 20–36.

Gordon, H. R. and A. Morel (1983). *Remote Assessment of Ocean Color for Interpretation of Satellite Visible Imagery. A Review*. Springer-Verlag, New York.

Gordon, H. R., R. H. E. O. B. Brown, J. W. Brown, R. C. Smith, K. S. Baker, and K. Clarke (1988). A semianalytic radiance model of ocean color. *Journal of Geophysical Research 93*(D9), 10909–10924.

Graham, L. E. and L. W. Wilcox (2000). *Algae*. Prentice Hall.

Griffin, S., M. Herzfeld, and D. Hamilton (2001). Modelling the impact of zooplankton grazing on the phytoplankton biomass during a dinoflagellate bloom in the Swan River estuary, Western Australia. *Ecological Engineering 16*, 373–394.

Hamilton, P., D. G. B., A. J. A., and R. L. C. (2006). Seasonal changes in major ions, nutrients and chlorophyll a at two sites in the Swan River estuary, Western Australia. *57*, 803–815.

Hedley, J., R. C, and P. SR (2009). Efficient radiative transfer model inversion for remote sensing applications. *Remote Sensing of Environment 113*, 2527–2532.

Hedley, J. D. (2008). A three-dimensional radiative transfer model for shallow water environments. *Optics Express 16*(26), 21887–21902.

Hedley, J. D. (2012). Modelling the optical properties of suspended particulate matter of coral reef environments using the finite difference time domain (FDTD) method. *Geo-Marine Letters 32*(2), 173–182.

Hestir, E. L., V. Brando, G. Campbell, A. Dekker, and T. Malthus (2015). The relationship between dissolved organic matter absorption and dissolved organic carbon in

reservoirs along a temperate to tropical gradient. *Remote Sensing of Environment 156*, 395 – 402.

Hick, P. (1997). Determination of water column characteristics in coastal environments using remote sensing.

Hipsey, M., L. Bruce, and K. Kilminster (2013). A 3d hydrodynamic-biogeochemical model for assessing artificial oxygenation in a riverine salt-wedge estuary. In J. Piantadosi, R. Anderssen, and B. J. (Eds.), *MODSIM2013, 20th International Congress on Modelling and Simulation*, pp. 1770–1776. Modelling and Simulation Society of Australia and New Zealand.

Hipsey, M., K. Kilminster, and B. B. (2016a). The Swan - Canning Estuary Response Model (SCERM) v1: Model validation and performance assessment. AED Report no. R29.

Hipsey, M., K. Kilminster, S. Robinson, G. A, and T. K. (2016b). The Swan - Canning Estuary Response Model (SCERM) v1: Model Science Basis and Parameterisation. AED Report no. R28.

Hoek, C., D. G. Mann, and H. M. Jahns (1995). *Algae: an introduction to phycology.* Cambridge University Press. Cambridge.

Huang, C., K. Shi, H. Yang, Y. Li, A. Zhu, and S. D. (2015). Satellite observation of hourly dynamic characteristics of algae with Geostationary Ocean Color Imager (GOCI) data in Lake Taihu. *Remote Sensing of the Environment 159*, 278–287.

Huang, P., M. Hipsey, and B. B. (2017). The Swan - Canning Estuary Response Model (SCERM) v2: Model validation, monitoring data assessment and real - time operation. AED Report no. R34.

Hulst, H. C. V. D. (1957). *Light scattering by small particles.* John Wiley & Sons, Inc. New York.

Huot, Y., M. Babin, F. Bruyant, C. Grob, M. S. Twardowski, and H. Claustre (2007). Does chlorophyll a provide the best index of phytoplankton biomass for primary productivity studies? *Biogeosciences Discussions 4*, 707–745.

IOCCG (2000). *Remote Sensing of Ocean Colour in Coastal, and Other Optically-Complex, Waters*, Volume 3. IOCCG, Dartmouth, Canada.

IOCCG (2006). *Remote Sensing of Inherent Optical Properties: Fundamentals, Tests of Algorithms, and Applications*. IOCCG.

IOCCG (2008). *Why Ocean Colour? The Societal Benefits of Ocean-Colour Technology*. IOCCG.

IOCCG (2014). *Phytoplankton Functional Types from Space*. IOCCG.

Jeffrey, S. W., R. F. C. Mantoura, and S. W. Wright (1997). *Phytoplankton pigments in oceanography*. United Nations Educational, Scientific and Cultural Organization.

Jerlov, N. (1968). *Optical Oceanography, Elsevier Oceanographic Series, v. 5*. Elsevier, Amsterdam, the Netherlands.

Jerlov, N. (1976). *Marine optics, Elsevier Oceanographic Series, v. 14*. Elsevier, Amsterdam, the Netherlands.

Jernakoff, P., P. Hick, C. Ong, W. Hosja, and S. Grigo (1996). Remote sensing of algal blooms in the Swan River. *CSIRO Marine Laboratories Report 226*, 1–39.

Jimenez, R. C., M. Kuzak, M. Alhamdoosh, M. Barker, B. Batut, M. Borg, S. Capella-Gutierrez, N. C. Hong, M. Cook, M. Corpas, M. Flannery, L. Garcia, J. L. Gelpi, S. Gladman, C. Goble, M. G. Ferreiro, A. Gonzalez-Beltran, P. C. Griffin, B. Gruning, J. Hagberg, P. Holub, R. Hooft, J. Ison, D. S. Katz, B. Leskosek, F. L. Gomez, L. J. Oliveira, D. Mellor, R. Mosbergen, N. Mulder, Y. Perez-Riverol, R. Pergl, H. Pichler, B. Pope, F. Sanz, M. V. Schneider, V. Stodden, R. Suchecki, R. S. Varekova, H.-A. Talvik, I. Todorov, A. Treloar, S. Tyagi, M. van Gompel, D. Vaughan, A. Via, X. Wang, N. S. Watson-Haigh, and S. Crouch. (2017). Four simple recommendations to encourage best practices in research software. *F1000Research 6:876*, 13pp.

Johansen, R., R. Beck, J. Nowosad, C. Nietch, M. Xu, S. Shu, B. Yang, H. Liu, E. Emery, M. Reif, J. Harwood, J. Young, D. Mackee, M. Martin, G. Stillings, R. Stumpf, and H. Suh (2018). Evaluating the portability of satellite derived chlorophyll-a algorithms for temperate inland lakes using airborne hyperspectral imagery and dense surface observations. *Harmful Algae 76*, 35–46.

John, J. (1984). *The taxonomy and distribution of diatoms of the Swan River Estuary, Western Australia: phytoplankton of the Swan River Estuary.* Ph. D. thesis.

John, J. (1987). *Phytoplankton in the Swan River Estuary*, pp. 71–90. Curtin University: Bentley, Western Australia.

John, J. and A. Kemp (2006). Cyanobacterial Blooms in the Wetlands of the Perth region, Taxonomy and Distribution: an Overview. *Journal of the Royal Society of Western Australia 89*, 51–56.

Keen, R., V. Brando, P. Daniel, D. McKenzie, L. Woodward, R. Palmer, D. Mills, M. Slivkoff, and W. Klonowski (2012). 2012 Ocean Sciences Meeting, Salt Lake City, Utah, 20-24 February 2012. pp. 2pp. American Geophysical Union.

Kiefer, D. A. and J. B. SooHoo (1982). Spectral absorption by marine particles of coastal waters of Baja California. *Limnology and Oceanography 27*(3), 492–499.

Kirk, J. T. O. (1983). *Light and photosynthesis in aquatic ecosystems*. Cambridge University Press.

Klonowski, W. Hyperspectral survey of Ningaloo Reef Western Australia. [Unpublished].

Klonowski, W., M. J. Lynch, B. T. McGann, P. R. C. S. Fearns, L. A. Clementson, and A. Dekker (2003). Hyperspectral Remote Sensing of Western Australian Coastal Waters. *International Society for Optical Engineering 5515*, 203–210.

Klonowski, W. M., P. R. Fearns, and M. J. Lynch; (2007). Retrieving key benthic cover types and bathymetry from hyperspectral imagery. *Journal of Applied Remote Sensing 1*.

Kostoglidis, A., C. Pattiaratchib, and D. P. Hamilton (2005). CDOM and its contribiution to the underwater light climate of a shallow, microtidal estaury in south-western Australia. *Estuarine, Coastal and Shelf Science 63*, 469–477.

Kuchinke, C. P., H. R. Gordon, and B. A. Franz (2009). Spectral optimization for constituent retrieval in Case 2 waters I: Implementation and performance. *Remote Sensing of Environment 113*, 571–587.

Kutser, T., S. Koponen, K. Y.Kallio, T. Fincke, and B. Paavel (2017). *Chapter 4 - Bio-optical Modeling of Colored Dissolved Organic Matter*, pp. 101–128. Elsevier Inc.

Kutser, T., L. Metsamaa, N. Srombeck, and E. Vahtmae (2006). Monitoring cyanobacterial blooms by satellite remote sensing. *Estuarine, Coastal and Shelf Science 67*(1-2), 303–312.

Ladner, S., R. Arnone, R. Gould, A. W. A. W. Haltrin, Z. Lee, P. Martinolich, and T. Bergmann (2002). Variability in the Backscattering to Scattering and F/Q Ratios Observed in Natural Waters. *Ocean Optics XVI*.

Latchford, J. A., P. Musk, W. Hoskia, A. Begum, R. Srdarev, A. Kidd, and K. King (2003). The determination, management and ramifications of multiple fish kills in the Swan Canning Estuary. In *River Symposium, Swan River Trust.*

Lee, Z., K. Carder, R. Arnone, and M. He (2007a). Determination of primary spectral bands for remote sensing of aquatic environments. *Sensors 7*, 3428–3441.

Lee, Z., K. L. Carder, and R. A. Arnone (2002). Deriving inherent optical properties from water color: a multiband quasi-analytical algorithm for optically deep waters. *Applied Optics 41*, 5755–5772.

Lee, Z., B. Lubac, J. Werdell, and R. Arnone (2009, March). An Update of the Quasi-Analytical Algorithm (QAA v5).

Lee, Z., A. Weidermann, J. Kindle, R. Arnone, K. L. Carder, and C. Davis (2007b). Euphotic zone depth: Its derivation and implication to ocean-color remote sensing. *Journal of Geophysical Research 112*, p. C03009.

Lee, Z. P. (1994). Visible-infrared remote-sensing model and applications for ocean waters. Ph.d. dissertation, University of South Florida, Department of Marine Science, St. Petersburg, Fla.

Lee, Z. P. and K. L. Carder (2002). Effect of spectral band numbers on the retrieval of water column and bottom properties from ocean color data. *Applied Optics 41*, 2191–2201.

Lee, Z. P., K. L. Carder, C. D. Mobely, R. G. Steward, and J. S. Patch (1999). Hyperspectral remote sensing for shallow waters: Deriving bottom depths and water properties by optimization. *Applied Optics 38*(18), 3831–3843.

Lee, Z. P., K. Du, K. J. Voss, G. Zibordi, B. Lubac, R. Arnone, and A. Weidemann (2011). An inherent-optical-property-centered approach to correct the angular effects in water-leaving radiance. *Applied Optics 50*(19), 3155–3167.

Li, L., L. Li, K. Song, Y. Li, L. P.Tedesco, Kun, Shi, and Z. Li (2013). An inversion model for deriving inherent optical properties of inland waters: Establishment, validation and application. *Remote Sensing of Environment 135*, 150–166.

Lucke, R., M. Corson, N. R. McGlothlin, S. Butcher, D. L. Wood, D. Korwan, R. Li, W. Snyder, C. O. Davis, and D. T. Chen (2011). Hyperspectral Imager for the Coastal Ocean: Instrument description and first images. *Applied Optics 50(11)*, 1501–1516.

Lymburner, L., E. Botha, E. Hestir, J. Anstee, S. Sagar, A. Dekker, and T. Malthus (2016). Landsat 8: Providing continuity and increased precision for measuring multi-decadal time series of total suspended matter. *Remote Sensing of Environment 185*, 108 – 118. Landsat 8 Science Results.

Mackinney, G. (1941). Absorption of light by chlorophyll solutions. *J. Biol. Chem 140*, 315 – 322.

Maffione, R. A. and D. R. Dana (1997, August). Instruments and methods for measuring the backward-scattering coefficient of ocean waters. *Applied Optics 36*(24), 6057–6067.

Marrable, D. (2008). Hyperspectral survey of the Swan and Canning Rivers, Perth Western Australia. Honours thesis, Department of Imaging and Applied Physics.

Marrable, D., P. Fearns, W. Klonowski, and M. Lynch (2009). Real-time retrieval of optical properties and bathymetry of coastline and inland waterways using parallel processing and CUDA GPU parallel computing architecture. Supercomputing Conference. Portland, Oregon.

Marrable, D., P. Fearns, M. Lynch, and W. Klonowski (2010). Spectral analysis of estuarine water for characterisation of inherent optical properties and phytoplankton classification. Ocean Optics Conference, Anchorage.

Marrable, D., J. Hedley, P. Fearns, and M. Lynch (2012). Numerical Solutions To Scattering Of Complex Shaped Hydrosols Using The Finite Difference Time Domain Algorithm On The Graphics Processing Unit (GPU). Ocean Optics Conference, Glasgow.

Matthews, M. (2017). *Chapter 6 - Bio-optical modelling of Phytoplankton Chlorophyll-a*, pp. 157–188. Elsevier Inc.

Mie, G. (1908). Contributions to the optics of turbid media, particularly of the colloidal metal solutions. *Annalen der Physik 25*(3), 377–445.

Mishra, S. and D. Mishra (2012). Normalized difference chlorophyll index: a novel model for remote estimation of chlorophyll-a concentration in turbid productive waters. *Remote Sensing of the Environment 117*, 394–406.

Mobley, C. and W. P. Bisset (2011). *CRISTAL user's guide and technical documentation.* Sequoia Scientific, Inc., Bellevue,.

Mobley, C. and L. K. Sundman (2001). *Hydrolight 4.2 Techniocal Documentation* (2 ed.). Sequoia Scientific, Inc.

Mobley, C. D. (1994). *Light and water: radiative transfer in natural waters.* Academic Press New York.

Mobley, C. D. (1999). Estimation of the remote sensing-reflectance from above-surface measurements. *Applied Optics 38*(36), 7442–7455.

Morel, A. (1974). *Optical aspects of oceanography.* Academic Press New York.

Morel, A. and D. Antoine (2000). Pigment index retrieval in Case 1 waters. Technical report, European Space Agency.

Morel, A. and A. Bricaud (1981). Theoretical results concerning light absorption in a discrete medium, and applications to specific absorption of phytoplankton. *Deep-Sea Research 28*(11), 1375–1393.

Morel, A., B. Gentili, H. Claustre, M. Babin, A. Bricaud, J. Ras, and F. Tieche (2007). Optical Properties of the "clearest" natural waters. *Limnology and Oceanography 52*(1), 217–229.

Morel, A. and L. Prieur (1977). Analysis of variations in ocean color. *Limnology and Oceanography 22*, 709–722.

Morris, V. J. and B. R. Jennings (1977). Anomalous diffraction approximation to the low-angle scattering from coated spheres. *Biophysical Journal 17*(1), 95–101.

Mouw, C., H. Chen, G. A. McKinley, S. Effler, D. O'Donnell, M. G. Perkins, and C. Strait (2013). Evaluation and optimization of bio-optical inversion algorithms for remote sensing of Lake Superior's optical properties. *Journal of Geophysical Research: Oceans 118*, 696–1714.

Mouw, C., S. Grebb, D. Aurin, P. diGiacomo, Z. Lee, M. Twardowski, C. Binding, C. Hu, R. Ma, T. Moore, W. Moses, and S. E.Craig. (2015). Aquatic color radiometry remote sensing of coastal and inland waters: Challenges and recommendations for future satellite missions. *Remote Sensing of Environment 160*, 15–30.

Mueller, J. L. and G. S. Fargion (2000). Ocean optics protocols for satellite ocean color sensor validation, revision 2. *National Aeronautics ans Space Administration 2*, 125 – 153.

Mueller, J. L., C. Pietras, S. B. Hooker, R. W. Austin, M. Miller, K. D. Knobelspiesse, R. Frouin, B. Holbern, and K. Voss (2003). Ocean optics protocols for satellite ocean color sensor validation: Instrument specifications, characterization and calibration. *National Aeronautics ans Space Administration 2*(Rev 4), 1–56.

Mueller, N., A. Lewis, D. Roberts, S. Ring, R. Melrose, J. Sixsmith, L. Lymburner, A. McIntyre, P. Tan, S. Curnow, and A. Ip (2016). Water observations from space: Mapping surface water from 25years of Landsat imagery across Australia. *Remote Sensing of Environment 174*, 341 – 352.

Naik, R., A. C. Anil, D. Narale, and V. Kulkarni (2011). Primary description of surface water phytoplankton pigment patterns in the Bay of Bengal. *Journal of Sea Research 65*, 435–441.

Nair, A., S. Sathyendranath, T. Platt, J. Morales, V. Stuart, M.-H. Forget, E. Devred, and H. Bouman (2008). Remote sensing of phytoplankton functional types. *Remote Sensing of the Environment 112*, 3366–3375.

Nice, H. (2013). Claisebrook in the Swan Estuary, Western Australia - A synthesis of environmental information and historical retrospective. *Department of Water Technical Report prepared for the Swan River Trust, Western Australia.*.

Odermatt, D., V. E. B. Anatoly Gitelson, and M. Schaepman (2012). Review of constituent retrieval in optically deep and complex from satellite imagery. *Remote Sensing of the Environment 118*, 116–126.

Ogashawara, I., D. R. Mishra, and A. A.Gitelson (2017a). *Chapter 1 - Remote Sensing of Inland Waters: Background and Current State-of-the-Art*, pp. 1–24. Elsevier Inc.

Ogashawara, I., D. R.Mishra, and A. A.Gitelson (2017b). *Chapter 1 - Remote Sensing of Inland Waters: Background and Current State-of-the-Art*, pp. 1–24. Elsevier.

Olmanson, L. G., M. Bauer, and P. Brezonik. (2008). A 20-year Landsat water clarity cencus of Minnesota's 10,000 lakes. *Remote Sensing of the Environment 112(11)*, 4086–4097.

Olmanson, L. G., J. C. F. Patrick L.Brezonik, and M. E.Bauer (2016). Comparison of Landsat 8 and Landsat 7 for regional measurements of CDOM and water clarity in lakes. *Remote Sensing of Environment 185*, 119–128.

Paavel, B., H. Arst, and A. Herlevi (2007). Dependence of spectral distribution of inherent optical properties of lake waters on the concentrations of different water constituents. *Hydrology Research*, 265–285.

Page, B., A. Kumar, and D. R.Mishra (2018). A novel cross-satellite based assessment of the spatio-temporal development of a cyanobacterial harmful algal bloom. *International Journal of Applied Earth Observation and Geoinformation 66*, 69–81.

Pahlevan, N. and J. R. Scott (2013). Leveraging EO-1 to evaluate capability of new generation of landsat sensors for coastal/inland water studies. *IEEE Journal of selected topics in applied earth observations and remote sensing 6(2)*, 360–374.

Palmer, S., P. D. Hunter, T. Lankester, S. Hubbard, E. Spyrakos, A. N. Tyler, M. Presing, H. Horvath, A. Lamb, H. Baltzer, and V. R. Toth. (2015a). Validation of Envisat MERIS algorithm for chlorophyll retrieval in a large, turbid and optically-complex shallow lake. *Remote Sensing of Environment 157(C)*, 158–169.

Palmer, S., T. Kutser, and P. D. Hunter (2015b). Remote sensing of inland waters: Challenges, progress and future directions. *Remote Sensing of Environment 157*, 1–8.

Pearlman, J., P. Barry, C. Segal, J. Shepanski, D. Beiso, and S. L. Carman (2003). Hyperion, a space-based imaging spectrometer. *IEEE Transactions on Geoscience and Remote Sensing 41*, 1160–1173.

Pennifold, M. and J. Davis (2001). Macrofauna and nutrient cycling in the Swan River Estuary, Western Australia: experimental results. *Hydrological Processes 15*, 2537–2553.

Petrone, K. (2010). Catchment export of carbon, nitrogen, and phosphorus across an agro-urban land use gradient, Swan-Canning River system, southwestern Australia. *Journal of Geophysical Research (Biogeosciences) 115*.

Petzold, T. J. (1972). Volume scattering functions for selected ocean waters. Report, Scripts Inst. Oceanogr.

Pond, S. and G. L. Pickard (1983). *Introductory Dynamical Oceanography* (2nd ed.). ElsivieAcademic Press New York. Oxford.

Pope, R. M. and E. Fry (1997). Absorption spectrum (380 - 700 nm) of pure water. II. Integrating cavity measurements. *Applied Optics 36*(33), 8710–8723.

Pozdnyakov, D., A. Lyaskovsky, H. Grassl, and L. Pettersson (2002). Numerical modelling of transspectral processes in natural waters: implications for remote sensing. *International Journal of Remote Sensing 22*, 1581–1607.

Preisendorfer, R. (1976). *Hydrologic Optics, Vol. II, Foundations.* U.S. Dept. of Commerce, Washington, D.C., USA.

Press, W. H., S. A. Teukolsky, W. T. Veterling, and B. P. Flannery (2007). *Numerical Recipes: The Art of Scientific Computing* (Third ed.). Cambridge University Press. Cambridge.

Quirantes, A. and S. Bernard (2004). Light scattering by marine algae: two-layer spherical and nonspherical models. *Journal of Quantitative Spectroscopy & Radiative Transfer 89*(1-4), 311–321.

Rao, P. V. L., N. Gupta, A. S. B. Bhaskar, and R. Jayaraj (2002, July). Toxins and bioactive compounds from cyanobacteria and their implications on human health. *Journal of environmental biology 23*(3), 215–224.

Richardson, L. (1996). Remote sensing of algal bloom dynamics: new research fuses remote sensing of aquatic ecosystems with algal accessory pigment analysis. *Bioscience 46(7)*, 492–501.

Robson, B. J. and D. P. Hamilton (2003). Seasonal flow event induces a cyanobacterial bloom in a seasonal Western Australian estuary. *Marine and Freshwater Research 54*, 139–151.

Ruiz-Verdu, A., S. Simis, C. de Hoyos, H. Gons, and R. Pena-Martinez (2008). An evaluation of algorithms for the remote sensing of cyanobacterial biomass. *Remote Sensing of the Environment 112*, 3996–4008.

Sathyendranath, S., L. Lazzara, and L. Prieur (1987). Variations in the spectral values of specific absorption of phytoplankton. *Limnology and Oceanography 32*(2), 403–415.

Smith, R. C. and K. S. Baker (1977). *The bio-optical state of ocean waters and remote sensing.* Visibility Laboratory, Scripps Institution of Oceanography, University of California, San Diego.

Smith, R. C. and K. S. Baker (1978). The bio-optical state of ocean waters and remote sensing. *Limnology and Oceanography 23*(2), 247–259.

Smith, R. C. and K. S. Baker (1981). Optical Properties of the clearest natural waters (200-800 nm). *Applied Optics 20*(2), 177–184.

Swan River Trust (2005). River Science. The Science behind the Swan-Canning Clean-up Program. Issue 3.

Swan River Trust (2008). Health Rivers Action Plan: An Action Plan to improve water quality in the Swan Canning river system.

Swan River Trust (2017). Swan Canning River Protection Strategy: 2017 Progress Report.

Thompson, C., T. Rose, and M. Robb (2001). Seasonal water quality patterns in the Swan River Estuary, 1994 - 1998, technical report. Technical Report 23, Swan River Trust, Western Australia.

Thompson, P. (1998). Spatial and Temporal Patterns of Factors Influencing Phytoplankton in a Salt Wedge Estuary, the Swan River, Western Australia. *Estuaries 21*, 801–817.

Thompson, P. and W. Hosja (1996). Nutrient limitation of phytoplankton in the Upper Swan River Estuary, Western Australia. *Marine and Freshwater Research 47*, 659–667.

Twardowski, M. S., E. Boss, J. M. Sullivan, and P. L. Donaghay (2004). Modeling the spectral shape of absorption by chromophoric dissolved organic matter. *Marine Chemistry 89*(1-4), 69–88.

Tweedley, J., C. Hallett, R. Warwick, K. Clarke, and I. Potter (2016). The hypoxia that developed in a microtidal estuary following an extreme storm produced dramatic changes in the benthos. *Marine and Freshwater Researc 67*, 327–341.

Twomey, L. and J. John (2001). Has the Swan River Estuary become more eutrophic? A comparison of the phytoplankton dynamics between 1980-81 and 1994-95. *Hydrological Processes 15*.

Tyler, A., P. D.Hunter, E. Spyrakos, SteveGroom, A. M. Constantinescu, and J. Kitchen (2016). Developments in Earth observation for the assessment and monitoring of inland, transitional, coastal and shelf-sea waters. *Science of The Total Environment 572*, 1307–1321.

Volten, H., J. F. de Haan, J. Hovenier, R. Schreurs, W. Vassen, A. G. Dekker, H. J. Hoogenboom, F. Charlton, and R. Wouts (1998). Laboratory Measurements of angular distributions of light scattered by phytoplankton and silt. *Limnology and Oceanography 43*(6), 1180–1197.

Vos, R., J. Hakvoort, R. Jordans, and B. Ibelings (2003). Multiplatform optical monitoring of eutrophication in temporally and spatially variable lakes. *Science of the Total Environment 312*, 221–243.

Wang, J., G. F. Cota, and D. A. Ruble (2005). Absorption and backscattering in the Beaufort and Chukchi Seas. *Journal of Geophysical Research 110*.

Wang, P., E. Boss, and C. Roesler (2005). Uncertainties of inherent optical properties obtained from semi-analytical inversions of ocean color. *Applied Optics 44*, 4074–4085.

Watanabe, F. S. Y., E. Alcantara, and J. L. Stech (2018). High performance of chlorophyll-a prediction algorithms based on simulated OLCI Sentinel-3A bands in cyanobacteria-dominated inland waters. *Advances in Space Research 62(2)*, 265–273.

Wilkinson, M. D., M. Dumontier, I. J. Aalbersberg, G. Appleton, M. Axton, A. Baak, N. Blomberg, J.-W. Boiten, L. B. da Silva Santos, P. E. Bourne, J. Bouwman, A. J. Brookes, T. Clark, M. Crosas, I. Dillo, O. Dumon, S. Edmunds, C. T. Evelo, R. Finkers, A. Gonzalez-Beltran, A. J. Gray, P. Groth, C. Goble, J. S. Grethe, J. Heringa, P. A. 't Hoen, R. Hooft, T. Kuhn, R. Kok, J. Kok, S. J. Lusher, M. E. Martone, A. Mons, A. L. Packer, B. Persson, P. Rocca-Serra, M. Roos, R. van Schaik, S.-A. Sansone, E. Schultes, T. Sengstag, T. Slater, G. Strawn, M. A. Swertz, M. Thompson, J. van der Lei, E. van Mulligen, J. Velterop, A. Waagmeester, P. Wittenburg, K. Wolstencroft, and J. Z. . B. Mons (2016). The FAIR Guiding Principles for scientific data management and stewardship. *Scientific Data 3*(160018).

Yacobi, Y., A. Gitelson, and M. Mayo (1995). Remote sensing of chlorophyll in Lake Kinneret using high spectral resolution radiometer and Landsat Thematic Mapper: spectral features of reflectance and algorithm development. *Journal of Plankton Research 17 (11)*, 1–19.

Yee, K. (1966). Numerical Solution of Initial Boundary Value: Problems Involving Maxwell's Equations in Isotropic Media. *IEEE Transactions on Antennas and Propagation 14*(3), 302–307.

Ylostalo, P., K. Kallio, and J. Seppala (2014). Absorption properties of in-water constituents and their variation among various lake types in the boreal region. *Remote Sensing of Environment 148*, 190 – 205.

Yoder, J. A., C. R. McClain, J. O. Blanton, and L.-Y. Oey (1987). Spatial scales in CZCS-chlorophyll imagery of the southeastern U.S. continental shelf. *Limnology and Oceanography 32*, 929–941.

Zanchett, G. and E. C. Oliveira-Filho (2013). Cyanobacteria and Cyanotoxins: From Impacts on Aquatic Ecosystems and Human Health to Anticarcinogenic Effects. *Toxins 5*(10), 1896–1917.

Zscheile, F. P. (1941). Plastid pigments with special reference to their physical and photochemical properties and to analytical methods. *Bot Rev 7*, 587 – 648.